# Computational Fluid Dynamics Modelling of Benzene Abatement using Cryogenic Condensation

# Computational Fluid Dynamics Modelling of Benzene Abatement using Cryogenic Condensation

A thesis submitted by

**James Robert Hendry**

For the award of Engineering Doctorate

In Biopharmaceutical Process Development

Biopharmaceutical and Bioprocessing Technology Centre

School of Chemical Engineering and Advanced Materials

Newcastle University

August 2018

# Abstract

This thesis presents a computational fluid dynamics model of aerosol nucleation and growth using a Eulerian-Lagrangian approach. The research aimed to assess the applicability of cryogenic condensation to controlling benzene emissions from an industrial process operated by the industrial research sponsors. Cryogenic condensation is an attractive option for controlling vent emissions of volatile organic compounds (VOCs). In speciality chemicals industries such as pharmaceuticals, nitrogen is often used to create an inert atmosphere in vessel headspace. Cryogenic condensation can utilise the cooling potential of existing nitrogen infrastructure, making the process energy efficient in comparison to conventional alternatives such as adsorption and thermal oxidation. However, many pollutants freeze or desublimate at the low temperatures (ca. -100°C) used in cryogenic condensation. For these high melting point VOCs, a fine particulate could form under the temperature gradients inside the condenser.

Through modelling the process, the research aimed to answer two main questions: will cryogenic condensation control benzene vapour emissions down to the limits set by the environmental regulators; and will it reach this limit without generating a benzene aerosol particulate that becomes entrained in the outlet gas. The research found that the cryogenic condensation alone would not reach the strict emissions limit required by the regulation, and that particle entrainment does make a contribution to this. The model showed roughly 97% of benzene is captured (compared to 99.978% removal that would be required to meet emissions limits) with around 1% escaping as particulate. This information is useful to the industrial sponsors of the research, and other industries considering using cryogenic condensation for benzene abatement. The modelling approach used is a novel contribution to the field with wider potential applications in other areas.

# Acknowledgements

I would like to thank my supervisors Dr Jonathan Lee and Dr Michael Battrum for their contributions to the EngD project. I would like to thank the head of department Professor Adam Harvey, and department coordinators Nikki Hawley, Sharon Corson and Alison Walker.

I would like to thank my family and friends for their support and encouragement during my time on the EngD programme.

Lastly, I would like to thank Professor Elaine Martin, Dr Lucy Foley and Professor Gary Montague, for their initial involvement in the BBTC. I'd like to thank Dr Ricardo Caldeira for his initial involvement with the EngD Project at Aesica.

# Nomenclature

| Symbol | |
|---|---|
| $a$ | Channel height (m) |
| $A_{0,1,2.}$ | Constants in polynomial expansions |
| $\mathbf{A_i}$ | face-normal vector in mesh metrics |
| $b$ | Channel width (m) |
| $\overline{c}_A$ | Mean molecular speed (m/s) |
| $C_c$ | Cunningham slip correction factor (dimensionless) |
| $C_d$ | Drag coefficient (dimensionless) |
| $C_g$ | Condensation rate for g-mer sized cluster (1/s) |
| $C_{g^*}$ | Condensation rate for a critical cluster (1/s) |
| $\mathbf{C_i}$ | vector between neighbouring cell centres in mesh metrics |
| $C_p$ | Specific heat capacity (J/kg-K) |
| $D$ | Diffusivity ($m^2/s$) |
| De | Dean number (dimensionless) |
| $D_\omega$ | Cross-diffusion term in turbulence model |
| $d_{hydraulic}$ | Hydraulic diameter (m) |
| $d_{intwin}$ | Size of interrogation area (m) |
| $d_p$ | Particle diameter (m) |
| $E_g$, $E_{g+1}$ | Evaporation rate for g-mer, g+1-mer sized cluster (1/s) |
| $E_{\theta t}$,$E_\gamma$, $P_{\theta t}$,$P_\gamma$ | Source terms in transition SST model |
| $F$ | Force |
| $F$ | Pre-exponential factor in classical nucleation theory ($1/m^3s$) |
| $F_1$ | Blending function in turbulence model |
| $F_s$ | safety factor used to calculate grid convergence index |
| $f$ | Any solution result used to test grid independence |
| $f^\#$ | f-number of lens in PIV study |
| $f_g$, $f_{g+1}$ | Gas concentration of g-mers, g+1-mers, in unsteady conditions ($1/m^3$) |
| $g$ | Number of monomers in a cluster |
| $g$ | Mesh inflation layer growth rate |
| GCI | Grid convergence index |

| | |
|---|---|
| $\Delta G_{cluster(r)}$ | Gibbs free energy change of a cluster of radius r (J) |
| $\Delta G_v$ | Volume free energy change (J/m$^3$) |
| $\Delta G^*$ | Critical Gibbs free energy change (J) |
| $h$ | Mesh spacing (m) |
| $h_{lat}$ | Latent heat (J/kg) |
| $I$ | Rate of transformation of g to g+1-mers (1/m$^3$s) |
| $I_{coag}$ | Coagulation integral |
| $J$ | Nucleation rate (1/m$^3$s) |
| $k$ | Turbulent kinetic energy (J/kg) |
| $k_B$ | Boltzmann constant (1.38 x10$^{-23}$ J/K) |
| $k_g$ | Thermal conductivity of gas (W/m-K) |
| $k_p$ | Thermal conductivity of particle (W/m-K) |
| $K_{GI}$ | Overall gas mass transfer coefficient () |
| $Kn_p$ | Knudsen number of particle (dimensionless) |
| $Kn_{AB}$ | Knudsen number of mass transfer to particle (dimensionless) |
| Le | Lewis number (dimensionless) |
| $M$ | Molar mass (kg/mol) |
| $m$ | Mass of a molecule (kg) |
| $\dot{m}$ | Mass flow rate (kg/s) |
| mf | Mass fraction |
| $m_p$ | Mass of a particle (kg) |
| $M_0$ | Lateral magnification |
| $\mathbf{n}$ | Particle number density function (m$^{-4}$) |
| N” | Molar flux (mol/m$^2$s) |
| $N_A$ | Avogadro’s number (6.022 x10$^{23}$ mol$^{-1}$) |
| $n_1$ | Concentration of condensable species, molecules per unit vol (1/m$^3$) |
| $n_{cells}$ | Number of mesh cells in the inflation layer |
| $n_g$ | Number concentration of clusters of size g (1/m$^3$) |
| $n_{(r)}^{equ}$ | Equilibrium number of particles of radius r (1/m$^3$) |
| $n_{sb}$ | Number of mesh cells in the swept method |
| Nu | Nusselt number (dimensionless) |

| | |
|---|---|
| p | Order of convergence in grid independence study |
| P | Pressure (Pa) |
| $P_e$ | Equilibrium vapour pressure (Pa) |
| $P_i$ | Partial pressure (Pa) |
| Pr | Prandlt number (dimensionless) |
| $P_T$ | Total pressure (Pa) |
| $q_c$ | Condensation coefficient (dimensionless) |
| r | Radius (m) |
| r* | Critical radius (m) |
| R | Universal gas constant (8.314 J/mol-K) |
| R* | Apparent convergence condition |
| $\dot{r}$ | Growth rate (m/s) |
| $\boldsymbol{r}$ | Mesh refinement ratio |
| $r_{bend}$ | Bend radius of pipe (m) |
| Re | Reynolds number (dimensionless) |
| $Re_{d\ hydraulic}$ | Reynolds number based on hydraulic diameter (dimensionless) |
| $Re_p$ | Reynolds number of particle (dimensionless) |
| $\widetilde{Re}_{\theta t}$ | Transported transition onset Reynolds number (dimensionless) |
| S | Degree of supersaturation (dimensionless) |
| $\mathbf{S}$ | Scalar invariant of strain rate tensor |
| $S_b$ | Mesh sweep bias |
| Sc | Schmidt number (dimensionless) |
| Sh | Sherwood number (dimensionless) |
| $S_{ij}$ | Strain rate tensor |
| Stk | Stokes number(dimensionless) |
| $S_\phi$ | Source term |
| t | Time (s) |
| T | Temperature (K) |
| $T_F$ | Temperature at condensate film (K) |
| $T^{in}$ | Temperature at inlet (K) |
| $\Delta t$ | Laser pulse delay in PIV study (s) |

| | |
|---|---|
| $u$ | Velocity (m/s) |
| $u^*$ | Dimensionless velocity (alternative formulation) |
| $U_{max}$ | Maximum velocity in PIV study (m/s) |
| $U_{\tau w}$ | Shear velocity (m/s) |
| $v_d$ | Deposition velocity ($m^3/m^2s$) |
| $V_m$ | Molar volume ($m^3$/mol) |
| $v_m$ | Volume occupied by a molecule in the condensed state ($\rho_p/m$ or $V_m.N_A$) ($m^3$) |
| $v_p$ | Particle velocity (m/s) |
| $v_{\mathbf{p}}$ | Particle volume ($m^3$) |
| $x$ | Co-ordinate (m) |
| $\mathbf{X}$ | Chi parameter |
| $x_A$ | Mole fraction of component A |
| $\Delta x$ | separation distance in PIV study (m) |
| $y$ | Co-ordinate (m) |
| $y_{1st\ cell}$ | First cell height (m) |
| $y_{total\ height}$ | Height of inflation layer (m) |
| $y_{last\ cell\ height}$ | Height of last cell in inflation layer (m) |
| $y^+$ | Dimensionless distance from the wall |
| $Y(T)$ | Vapour concentration, mass ratio (g/kg) |
| $Y_s(T_F)$ | Saturation vapour concentration at condensate film, mass ratio (g/kg) |
| $Y^{in}$ | Vapour concentration at inlet, mass ratio (g/kg) |
| $Z$ | Zeldovich factor |

Greek

| | |
|---|---|
| $\alpha$ | Dampening function in turbulence model |
| $\beta$ | Turbulence model constant |
| $\beta^*$ | Turbulence model constant |
| $\gamma$ | Heat capacity ratio (dimensionless) |
| $\boldsymbol{\gamma}$ | Intermittency |
| $\Gamma$ | Diffusion coefficient |
| $\delta(r-r^*)$ | Dirac function |
| $\delta_{ij}$ | Kronecker delta |

| | |
|---|---|
| $\varepsilon$ | Turbulent dissipation rate (J/kg-s) |
| $\rho_g$ | Gas density (kg/m$^3$) |
| $\rho_p$ | Particle density (kg/m$^3$) |
| $\theta$ | Angle in mesh metrics |
| $\theta_{Fletcher}$ | Fletcher factor |
| $\theta_{Kantrowtiz}$ | Kantrowitz factor |
| $\Theta_{cf}$ | Fog correction factor for mass transfer (dimensionless) |
| $\Theta_{tf}$ | Fog correction factor for heat transfer (dimensionless) |
| $\lambda$ | Wavelength of light (m) |
| $\lambda_{AB}$ | Mean free path of diffusing species (m) |
| $\lambda_g$ | Mean free path of gas (m) |
| $\mu_g$ | Gas dynamic viscosity (kg/m-s) |
| $\mu_t$ | Turbulent viscosity (kg/m-s) |
| $\sigma$ | Interfacial energy (N/m) |
| $\sigma_k$ | Turbulent Prandlt number for kinetic energy |
| $\sigma_\omega$ | Turbulent Prandlt number for turbulent frequency |
| $\tau_f$ | Characteristic time of the fluid (s) |
| $\tau_p$ | Response time of the particle (s) |
| $\tau_{ij}$ | Reynolds stress tensor |
| $\tau_w$ | Wall shear stress (Pa) |
| $\vartheta$ | Contact angle |
| $\phi$ | Any transported variable |
| $\phi'(t)$ | Instantaneous fluctuation component of transported variable |
| $\Phi$ | Time-averaged component of transported variable |
| $\omega$ | Turbulent frequency (s$^{-1}$) |

Subscripts

| | |
|---|---|
| 0,1,2. | Denotes constant terms in expressions |
| 1,2,3 | Of mesh refinement, in the order of finest first (1) |
| a | diameter of an apperated image point source (m) |
| A | Of component A |
| AB | Of component A in component B |

| | |
|---|---|
| bend | Of a pipe bend |
| Bz | Of benzene |
| c | At the critical point |
| coag | Coagulation |
| cr | Critical degree of |
| div | Divergence |
| F | Of film |
| g | Of gas |
| g | Of a cluster, size g molecules |
| grad | Gradient |
| het | Heterogeneous |
| hom | Homogeneous |
| i,j,k | Components of vectors in x,y, and z direction |
| in | At inlet |
| lat | Latent |
| nucl | Nucleation |
| $N_2$ | Of nitrogen |
| ref | Denotes constant terms in Sunderland’s formula. |
| o | At the gas/liquid interface |
| p | Of particle |
| s | Diffraction-limited spot diameter (m) |
| sat | Saturation |
| t | Particle image diameter (m) |
| $\infty$ | In the bulk fluid |
| $\theta t$ | Relating to the transition onset Reynolds number |
| $\gamma$ | Relating to intermittency |

# Glossary of Terms

Abatement technology: a unit operation used to control VOC emissions to atmosphere. Cryogenic condensation, regenerative thermal oxidation, and absorption are all abatement technologies.

CCD: Charge coupled device. Digital camera used in PIV study.

CFD: Computational fluid dynamics.

COP: Coefficient of performance. Measure of efficiency for refrigeration and heat pump systems. ratio of heat moved to work input.

DCM: Dichloromethane.

DES: Discrete Eddy Simulation.

Desublimation: describes the process of phase transitions directly from a gas to a solid.

Deposition: describes the process whereby particles collide with a surface, becoming attached to it.

DI: De-ionised water.

DPM: Discrete phase model. The Eulerian-Lagrangian approach in the commercial CFD software ANSYS® FLUENT®.

DSMC: direct simulation Monte-Carlo.

EWT: Enhanced wall treatment.

FIC: Flow indicator and controller (process flow diagram symbol).

Flurbiprofen manufacture: As Aesica is the main manufacturer of flurbiprofen globally, “flurbiprofen manufacture” is used in this text to both refer to the process of manufacturing flurbiprofen as an active pharmaceutical ingredient generally, and to refer to the specific process equipment and unit operations used to manufacture flurbiprofen at Aesica Cramlington.

FTIR: Fourier transform infra-red.

LNG: Liquefied natural gas.

MEA: Monoethanolamine.

MUSCL: Monotonic upwind scheme for conservation laws.

NSAID: Non-steroidal anti-inflammatory drug.

PIV: Particle image velocimetry.

PSA: Pressure swing adsorption.

Pseudo-continuous: describes the practice of operating several units in batch mode and alternating between those units to achieve continuous operation.

QUICK: Quadratic upstream interpolation for convective kinematics.

RANS: Reynolds averaged Navier-Stokes model.

RTO: regenerative thermal oxidisation. An abatement technology that destroys air pollutants using high temperatures, usually made efficient though heat exchange.

SIMPLE: Semi-implicit method for pressure-linked equations. algorithm used to solve pressure field.

SLD: Super-cooled large droplet. Type of ice accretion on aircraft.

SST: Shear-stress transport model.

UDF: user-defined functions. User computer code used inside the commercial CFD software ANSYS® FLUENT®.

URF: under-relaxation factor.

VOCs: volatile organic compounds. Compounds that have organic chemistry (usually hydrocarbons) that are pollutants, usually in the form of vapour in the atmosphere.

Nd:YAG: neodymium-doped yttrium aluminium garnet. type of laser used commonly in PIV.

# Contents

# Chapter 1. Introduction

Controlling the emission of volatile organic compounds (VOCs) is a challenge for a broad spectrum of industries. The pharmaceutical industry relies on VOCs as solvents and reactants to make medicines that are vital to many people's quality-of-life. The abatement of VOC emissions is required in other industries not associated with chemicals manufacture, ranging from the food industry to wastewater treatment. VOCs are a broad class of environmental pollutants, with a range of material properties, and posing a range of environmental hazards. The choice of best-available technique in abating atmospheric VOC emissions is highly case-specific. Factors such as the volatility, solubility and the required abatement level of the VOC, together with carrier gas properties such as flowrate and concentration are factors in the appropriate choice of VOC abatement technology.

Cryogenic condensation is a recent addition to the choice of VOC abatement technologies that are commercially available in the speciality chemicals sector. This growing market has been driven by the development and sale of pre-constructed modular units. Inside these units vent gases are cooled by indirect heat exchange with a cryogen (typically, liquid nitrogen) condensing and separating the VOC from the vent gas stream.

This thesis focusses on the potential applicability of cryogenic condensation to benzene abatement. Benzene freezes at +5.5°C, solid benzene will therefore form inside a cryogenic condenser. At low inlet concentrations this will occur through a process of desublimation. This thesis covers the development of a computational fluid dynamics (CFD) model of the process. The study has two main goals: to determine the outlet vapour concentration from a cryogenic condenser applied to desublimate benzene from an industrial flue gas stream, and to determine whether an aerosol benzene particulate will form, becoming entrained in the outlet gas. In this work a Eulerian-Lagrangian model is developed that models the nucleation, growth and trajectory of benzene particulate as it desublimates within the condenser. The remainder of this chapter gives a brief background to the research, with a focus on the need to control atmospheric emissions of benzene. Fundamentals regarding the control of atmospheric emissions are explored in a broad sense and discussed in the context of the industrial case study that forms the basis of the research. Conventional abatement technologies are also discussed in a similar manner. The chapter concludes with a justification of the approach, and an outline of the remainder of the thesis.

## 1.1 Background to the Research

The research project has been conducted through an industry-academia partnership. The industrial sponsors of the research are Aesica Pharmaceuticals Ltd. The research is specific to the Aesica Pharmaceuticals active pharmaceutical ingredient (API) manufacturing site in Cramlington, Northumberland (hereon: Aesica Cramlingon). The site is the world's largest manufacturer of flurbiprofen, a non-steroidal anti-inflammatory drug (NSAID) chiefly used to alleviate symptoms of arthritis. Flurbiprofen manufacture generates vent emissions containing benzene vapours. This research is focussed on determining whether cryogenic condensation is a valid alternative to the current method of abatement used in flurbiprofen manufacture.

## 1.2 Control of VOCs in the United Kingdom (UK)

Commitment to national and international emissions targets can drive scientific development. The UK is a signatory to the convention on long-range transboundary air pollution (CLRTAP). Emission of non-methane VOCs such as benzene is covered by the Gothenburg protocol[*]. The UK met the original Gothenburg protocol ceilings in 2010 (1200 kilotonnes/a), and is currently on-track to meet the revised Gothenburg protocol ceiling 2020 (740 kilotonnes/a (EPA, 2010)). Meeting these and future targets is becoming more difficult with time as 'low hanging fruits' are eliminated, creating a need to develop new technological solutions (Drabble, 2015).

## 1.3 Benzene Toxicity

Benzene is both a chemical toxicant and a genotoxic carcinogen. Toxic effects of benzene exposure have been known for at least a century (Kamrin, 1988, p. 96), and by 1981 regulators in six countries recognised benzene as carcinogenic (IARC, 1982). Benzene is a group one carcinogen under IARC classifications (IARC, 2012). Carcinogenic and chronic toxicity impact the haemopoietic system (blood production). Epidemiological studies have definitively established benzene as a leukaemogen. Aplastic anaemia is the most common manifestation of chronic occupational exposure (Chilcott, 2013).

## 1.4 Benzene Use

Despite the well-known health effects of benzene, its use remains ubiquitous in the process industries. In 2014 it was the sixth most common chemical product by volume in the United States (Schillaci, 2014). Global production is predicted to increase by 3.5% annually, exceeding 50 million metric tonnes per annum by 2020 (Yennigalla and Hetian, 2015). The dominant

---

[*] The Gothenburg protocol is implemented through the National Emissions Ceilings Directive. Under the EU Withdrawl bill this will remain UK law post march 2019 (at the time this goes to print. see Appendix 8.2).

source (over 95% (Matar *et al.*, 1989, p. 54)) of benzene is as a coproduct from refinery and petrochemical operations, such as catalytic reforming, pyrolysis gasoline (ethylene/propylene cracking), and production from toluene de-alkylation.

Benzene is an important chemical intermediate. The majority of benzene is used in polymers: ethylbenzene/styrene accounting for over half of benzene use; cyclohexane, used to manufacture nylon intermediates, taking a further 10%; 17% is used to manufacture cumene, which is almost totally consumed in phenol manufacture (IARC, 2012; Yennigalla and Hetian, 2015); itself used primarily in resins and copolymers. Though historically important as an industrial solvent, benzene use in this area has diminished significantly in recent decades, being replaced with safer alternatives in most applications. Replacing benzene as a chemical intermediate however is more difficult. This is particularly true in pharmaceutical manufacture, in which process changes are burdened with costs and risks not present in other industries. This is discussed in more detail in section 1.6 below.

## 1.5 Environmental Controls on Benzene

As a genotoxic carcinogen, no residual concentration of benzene can be considered absolutely safe. However, long-term work place exposure of less than 1ppm, (ca. 3.2 mg/Nm$^3$) has not been correlated to an increase in deaths from leukaemia (IPCS, 1993). Most workplace exposure limits reflect this, requiring parts-per-million level control of benzene concentration in the air. Historically, workplace exposure limits have informed the setting of environmental limits by providing consistent evidence-based sources for risks associated with exposure levels (Drabble, 2015).

| | | |
|---|---|---|
| UK: | 9.6 mg/Nm$^3$ | (time-weighted average) |
| US: | 3.2 mg/Nm$^3$ | (permissible exposure limit,) |
| | 16 mg/Nm$^3$ | (short-term exposure limit) |
| Australia: | 16 mg/Nm$^3$ | (time-weighted average) |
| Finland: | 15 mg/Nm$^3$ | (time-weighted average) |
| | 30 mg/Nm$^3$ | (short-term exposure limit) |
| Thailand: | 30 mg/Nm$^3$ | (time-weighted average) |
| | 75 mg/Nm$^3$ | (short-term exposure limit) |

*Table 1. Selected workplace exposure limits (Pohanish, 2011, p. 344).*

Inhalation is a significant route to benzene exposure in the workplace. Benzene is a VOC, with an ambient vapour pressure equivalent to a concentration of 140g/Nm$^3$ in air. Benzene is a non-polar hydrocarbon, but is sparingly soluble in water (1700g/m$^3$ water, 20°C) making inhalation an effective route to exposure. Industrial processes which handle or create benzene must control benzene concentrations in vent gas emissions from these processes. Regulators typically set benzene vent emission targets at the ppm (mg/Nm$^3$) level - see Table 2. These are set based on 'best available techniques': as mature technologies (such as adsorption and thermal oxidation) are capable of achieving these concentrations, the limits are set at these values to encourage best practice in industry (BAuA, 2006).

The motives behind environmental regulations are twofold, aiming to reduce the impact of individual installations, and to improve air quality on a regional and national level. Controlling vent emissions at-source also controls ambient benzene concentrations. Ambient benzene concentrations in the UK are monitored by the Non-Automatic Hydrocarbon Network. This organisation assesses regional compliance to UK objectives (3.25 µg/m$^3$ to 16.25µg/m$^3$ running annual mean) and the European Commission Air Quality Directive Limit Value (5 µg/m$^3$ annual mean) (DEFRA, 2012). For flurbiprofen manufacture at Aesica Cramlington, vent gas emissions to atmosphere must meet a concentration limit of 5mg/Nm$^3$ set by the environmental regulators (Simmons, 2009).

| Limit | Source | |
|---|---|---|
| 1mg/Nm$^3$ | German Technical Instruction on Air Quality | (BAuA, 2006) |
| 2mg/Nm$^3$ | European Commission | (Verspoor, 2007) |
| 5mg/Nm$^3$ (proposed) | India – Central Pollution Control Board | (CPCB, 2007) |
| 5mg/Nm$^3$ | Slovakia | (BAuA, 2006) |
| 5mg/Nm$^3$ | World Bank Group | (UN Environment Programme, 1998) |

*Table 2. Selected benzene concentration limits for industrial vent emissions to atmosphere.*

## 1.6 Benzene Use in Flurbiprofen Manufacture

Benzene is necessary for a single reaction step during flurbiprofen manufacture. Benzene is used as both a solvent and a reactant in a modified Gomberg-Bachmann reaction (Adams *et al.*, 1976). Emissions of benzene originate from this reaction step, related separation steps, and steps which purify benzene for re-use. Vents from these processes are treated for bulk removal of contaminants using a system comprising condensers (water or refrigerant cooled), toluene absorption, and $NaOH_{(aq)}$ absorption (eliminating $HCl_{(g)}$ vapours). When considering any pollution prevention measure, it is wise to first consider whether emissions may be reduced or eliminated at the source. This subsection will discuss benzene use in flurbiprofen manufacture.

The modified Gomberg-Bachmann reaction is described by Adams *et al.* (1976). This description is reproduced schematically in Figure 1. The reaction produces the biphenyl group in the final flurbiprofen product, shown in blue in Figure 2. This illustrates the reactant role of benzene. The Gomberg-Bachmann reaction proceeds through a free radical mechanism (Li, 2014, p. 287). Due to the short lifespan of the reaction intermediate, benzene must be present at high concentrations, as a solvent, to prevent side-reactions that reduce yield. This key role makes it difficult to replace or reduce benzene use in flurbiprofen manufacture.

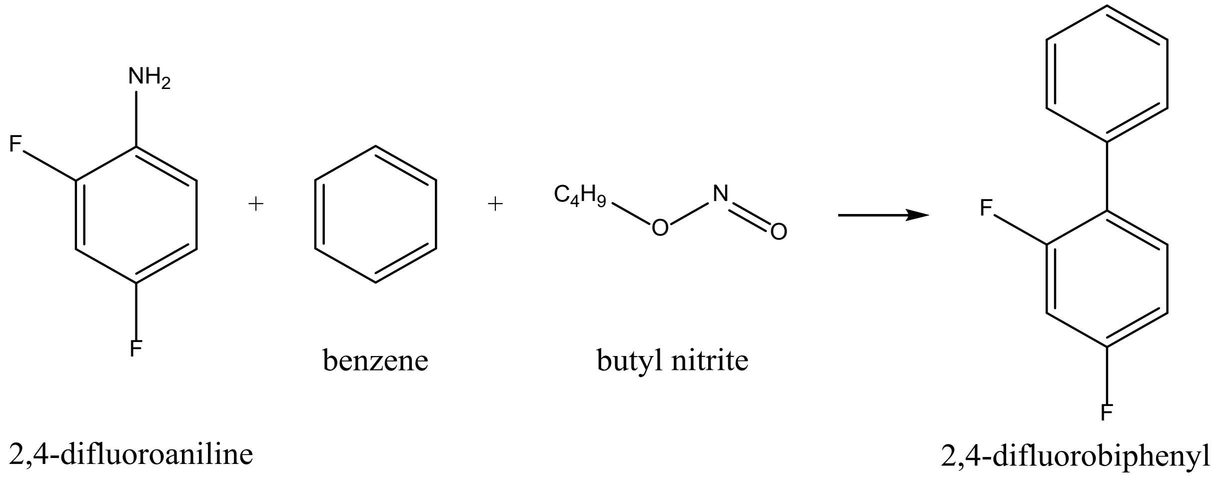

*Figure 1: Gomberg-Bachmann reaction.*

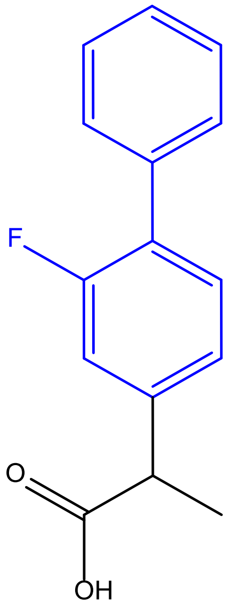

*Figure 2: Flurbiprofen.*

Alternatives to the Gomberg-Bachmann reaction have been proposed. The Ullmann reaction is one alternative referred in patent literature (Adams *et al.*, 1976; Schlosser and Geneste, 1998). Lu *et al.* (2006) synthesised flurbiprofen in aqueous solution using a Pd/C-catalysed Suzuki reaction. A Suzuki reaction was also proposed by Schlosser and Geneste (1998). Ullmann reactions can have unpredictable selectivities and yields. The conventional Ullmann reaction requires stoichiometric quantities of copper catalyst, which is costly and risks product contamination, though modern versions often require much lower catalyst concentrations. The

Suzuki reaction reported by Schlosser and Geneste (1998) required a temperature of -75°C. These can be reached in industrial processes using cryogenic stirred tank reactors. Liquid nitrogen is used to cool an intermediate heat transfer fluid, providing jacket cooling to a built-for-purpose stirred tank reactor (eg: Praxair inc. NCOOL$^{TM}$). This is typically applied as a last-resort for scaling up valuable products.

In practice, implementing process changes to the existing facility faces several barriers. New process development and scale-up would require a large capital investment and would carry a high degree of technical and commercial risk. The plant at Aesica Cramlington has been optimised for flurbiprofen manufacture using the current process. Reuse of solvents such as benzene has improved the process economics considerably, but entrenches the plant operation through high-capex downstream operations. As a raw material, benzene is cheaper in comparison to substituted aromatics, proposed in the alternatives to the Gomberg-Bachmann reaction, that are listed above. Substituted aromatics may still require parts-per-million level abatement of atmospheric emissions (Simmons, 2009). These may include unwanted volatile reaction by-products. For these reasons, Aesica are currently focussed on end-of-pipe technologies as a means to control benzene vent emissions from flurbiprofen manufacture.

## 1.7 **Conventional Techniques in VOC Abatement**

At Aesica Cramlington, benzene emissions are currently controlled using regenerative thermal oxidation (RTO). This is an established technique for parts-per-million level control of VOC emissions in vent gases. This section will describe this and other conventional techniques used in VOC abatement. Whilst a full consideration of every alternative abatement technology is outwith the scope of this work, each subsection concludes with a consideration of the abatement technology in the context of controlling benzene emissions from flurbiprofen manufacture.

### *1.7.1 Thermal oxidation*

Thermal oxidisers destroy VOCs by oxidation. Conventionally, this is achieved through combustion or catalysis at high temperature. Thermal oxidation without heat recovery is the simplest option for thermal oxidation, but is only economical for low and intermittent flows of high VOC content. Combustion is achieved by igniting the VOC-laden stream itself (flaring) or by burning the VOC-laden gas with additional fuel inside a combustion chamber (afterburner). Heat recovery is economical in most cases, and may be recuperative or regenerative. Recuperative heat recovery is achieved using heat exchangers (cross flow, shell-and-tube designs are the most common). Thermal efficiencies of 60 to 70% are typical with this design. Cost-effective operation can therefore rely on heating value of the VOC present in the incoming stream. Units are limited to cooler temperatures due to the metallurgical limits of the heat exchanger. Catalytic oxidisers operate at lower temperatures (ca. 400°C) and for this reason often use recuperative heat recovery.

Regenerative heat recovery is achieved by direct heat exchange using packed beds of ceramic material. Heat from the outlet of the combustion chamber is transferred to one bed before venting to atmosphere. Incoming gas is heated by passing through a hot bed of ceramic packing. Beds are periodically switched using a diverter valve. Common designs use two separate beds, or a single cylindrical bed subdivided into sections. Regenerative designs can achieve thermal efficiencies as high as 97% (Lewandowski, 1999, p. 218). Regenerative thermal oxidisers (RTOs) may run without external energy input during normal operation if the initial VOC concentration is high (over 2.1g/Nm$^3$ typically).

Regenerative thermal oxidisers achieve destruction of VOCs by combustion. Gases are typically held at ca. 900°C for a residence time of ca. 1 s inside the combustion chamber. These conditions lead to a destruction efficiency of 99% for benzene (Cheremissinoff, 2002, p. 482). RTOs typically have a short working life (ca. 14 years) due to deterioration of the diverter valve and refractory lining (Slaughter, 2006).

In flurbiprofen manufacture, the RTO provides the final emission control before vent gases are released to the atmosphere. The combustion chamber operates at 925°C for ca. 2.4s. Based on recent on-site data, the RTO has a thermal efficiency of 95% and a destruction efficiency of 96% for benzene. There are two main issues with the RTO currently: the unit is nearing the end of its working life; and incurring substantial energy costs (£140,000/a) during operation. The unit was originally installed in 2003, and a residual concentration of $HCl_{(g)}$ present in the combustion gases has accelerated internal corrosion. 90% of this energy cost is due to fuel (natural gas) used to run the RTO (the remaining costs stem from electrical demand of the associated duct fans and valve drives). The financial benefit of using cryogenic condensation in place of RTO in flurbiprofen manufacture is the motivation for this research.

### *1.7.2 Adsorption*

Adsorption is the main alternative to thermal oxidation for parts-per-million level control of VOCs. Common adsorbents include activated carbon and hydrophobic zeolite. Adsorption units may consist of a rotating wheel, or a system of packed beds operated pseudo-continuously. Rotary adsorption units may be used in conjunction with thermal oxidation for VOC control, and are appropriate for large flows (over 21,000 Nm$^3$/hr typically) of low VOC concentration (Noordally *et al.*, 1994). Pseudo-continuous operation of packed beds is a more common design. Bed regeneration may be accomplished using temperature swing, pressure swing adsorption (PSA) or periodic disposal. Periodic disposal is appropriate for low abatement targets, but incurs high operating costs and creates hazardous solid wastes. PSA is normally applied in cases where the untreated gas is under pressure (such as in natural gas processing applications, e.g. hydrocarbon dewpt. control). Vacuum desorption is also possible following adsorption at atmospheric pressure. Desorbed VOC may be captured by condensation downstream of the vacuum pump.

In an industrial setting, desorption by temperature swing may be accomplished by passing steam through the bed. Resulting vapours may then be captured as a two-phase condensate, and the organic layer may be recovered. This desorption step is followed by a bed drying/cooling stage and therefore commonly uses three beds. Thermal desorption may also be accomplished with a hot gas. Hot air can be used with a compact incinerator design (such as an afterburner or recuperative catalytic oxidiser) for destruction of the gases downstream.

In flurbiprofen manufacture, adsorption using activated carbon has been applied in the past for controlling benzene emissions. This unit experienced a bed fire in 2002, which led to its replacement with the RTO. This experience has resulted in a culture at Aesica Cramlington that views adsorption as a risk to plant safety. Hydrophobic zeolites, which would eliminate the risk of bed fire, are typically used as a final polishing step downstream of other abatement technologies due to the cost of the adsorbent itself (Ojala *et al.*, 2015).

### *1.7.3 Absorption*

Absorption is appropriate for bulk removal of VOCs. It is impractical for use in parts-per-million level VOC control. . Using oil absorption, Ozturk and Yilmaz (2006) reduced benzene vapour concentrations from an initial $8g/Nm^3$ to $800mg/Nm^3$. This is orders of magnitude higher than typical environmental emissions limits. The benzene vapour pressure approaches equilibrium with the liquid phase at the top of the absorption column. To reach lower gas concentrations requires higher liquid flowrates and better regeneration of the returning liquid. So absorption becomes unfeasible for very low outlet vapour concentrations, due to issues such as equipment size.

In flurbiprofen manufacture, absorption is used to control bulk emissions of benzene during the Gomberg-Bachmann reaction. A packed column is used with a recirculating volume of chilled (+1°C) toluene, which is replaced periodically. Another absorption step is applied downstream. This uses $NaOH_{(aq)}$ to control $NO_x$ and HCl emissions from flurbiprofen manufacture. This is unlikely to capture benzene, which is unreactive with NaOH and has a low solubility in water

(1.18g/l at 10°C (Hefter, 1986)). However these absorbers affect the operations downstream. The vent gas is expected to be saturated with water. During adsorption on activated carbon, benzene is preferentially displaced by toluene (Gupta and Verma, 2002). This would affect the applicability of adsorption as the final removal step.

### *1.7.4 Biological treatments*

Biological treatments accomplish destruction biologically, by metabolising the pollutant in a mixed culture of microorganisms. Designs fall into three broad categories: biofilters, biotrickling filters, and bioscrubbers.

Biofilters consist of packed beds of immobilised culture on a carrier. Peat is one common carrier for treating gases containing monoaromatics. Peat supplies a nutrient mix and stable pH level that promotes growth of a microbiome suited to metabolising monoaromatics. Peat also offers good adsorption properties for benzene: it can adsorb benzene that the culture later metabolises and destroys (Kennes and Veiga, 2002). Khan and Ghoshal (2000) report removal efficiencies for aromatics between 53-98% using biofiltration.

Biotrickling filters promote biofilm growth on an inert packed bed, using a recirculating water flow. This water may be seeded with nutrients to promote growth. Biotrickling filters have been applied to the abatement of monoaromatics. Several sources (Choi *et al.*, 2004; Maliyekkal *et al.*, 2004; Zhang *et al.*, 2010) report a removal efficiency of 70%, which is insufficient for the application in this study. Rada *et al.* (2014) report some success using a biofilter to remove remaining benzene downstream of a biotrickling filter.

Bioscrubbers recirculate a suspended liquid culture in a packed column. In comparison to other biological treatments, bioscrubbers offer a smaller footprint, faster start-up, and more conventional process control. The liquid phase culture also avoids plugging issues from sloughing biofilm, and allows more options for strain specific inoculation. Bioscrubbers can be the most cost-intensive biological treatment, as they require high nutrient demand and produce liquid waste for disposal. Novel bioscrubber designs show promise. One simulation case study of an airlift bioscrubber reports destruction efficiencies above 99% for benzene loads appropriate to flurbiprofen manufacture (Mudlair *et al.*, 2010). The low solubility of benzene in water is one barrier to biological treatments. Two-phase bioscrubbers use a non-volatile oil to improve absorption of hydrophobic compounds.

Biological treatments can be significantly cheaper, in both capital cost and operational cost, in comparison to adsorption or thermal oxidation. Biological treatments are appropriate for high flowrates of low VOC concentration (particularly, ppm level (Khan and Ghoshal, 2000)).

Kosteltz *et al.* (1996) state that in the past, industrial uptake of biofiltration has suffered from exaggerated claims of vendors. Mudlair *et al.* (2010) showed that industrial use of biofiltration concentrated on odours and water-soluble pollutants. Most industrial VOC emissions are hydrophobic: a recent review of novel technologies in this area concluded that more research could help to bring these to technical maturity (Cheng *et al.*, 2016).

Conventional techniques can be effective at controlling benzene emissions. However all of these techniques require an energy input, incurring operating costs. Cryogenic condensation in contrast will save energy in flurbiprofen manufacture, as is discussed below.

## 1.8 **Cryogenic Condensation**

Cryogenic condensation is a VOC abatement technology that has recently become widely available in the pharmaceutical industry. This growing market has been driven by the development and sale of pre-constructed modular units. Examples include: (Air Liquide SA) voxal$^{\text{TM}}$; (Messer Group GmbH) duocondex®; (Air Products & Chemicals inc.) cryocondap® and (Praxair inc.) 'cryo-condensation, VOC recovery system'. These units use a cryogen (commonly liquid nitrogen) to cool vent gases through indirect heat exchange, allowing VOC to condense and separate from the vent gas flow.

Nitrogen gas raised in the unit can be used elsewhere in the process. The plants at Aesica Cramlington collectively use ca. 200 kg/hr of nitrogen gas, mainly in the blanketing and inertion of vessel headspace. Meeting this demand involves heating liquid nitrogen, which currently uses combination of a water-bath vaporiser and heat exchange with ambient air. Replacing or reducing the energy demand of the water-bath vaporiser could save energy costs of ca. £14,000/a, in addition to the aforementioned saving possible by eliminating the RTO.

### *1.8.1 Background in open literature*

Direct cooling methods (such as spray-injections of liquid nitrogen) are technically feasible but incur high operating costs, as the injected nitrogen cannot be recovered for further use. The cryogenic condenser described in this thesis uses a heat exchanger to cool the process gas. This is typical of industrial cryogenic condensers. This means that the resulting nitrogen gas stream is pure and can be used in plant duties, while the treated process gas stream is vented to atmosphere. This is usually accomplished by a system of heat exchangers similar to the diagram shown in Figure 3.

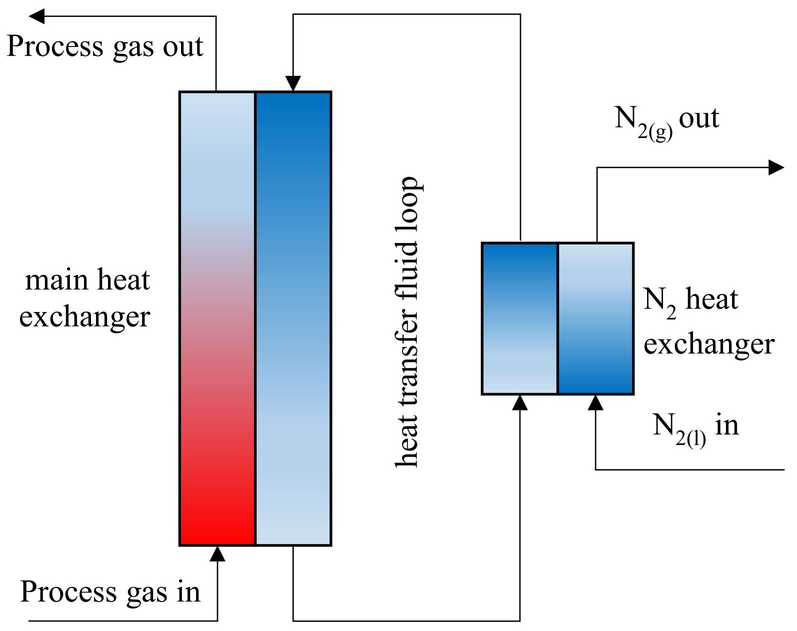

*Figure 3: Basic configuration of a typical industrial cryogenic condenser.*

Whilst it is common in a laboratory setting to cool gas using heat exchange with boiling nitrogen, commercial cryogenic condensers generally use an intermediate heat transfer fluid to exchange heat between boiling liquid nitrogen and the process vapours. Herzog (1994) provides the justification for this. Controlling the temperature by controlling the pressure of the liquid nitrogen evaporation is impractical. Liquid nitrogen boils at -196°C (1 atm), cryogenic condensation is typically conducted at ca. -100°C, which is above the critical point of nitrogen (-147°C, 34 atm). The extreme cold of liquid nitrogen leads to excessive solids formation in the heat exchanger. This shortens cycle times for condensers operating in pseudo-continuous mode, and reduces heat transfer requiring larger heat exchange surfaces. Uncontrolled convection also affects the mass transfer inside the unit. Lastly, there is a risk of condensing oxygen present in the process gas, creating a flammable VOC/oxygen condensate. Refrigerant R-507 is used as the intermediate heat transfer fluid in one commercial unit. Nitrogen gas itself can also be recirculated as an intermediate heat transfer fluid (Davis and Zeiss, 2002).

In this thesis, heat exchange between the VOC-laden process gas and the cold nitrogen gas coolant is modelled inside a plate heat exchanger. The heat exchanger design is similar to (Kelvion Holding GmbH) ‘Pluto’ desublimator available commercially. This is a shell-in-plate, counter-current, ‘lamella’ heat exchanger. Process gas flows through the shell, and coolant nitrogen gas flows through the plates (lamellae). This design is robust to solids formation and thermal stress, and is appropriate for operating in pseudo-continuous mode.

### *1.1.1 Unit Description*

In the envisioned setup, two cryogenic condenser units would be installed for benzene emission control, and the two would be operated pseudo-continuously. This would yield the financial benefits stated previously. The description that follows describes the cryogenic condenser unit modelled in this thesis.

The unit consists of separate heat exchangers. The cryogenic condenser block is the main heat exchanger within the unit. The cryogenic condenser block consists of a plate-in-shell construction (lamella heat exchanger). The shell is constructed from welded stainless steel. The plates (lamellae) are also constructed from stainless steel and are independent of the shell. Fifteen lamellae are supplied through tube manifolds. The duty-side consists of cryogenic nitrogen gas flowing inside the lamellae. The process-side consists of the vent gases to be treated by the unit: these flow over the lamella surface within the shell. A basic description of Lamella heat exchangers can be found in Thulukkanam (2013, p. 14). Benefits of this design include: resistance to thermal expansion stresses; high operating pressures (duty-side); robustness to solids-containing streams (process-side).

Fourteen baffles direct this flow, with a reducing baffle spacing as process gases move upwards through the condenser. Liquid condensates exit from the base of the condenser under gravity. This design has similarities to a tray-type condenser (Hewitt et al., 1994). Specific to cryogenic condensation, the benefits of this design are discussed in Cheng (1995).

Liquid nitrogen is evaporated in a separate heat exchanger (Figure 4: stream 3). Nitrogen gas is the intermediate heat transfer fluid. Connections have been redacted. Examples are covered in Cheng and Devack (1999); Davis and Zeiss, (2002); Lee et al. (1996).

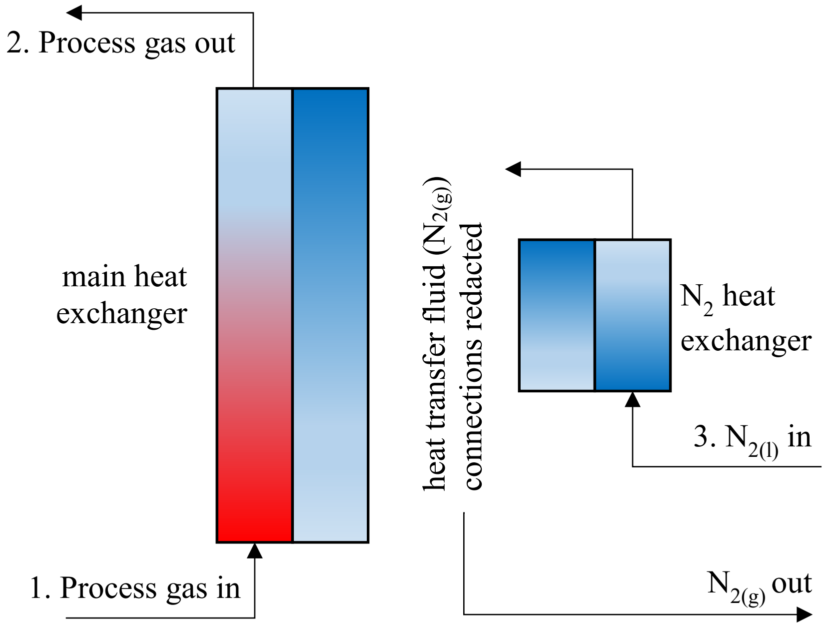

*Figure 4: Process flow diagram of the cryogenic condenser unit.*

### *1.1.2 Mass Balance*

The mass balance is important for definition of inlet conditions to the CFD model. A mass balance for the system is given below in Table 3. Stream names follow the diagram in Figure 4 (p. 13). A flowrate of 150Nm$^3$/hr is the upper limit of the normal operating range of the cryogenic unit, and also fits design data obtained for existing upstream equipment. A partial pressure of 543 Pa benzene was obtained from measurements of the regenerative thermal oxidiser (RTO). An outlet benzene concentration of 5 mg/Nm$^3$ was assumed. This gave an equilibrium vapour temperature of 185 K, according to De-Kruif (1980) that was used to find the equilibrium water vapour pressure (Wexler, 1977).

| **Stream composition (kg/hr)** | **1** | **2** | **3** |
|---|---|---|---|
| | *Process inlet* | *Process outlet* | *Coolant flow* |
| Nitrogen | 184 | 184 | 88.7 |
| Benzene | 2.79 | 7.37 x10$^{-4}$ | - |
| Water | 1.33 | 1.61 x10$^{-5}$ | - |

*Table 3: Mass balance for cyrogenic condenser.*

A predicted cooling demand of 6.96 kW was found based on this mass balance. Based on inlet (sat. liq. At 9 barg) and outlet (gas at 6 barg, ca. -60°C) conditions for coolant nitrogen flows to and from the unit, the coolant nitrogen gas flow was approximated based on standard state enthalpy. As there are 15 lamellae inside the cryogenic condenser, this creates 16 spaces inside the cryogenic condenser shell. Therefore for the flow through the CFD model, the above is divided by 16, or in the case of a symmetric CFD geometry, by 32.

## 1.2 Desublimation

Desublimation is a phase transition from the gaseous to the solid phase. Desublimation involves crossing the phase boundary between the solid and vapour phases. In order for desublimation to occur, the initial conditions must be below the triple point of the desublimating species. There are three conditions under which this occurs in a practical setting:

1. The substance has a high triple point, above atmospheric pressure. For example dry ice, $CO_{2(s)}$ sublimates due to a high triple point pressure (5.1 atm).
2. The system is operated under partial vacuum. This occurs in freeze drying: water sublimates from the product, and desublimates on a heat exchanger upstream of the vacuum pump. The vacuum pump maintains the system below the triple point pressure of water.
3. The partial pressure (gas phase concentration) is below the triple point pressure. This occurs in a natural setting during the formation of snowflakes and hoarfrost from ambient water vapour.

The expected partial pressure of benzene in the untreated vent gas (543 Pa, depicted as the cross in Figure 5) is below the triple point pressure of benzene (4.8 kPa). This fits the third category above: benzene is expected to desublimate on cooling in the cryogenic unit.

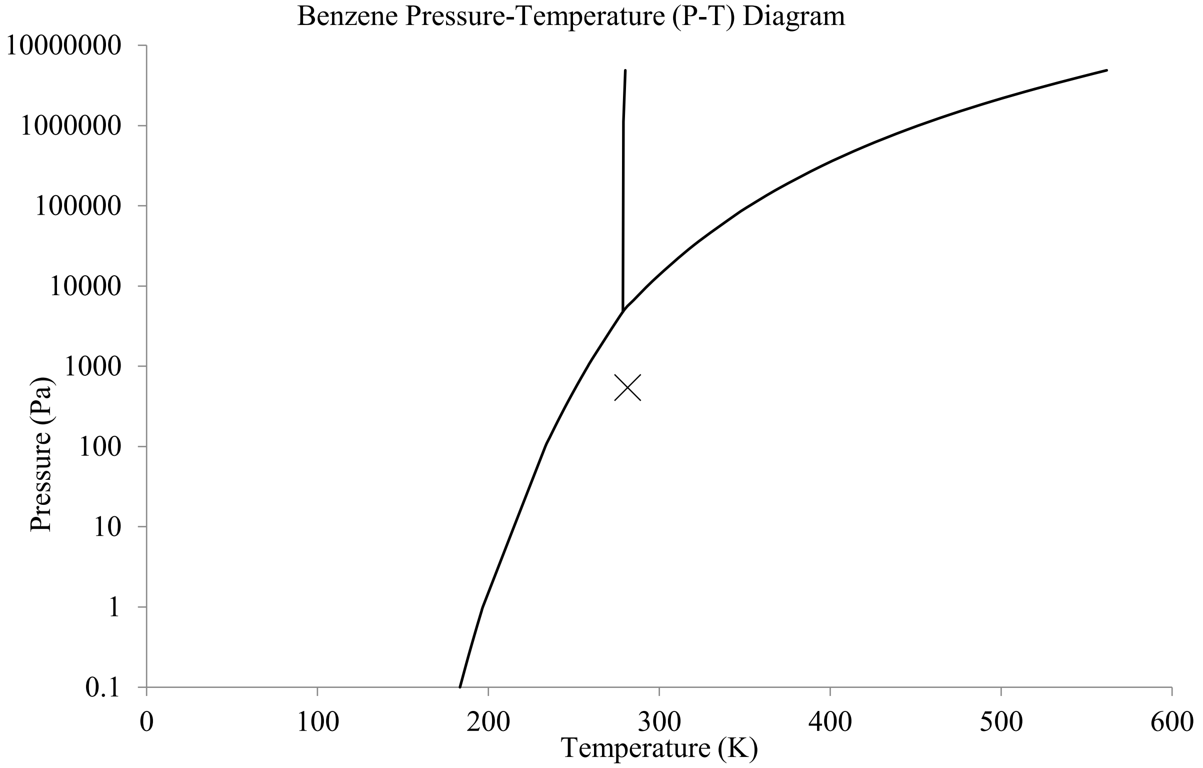

*Figure 5: Benzene pressure-temperature diagram.*

## 1.3 **Justification of the Approach**

An answer to the research question is of use to Aesica Cramlington, the potential financial and operational benefits to the flurbiprofen process are clear. This information could also be useful to other manufacturers which generate emissions containing benzene, or any other high melting-point solvent, in consideration of cryogenic condensation as an abatement technology.

The modelling work also covers several research areas where new contributions to knowledge could be made. The development of a Eulerian-Lagrangian CFD model that fully incorporates particle formation and growth could be of utility in modelling related processes. In literature on condenser design, aspects which affect this work such as desublimation, solid phase formation, the effects of transitional flow, and the effects of bulk condensation with inert gases are understudied relative to other design factors that affect condenser performance.

The hazardous nature of both benzene and cryogenics results in technical barriers to direct experimentation at the laboratory scale. At the full (industrial) scale, there are financial and technical barriers that prevent the recovery of detailed information from physical testing. A modelling approach for initial investigation of the process is therefore justified on these grounds.

Condensation processes may be modelled using one-dimensional approaches. These include heat-mass transfer analogies, such as the Chilton-Colburn analogy and others. Such approaches incorporate empirical relationships, or assume a fully developed flow that may be described by wall functions (Dehbi *et al.*, 2013). These are not applicable to the three-dimensional flows present in the equipment. CFD is therefore appropriate as a tool in this modelling work. CFD also allows modelling of particles in fluid flow fields through Lagrangian particle tracking. This allows insight into the behaviour of particles in the flow that is impossible to obtain through other modelling methods. CFD modelling is therefore an appropriate tool to use in investigating the two questions posed above. A particle image velocimetry (PIV) study is also included that provides validation for the flow modelling from the CFD modelling work.

## 1.4 **Content of the Thesis**

This introduction has provided a background to the need for benzene abatement and the motivation for the research at Aesica Cramlington. In the next chapter, the literature review focusses on literature related to modelling of the physical processes involved, and studies in the literature relating to desublimation and related phase change behaviour. Development of the

CFD model and the PIV validation study is described in the methods section. The results and discussion section show the main outcomes from the study. The conclusion section also explores implications of the research and possible area for future work.

# Chapter 2. Literature Review

This literature review is composed of two main parts. Part one deals with literature relating to desublimation of volatile organic compounds (VOCs), aiming to review how similar problems have been addressed in research. Film models are first discussed. Fog-film models are shown to predict fog formation inside the condenser. Studies exist that apply film models to desublimation: these cases are briefly reviewed. A discussion is given on desublimation in an industrial context, as a separation technique. There are few sources that relate directly to the research topic: several sources exist on benzene desublimation and on cryogenic condenser modelling, and these are briefly reviewed. Low-temperature separation of carbon dioxide is an exception here: this topic is addressed in isolation under its own section. Following this, the literature review focusses on research relating to computational-fluid dynamics (CFD). Frost modelling in CFD is discussed under two main categories (frosting on heat exchanger surfaces and aircraft ice accretion models), as the two sectors take very different approaches to frost modelling. Population balance modelling, the main alternative to the Eulerian-Lagrangian method used in this work, is briefly reviewed. Several sources exist that have used Eulerian-Lagrangian methods to model nucleation or growth, these are reviewed in the section immediately after.

Part two of the literature review starts from section 2.10 onwards. From here the focus shifts away from research literature and towards a general background information relating to the CFD model itself. Laminar-turbulent transition is first covered, as this is present in the flow conditions in the model and affects the choice of turbulence model. The generalised transport equations are then discussed as an inroad to discussing the turbulence modelling itself. Following this, classical nucleation theory used to predict the nucleation process is addressed. The section then concludes with a discussion of inertial deposition and thermophoresis, the dominant mechanisms by which particles become separated from the flow.

## 2.1 Film Models

Condensation of pure components can yield very high heat transfer rates. For pure components heat transfer is liquid-side controlled. The liquid film poses the highest heat transfer resistance, and the gas-phase heat transfer resistance is negligible. When the gas-phase contains a non-condensable component such as nitrogen or air, even at low concentrations, this reduces heat transfer significantly. Non-condensables accumulate in the gas film, and the condensable component must diffuse through this layer, under a concentration gradient. The concentration gradient means the interface temperature (which is fixed at equilibrium vapour pressure) is lowered. In condensation from non-condensable carrier gases, heat and mass transfer often becomes gas-side controlled. This section will discuss issues with condensation from non-condensable components and improvements to these models that aim to account for fog formation in the gas phase.

In one-dimensional condensation modelling (film models), the effect of non-condensables may be incorporated using empirical corrections to the heat transfer coefficient found by Nusselt's method. These include the Meisenburg and Hampton correlations (Ghiaasiaan, 2007). Alternatively an empirical correlation such as the Berman and Fuk's correlation can be used to find gas-side heat transfer coefficient directly. A stagnant film model can also be used, such as the one in equations 2-6 and 2-7 below.

### 2.1.1 Chilton-Colburn j-factor analogy

The Chilton-Colburn j-factor analogy is a heat-mass transfer analogy. It allows empirical correlations for heat transfer to be used to find mass transfer coefficients. It is most commonly expressed by replacing the Prandtl number with the Schmidt number, and the Nusselt number with the Sherwood number. One common example used to compute droplet evaporation is the Ranz-Marshall correlation shown in equations 2-1 and 2-2 below. The Chilton-Colburn analogy is often used to find mass transfer coefficients in film models of condensation from non-condensable gas.

$$Nu = 2 + 0.6Re^{0.5}Pr^{\frac{1}{3}} \tag{2-1}$$

$$Sh = 2 + 0.6Re^{0.5}Sc^{\frac{1}{3}} \tag{2-2}$$

### 2.1.2 Fog-film models

The possibility of fog formation inside condensers can be examined analytically using a one-dimensional film model. The concept was initially proposed by Colburn and Edison (1941); (Noordally *et al.*, 1994). Fog formation is predicted when the concentration profile of the gas film becomes supersaturated. Equilibrium vapour pressure[†] is determined by the temperature profile (heat transfer) in the film, whereas the concentration profile is determined by mass transfer.

---

[†] Or, the vapour pressure at the critical degree of supersaturation.

Manthey and Schaber (2000) provide a simple formula (equation 2-3) for assessing fog formation in the gas film in this manner. The function is plotted below in Figure 6 for conditions appropriate to the cryogenic condenser inlet in the case-under-study. The curve is convex for Lewis numbers (Le) higher than unity as is the case for a benzene-nitrogen mixture. The Lewis number is the ratio of the Schmidt and Prandlt numbers, and therefore the ratio between heat and mass diffusivity; fog formation occurs when heat transfer outpaces mass transfer. This line intersects the vapour pressure line, indicating fog formation in the boundary layer. The second plot indicates a maximum supersaturation of 7.4 is achieved under these conditions.

$$Y(t) = Y_{sat}(T_F) + (Y^{in} - Y_{sat}(T_F))\left[\frac{T - T_F}{T^{in} - T_F}\right]^{Le^{-0.6}} \tag{2-3}$$

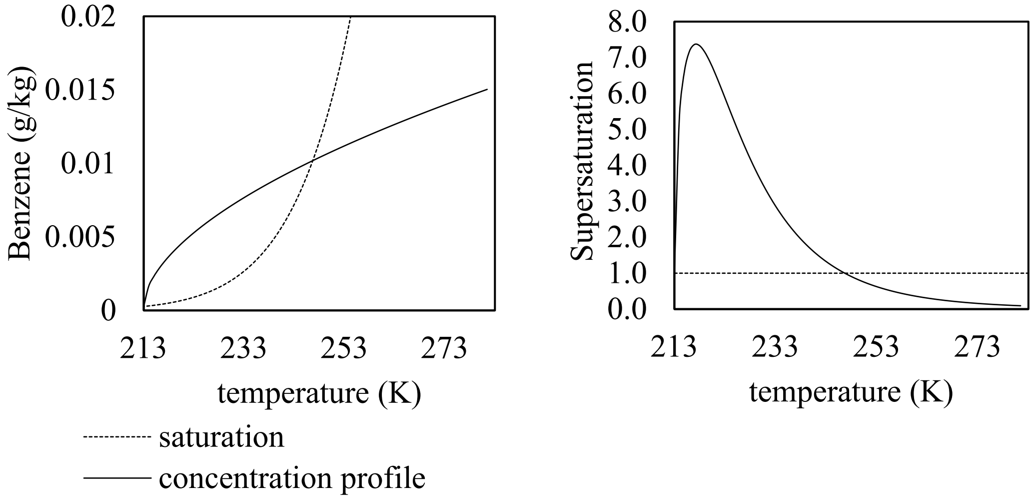

*Figure 6: Illustration of equation* 2-3.

Manthey and Schaber (2000) also conducted CFD simulations and experiments. The paper covered particle growth and nucleation in a one-dimensional model. In the CFD model, particles injections were studied with a Eulerian-Lagrangian model, but the Eulerian-Lagrangian modelling did not include nucleation or growth. They concluded their one-dimensional model was acceptable for predicting the occurrence of fog in condensers. In experiments fog formed immediately at the inlet to the cooled surface inside the condenser. This differed to the prediction of the one-dimensional model (which predicted fog formation at varying distances into the condenser) but was modelled accurately by the temperature gradation in the CFD model.

LoPinto (1982) describes a calculation procedure to assess whether fog formation will occur inside a condenser. Repeating this calculation at conditions and material properties relevant to the case-under-study predicts benzene fog formation will occur in the condenser. A maximum supersaturation of 12.7 being above the critical supersaturation (2.5) predicted by Frenhel's formula, given in equation 2-4 below.

$$S_{cr} = e^{\left[0.22\frac{M}{\rho_l}\left(\frac{\sigma}{T}\right)^{0.5}\right]} \qquad \text{2-4}$$

Karl (2000) describes another fog-film model. In this model the conditions predicting fog formation are the gas-side gradients at the gas/liquid film interface, shown in equation 2-5 below.

$$\left.\frac{\partial T_g}{\partial y}\right|_{y=0} < \left.\frac{\partial T_{sat}}{\partial y}\right|_{y=0} \qquad \text{2-5}$$

A stagnant film model may be used to calculate the temperature and concentration profiles in the gas-side film, as shown in equations 2-6 and 2-7 below ($\rho_g$, $C_p$ and $k_g$ in molar units).

$$x_A(y) = x_{A\infty} - (x_{A\infty} - x_{A0})e^{\frac{-N''}{\rho_g D_{AB}}y} \qquad \text{2-6}$$

$$T_g(y) = T_{g\infty} - \left(T_{g\infty} - T_0\right)e^{\frac{-N'' C_p}{k_g}y} \qquad \text{2-7}$$

The molar flux can be found using equation 2-8.

$$N'' = -K_{GI} ln\frac{(1 - x_{A,g})}{(1 - x_{A,sat})} \qquad \text{2-8}$$

The mass-transfer coefficient $K_{GI}$ can be found by applying the Chilton-Colburn analogy to an empirical correlation appropriate for the case. This analysis predicted fog formation inside the condenser at conditions appropriate to the case under study in this thesis.

Fog formation in the boundary layer can impede mass transfer inside condensers. Correction factors may be applied to the film heat and mass transfer coefficients ($\Theta_{tf}$, $\Theta_{cf}$) to account for these effects (Brouwers, 1992; Ghiaasiaan, 2007, p. 458). In Brouwers (1992) the correction fitted experimental data well for a water-air system.

$$\Theta_{cf} = \frac{1 + \left[\frac{h_{lat}}{C_{p,g}}\frac{1}{Le}\frac{x_{A,\infty} - x_{A,sat}}{T_{g\infty} - T_0}\frac{Sh}{Nu}\right]^{-1}}{1 + \left[\frac{h_{lat}}{C_{p,g}}\frac{1}{Le}\left.\frac{dx_{A,sat}(T)}{dT}\right|_{T_0}\right]^{-1}} \qquad 2\text{-}9$$

$$\Theta_{tf} = \frac{1 + \left[\frac{h_{lat}}{C_{p,g}}\frac{1}{Le}\frac{x_{A,\infty} - x_{A,sat}}{T_{g\infty} - T_0}\frac{Sh}{Nu}\right]}{1 + \left[\frac{h_{lat}}{C_{p,g}}\frac{1}{Le}\left.\frac{dx_{A,sat}(T)}{dT}\right|_{T_0}\right]} \qquad 2\text{-}10$$

### 2.1.3 *In the context of desublimation*

Film models constitute the bulk of desublimation modelling work available in open literature. Particle formation is a problem identified in these studies. Krupiczka and Pyschny (1990) use a fog-film model to predict a 5% drop in capture efficiency in a phthallic anhydride desublimator. Smolkin *et al.* (2011) report a 10-20% drop in capture efficiency for metal fluorides. Conditions during sublimation often favour aerosol formation: large molecules diffusing through light gases (Lewis numbers greater than 1) and cold surface temperatures well below the dew point (frost point).

### 2.1.4 *Conclusions on film models*

Both condensation from non-condensable carrier gases and fog formation are important in modelling mass transfer. One-dimensional film models of both processes are established. CFD modelling can contribute a method to look at these processes in more detail, avoiding the use of empirical correlations for transfer coefficients along with other simplifications that may affect the accuracy of predictions. A possibility for novel contribution exists here, as even recent studies (Fernandez and Priesto, 2016) assess fog formation using one-dimensional models. Also, relatively few publications (Li, 2013; Zschaeck *et al.*, 2014) exist focussing on CFD models of condensation from inert gases. These problems are important during cryogenic condensation and desublimation. There are also broader implications for condensation as a VOC abatement technique generally.

## 2.2 **Desublimation as a Separation Technique in the Process Industries**

Desublimation is uncommon as a separation technique in the process industries. It is more expensive than other techniques which do not involve handling solids. As the solids grow, they create a resistance to heat transfer. Desublimators may include large heat transfer surfaces to get around this issue. Condensation of a liquid in contrast tends to yield very high heat transfer rates, particularly in the drop-wise regime. Due to the infrequent use of desublimation industrially, there are no established design procedures for desublimators.

As a separation technique, desublimation may be used to separate a valuable product from non-volatile impurities at temperatures which avoid thermal degration. Salicylic acid, for example, may be purified using desublimation to prevent decarboxylation (Couper *et al.*, 2010, p. 701). Desublimation is also used during uranium enrichment to separate $UF_6$ from $F_2$, HF and other volatile impurities following fluorination (Smolkin *et al.*, 2007). The main industrial application of desublimation is in phthallic anhydride manufacture, separating phthallic anhydride from maleic acid.

Continuous desublimators are possible if the desublimated material is removed mechanically. The List AG discotherm-b is one commercial example (Mullin, 2003). Moving-bed designs such as the ball-bed desublimator (Herzog, 1994) are also capable of continuous operation. However the use of multiple heat exchanger units, operating in pseudo-continuous mode with periodic defrosting, is the most common desublimator design. Phthallic anhydride desublimation uses specialised shell-and-tube heat exchangers known as ‘switch condensers’. Process vapours enter the shell, where the product desublimates onto finned tube banks (McKetta, 1991, p. 44). Plate heat exchangers such as the one proposed in this thesis are more common at smaller scales.

## 2.3 Academic Studies on Benzene Desublimation

There are some sources available in the literature specific to benzene desublimation. These are useful as they provide experimental evidence of the expected result of benzene desublimation.

Frost growth may be split into two main mechanisms. In layer growth, vapour diffuses to the surface of the frost layer, causing it to thicken as this freezes or desublimates. In pore diffusion growth, vapour diffuses into the porous frost layer increasing bulk density. Both mechanisms occur simultaneously in different proportions depending on the conditions.

Wintermantel *et al.* (1987) report experimental results for benzene desublimation. The work focussed on conditions that benefit densification of the layer by pore diffusion into the frost, rather than growth of the frost layer. They found that a high concentration gradient across the boundary layer led to a high-porosity sublimate layer. The benzene desublimate grew as needlelike or dendritic crystals resembling hoarfrost. The initial voidage of this layer was 0.7, compared to 0.9 for similar experiments with water ice.

Ueda and Takashima (1976); (1977) describe experiments using an annular cold trap to capture benzene by desublimation. In their experiments they describe benzene desublimation from helium and nitrogen carrier gases under laminar flow at pressures below atmospheric. Different desublimates formed (porous or non-porous) depending on the experimental conditions. Porous desublimate was favoured by high gas concentrations of benzene at the inlet, and by using nitrogen as oppose to helium as carrier gas. In these experiments an outlet concentration was obtained that was close to saturation. This result is important because it demonstrates that benzene outlet concentrations close to saturation are possible for low-temperature (-61°C) desublimation of benzene. In later work Mitani and Takashima (1981), experimented with mechanical removal of benzene desublimate, reporting that a force of ca. 2 to 6 N/cm$^2$ was required to remove the desublimated benzene layer. This force was negatively correlated with the cold surface temperature and positively correlated with bulk density of the desublimate. This information would be useful if mechanical removal is to be considered in future design alternatives.

## 2.4 Academic Studies on Cryogenic Condensation

Publications relating to cryogenic condensation of VOCs tend to focus on comparisons with other abatement techniques. These mostly consist of grey literature, (e.g. Rijneek (2005)). Several studies also concentrate on the energy efficiency of the processes based around refrigeration. Belaissaoui *et al.* (2016) assume equilibrium vapour pressure is achieved during low-temperature condensation of VOC, and (as they acknowledge in the text) target outlet concentrations in excess of emissions limits. Dunn and El-Halwagi (1994a); (1994b) also assume equilibrium vapour pressure for VOC in the flue gas. Few publications attempt to model the process in detail.

Cryogenic condensation can be applied to remove water vapour from gases. Housiadas *et al.* (1998) studied a laminar airflow through a cold-trap. This is of interest for atmospheric detritiation systems, used to control emissions-to-atmosphere of tritiated water from nuclear facilities. The authors report both experimental and modelling work. In the experimental work, the cold-trap design consisted of a shell-and-tube heat exchanger. Water vapour desublimated onto the tube internal surfaces, and the shell contained a liquid nitrogen bath. They solve the aerosol general dynamic equation (a population balance model) in one dimension along the length of the pipe. This work is important due to its parallels with the subject of this thesis. The investigators were interested in modelling the capture efficiency, as at very low temperatures a considerable fraction of the water vapour forms particles that escape the cold-trap.

Gupta and Verma (2002) modelled cryogenic condensation of several VOCs in a cryogenic condenser. They modelled a tube condenser in one dimension, using a film model that did not incorporate bulk nucleation. A modelling result for cryogenic condensation/desublimation of benzene is briefly reported though benzene solidification is not addressed in the text. Outlet concentrations of benzene were significantly supersaturated in the model ($S = 15.3$ to 165). The authors argue in favour of a system where adsorption is used as a polishing step following cryogenic condensation, in order to meet regulatory limits for VOC emissions. The results showed difficulty in removing VOC at low concentration levels using cryogenic condensation alone. Dichloromethane and toluene results are also reported. Cryogenic condensation alone was able to meet regulation levels for outlet concentrations of these solvents, but only when the VOC inlet concentrations were low and coolant flow was high. Adsorption was also found to be impractical at high inlet VOC concentrations, due to short breakthrough times. The model was compared to experimental results in later work (Dwivedi *et al.*, 2004), which compared the model predictions of temperature profile in a double-pipe tube condenser. The experimental results reported in this paper are inconsistent: a minimum toluene outlet gas concentration of 0.1vol% is reported in the text, but graphical plots appear to show far lower outlet concentrations than this.

## 2.5 Carbon Capture using Cryogenic Desublimation of Carbon Dioxide

Low-temperature separation of carbon dioxide ($CO_2$) is well established in the natural gas industry, with research dating back to the 50's and 60's (Chang *et al.*, 2009a). The technique is suited to high initial concentrations of $CO_2$, either present in the well initially or in the 'associated gas' resulting from enhanced oil recovery by $CO_2$ injection. Absorption is normally used for $CO_2$ removal from natural gas, but at concentrations above 20% $CO_2$ energy costs associated with the solvent regeneration makes this cost prohibitive (Van Benthum *et al.*, 2012).

For carbon capture from power generation (and other carbon-intensive industries) to control greenhouse gas emissions, other methods (chemical and physical sorption, membrane processes) have dominated recent research. Oxy-derived processes such as oxy-fuel, chemical looping and molten carbonate fuel cells, are an exception. For oxy-derived processes $CO_2$ separation by condensation has been considered due to the high initial $CO_2$ content of the stream. Carbon capture by $CO_2$ phase change (condensation/freezing/desublimation) is often dismissed on the grounds of unfavourable costs, high specific capture work (energy expended in separation and compression per unit mass of carbon dioxide. MJ/kg $CO_2$), and limited range of applications. This is reflected by the comparatively low levels of interest in the area when compared conventional capture methods. However opinions vary on the competiveness of low-temperature $CO_2$ separation methods. It has additional advantages over absorption: the use of solvents is avoided, including associated emissions hazard and cost for solvent make-up; also there is no requirement for steam supply, reducing the modifications required to existing turbines or utilities.

Condensation is appropriate for treating gases with a high initial concentration of $CO_2$. For more dilute streams, such as post-combustion processes, the high specific capture work and the low capture ratio (%age of $CO_2$ removed) make condensation impractical (Meisen, 1997). However if solid $CO_2$ formation (by freezing and desublimation) is permitted this alleviates these problems. The number of publications in this area is comparatively low (Berstad *et al.*, 2013). This section aims to provide a brief review of literature specific to cryogenic desublimation and condensation of $CO_2$.

### *2.5.1 Examples in the natural gas industry*

In the natural gas industry, $CO_2$ removal by cryogenic distillation processes has been practiced commercially for several decades. Examples include the Ryan/Holmes, controlled freeze zone™, and sprex®$CO_2$ methods. Some of these processes generate solid $CO_2$. The controlled freeze zone™ method distributes down coming liquid $CO_2$ as a spray, allowing it to freeze as particles. Particles fall to the next plate, which is maintained above the melting point to allow liquid $CO_2$ to flow to the plate below (Kelley *et al.*, 2011). Deliberate formation of $CO_2$ hydrates has also been tested in a cryogenic distillation context (Surovtseva *et al.*, 2011).

Two other methods used in natural gas processing are the cryocell® method and supersonic gas separators. The cryocell® method uses Joule-Thomson (J-T) expansion to form a three-phase mixture, separating the $CO_2$-rich phase as a slurry (Hart and Gnanendran, 2009). Supersonic gas separators also use expansion to cool the gas.

### 2.5.2 *Supersonic gas separators*

This technique (twister® technology) is an established technology in natural gas applications such as dehydration. It is currently in development for $CO_2$ removal in natural gas sweetening. The supersonic gas separator first uses guide vanes to create rotational motion in the flow. The gas is then expanded through a converging-diverging nozzle. Expansion cools the gas flow promoting nucleation. The droplets/particles are separated immediately downstream due to centrifugal force.

Numerical modelling studies of supersonic gas separators were summarised in a recent review (Haghighi *et al.*, 2015). 19 studies (31 publications) are listed: three of these studies use Eulerian multiphase population balance models; two use Eulerian-Lagrangian models. Both Eulerian-Lagrangian studies treat droplets as inert particles, no attempt is made to model nucleation or growth (Chuang *et al.*, 2012; Xingwei *et al.*, 2014). Elsewhere Ma (2012) similarly deal solely with inert particles. This shows a gap in the knowledge, a novel contribution could be made using a Eulerian-Lagrangian approach to model nucleation and growth.

### 2.5.3 *$CO_2$ desublimation in heat exchangers*

Several examples exist in the literature of studies involving $CO_2$ desublimation in heat exchangers. Clodic and Younes (2002) investigated a design using two desublimation heat exchangers operating in pseudo-continuous mode, to separate $CO_2$ from flue gases from a conventional power plant (post combustion in air, at atmospheric pressure). Cooling is achieved using a refrigerant blend with a temperature glide (bubble pt. line for the refrigerant blend) that matches the necessary cooling temperature range for the $CO_2$/gas mixture (15vol% $CO_2$: -99°C to 1vol% $CO_2$: -122°C) minimising exergy losses. The process has been tested at the bench scale (Clodic *et al.*, 2004). In later work Clodic *et al.* (2005) compare the energy penalty to monoethanolamine (MEA) absorption, to show $CO_2$ desublimation has a lower impact on the power plant efficiency. This work also mentions water freezing and desublimation (used for dehydration upstream) was found to be more energy-efficient than dehydration by adsorption.

Chang and Smith (1990) initially studied desublimation of $CO_2$ from helium. $CO_2$ desublimation is a problem in commercial helium refrigeration and liquefaction systems, as it causes blockages during long term use. They compared experiments in a laminar pipe flow with a one-dimensional frost model. The frost model predicted a single peak in frost accumulation on the wall, but the experiment showed a second peak further downstream. This second peak was attributed to deposition of $CO_2$ particles. This demonstrates a gap in the knowledge – modelling of the particles could give a better overall model for the frost formation in heat exchangers.

Chang *et al.* (2009a); (Chang *et al.*, 2009b) later proposed using cryogenic desublimation to convert landfill gas to liquefied natural gas (LNG). They suggest using a single cryogenic condenser to both desublimate $CO_2$ and liquefy $CH_4$. This would simplify landfill gas upgrading by removing a unit operation from the process ($CO_2$ removal by conventional methods (eg: pressure swing adsorption (PSA), absorption)). $CO_2$ is removed using two heat exchangers operating in pseudo-continuous mode, and the cooling effect of $CO_2$ sublimation during the regeneration step is used to pre-cool the untreated gas. Cryogenic temperatures are achieved using a reverse Brayton cycle, with nitrogen as the refrigerant, in their design.

Jonsson and Westman (2011) report experiments using desublimation to capture $CO_2$ from a synthetic $CO_2/CH_4$ mixture. They report reducing the $CO_2$ concentration in a binary $CO_2/CH_4$ mixture, from 38% to 1 vol% in the unit. There is no mention of particulate formation in the bulk. They report long regeneration times as a potential area for improvement.

Naletov *et al.* (2014a); (Naletov *et al.*, 2014b) have worked on a mathematical model and conducted an experiment on $CO_2$ desublimation, in two separate papers. Their mathematical modelling work concentrated on frost modelling. Essentially a one dimensional model using a heat-mass transfer analogy, frost build-up was represented by a pipe diameter that varies with time and location. For a full-scale system they suggest continuous operation using mechanical removal of the frost (with a scraper or screw). Their experimental work also focussed on a cylindrical geometry, and yielded some results worthy of note. Increasing inlet $CO_2$ concentration reduced separation efficiency, this contrasts with the equilibrium assumptions made in most whole-process designs. Lower temperatures resulted in increasing separation efficiency overall, but a small reversal in this result between -140°C and -120°C was attributed to the diffusivity of $CO_{2(g)}$. Although the authors do not compare their model with their experimental work directly, both their model and their experiment suggest a time-on-stream of several minutes if frost is not removed.

### *2.5.4 $CO_2$ desublimation in packed beds*

Tuinier and Annaland (2012) investigated using inert packed beds for $CO_2$ desublimation by direct heat exchange with the packing. The beds undergo a three step cycle of cooling, capture and recovery. The bed is cooled using a precooled gas flow, the authors recommend refrigeration or evaporation of liquefied natural gas (LNG) for this purpose (Tuinier *et al.*, 2011). During capture, $CO_2$ desublimates onto the packing surface, a front of desublimating $CO_2$ then moves through the bed until breakthrough is observed. When applied to biogas purification, the authors suggest the same technique would eliminate $H_2S$, siloxanes and water. The authors report improved performance in comparison to vacuum pressure swing adsorption in this application. However, for $CO_2$ removal the specific capture work of a refrigerated process is reported at 3.6MJ/kg $CO_2$.

The main design benefit of cryogenic packed beds lies in an ability to deal with the mechanical challenges of solid build-up. As the gas and $CO_2$ are cooled, the packing is warmed. This prevents an excessive layer of frost forming on the packing, avoiding plugging and heat transfer resistance issues caused by excessive frost in heat exchangers.

Fibres may be used as an alternative to conventional packing (Lively *et al.*, 2012). Advantages over conventional packing include higher specific surface area, smaller bed sizes and lower pressure drop. The authors use liquid nitrogen during the cooling phase, but suggest indirect cooling using LNG evaporation for full-scale systems.

### *2.5.5 $CO_2$ desublimation using Stirling coolers*

Stirling coolers are one alternative that may be used to reach cryogenic temperatures. This may be applied to directly desublimate $CO_2$ on a heat exchange surface. Song *et al.* (2012) describe tests using a three stage system. The three stages are used for dehydration, desublimation of the $CO_2$ itself, and to maintain storage conditions of $CO_2$ solid. Cryogenic Stirling coolers often have a low coefficient of performance (COP). The ideal Stirling cooler follows a Carnot cycle, and the COP of real Stirling coolers is typically some factor of this (e.g. 35%) (Kreith, 2000, pp. 4-323). This limits their application in comparison to other technologies at the industrial scale.

### *2.5.6 Novel heat exchangers for desublimation*

Sustainable Energy Solutions LLC (SES, 2015) have worked on three types of desublimating heat exchangers for carbon capture: bubble column; spray tower and fluidised beds. In the fluidised bed, the bed is cooled by internal coils. The action of the fluidised particles is theorised to lead to a continual renewal of the heat exchanger surface, preventing a frost layer from developing (James, 2011). Inorganic media (silica, oxides or carbonates) or $CO_{2(s)}$ itself, are listed as potential bed materials in patent literature (Baxter, 2014). In both bubble column and spray tower designs a liquid contact medium is recirculated. During recirculation, solid $CO_2$ is separated, and the cooling medium is precooled before returning to the column. The nature of the liquid contact medium is withheld (Nielson, 2013); isobutyl mercaptan is mentioned in laboratory work (James, 2011).

It is worth noting in this context, Steigman (1988) covers the use of the spray tower design for VOC abatement using cryogenic desublimation.

Tests conducted by SES have included a pilot scale plant installation in a commercial coal-fired power plant. Research suggests further advantages of low-temperature carbon capture. Other contaminants were found to be eliminated from coal flue gas in addition to $CO_2$, including mercury, $SO_x$, $NO_2$ and particulates. Additionally, SES have proposed using LNG as an energy storage media during peak electrical supply. This would reduce the parasitic load of the $CO_2$ separation unit on electricity generation. Energy storage through liquefaction of gases shows promise as a technology: Highview Power Storage Ltd for example have constructed a 350kW pilot plant using air liquification, with a 5MW plant mid-construction.

### *2.5.7 Rotational particle separators*

Conventional cyclones can typically separate aerosols with droplet sizes above 15 μm. Nucleation processes can generate fine aerosols of the order of 1-10 μm, making these difficult to separate. Rotational particle separators achieve this separation using a rotating filter element to promote coalescence of droplets. Van Benthum *et al.* (2012) investigate the system through process modelling. Liquid $CO_2$ droplets are first generated in the gas flow by compression and J-T expansion. This study was limited to liquid-phase $CO_2$ but mentions that the separation of solid $CO_2$ as slurry is also under investigation. As this study was limited to recovering a liquid phase, acceptable capture ratios could not be achieved for typical $CO_2$ concentrations from combustion in air. These authors suggest application of the technique to flue gas already enriched in $CO_2$ – oxygen enriched combustion (rather than pure oxygen (oxy-fuel)) is suggested as a possible application. A specific capture work of 440 $kJ/kg_{CO2}$ is reported for an inlet $CO_2$ concentration of 80% and a 90% capture ratio.

In another paper (Theunissen *et al.*, 2011) experimental results show the particle size distribution of particles upstream of the rotational particle separator. Smaller particles are formed by homogeneous $CO_{2(l)}$ condensation from $N_{2(g)}$ carrier gas when compared to $CH_{4(g)}$ carrier gas. The authors stipulate this is due to increased solubility of methane in $CO_{2(l)}$. Brief discussion is given on the effect of residual water vapour on promoting heterogeneous nucleation at commercial scale (by providing foreign nuclei through the homogeneous nucleation of the water). The droplets grew (following J-T expansion) in a length of pipe with a residence time of 0.2s. The residence time of this pipe was found to be important, but the geometry was not important.

### *2.5.8 Conclusion on carbon capture using cryogenics*

This literature review reveals several points relevant to this thesis. The commercial application of low-temperature $CO_2$ capture methods in the natural gas industries indicates these technologies can be commercially viable. Recent efforts in pilot plant demonstration show the technical challenges involved in solids handling can be surmounted. Particle nucleation and growth is a barrier to designing cryogenic $CO_2$ processes that could be tackled in future using the Eulerian-Lagrangian model described in this thesis.

An extremely cold source is needed for low-temperature $CO_2$ capture methods. Access to a liquid cryogen source is often stated as a limitation, both for $CO_2$ capture (LNG) and for cryogenic condensation of VOCs ($N_{2(l)}$). However several of these sources suggest ways in which this could be achieved using refrigeration. This would increase the applicability of condensation/desublimation, both to VOCs and $CO_2$ capture. This thesis focusses on pseudo-continuous operation of heat exchangers for benzene desublimation. The literature review indicates a variety of alternative heat-exchange methods that could also be considered for VOC abatement. The energy efficiency (the specific capture work) is of vital importance to the viability of low-temperature $CO_2$ separations in carbon capture. Energy efficiency is less important for VOC abatement, many established VOC abatement technologies used industrially are energy intensive. Designs that are not suitable for $CO_2$ capture in the energy industry may still have wider applicability in VOC abatement.

## 2.6 **Multiphase CFD modelling**

Multiphase CFD modelling is necessary for modelling desublimation in CFD. Multiphase CFD models split into two broad categories. Eulerian-Eulerian simulations treat both phases as two continua within the mesh. The two phases are defined with fractional volumes in each mesh cell. This approach can be applied to a wide range of multiphase flows. Eulerian-Eulerian models can be used to model frost layer growth as is discussed in section 2.7. Eulerian-Lagrangian models treat the continuous phase as a Eulerian flow and the dispersed phase as particles tracked in a Lagrangian frame. Eulerian-Lagrangian models can be applied to droplet or particle-laden flows. These can be applied to nucleation and growth as is discussed in section 2.9 below.

## 2.7 **Frost Models**

Modelling of frost formation (freezing and desublimation of water ice on surfaces) is well-studied. Models concentrate on predicting the shape and structure of the water ice layer as it forms over time. Applications have concentrated on two main areas: frosting of heat exchanger surfaces and ice accretion on aircraft. Comparatively little emphasis has so-far been placed on modelling frost formation as a separation technique and the factors that would affect this, such as gas-phase concentration or the effects of bulk nucleation. This section will provide a brief review of literature relating to these two areas.

### *2.7.1 Frosting on heat exchanger surfaces*

Frosting on heat exchanger surfaces affects the performance of heat exchangers and is a common problem in refrigeration and cryogenics. Frost models generally use a mix of theoretical and empirical modelling to predict changes in the properties of the ice over time. Approaches are eclectic: authors (Yang *et al.*, 2006; Hermes *et al.*, 2009; Lenic *et al.*, 2009; Cui *et al.*, 2011a; Cui *et al.*, 2011b; Kim *et al.*, 2015) make an effort to sub-categorise frost modelling approaches, but these distinctions are without consensus in the literature. In the last decade, frost modelling using CFD has become important in reducing reliance on empirical models and other simplifications. These efforts have focussed on Eulerian-Eulerian simulations.

Most studies focus on a 2D parallel plate geometry under laminar flow. Lenic *et al.* (2009) developed a frost CFD model using Fortran code. Correlations were used to define the degree of supersaturation at the frost surface and the thermal conductivity of the frost. Vapour mass flux to the frost layer is defined by concentration gradient in the flowing gas above. Pore diffusion is then limited by tortuosity, and the remaining mass flux contributes to layer growth. The model was experimentally validated. Results indicated the frost layer growth was enhanced by high inlet temperature and humidity, and was relatively independent of velocity. Kim *et al.* (2015) also developed and validated a frost model. Their model approximates frost density as uniform throughout the layer. They report on humidity changes in the bulk gas as it travels through the model: noteworthy as this is, it is unusual in frost modelling. Wu *et al.* (2016) validated a CFD model against experiments conducted previously. The model predicted the frost mass that accumulated with time to within 4% of experiment. It also predicted the shape of the frost layer.

The velocity boundary layer occurs on the surface of the growing frost layer. This presents a problem for turbulence models that require a mesh refinement in the boundary layer, because the location of the velocity boundary layer moves as the frost layer grows. Yang *et al.* (2006) consider a flat plate geometry, and examine the difference between laminar and turbulent (k-ε model) cases. Turbulent flow increased the heat and mass transfer. This resulted in faster frost growth. Under constant humidity, increasing inlet temperature led to a smaller, denser, frost layer, but did not affect overall mass flux. Unlike Lenic *et al.* (2009), they found that in the laminar case, total mass flux for vapour-to-frost mass transfer increased with velocity. However, this mass flux was independent of velocity under turbulent conditions. Cui *et al.* (2011b) deals with turbulent flow (k-ε model) in a 3D geometry representing a fin-and-tube heat exchanger. Frost formation was found to occur on predominantly on the upstream-facing surface of the tubes. This illustrates the importance of 3D geometries, as approximating the exchange surface as a 2D parallel plate would not have identified this 3D ice shape.

### *2.7.2 Ice accretion on aircraft*

Ice accretion on aircraft occurs during flight through collisions with super-cooled liquid droplets in the atmosphere, and is commonly separated into several categories. **Glaze ice** forms when water droplets do not freeze instantly on impact, instead forming a liquid layer that subsequently freezes into a smooth, clear build-up over the wing. **Rime ice** forms when super-cooled mist freezes instantly, causing rough and irregular ice structures to form on the wing tip. **Mixed ice** is a combination of glaze and rime ice. **Super-cooled large droplet (SLD) ice** forms similar to glaze ice, but the larger droplets create problems through the amount of liquid water that freezes aft of de-icing systems, affecting stabilisers and control surfaces of the aircraft. **Ground frost** forms when the aircraft is stationary, and is dangerous during take-off. Ice accretion is dangerous because it affects the aerodynamics of the aircraft, such as lift, drag, stall angle and surface roughness (Cao *et al.*, 2015).

The aerodynamic effects of ice geometries can be studied as static shapes, independent of any phase-change behaviour. This may be explored in CFD: examples include Cao *et al.* (2008a) and Chara *et al.* (2009). Ice accretion models aim to predict collisions with super-cooled droplets and the resulting ice growth. Examples of ice accretion models go back several decades. Numerous computer codes have been developed. Older codes often use 2D geometry, make engineering approximations to calculate flow field (such as the panel method or integral boundary method), and track droplets in the Lagrangian frame.

Newer codes have instead focussed on applying ice accretion models to RANS (Reynolds average Navier-Stokes) models in commercial CFD codes. Typically in aircraft ice accretion models, ice itself is modelled as a fluid-structure interaction as oppose to a Eulerian phase. The geometry is altered at successive time steps, and the problem is re-meshed based on the new surface the ice creates. Droplet trajectories however may be tracked in the Eulerian frame.

| **Code** | **Developer** | **Fluid Model** |
|---|---|---|
| ONERA-2000 | France, French National Aerospace Centre (ONERA) | velocity potential equation |
| Multi-Ice | Italy, Italian Aerospace Research Centre (CIRA) | 2D, Panel method |
| HELICE | Italy, Italian Aerospace Research Centre (CIRA) | 3D, Integral boundary layer method |
| TRAJICE2 | UK, Defence Evaluation and Research Authority (DERA) | Panel method |
| CANICE 3.0-beta | Canada (Montreal University) | Panel method |
| LEWICE 2.0 | USA, (NASA) | Panel method |
| ICECREMO 3.1 | UK, (BAE Systems Plc) | 3D RANS (BAE Systems, RANSMB solver) |

*Table 4. Ice accretion codes (Kind, 2001)*

Eulerian droplet modelling has several advantages. The information on the droplet trajectories can be extracted directly from the flow field. This makes it more straightforward to extract the information on droplet collisions used to find the growth rate of the ice (Cao *et al.*, 2008b). Whilst Lagrangian codes were developed for steady flow over fixed-wing aircraft, flows over helicopter rotors are characteristically unsteady (Zhao *et al.*, 2016). In the unsteady case, the advantages of data-extraction become more important. Fu and Farzaneh (2010) suggest Lagrangian tracking is impractical in 3D due to the high computational load.

These advantages are linked to the ease of computation, rather than accuracy. Eulerian modelling typically assume a single particle size: Fu *et al.* (2006) compared results from simulating particle-size distributions typical in ice accretion with a single particle size (mean volume diameter), and obtained an equivalent result. This demonstrates the single size assumption is not important in aircraft ice accretion models. Yu *et al.* (2015) compared Lagrangian and Eulerian methods directly and found them to be of comparable accuracy. This demonstrates that Lagrangian droplet models are not in principle less accurate.

These second-generation ice accretion codes improve upon older ice accretion codes. They allow greater accuracy in 3D, for example, to account for centrifugal forces, which lead to uneven ice distributions on rotating aerofoils (Zhao *et al.*, 2016). Ice accretion models are sensitive to heat fluxes calculated at the walls, newer models allow this to be calculated with greater accuracy. Older models also fail to predict separated flow (Beaugendre *et al.*, 2006). In the current state of the art, irregularities in real ice tend to be smoothed-out in simulations. This leads to the aerodynamic effects of ice being under-predicted in CFD models (Cao *et al.*, 2008b). Generally, rime ice is easier to model than glaze ice. 3D modelling tends to focus on rime ice (Fu and Farzaneh, 2010; Cao *et al.*, 2012), with the exception of Zhao *et al.* (2016).

## 2.8 The Aerosol General Dynamic Equation

Nucleation of aerosols may be modelled in Eulerian-Eulerian simulations. Basic wet-steam models for example can model Eulerian droplet formation using classical nucleation theory. These models use a constant particle diameter, so cannot include growth of the particle or changes in particle trajectories based on these changes in mass.

Aerosols can be modelled using the aerosol general dynamic equation, a type of population balance model. Changes in the aerosol from nucleation, growth and deposition can be modelled as changes to a distribution (**n**, the particle number density function, $m^{-3}$). An example for a one spatial dimensional case is given below in equation 2-11 (Housiadas *et al.*, 1998).

$$\frac{\partial \boldsymbol{n}}{\partial t}+\frac{\partial(u_g\boldsymbol{n})}{\partial x}+\frac{\partial(\dot{r}\boldsymbol{n})}{\partial r}=I_{coag}+J_{nucl}\delta(r-r^*)-\frac{4}{d_h}\frac{4}{d_{hydraulic}}v_d\boldsymbol{n} \qquad \text{2-11}$$

The first and second terms are transient and convective terms. The third term accounts for particle growth, where $\dot{r}$ is the growth rate (m/s). The fourth term $I_{coag}$ is the coagulation integral, accounts for growth by collisions and is relevant at high particle concentrations. The fifth term is the nucleation term; a Dirac function ($\delta(r-r^*)$) accounts for creation of particles at the critical radius (Ramkrishna, 2000, p. 20). The last term describes particle deposition: in this example $d_h$ is the hydraulic diameter of the domain; $v_d$ is the deposition velocity ($m^3$/s particles deposited per $m^2$ area).

Population balance models can be applied to CFD in the form of a Eulerian-Eulerian model. Approaches separate into two categories: the method of classes and the method of moments. The method of classes separates the distribution into discrete size bins. The method of moments models the moments of the distribution in place of the distribution itself. Population balances normally use a single velocity field for the particle phase. Some models can include the effect of diameter on droplet trajectories by treating separate size bins as separate Eulerian phases. This is possible both in the method of classes and method of moments (direct quadrature method of moments) but incurs increased computational cost.

Population balance models are also subject to constraints that restrict how growth and nucleation can be modelled. The standard method of moments requires a growth law in a linear form. This cannot model more complex growth behaviour such as diffusion-controlled growth, or the Kelvin effect. This can be circumvented using the quadrature method of moments (McGraw, 2007). The software used in this thesis (Ansys Fluent) includes options for solving population balance models, but it is not able to model nucleation, growth and changes in trajectory based on particle size, at the same time, using population balance methods. The use of population balance modelling in CFD is a recent development in the field (Rigopoulos, 2010). Eulerian-Lagrangian methods have some advantages over population balance modelling. Nucleation, growth and trajectory of the particle can be accounted for in Eulerian-Lagrangian methods in a manner that is arguably more intuitive than population balance models. This can make Eulerian-Lagrangian methods more straightforward to implement in cases where complex particle behaviour is to be modelled.

## 2.9 **Academic Studies using Eulerian-Lagrangian models**

Rigorous modelling of phase-change is possible using Eulerian-Lagrangian models in CFD. This is established in fields such as spray modelling, and is effective at modelling evaporation of droplets. By comparison however, relatively few sources attempt to model condensation/desublimation using a Eulerian-Lagrangian model. This subsection will review some sources that exist in this area.

Jassim *et al.* (2010) studied hydrate formation and deposition in flow through an orifice plate. A CFD model of the orifice was used to find the flow field and temperature around the orifice. This data was then extracted from Fluent in order to perform the rest of the analysis – the authors did not model nucleation and growth using CFD. Particle behaviour was modelled using Fortran code, outside of the CFD simulation (Jassim, 2008).

Gerber (2002) prepared a Eulerian-Lagrangian model of nucleating steam flow. A 'no-slip' condition was applied between the droplet and the gas: particles always followed the flow. Nucleation was modelled based on classical nucleation theory, and growth was calculated based on heat transfer from the particle. The author proposes several strengths of the Eulerian-Lagrangian method over Eulerian-Eulerian methods:

- When modelling changes in particle diameter (due to growth), population balance models pose a comparatively higher computational load.

- Eulerian-Lagrangian methods allow droplet integration to be separated from mesh density, so the accuracy of particle simulations can be increased without increasing mesh density.
- Eulerian-Lagrangian methods also enable easier and more intuitive inclusion of behaviour changes between size regimes (such as Knudsen-number effects).
- Lastly, the author claims Eulerian-Lagrangian are more capable of handling strongly coupled heat and mass transfer.

Sasao *et al.* (2013) used Eulerian-Lagrangian modelling to focus on droplet behaviours, such as breakup and coalescence, through Lagrangian tracking. The nucleation and growth however was modelled using a Eulerian model.

Jansen *et al.* (2011) cover a Eulerian-Lagrangian model of nucleation based on a DSMC (direct simulation Monte-Carlo)-like particle-based algorithm, rather than classical nucleation theory. The authors describe a non-equilibrium, kinetic model of nucleation nozzle flows. Assumptions in classical nucleation theory (section 2.13.2) are an oversimplification for some nozzle flows due to the extreme conditions. As opposed to critical-radius clusters, dimers were introduced into positions randomly selected inside each cell. The particles always followed the flow. Monomer-cluster collisions modelled energy transfer, growth (monomer sticking) and evaporation (Rice, Ramsperger, and Kassel model) cluster-cluster collisions modelled coalescence. Collisions were modelled in a DSMC collision algorithm based on a majorant frequency scheme.

To conclude this section, there are very few Eulerian-Lagrangian modelling examples in literature that make a comprehensive attempt to model nucleation and growth. The examples reviewed, concentrate on pure component (steam) condensation which tends to be controlled by the removal rate of latent heat from the droplet.

## 2.10 **Laminar-Turbulent Transition**

The first part of this chapter has focussed on a review of previous work relating to the research topic. In this second part, the subject now shifts towards more general topics of discussion to provide a background justifying the approach used in the modelling work. Laminar–turbulent transition is predicted to occur at the flowrates under study for the cryogenic condenser. The turbulence modelling, which takes this into account, is discussed following a general introduction to CFD. Backgrounds to nucleation, thermophoresis and Stokes number are also provided.

### *2.10.1 Transition modes*

Langtry (2006) describes five modes of transition to turbulent flow: natural transition; bypass transition; separated flow transition; wake induced transition and reverse transition. **Natural transition** occurs due to an inflection point in the laminar velocity profile. In flow over a single flat plate, transition occurs due to viscous instability waves known as Tollmien-Schlichting waves. In addition, stationary and travelling cross-flow disturbances can also cause natural transition: for example, over swept-wing aerofoils. In **bypass transition** high freestream turbulence forces transition in the boundary layer, far upstream of the location of natural transition. This is the dominant mechanism for internal flows. **Separated flow transition** occurs due to boundary layer separation. Adverse pressure gradients result in flow deceleration, to which the boundary layer is especially sensitive. Under the adverse pressure gradient, the velocity of the near-wall boundary layer reverses, creating a separation bubble. The boundary layer then reattaches downstream, as a turbulent boundary layer. **Wake-induced transition,** also known as periodic-unsteady transition, occurs when a wake periodically interrupts a boundary layer. Examples occur in gas turbines (due to wakes from upstream blades) and in supersonic aircraft (due to periodic shockwaves) (Mayle, 1991). **Reverse transition** occurs in strongly accelerating flows, such as turbomachinery.

The model geometry used in this thesis represents a plate heat exchanger. As an investigation into predicting laminar-turbulent transition, benchmark studies on flow between parallel plates provide an appropriate starting point for comparison to the model geometry. The high aspect ratio of the flow cross section in the model geometry makes flow between parallel plates an appropriate reference case. A brief review is provided below.

### *2.10.2 Literature sources for transition Reynolds numbers*

Textbooks generally state that transition in any internal channel flow may be predicted using hydraulic diameter. Reynolds number ($Re_{d\ hydraulic}$) may be calculated by direct comparison with pipe flow, replacing pipe diameter with hydraulic diameter. The flow may be considered turbulent for Reynolds numbers above 2300. Literature sources are summarised in Table 5, demonstrating some variation in the reported values for laminar-turbulent transition between parallel plates.

| Source | Transition Reynolds number |
|---|---|
| Andersson *et al.* (2011, p. 70) | $Re_{d\ hydraulic}$ = 1600 for parallel plates. Differs from pipe flow (Re = 2100). |
| ASHRAE (2009, p. 3.7) | $Re_{d\ hydraulic} < 2000$ for fully developed laminar flow;<br>$Re_{d\ hydraulic} > 10000$ for fully developed turbulent flow.<br>As pipe flow. |
| Mills (1992, p. 345) | $Re_{d\ hydraulic}$ = 2800 for laminar-turbulent transition between parallel plates. Differs from pipe flow (Re = 2300). |
| Potter *et al.* (2011, p. 105) | $Re_{d\ hydraulic} < 3000$ for laminar flow between parallel plates. Differs from pipe flow (Re = 2000). |
| Remsburg (1998, p. 181) | $Re_{d\ hydraulic}$ = 1000 for onset of turbulence between parallel plates. Differs from pipe flow (Re = 2300). |
| Walas (1990, p. 190) | $Re_{d\ hydraulic}$ = 2300 for plate heat exchangers. As pipe flow. |
| Whan and Rothus (1959) | Demonstrate experimental results for parallel plates: transition occurs between $Re_{d\ hydraulic}$ 2700 to 3300. Fully developed turbulent flow not achieved until $Re_{d\ hydraulic} >$ 6000. |

*Table 5: selected sources on transition flow.*

Identifying a single Reynolds number at which laminar-turbulent transition occurs is complicated by the unpredictable nature of the transition itself. For example, by controlling sources of disturbances such as pump vibrations and pipe roughness laminar flows have been observed experimentally in pipe flows at Reynolds numbers well above 10000 (Potter *et al.*, 2011). There are alternatives to Reynolds number for describing the onset of transition. Garde (1997, p. 253) states that transition occurs due to repeated breakdown of external disturbances imposed on the flow, such as pressure or velocity fluctuations. Local instability occurs when the chi parameter (***X***, equation 2-12**)** exceeds 500. McFarland *et al.* (1997) state that for pipe flow in bends, flow is considered laminar when the Dean number is less than 370.

$$\boldsymbol{X} = \rho_g y \frac{du_g}{dy} / \mu_g \qquad 2\text{-}12$$

$$De = Re_{d\ hydraulic} \times \sqrt{\frac{d_{hydraulic}}{2\ r_{bend}}} \qquad 2\text{-}13$$

As is discussed in greater detail later (section 3.4), a range of Reynolds numbers exist in the three dimensional model geometry. For the three dimensional case including the baffles, the Dean number of flow around the baffles predicts turbulent flow. However, in cases where the geometry is treated as a two dimensional flow between parallel plates, the Reynolds number (ca. 1500) predicts laminar flow according to several sources in Table 5. On this basis, laminar-turbulent transition and low-Reynolds number turbulent flow are expected to play a role in the CFD model.

## 2.11 **General CFD considerations**

In the previous subsection, the importance of turbulent flow considerations for the model geometry were introduced. This subsection provides a general introduction to CFD modelling. The generalised transport equation is used as an introduction, leading to discussion on the turbulence modelling used in this work.

### *2.11.1 Generalised transport equations*

Industrial problems often involve cases where the effects of mass transfer, heat transfer and fluid flow influence each other. In these cases, a generalised representation of transport equations can be made in which heat, mass and momentum transfer are treated as analogous transport phenomena. The transport of any variable ($\phi$) can be expressed using the generalised transport equation, shown below in vector differential form and Cartesian tensor notation in equations 2-14 and 2-15 respectively.

$$\frac{\partial(\rho_g \phi)}{\partial t} + \nabla_{div} \cdot (\rho_g \phi \vec{u}) = \nabla_{div} \cdot (\Gamma \nabla_{grad} \phi) + S_\phi \qquad 2\text{-}14$$

$$\frac{\partial(\rho_g \phi)}{\partial t} + \frac{\partial(\rho_g \phi u_j)}{\partial x_j} = \frac{\partial}{\partial x_j}\left(\Gamma \frac{\partial \phi}{\partial x_j}\right) + S_\phi \qquad 2\text{-}15$$

This equation can be considered as four terms. The transient term $\partial(\rho_g\phi)/\partial t$ accounts for accumulation of variable $\phi$ inside the control volume. This is only relevant when considering the transient state. The convective term $\nabla_{div}(\rho_g \phi u)$ accounts for transport of the variable $\phi$ due to the velocity field. For example, mass flows into and out of an individual cell are described by this term. The diffusive term $\nabla_{div}(\Gamma \nabla_{grad}\phi)$ accounts for diffusion as a transport mechanism. $\Gamma$ is the diffusion coefficient. In laminar flows, this represents kinematic viscosity, thermal conductivity or molecular diffusivity for momentum, heat and mass transfer respectively. In turbulent flows the motion of eddies dominates all the diffusion terms. The source term $S_\phi$ accounts for creation or destruction of variable $\phi$ within the cell. In the context of the generalised transport equation, any terms that do not fit the above structure are treated as source terms. Values of $\phi$, $\Gamma$ and $S_\phi$ for the conservation equations are given in Date (2005, p. 4).

### 2.11.2 Discretisation

In this work as with most CFD a finite volume method is used to discretise the PDEs. The PDEs are integrated, putting them in a form that applies to a single mesh cell. Divergence theorem integrates over the cell faces, the result balances flows into and out of the cell (Craft, 2011). This is demonstrated in equations 2-16 and 2-17 below.

$$\int_V \frac{\partial(\rho_g \phi)}{\partial t} dV + \oint \rho_g \phi \vec{u}\, d\vec{A} = \oint \Gamma \nabla_{grad} \phi\, d\vec{A} + \int_V S_\phi dV \qquad 2\text{-}16$$

$$\frac{\partial(\rho_g \phi)}{\partial t} V + \sum_f^{N_{faces}} \rho_g \vec{u}_f \phi_f \cdot \vec{A}_f = \sum_f^{N_{faces}} \Gamma \nabla_{grad} \phi_f \cdot \vec{A}_f + S_\phi V \qquad 2\text{-}17$$

During the calculation, the value of the variable at the cell-centre $\phi$ and cell-face $\phi_f$ are unknown and must be obtained from the surrounding cells. A first order upwind scheme applies the upstream cell-centre values directly to the cell-faces, a second order upwind schemes uses the gradient in the upstream cell to extrapolate the upstream cell-centre value to the cell-face. This gives a set of linearised equations that calculate the field for the variable $\phi$, by recalculating iteratively for all cells in the domain.

### 2.11.3 Turbulence modelling

Turbulence introduces chaotic fluctuations in flow variables. Figure 7 represents a typical point-source measurement of any variable in a turbulent flow. Reynolds decomposition (equation 2-18) describes these fluctuations in terms of an instantaneous fluctuating component $\phi'(t)$ and a time-averaged component $\Phi$. The time-averaged component is constant for steady-state simulations. The fluctuating component has a value of zero when averaged over a sample time $\Delta t$.

$$\phi(t) = \Phi + \phi'(t) \qquad 2\text{-}18$$

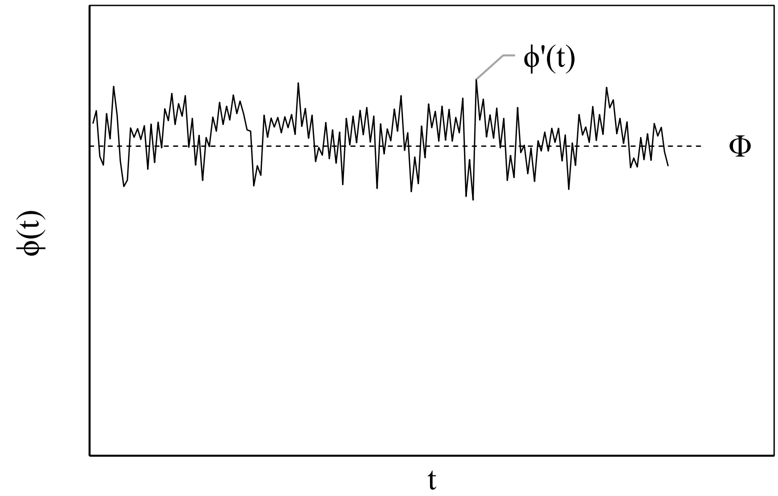

Figure 7: Illustration of Reynolds decomposition (Versteeg and Malalasekera, 2007, p. 41).

Time-averaging creates an additional term in the transport equation, $\partial(-\rho_g \overline{u_i'u_j'})/\partial x_j$ which results in additional turbulent stresses, known as Reynolds stresses. This results in time-averaged transport equations known as Reynolds averaged Navier-Stokes (RANS) equations. These are shown below in equations 2-19 and 2-20, where $S_{ij}$ is the strain rate tensor (Wilcox, 2006, p. 40). RANS CFD simulations model turbulence using this approach. These simulations aim to calculate the time-averaged components of the flow variables. The Reynolds stresses represent a closure problem usually solved through an empirical approach.

$$\frac{\partial \rho_g}{\partial t} + \frac{\partial}{\partial x_i}(\rho_g u_i) = 0 \qquad 2\text{-}19$$

$$\frac{\partial(\rho_g u_i)}{\partial t} + \frac{\partial}{\partial x_j}(\rho_g u_i u_j) = -\frac{\partial P}{\partial x_i} + \frac{\partial}{\partial x_j}(2\mu_g S_{ij}) + \frac{\partial}{\partial x_j}(-\rho\overline{u'_\iota u'_J})(-\rho_g\overline{u'_\iota u'_J}) \qquad 2\text{-}20$$

The Reynolds stresses consists of six individual stress terms. Isotropic turbulence models approximate these Reynolds stresses using the Boussinesq hypothesis. In the Boussinesq hypothesis, the Reynolds stresses are assumed to be proportional to the mean deformation rate (velocity gradients). Turbulent viscosity, also known as eddy viscosity $\mu_t$ is introduced, a scalar variable operating in a similar manner to the dynamic viscosity. The Boussinesq hypothesis is shown in equation 2-21, for an incompressible flow.

$$\tau_{ij} = -\rho_g \overline{u'_i u'_j} = 2\mu_t S_{ij} - \frac{2}{3}\rho_g k \delta_{ij} \qquad 2\text{-}21$$

Two-equation models (k-ε and k-ω models) are the most common turbulence modelling approach used in engineering CFD. Both k-ε and k-ω models are RANS models, and use the Boussinesq hypothesis making them isotropic turbulence models. The transition SST (shear stress transport) model used in this work is an isotropic RANS model based on two-equation modelling. k-ε models, use transport of turbulent kinetic energy (k) and eddy dissipation (ε) to predict eddy viscosity in the fluid domain. k-ε models require wall functions as is elaborated in section 2.11.5. k-ω models use turbulence frequency (ω) in place of eddy dissipation which frees them of this constraint. Both k-ε and k-ω models are empirical, relying to some degree on constants derived from experimental data.

### *2.11.4 SST model and transition SST model.*

The transition SST model is a modification of the shear stress transport (SST) model. It models laminar-turbulent transition using two transported variables in addition to the SST model. These additional variables are the transition-onset Reynolds number ($Re_{\delta t}$) and intermittency (γ).

The SST model is a two-equation k-ω turbulence model. It uses a k-ω model in the boundary layer, and a modification of the k-ε model in the bulk flow. The main benefit of the SST model is that it allows the boundary layer resolution of the standard k-ω model to be partnered with the stability of the k-ε model in the bulk flow, overcoming the respective weaknesses of both models in these areas. This is achieved through the cross-diffusion term $D_\omega$, which is the main difference between the SST model and the standard k-ω model. The models are based around the transport of turbulence frequency (ω) and turbulent kinetic energy (k). The problem of closure is solved using the two transported variables to find turbulent viscosity through the proportion $\mu_t = \rho_g k/\omega$. Transport equations for these two variables are given below in equations 2-22 and 2-23 (Versteeg and Malalasekera, 2007). $\mathbf{S} = (2S_{ij}S_{ij})^{0.5}$ is the scalar invariant of the strain rate tensor**.**

$$\frac{\partial(\rho_g k)}{\partial t} + \frac{\partial}{\partial x_j}(\rho_g k u_j) = \frac{\partial}{\partial x_j}\left[\left(\mu_g + \frac{\mu_t}{\sigma_k}\right)\frac{\partial k}{\partial x_j}\right] + \mu_t \boldsymbol{S}^2 - \beta^* \rho_g k \omega \qquad 2\text{-}22$$

$$\frac{\partial(\rho_g \omega)}{\partial t} + \frac{\partial}{\partial x_j}(\rho_g \omega u_j) = \frac{\partial}{\partial x_j}\left[\left(\mu_g + \frac{\mu_t}{\sigma_\omega}\right)\frac{\partial \omega}{\partial x_j}\right] + \frac{\alpha \rho_g}{\mu_t}\mu_t \boldsymbol{S}^2 - \beta^* \rho_g \beta \rho_g k \omega^2 + D_\omega \qquad 2\text{-}23$$

$D_\omega$ is the cross-diffusion term, shown below in equation 2-24. Equation 2-23 may be obtained by replacing the turbulent dissipation rate (ε) in the k-ε model using the relationship $\omega = \varepsilon/k$. $F_1$ is a switching function that activates the cross-diffusion term outside the boundary layer.

$$D_\omega = 2(1 - F_1)\rho_g \frac{1}{\omega\sigma_{\omega 2}} \frac{\partial k}{\partial x_j} \frac{\partial \omega}{\partial x_j} \qquad 2\text{-}24$$

### *2.11.5 SST model wall boundary conditions and near-wall behaviour*

The strength of the k-ω model is that it can be integrated to the boundary layer, this is not possible with the standard k-ε model. The standard wall function used in the k-ε model is a significant simplification responsible for many of the disagreements between simulation and experiment observed using the standard k-ε model. The SST model switches to the k-ω model in the boundary layer instead of using wall functions. This low-Reynolds number approach allows more accurate modelling of the boundary layer.

A blending function $F_1$ switches between k-ε and k-ω type models in the SST model (by turning the cross-diffusion term on or off as aforementioned). This blending function takes the following form:

$$F_1 = tanh(\text{arg}_1^4) \qquad 2\text{-}25$$

$$\text{arg}_1 = min\left[max\left(\frac{\sqrt{k}}{0.09\omega y}, \frac{500\mu_g}{\rho_g y^2 \omega}\right), \frac{4\rho_g k}{\sigma_{\omega 2} D_\omega^+ y^2}\right] \qquad 2\text{-}26$$

$$D_\omega^+ = \max\left[2\rho_g \frac{1}{\omega\sigma_{\omega 2}} \frac{\partial k}{\partial x_j} \frac{\partial \omega}{\partial x_j}, 10^{-10}\right] \qquad 2\text{-}27$$

Justification for this is given in Menter (1993). The first argument ($\sqrt{k}/0.09\omega y$) is the turbulent length scale divided by the wall distance. This argument equals 2.5 in the logarithmic layer and goes to zero at the boundary layer edge. The second argument ensures that $F_1$ does not go to zero in the viscous sublayer. Third argument prevents degenerate solutions from low freestream values of ω. $D_\omega^+$ is the cross-diffusion term itself, with a limit to prevent it going to zero.

$F_1$ activates the cross diffusion term and is also used elsewhere. The turbulent Prandlt numbers are blended using $F_1$, shown below:

$$\sigma_k = \frac{1}{F_1/1.176 + (1 - F_1)/1.0} \qquad \text{2-28}$$

$$\sigma_\omega = \frac{1}{F_1/2.0 + (1 - F_1)/1.168} \qquad \text{2-29}$$

$F_1$ is also used to switch between values of $\beta_i$ (model constant in the dissipation term of the ω transport equation 2-23 above).

$$\beta_i = 0.075(F_1) + 0.0828(1 - F_1) \qquad \text{2-30}$$

Generally turbulent viscosity $\mu_t$ is related to k and ω by the proportion $\mu_t = \rho k/\omega$. However in the turbulence modelling this is subject to some modifications. In the SST model, one of these modifications is Bradshaw's assumption, ($\mu_t = 0.31\ \rho k/\mathbf{S}$), which improves the result for adverse pressure gradients. Bradshaw's assumption is subject to another blending function $F_2$. This also activates in the boundary layer, $F_2$ is switched more gradually than $F_1$ because Bradshaw's assumption is used in the outer (wake) layer. Bradshaw's assumption is deactivated in the freestream by the maximum ("max") function to prevent infinite values of turbulent viscosity $\mu_t$ for zero shear rate S. $F_2$ also prevents Bradshaw's assumption activating outside of the wall-affected region, for example in free shear layers in the flow.

$$\mu_t = \frac{\rho k}{\omega} \frac{1}{max\left[\frac{1}{\alpha^*}, \frac{SF_2}{0.31\omega}\right]} \qquad \text{2-31}$$

$$F_2 = tanh(\mathrm{arg}_2^2) \qquad \text{2-32}$$

$$\mathrm{arg}_2 = max\left[2\frac{\sqrt{k}}{0.09\omega y}, \frac{500\mu_g}{\rho_g y^2 \omega}\right] \qquad \text{2-33}$$

When Bradshaw's assumption is not in effect, the SST model reverts to the k-ω model definition for turbulent viscosity given in Ansys fluent, this is subject to the turbulence dampening correction α* in low Reynolds number flows.

$$\alpha^{*} = 1\left(\frac{\frac{\beta_i}{3} + \frac{\rho_g k}{\mu_g \omega}\Big/ 6}{1 + \frac{\rho_g k}{\mu_g \omega}\Big/ 6}\right) \qquad 2\text{-}34$$

The coefficient for the production term in the ω transport equation α is also subject to switching from $F_1$:

$$\alpha = \frac{0.553F_1 + 0.440(1 - F_1)}{\alpha^{*}}\left(\frac{0.11111 + \frac{\rho_g k}{\mu_g \omega}\Big/ 2.95}{1 + \frac{\rho_g k}{\mu_g \omega}\Big/ 2.95}\right) \qquad 2\text{-}35$$

Wall boundary conditions are defined using an enhanced wall treatment (EWT-ω). This allows for a solution for a range of grid sizes. It involves applying a blending function so that for refined meshes, conditions in the first cell are defined as a laminar sublayer and the boundary layer is integrated to the wall using the turbulence model, whereas for coarse meshes a wall function approach is used. In this work $y^{+}_{1\text{st cell}}$ is less than unity for the entire mesh, so the boundary layer is solved by the turbulence model without the wall function approach, and the wall function approach is included below for completeness only.

As ω is undefined at the wall, the value of ω in the first cell is defined using the hyperbolic variation $\omega = 6\nu/\beta y^2$ (Versteeg and Malalasekera, 2007, p. 91). This is expressed in dimensionless units in Fluent as follows:

$$\omega_{1st\ cell} = \frac{\rho_g (u^{*})^2}{\mu_g}\omega^{+} \qquad 2\text{-}36$$

$$\omega^{+} = \frac{6}{\beta_i (y^{+})^2} \qquad 2\text{-}37$$

As aforementioned, for coarse meshes this is blended with a wall function approach, for example:

$$\omega^+ = \frac{1}{\sqrt{0.09}} \frac{du^+_{turb}}{dy^+} \qquad 2\text{-}38$$

$$\omega_{1st\ cell} = \sqrt{(\omega^2_{viscous} + \omega^2_{logarithmic}} \qquad 2\text{-}39$$

The boundary condition for turbulence kinetic energy k are found as follows. A reflective boundary condition is applied to the wall, see equation 2-40 below. The local equilibrium hypothesis is applied to the wall adjacent cell, which assumes production and dissipation are equal. The production term $G_k$ is found based on the velocity gradient.

$$\frac{\partial k}{\partial n_{cells,from\ wall}} = 0 \qquad 2\text{-}40$$

$$G_k \approx \tau_w \frac{\partial u}{\partial y} \qquad 2\text{-}41$$

The velocity gradient is found using velocities from the enhanced law-of-the-wall, which again defines the near-wall cell conditions based on a blend between a linear (viscous sublayer) or a wall function (logarithmic) based on mesh density. In this work, $y^+_{1st\ cell}$ is less than one everywhere, so the near-wall conditions are defined as a laminar sublayer. α corrects for pressure gradient effects.

$$\frac{du^+_{lam}}{dy^+} = 1 + \alpha y^+ \qquad 2\text{-}42$$

$$\alpha = \frac{\mu_g}{\rho_g^2 (u^*)^3} \frac{dP}{dx} \qquad 2\text{-}43$$

For completeness, switching to a wall function for coarse meshes is achieved as follows:

$$\frac{du^+}{dy^+} = e^{\Gamma}\frac{du^+_{lam}}{dy^+} + e^{1/\Gamma}\frac{du^+_{turb}}{dy^+} \qquad 2\text{-}44$$

$$\Gamma = -\frac{0.01(y^+)^4}{1+5y^+} \qquad 2\text{-}45$$

$$\frac{du^+_{turb}}{dy^+} = \frac{1}{0.41y^+}\left[\boldsymbol{S}'(1-\beta_{therm\,cor}u^+ - \gamma_{therm\,cor}(u^+)^2)\right]^{0.5} \qquad 2\text{-}46$$

$$\mathbf{S'} = \begin{cases} 1+\alpha y^+ \; for \; y^+ < 60 \\ 1+60\alpha \; for \; y^+ \geq 60 \end{cases} \qquad 2\text{-}47$$

$$\beta_{therm\,cor} = \frac{\sigma_t q_w}{\rho_g C_p u^* T_w} \qquad 2\text{-}48$$

$$\gamma_{therm\,cor} = \frac{\sigma_t (u^*)^2}{2C_p T_w} \qquad 2\text{-}49$$

## 2.12 Nucleation

Nucleation is the necessary first step in the phase changes governing particle formation. Both desublimation and condensation may be described by classical nucleation theory.

## 2.13 Classical Nucleation Theory

Classical nucleation theory can be used to predict nucleation of a condensed phase from a gaseous phase. In this thesis, classical nucleation theory is used to predict the nucleation rate of benzene from the vapour phase. This section will introduce some basic principles in classical nucleation theory.

### *2.13.1 Homogeneous nucleation*

Homogeneous nucleation proceeds when unstable, sub-critical clusters grow by addition of molecules to beyond a critical radius. At sizes above the critical radius, clusters become stable nuclei. Growth of the stable nuclei continues and eventually leads to drops or particles visible to the naked eye.

Sub-critical clusters are continually created and destroyed because of molecular collisions in the gas. The resulting steady-state cluster distribution may be described by Boltzmann statistics (Raoux and Wuttig, 2009, pp. 125-129):

$$n^{equ}_{(r)} = n_1 \cdot e^{\left(\frac{-\Delta G_{cluster(r)}}{k_B T}\right)} \qquad 2\text{-}50$$

$\Delta G_{cluster(r)}$ is the Gibbs free energy change forming a cluster of radius r. This consists of two competing contributions: the volume free energy change $\Delta G_v$ and the interfacial energy. This results in the classical expression for $\Delta G_{cluster(r)}$:

$$\Delta G_{cluster(r)} = 4\pi r^2\sigma + \frac{4}{3}\pi r^3 \Delta G_v \qquad \text{2-51}$$

The volume free energy change $\Delta G_v$ is given by the expression:

$$\Delta G_v = -\frac{RTln(S)}{V_m} \qquad \text{2-52}$$

Equation 2-51 is plotted below in Figure 8. A negative $\Delta G_{cluster(r)}$ is required for a stable nucleus. In a supersaturated system sub-critical clusters grow, eventually reaching a size where this condition is satisfied after passing through a maximum (critical) Gibbs free energy ΔG* at the critical radius r*. This is not the case for under-saturated systems, as is shown by the grey line in Figure 8. At higher degrees of supersaturation (S > 1), the critical radius decreases and the likelihood of sub-critical clusters growing to stable nuclei increases.

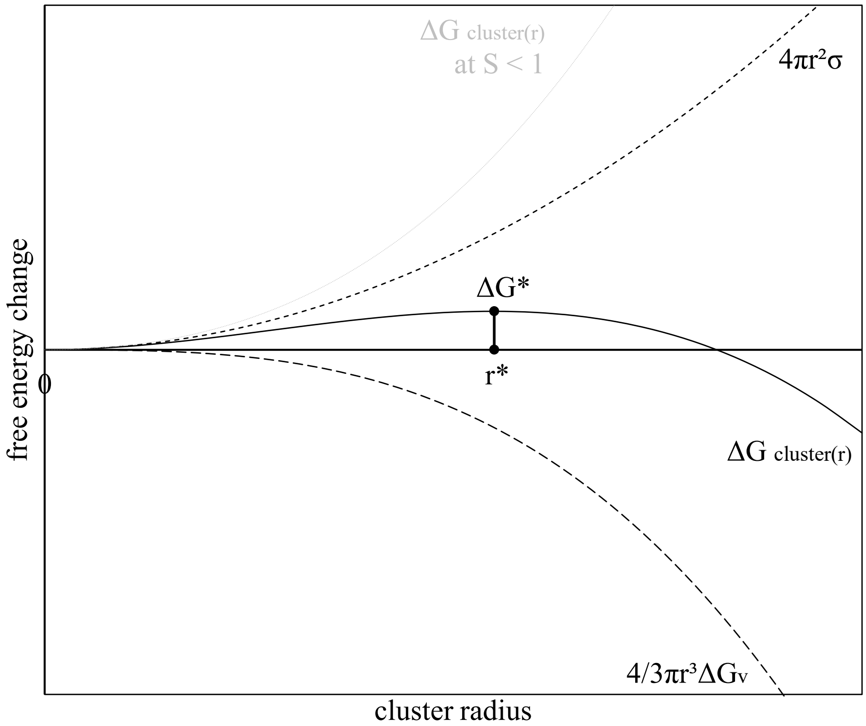

*Figure 8: Illustration of equation 2-51.*

The critical radius can be determined by setting the partial derivative (with respect to radius) of equation 2-51 equal to zero. This results in the Kelvin equation for critical radius shown in equation 2-53. The critical Gibbs free energy equation 2-54 may be found by substituting the critical radius into equation 2-51:

$$r^* = \frac{2\sigma V_m}{RTlnS} \tag{2-53}$$

$$\Delta G^* = \frac{16\pi\sigma^3 V_m^2}{3R^2T^2(\ln(S))^2} \tag{2-54}$$

Expressions for the nucleation rate J derived from classical theory typically take a form similar to that shown below in equation 2-55 (Richardson *et al.*, 2002, p. 841). The exponential term makes this nucleation rate sensitive to the degree of supersaturation as is elaborated in section 2.13.3.

$$J = F \cdot e^{\left(-\frac{\Delta G^*}{k_B T}\right)} \tag{2-55}$$

### *2.13.2 Derivation of the nucleation rate expression*

The following description is based on Bakhtar *et al.* (2004). A nucleation rate expression may be derived by first considering the following balance for any cluster containing g number of molecules, (the cluster may be referred to as a 'g-mer'):

$$I_g = C_g f_g - E_{g+1} f_{g+1} \tag{2-56}$$

$I_g$ is the net rate for the transformation of g-mers to g+1-mers. $C_g$ and $E_{g+1}$ are the condensation and evaporation rates respectively. $f_g$ is the gas concentration of the g-mers in unsteady conditions. At steady state, the *principle of detailed balance* (equation 2-57) can be used to eliminate $E_{g+1}$ from equation 2-56. This leads to equation 2-58. This discrete form can be approximated by the partial differential on the right hand side.

$$C_g n_g = E_{g+1} n_{g+1} \tag{2-57}$$

$$\frac{I_g}{C_g n_g} = \frac{f_g}{n_g} - \frac{f_{g+1}}{n_{g+1}} \cong -\frac{\partial}{\partial g}\left(\frac{f_g}{n_g}\right) \tag{2-58}$$

The assumption of a steady state nucleation rate is normally justified based on the short timescale of nucleation. Nucleation rate is initially transient, reaching a steady state after timescale of 0.1μs, the steady state assumption is justified as the characteristic times of the fluid flows are typically larger. Under steady state conditions, $f_g$ is a function of g but not of t, and $I_g$ is the same for all g. With these conditions equation 2-58 may be integrated:

$$I\int_{g=1}^{\infty}\frac{1}{C_g n_g}dg=\int_{g=1}^{\infty}-1\,d\left(\frac{f_g}{n_g}\right) \qquad \text{2-59}$$

The integral on the right-hand side may be eliminated by considering the limits. $f_g/n_g \rightarrow 1$ for g = 1 and $f_g/n_g \rightarrow 0$ for $g \rightarrow \infty$.

$$I=\left[\int_{g=1}^{\infty}\frac{1}{C_g n_g}dg\right]^{-1} \qquad \text{2-60}$$

The $n_g$ term may be replaced with reference to equation 2-50.

$$I=\left[\int_{g=1}^{\infty}\frac{1}{C_g n_1 e^{\left(\frac{-\Delta G_{cluster}}{k_B T}\right)}}dg\right]^{-1} \qquad \text{2-61}$$

The condensation rate is found from the Hertz-Knudsen equation for monomer flux, multiplied by the surface area of the droplet. For a spherical cluster, the surface area of the droplet is expressed in terms of g as $4\pi r^2 = \mathbf{A}g^{2/3}$. The factor $\mathbf{A} = \sqrt[3]{(36\pi v_m^{-2})}$ is found by rearranging the mass of the cluster $4/3\pi r^3\rho_p = gm$. This is important for the integral because the condensation rate is proportional to $g^{2/3}$, whereas the exponential is a very steep peak at $g = g^*$. The integral is then simplified by approximating the $C_g$ as $C_{g^*}$.

$$C_g = q_c \boldsymbol{A} g^{\frac{2}{3}}\frac{P_i}{\sqrt{2\pi m k_b T}} \qquad \text{2-62}$$

$$I=\left[\int_{g=1}^{\infty}\frac{1}{C_{g*} n_1 e^{\left(\frac{-\Delta G_{cluster}}{k_B T}\right)}}dg\right]^{-1} \qquad \text{2-63}$$

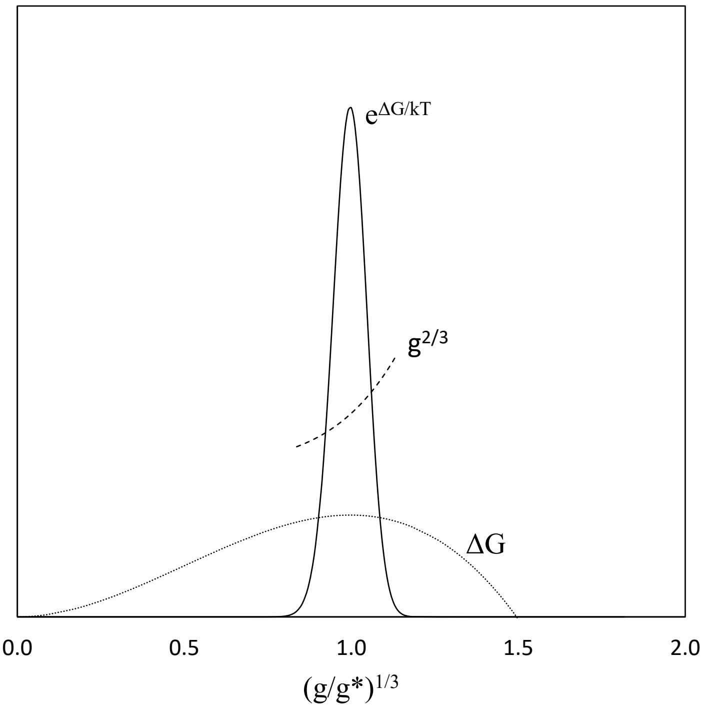

*Figure 9: Illustration of the variation in* $g^{2/3}$ *in equation* 2-61*, not to scale (Markov, 2003, p. 113).*

The free energy of the cluster $\Delta G_{cluster}$ is approximated using a second-order Taylor expansion around the critical Gibbs free energy ΔG* (equation 2-64). As the critical Gibbs free energy is a maximum, the first derivative $(\partial\Delta G/\partial g)_*$ is zero and can be removed.

$$\Delta G_{cluster} \cong \Delta G^* + (g - g^*)\left(\frac{\partial \Delta G}{\partial g}\right)_* + \frac{(g - g^*)^2}{2}\left(\frac{\partial^2 \Delta G}{\partial g^2}\right)_* \qquad 2\text{-}64$$

This affects the integration. ΔG* is no longer a function of g and can be placed outside of the integral along with other constants. The integration is grouped into the factor Z, known as the Zeldovich factor. The overall expression for nucleation rate (I) then takes the form shown in equation 2-65, which resembles equation 2-55 as desired.

$$I = C_{g^*} n_1 Z e^{\frac{-\Delta G^*}{k_B T}} \qquad 2\text{-}65$$

$$\frac{1}{Z} = \int_{g=1}^{\infty} e^{\left[-\left(\frac{\partial^2 \Delta G}{\partial g^2}\right)_* \frac{(g-g_*)^2}{2k_B T}\right]} dg \qquad 2\text{-}66$$

This integration can be solved through the following procedure (Khvorostyanov and Curry, 2014, p. 297) resulting in equation 2-67.

1. Extending the lower limit g = 1 to -∞.
2. The substitution rule u = (g-g*) can be used to remove g*.
3. The integration is in the form of the Gaussian integral.
4. The second partial derivative $-(\partial \Delta G^2/\partial g^2)_*$ can be found by first expressing $\Delta G_{cluster}$ from equation 2-51 in terms of g, using the same replacements as given above (pg. 50), and differentiating twice (Vehkamaki *et al.*, 2007, p. 94).

$$Z = \sqrt{\frac{-(\partial \Delta G^2/\partial g^2)_*}{2\pi k_B T}} = \sqrt{\frac{\sigma}{k_B T}\frac{v_m}{2\pi r^{*2}}} \qquad 2\text{-}67$$

The classical nucleation rate expression 2-65, with the inclusion of the Zeldovich factor, is known as the Becker-Doring model. Without the Zeldovich factor, the same expression is known as the Volmer-Weber model (Vehkamaki *et al.*, 2007). Physically, the Zeldovich factor accounts for the possibility that some clusters which grow to above the critical size may still decay (Adamson and Gast, 1997, p. 329).

Literature sources are highly varied in the reporting of the classical nucleation rate expression. However, most are derived from the above equations, with some substitutions. Equation 2-68 below is taken from Katz and Ostermier (1967), and is found by the following:

1. Substitute equation 2-62 (with $4\pi r^{*2} = \mathbf{A}g^{*2/3}$), 2-67 and 2-54 into equation 2-65.
2. Substitute $n_1 = P_i/k_bT$ by rearrangement of the ideal gas law.
3. $S = P_i/P_e$ allows $P_i$ to be replaced by $SP_e$.
4. Substitute $k_b$ for $R/N_a$, where $N_a$ is Avogadro's number, R is the universal gas constant.
5. Assume $q_c = 1$. This is equivalent to assuming a 100% success rate for cluster-monomer collisions.
6. The molar volume $V_m$ can be substituted based on density, $M/\rho_p$.

$$J = \left(\frac{2N_A^3}{\pi}\right)^{0.5}\left(\frac{P_e}{RT}\right)^2 S^2\frac{(\sigma M)^{0.5}}{\rho_p}e^{\left(\frac{-16\pi N_A}{3R^3}\left(\frac{M}{\rho_p}\right)^2\left(\frac{\sigma}{T}\right)^3(lnS)^{-2}\right)} \qquad 2\text{-}68$$

This classical nucleation theory is important because it allows both the onset and the rate of homogenous nucleation to be predicted. This allows the equation to be used to predict where particles will form and at what rate in the CFD model. This section has described the assumptions underlying classical nucleation theory. It is important to understand how the expression is derived and what assumptions have been made. As is elaborated in the conclusion of this work (section 7.4.5) classical nucleation theory is an imperfect simplification of the nucleation process. Stating these assumptions clearly is prudent for the research described in this thesis.

### *2.13.3 Onset of homogeneous nucleation*

Homogeneous nucleation is possible for any supersaturated system. Below the critical degree of supersaturation this rate in negligibly low. Due to the exponential relationship, nucleation rate is an extremely strong function of the degree of supersaturation. Homogeneous nucleation happens abruptly once the critical degree of supersaturation is reached, forming what is sometimes referred to as the "Wilson point" (location of maximum supersaturation in expanding steam flows (Ding *et al.*, 2014)) or a "nucleation front" (Housiadas *et al.*, 1998). A finite value of J is chosen to predict the onset of nucleation in modelling work (typ. J = 1 nuclei/cm$^3$s (Friedlander, 2000)). The critical degree of supersaturation can be found by iterative solution from equation 2-68.

### *2.13.4 Non-isothermal correction factors*

Nucleation liberates latent heat. If nucleation occurs rapidly, this raises the temperature of the cluster, reducing the degree of supersaturation. This affects nucleation in rapidly expanding steam flows in nozzles and turbomachinery. It may reduce the nucleation rate to ca. 100th of that predicted by classical nucleation theory. It can be accounted for using a correction factor, such as the Kantrowitz factor (Dykas and Wroblewski, 2012) or Feder's correction factor (Dawson *et al.*, 1969). The former is applied to the isothermal nucleation rate as shown in equation 2-69. This is found from the enthalpy and ratio of specific heats (equation 2-70). Derivation is based on the Clausius-Capeyron equation, more information is given in Kantrowitz (1951).

$$J_{non-isothermal} = \frac{1}{1+\theta_{Kantrowitz}} J_{isothermal} \tag{2-69}$$

$$\theta_{Kantrowitz} = \frac{2(\gamma - 1)}{(\gamma + 1)} \frac{h_{lat}}{RT} \left( \frac{h_{lat}}{RT} - 0.5 \right) \tag{2-70}$$

This non-isothermal correction is not necessary in this work. In the presence of large volumes of inert gas, collisions with the inert components (which transfer heat) are much more common than those of the condensing/desublimating species. Isothermal assumptions are therefore valid during condensation from an inert carrier gas (Bakhtar *et al.*, 2004).

### *2.13.5 Heterogeneous nucleation*

Heterogeneous occurs when the new phase nucleates on the surface of a contaminant present in the parent phase. This has an effect similar to catalysis in chemical reactions, lowering the energy barrier. Heterogeneous nucleation accelerates the nucleation rate at lower degrees of supersaturation due to this change in the critical Gibbs free energy.

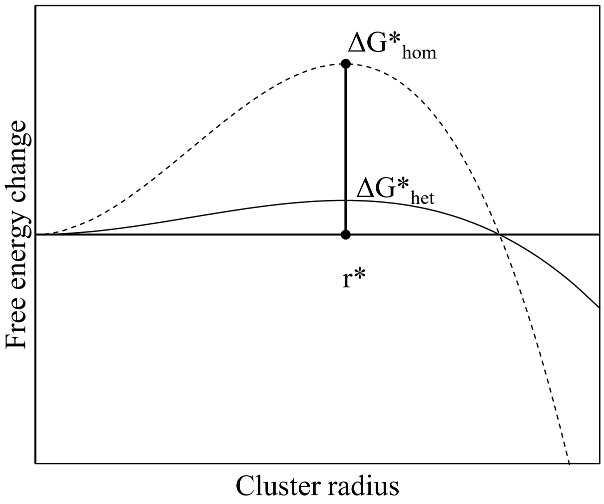

*Figure 10: Illustration of effect of heterogeneous nucleation on Gibbs free energy.*

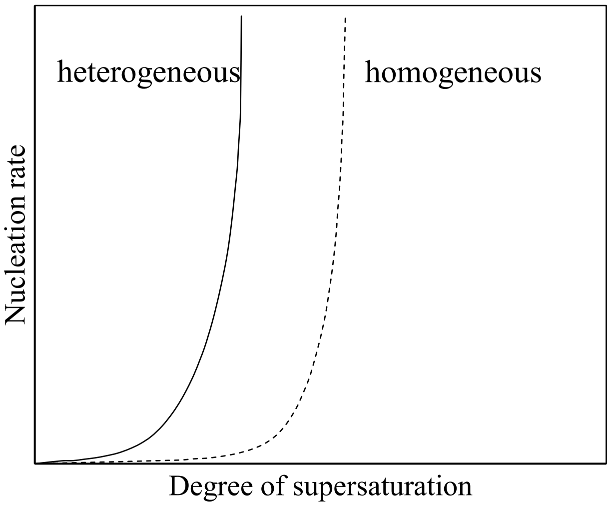

*Figure 11: Illustration of effect of heterogeneous nucleation on nucleation rate (Richardson et al., 2002, p. 842).*

Heterogeneous nucleation is the dominant mechanism of aerosol formation in most industrial flows, and normally occurs at low degrees of supersaturation (typ. 1.001 to 1.12, (Krupiczka and Pyschny, 1990)). As the degree of supersaturation is so low, it is normal for modelling purposes to assume that any supersaturated flow undergoes heterogeneous nucleation.

The Fletcher factor may be applied to classical nucleation theory to account for the effects of heterogeneous nucleation. The assumption of a flat foreign nucleus simplifies this expression to its most common form (equation 2-71, 2-72). In practice, the Fletcher factor should be viewed as a conceptual tool and not an accurate prediction of heterogeneous nucleation rate. The Fletcher factor acts on the exponential term (equation 2-55), but heterogeneous nucleation also changes the pre-exponential factor (Fletcher, 1959). This pre-exponential factor may be found by experiment.

$$\theta_{Fletcher} = \frac{1}{4}(2 - 3\cos\vartheta + cos^3\vartheta) \tag{2-71}$$

$$\Delta G^*_{het} = \theta_{Fletcher}\,\Delta G^*_{hom} \tag{2-72}$$

## 2.14 Mechanisms for Particle Deposition on Surfaces

Particles suspended in a flow can become deposited on a surface through a number of mechanisms. In the context of aerosol deposition these are typically split into several categories. Inertial deposition occurs for particles larger than 1 µm, when particles deviate from the fluid flow stream. Particle deposition can also occur due to only physical size while following the fluid flow stream (interception). Brownian diffusion drives submicron particles to the surface through random motion. Thermophoreis is a type of directional Brownian diffusion caused by temperature gradient. Particle deposition through sedimentation occurs under gravity. Other forces, such as electrostatic forces, can also drive particle deposition (Tien and Ramarao, 2007). Inertial deposition and thermophoresis are discussed in sections 2.15 and 2.16 below.

## 2.15 Inertial Deposition and Stokes Number

When particles are entrained in a fluid flow, they can become separated from the flow if the flow accelerates, slows or changes direction. This can be used to separate particles from gas flows by deposition on a surface. Industrial examples include impact filtration, cyclones and mist eliminators. This form of particle deposition is important for particles inside the cryogenic condenser. The degree to which particle trajectories deviate from the fluid flow can be described using the Stokes number. The Stokes number is the ratio of the momentum response time of the particle $\tau_p$ to a characteristic time for the fluid $\tau_f$, shown in equation 2-73.

$$Stk = \frac{\tau_p}{\tau_f} \qquad \text{2-73}$$

Increasing Stokes number leads to increased inertial deposition. This is illustrated in Figure 12 below. Red, green and blue colours represent particles of increasing diameter, which increases Stokes number. With increasing Stokes number particles struggle to follow the curvature of the flow. Small particles, with small Stokes numbers, remain entrained in the gas flow whilst large particles with large Stokes numbers deviate from the flow and deposit onto surfaces.

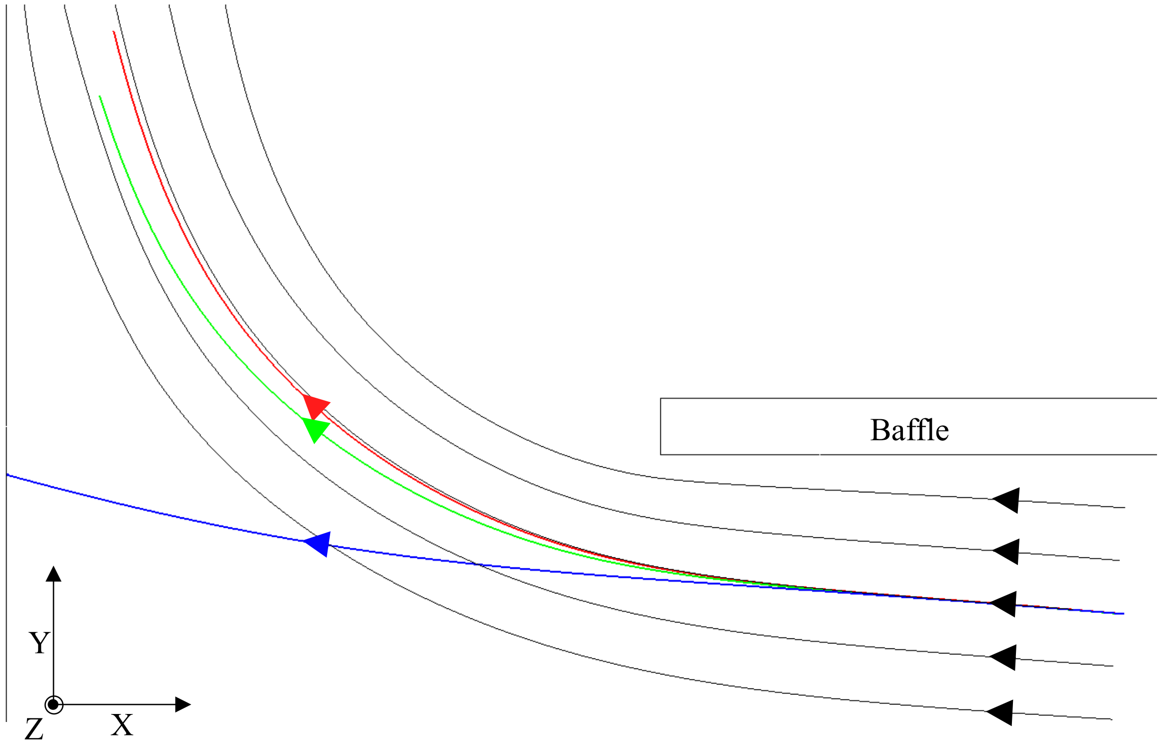

*Figure 12: Illustration of particle deviation from the flow streams (black) with increasing particle diameter (red, green, blue).*

The momentum response time of the particle is the time taken for the particle to reach 63.2% of the free-stream velocity from rest. This is the time constant for a first order system = 1- $^1/_e$ (Clark, 2011). In the case of simple Stokes drag on a dense sphere, $\tau_p$ can be determined entirely by the blue-highlighted text in equation 2-74. This thesis considers two additional effects that result in deviation from Stokes drag. These are the effects of the particle Reynolds number and the effects of the particle Knudsen number $Kn_p$. The particle Reynolds number affects the drag coefficient $C_d$ in a manner that is straightforward, and discussion surrounding this point is deferred to the methods section (3.7.5). The effects of particle Knudsen number are discussed in the next subsection.

$$\frac{dv_p}{dt} = \frac{18u_g}{\rho_p d_p^2}\frac{C_d Re_p}{24}\left(u_g - v_p\right) = \frac{1}{\tau_p}\left(u_g - v_p\right) \tag{2-74}$$

### 2.15.1 Cunningham slip correction factor

Aerosol flows involve small particles suspended in a gas. For this reason it is common to assume Stokes drag, and to include the Cunningham slip correction factor $C_c$ to account for non-continuum effects. In this case, the momentum response time for the particle is as shown in equation 2-75.

$$\tau_p = \frac{C_c \rho_p d_p^2}{18\mu_g} \tag{2-75}$$

The Cunningham slip correction factor is a function of particle Knudsen number, $Kn_p$. $Kn_p$ is the ratio of gas mean free path $\lambda_g$ to particle radius. At low $Kn_p$, flow occurs in a continuum regime. The suspended particle behaves as a solid body surrounded by a continuum of fluid. Velocity gradients form because of the viscosity of the fluid $\mu_g$, these define the flow behaviour of the particle. At high $Kn_p$, flow occurs in the free molecular regime. At small particle sizes, collisions between gas molecules and the particle, necessary to exchange momentum, become less common. In the free-molecular regime particles motion becomes more akin to a gas molecule in kinetic theory. A transitional regime exists at $Kn_p$ between 0.1 and 10 (Schetz and Fuhs, 1999, p. 671). The Cunningham slip correction factor and gas mean free path were calculated in this work using equations 2-76 to 2-78 below (Flagan and Sienfield, 2012). Note the constants approximate the carrier gas as air.

$$C_c = 1 + Kn_p\left(1.257 + 0.4e^{-\left(\frac{1.1}{Kn_p}\right)}\right) \tag{2-76}$$

$$Kn_p = \frac{2\lambda_g}{d_p} \tag{2-77}$$

$$\lambda_g = \frac{\mu_g}{0.499 P_T \sqrt{\frac{8M}{\pi R T}}} \tag{2-78}$$

### 2.15.2 Fluid characteristic time

The characteristic time of the fluid $\tau_f$ is typically found from a characteristic length scale divided by the average velocity. However, this is highly application dependent. A length scale of half the hydraulic diameter has been used for 90° rectangular duct bends (Sun *et al.*, 2013). This has also been applied to pipe bends (McFarland *et al.*, 1997; Breuer *et al.*, 2006). It is noteworthy that the length scale was not the bend radius for these cases. Overcamp and Scarlett (1993) when assessing a cyclone, used the overall body diameter as the length scale, and the average inlet velocity as the velocity scale. This is also the case in more recent publications (Luliano and Perez, 2016, p. 61) which suggests it is a standard approach to cyclones. When particles impact a flow obstruction, the length scale is typically a measure of the size of the flow obstruction. Ingham *et al.* (1990) used radius for cylindrical and spherical flow obstructions. Brandon and Aggarwal (2001) studied deposition on a square cross-section cuboid between two parallel plates. They define the length scale as the length of one square side of the cuboid. Galletti *et al.* (2008) provide a CFD study of a wave-plate mist eliminator, under weakly turbulent flows with recirculation patterns. They used an average velocity based on continuity as the characteristic velocity, and the plate spacing as the characteristic length.

The choice of an appropriate characteristic velocity and length scale is highly application dependent, and appears to be subject to a degree of subjectivity. Stokes number may be found *a priori,* based on particle properties, average velocity and a chosen dimension of the geometry. Stokes number can be viewed as a control variable in this case, defined by experimental or simulated conditions. Stokes number can also be used to apply experimental results to predict the performance of particle separations, for variations in particle density and diameter.

## 2.16 **Thermophoresis**

Particles suspended in a fluid experience a force due to temperature gradients, known as thermophoresis. The force is caused by collisions between the particle and molecules of the gas. The side of the particle facing the hot gas experiences collisions that impart a higher average kinetic energy than the side facing the cold gas (Bott, 1995, p. 67). This results in a force on the particle acting towards the cold region of the gas.

This effect has been proposed for industrial gas cleaning, in the form of a ‘thermoprecipitator’ or ‘thermopositor’. Similar to an electrostatic precipitator, thermophoresis creates an attractive force on the particle towards cold surfaces. Particles collide with and deposit onto cold surfaces (Davis and Schweiger, 2002, p. 756). Thermophoresis affects particles with radii of less than 10μm, exposed to temperature gradients of the order 50 K/cm (Srikanth and Jayaraj, 1995).

This is within the range experienced in the cryogenic condenser. Initial CFD modelling results have shown thermophoresis affects the deposition of particulate benzene in the cryogenic condenser. Thermophoresis is therefore included in the CFD model in this thesis. Thermophoresis is modelled using the Talbot coefficient. The equation (2-79) assumes ideal gas behaviour and spherical particles, and is valid for the entire particle Knudsen number range (Talbot *et al.*, 1980).

$$\vec{F} = -\frac{6\pi d_p \mu_g{}^2 1.17\left(\frac{k_g}{k_p} + 2.18Kn_p\right)}{\rho_g\left(1 + 3.42Kn_p\right)\left(1 + 2\frac{k_g}{k_p} + 4.36Kn_p\right)} \frac{1}{m_p T} \nabla T \qquad \text{2-79}$$

## 2.17 **Conclusions on Literature Review**

Previous literature relating to desublimation modelling demonstrates particle formation is a concern during desublimation operations. The drop in separation efficiency this can cause is sufficient to prevent the target benzene concentration at the outlet from being reached – particle behaviour is therefore worthy of further investigation. Desublimation is rarely used as a separation technique, but still has important industrial applications, notably in the separation of $CO_2$ and phthallic anhydride. Some sources exist covering benzene desublimation and cryogenic condensation modelling. These show that the process is worth studying in more detail. The literature review above covered some sources where Eulerian-Lagrangian models have been applied to nucleation and growth problems previously. The work presented in this thesis aims to build a similar CFD model that incorporates nucleation and growth of benzene particulate through a Eulerian-Lagrangian model.

# Chapter 3. Methods: Flow Modelling, Particle Formation and Transport

This chapter outlines the procedures used in the modelling work. The chapter first describes the computing platforms used in the simulation. The geometry section describes the model geometry used in the simulation. The Reynolds number of the flow affects the choice of turbulence modelling and the approach used in meshing. The meshing and grid independence study are covered following this. As grid independence is a vital verification practice in computational fluid dynamics (CFD) modelling, it is covered in some detail. Following this the numerical simulation section covers the conditions in the CFD model. Conditions for the fluid simulation, such as the material properties, inlet flowrate and temperature, boundary conditions and geometry have been assigned to match the physical conditions in the cryogenic condenser as close as is practical. To compare the experimental particle image velocimetry (PIV, covered in the next chapter) to the CFD model, some additional CFD simulations were completed using the conditions from the experiment, (airflow, geometric scaling). The conditions used in these CFD models are also covered in this chapter. The numerical simulation section first describes the set-up of the case. Implementing nucleation and growth of the particles into the model involved using several user-defined functions. This is explained following on from the set-up of the fluid flow modelling.

## 3.1 Basic Overview of the CFD Modelling Approach.

A basic overview of the particle modelling approach is shown in Figure 13 below. The fluid flow is simulated as a gas mixture of nitrogen and benzene vapour. In the fluid simulation this gas flow is cooled through the temperature profile. This is described in section 3.7.2. This cooling eventually leads to nucleation once the critical degree of supersaturation is reached. If this occurs ($S > S_{crit}$) inside a mesh cell, then the nucleation rate J is modelled to occur in that cell. Benzene vapour is removed from the fluid flow, and latent heat is released into the fluid flow. A discrete-phase model (DPM) particle is injected in the cell-centre to represent the nucleation. This is assigned an appropriate particle massflow J and critical radius $r_{crit}$ to represent the nucleated benzene particles as covered in section 3.7.5. Once injected, the DPM particle grows. It exchanges mass, energy and momentum with the fluid flow cells that it passes through. The exchange of mass and energy is covered in section 3.7.6. The particle trajectory is defined by the drag law (covered in section 3.7.5) along with thermophoretic force (see section 2.16) and other forces such as gravity and random motion due to turbulence. These trajectories lead to collisions with the flow domain walls causing particle deposition. The DPM particle simulation escapes the domain, and the mass of benzene that this particles represents is removed.

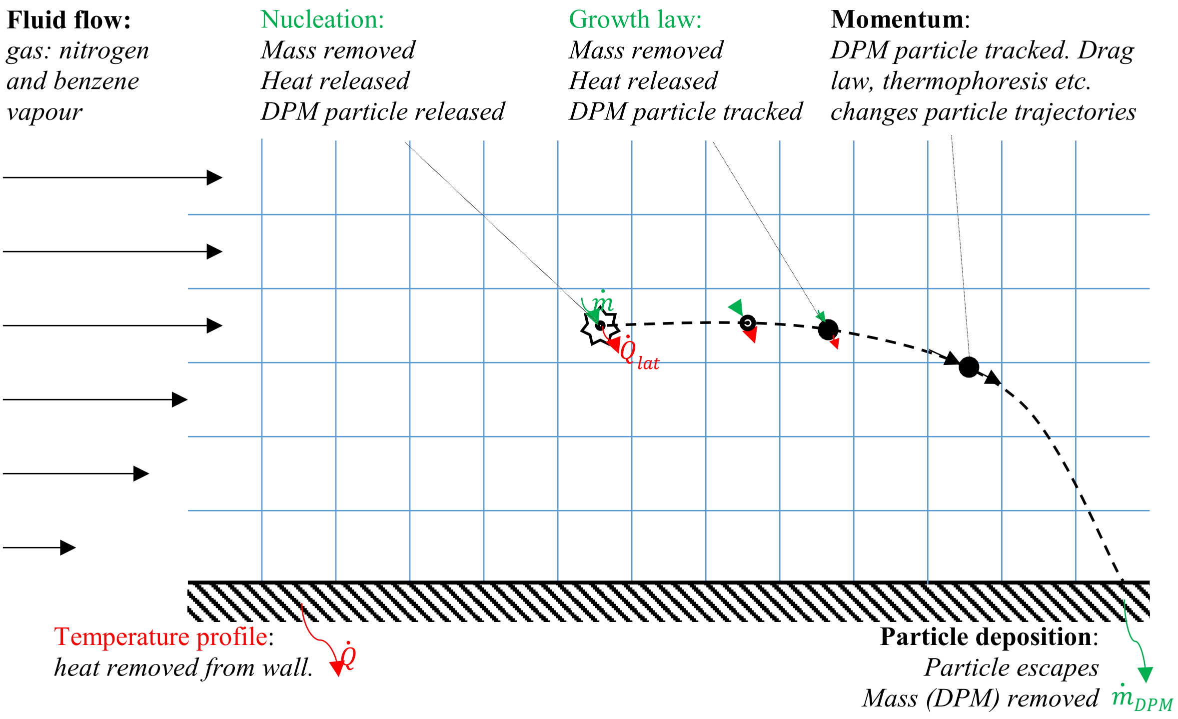

*Figure 13: Basic overview of the CFD modelling approach*

Physically, this particle deposition represents particles being captured and incorporated into the frost layer as it forms on the condenser wall. The benzene particles are removed from the gas flow. The frost layer itself is not modelled in this work. Most of the simulated particles are generated in cells near the cooled walls. This approximates conditions at the surface of the air-frost phase interface (saturation vapour concentration). The growth law removes benzene vapour until the vapour concentration returns to saturation (S = 1).

## 3.2 Computing Platforms

A combination of computing platforms were used to conduct the simulations. A desktop PC was used in most cases for pre-processing applications (geometry, meshing, case set-up). A high performance computer was used for some cases (ceamansys01), accessed via a remote desktop (www.ras.ncl.ac.uk). High computational load problems were processed as batch simulations on a computing cluster (Topsy). This is covered in greater detail in Appendix 8.2. The simulations were conducted using the commercial software ANSYS® FLUENT®. Pre- and post-processing was accomplished using the software package ANSYS® Workbench as outlined in Table 6.

| | |
|---|---|
| Geometry software | ANSYS® DesignModeller™ 15.0.7 |
| Meshing software | ANSYS® Meshing™ 15.0.7 |
| Numerical simulation software | ANSYS® FLUENT® 15.0.7; 15.0.0; 14.5.7 |
| Post processing software | ANSYS® FLUENT® 15.0.7;<br>ANSYS® CFD-Post 15.0.7 |

*Table 6: Software for CFD.*

## 3.3 Geometry

The geometry was created using Ansys Design Modeller software. An image of the geometry is shown below in Figure 14, viewed from the z-direction and rotated 90°clockwise. This geometry represents the space between two lamellae within the condenser: essentially a single process-side plate. (For the basic cryogenic condenser unit design, see section 1.8). The heat exchange is counter-current. Cold nitrogen gas flows downwards inside the lamellae, this is modelled as a linear wall temperature profile in the model geometry as is elaborated below (section 3.7.2). The process gas flows upwards through the model geometry as it cools. Fourteen baffles direct the process gas flow in the model geometry. The baffle spacing reduces as the gas cools, to account for the reduction in volume flowrate with cooling. The geometry was extended at the inlet to provide a developed flow profile at the base of the plates. The geometry was also extended at the outlet, and a porous zone (not shown) was added to prevent recirculation at the outlet that would otherwise hinder convergence in the flow solver. The overall size of the model geometry was 235 by 2,804 by 11.75 mm. The size representing the physical plate inside the condenser was 1.98m in the y-direction. To reduce computational load, a symmetry plane was applied to the model in the z-direction, resulting in overall domain dimensions of 235 by 2,804 by 5.875 mm.

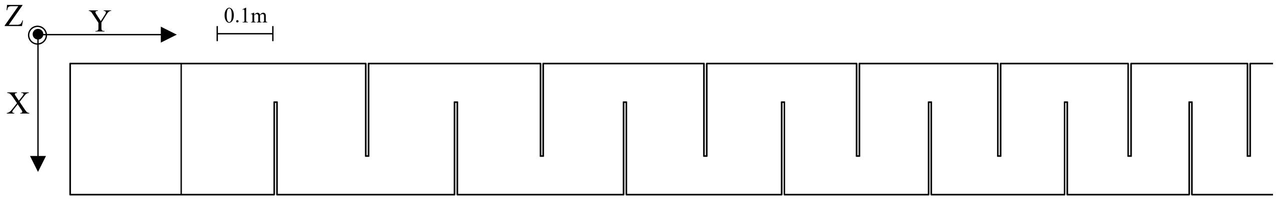

*Figure 14: CFD geometry.*

A 2D parallel plate model was also used in this work. This consisted of a simple rectangular shape, dimensioned 1,980 by 11.75 mm to represent the space between two lamellae inside the condenser. This represented the 3D model in the Y and Z directions, ignoring the baffles. Another 2D simplification of the geometry, in the X and Y directions, was used in the grid independence study, incorporating four baffles.

## 3.4 Reynolds Number in the Model

The flow Reynolds number has a substantial impact on the methods used in the simulation. The choice of the appropriate turbulence model is justified based on this Reynolds number. This in turn affects the meshing of the geometry. Turbulence models which resolve the boundary layer require greater refinement in the near-wall region when compared to wall-function approaches (such as the standard k-ε model).

The flow Reynolds number is not constant in the model geometry. Variables impacting the Reynolds number vary with location in the model. As the temperature of the gas decreases, the dynamic viscosity decreases and the density increases. The average velocity falls with this increasing density according to continuity. The spaces between baffles change along the length of the condenser. The cross-sectional area available for flow affects both the velocity and the hydraulic diameter.

The channel Reynolds number $Re_{d\ hydraulic}$ based on hydraulic diameter is used in this work. $Re_{d\ hydraulic}$ is defined in equation 3-2. The hydraulic diameter is defined for a rectangular channel as shown in equation 2-12. To determine how this Reynolds number changes with location in the model, sample planes were located between baffle cuts and baffle spaces in the model, as shown in Figure 64 (p.146). The baffle cut is defined by the horizontal length of the baffle. The baffle spacing is defined by the vertical distance between one baffle and another. Under steady-state conditions, the mass flowrate through each of these sample planes must be equal. The height of the channel, a, is fixed by the plate spacing at 11.75 mm. This simplifies the variables affecting Reynolds number as shown in equation 3-3. The channel Reynolds number varies according to the channel width, b, and the dynamic viscosity, $\mu_g$.

$$d_{hydraulic} = \frac{2ab}{a+b} \tag{3-1}$$

$$Re_{d\ hydraulic} = \frac{\rho_g \bar{u}_g d_{hydraulic}}{\mu_g} \tag{3-2}$$

$$Re_{d\ hydraulic} = \frac{2\dot{m}}{(a+b)\mu_g} \tag{3-3}$$

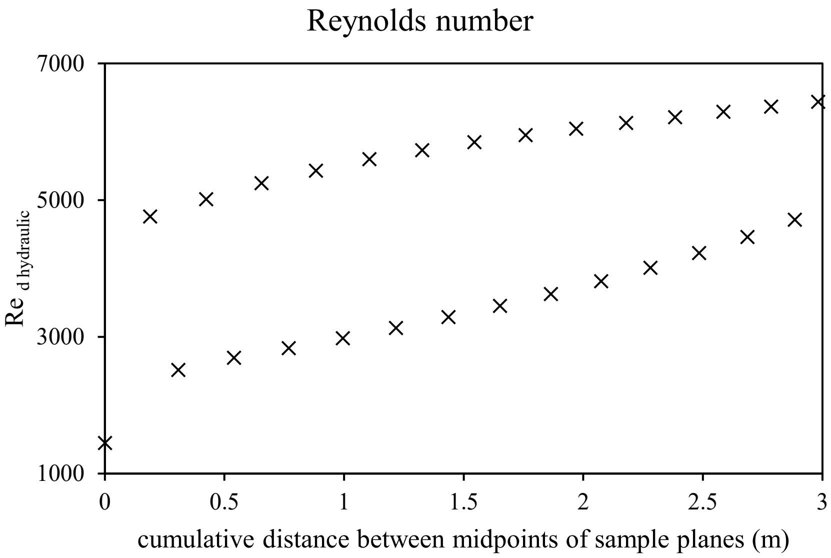

*Figure 15: Reynolds number variation along flowline through the condenser.*

## 3.5 Meshing and Grid Independence Study - Methods

The purpose of a grid independence study is to establish the appropriate mesh size for the CFD model. The appropriate mesh size captures all of the flow behaviours present in finer meshes and introduces an acceptable level of discretisation error into the results. This is assessed by examining how simulation results change as the mesh is refined, and mesh cell size is reduced. Refining the mesh increases the accuracy of the simulation, but at the cost of increased computational load. The grid independence study aims to strike an appropriate balance between these two factors and to quantify discretisation errors in the result. The mesh used quadrilateral and hexahedral mesh cells in two and three dimensional meshes respectively. This was more appropriate for the rectilinear, high aspect-ratio domain geometry than the alternative (tetrahedral meshing, for example Tsai *et al.* (2009)).

This section introduces the methods that have been used to create the mesh and establish grid independence. The mesh is generated with a local refinement in the boundary layer. From this initial mesh, several other meshes were generated to conduct the grid independence study. The mesh quality metrics and the conditions used for the numerical simulations are then described. The methods used in the grid independence study are covered. Quantitative grid independence methods have been applied to point velocity values in the model following this. Some other basic results also quantify other errors in the simulation, and show that discretisation error (which grid independence assesses) makes the largest contribution to error. Lastly, a description of the 3D meshing approach is also given. This uses the meshing sizing established in the grid independence study, and is subject to the same mesh metrics, so is appropriate to discuss in this section.

### *3.5.1 First layer (near-wall) cell height*

Turbulence models that resolve the boundary layer, such as those used in this work, require mesh refinements in the boundary layer. This requires several mesh elements within the laminar sublayer immediately next to the wall. For transition flow modelling it is recommended that the dimensionless distance to from the wall $y^+$ equals one for the first cell height, and the growth rate of the boundary elements, $g = 1.1$. This is recommended by the software developers (Hart, 2012) and publications using the transition SST (shear stress transport) model have adopted this (Sun *et al.*, 2013; Lam and Peng, 2016). An initial estimate for the first cell height $y_{1st\ cell}$ is required in order to generate the mesh. In practice this requires an estimate of shear velocity $U_{\tau w}$. Shear velocity is the wall shear stress $\tau_w$ expressed in units of velocity as demonstrated in equation 3-5. With $U_{\tau w}$ known, the height of the first cell $y_{1st\ cell}$ is then found from equation 3-4 with $y^+ = 1$.

$$y = \frac{y^{+}\mu_g}{U_{\tau w}\rho_g} \tag{3-4}$$

$$U_{\tau w} = \sqrt{\frac{\tau_w}{\rho_g}} \tag{3-5}$$

### 3.5.2 *Refinement method*

The grid independence study was conducted using an integer refinement method. This method uses a refinement ratio $\boldsymbol{r}$ of two, halving the mesh spacing between the coarser $h_2$ and finer mesh $h_1$ (see equation 3-6). In this study, mesh refinements have been created individually. The mesh constraints have been scaled in order to keep mesh sizes as consistent as possible across refinements whilst avoiding issues with mesh quality, such as high aspect ratio cells. Conventionally, the mesh refinements are obtained directly from the initial mesh through "mesh doubling". Mesh doubling divides each mesh cell along the midpoints of its sides, creating four new cells in two dimensional meshes. However, mesh doubling does not preserve the growth rate of boundary elements, g = 1.1. In order to preserve g = 1.1 new meshes were generated instead of mesh doubling in the grid independence study.

$$\boldsymbol{r} = \frac{h_2}{h_1} \tag{3-6}$$

The local mesh refinement in the boundary layer is accomplished using an inflation layer. The inflation layer is created during meshing. High-aspect ratio cells are generated immediately next to the wall satisfying the constraint for first cell mesh height $y_{1\text{st cell}}$. These cells then grow geometrically at a rate defined by the growth rate g. This creates the local mesh refinement that captures the boundary layer and provides a smooth transition to the low-aspect ratio mesh cells in the bulk flow (known as the 'transition ratio').

For the mesh generation in the grid independence study, several attributes should remain consistent in the inflation layers of the refined and coarsened meshes. Due to the geometric scaling of the layer, these attributes did not scale proportionally with refinement ratio. These attributes were as follows:

(a) The growth rate, g, remains constant at 1.1.

(b) The first cell height, $y_{1\text{st cell}}$, scales proportionally with refinement ratio.

(c) Overall height of the inflation layer, $y_{total\ height}$, is constant between mesh refinements. This avoids generating meshes that are characteristically different. $y_{total\ height}$ must be less than 30mm to avoid overlapping inflation layers at the narrowest point in the model geometry.

(d) The inflation layer does not contain mesh cells of poor quality, such as cells with high skewness (see Appendix 8.3).

(e) The transition ratio, the ratio in size between the last cell in the inflation layer and bulk mesh size, must be acceptable. In this work a target value for transition ratio of 0.5 was used, that is to say the final inflation layer mesh cell $y_{last\ cell\ height}$ must be 50% of the bulk mesh size.

The relationship between the overall height of the inflation layer $y_{total\ height}$ and the final inflation layer mesh cell $y_{last\ cell\ height}$ to the height of the first cell $y_{1st\ cell}$ is the result of a finite geometric series. The relationships are given below in equations 3-7 and 3-8.

$$y_{total\ height} = y_{1st\ cell} \times \frac{1 - g^{n_{cells}}}{1 - g} \qquad 3\text{-}7$$

$$y_{last\ cell\ height} = y_{1st\ cell} \times g^{n_{cells}-1} \qquad 3\text{-}8$$

### *3.5.3 Mesh quality metrics*

Whilst the grid independence study will capture all discretization errors, including 'grid generation errors' introduced by mesh quality (Roache, 1997), it is desirable to use meshes of comparable quality when conducting a grid independence study. Poor mesh elements can cause problems with convergence during numerical simulation, including producing erroneous results. Mesh quality can be assessed using mesh quality metrics, and compared against acceptance criteria. Mesh quality metrics for skewness, aspect ratio and orthogonal quality have been used in this work. Definitions and sources for these are given in appendix 8.3.

### *3.5.4 Numerical simulation in grid independence study*

Constant fluid properties were applied in the simulation ($\mu_g = 1.71\ \text{x}10^{-5}$ Pa.s, $\rho_g = 1.204$ kg/m$^3$) corresponding to pure nitrogen at a temperature of 10°C. The force of gravity was neglected. The properties of the porous zone were chosen arbitrarily to eliminate backwards flow. Both viscous and inertial resistance of 100 m$^{-2}$ and 100 m$^{-1}$ respectively successfully eliminated reverse flow and introduced a pressure drop of ca. 30 Pa across the porous zone. Inlet conditions were set to a uniform velocity of 0.907m/s normal to the boundary, based on a mass flowrate of 150Nm$^3$/hr in the full 3D model. The inlet turbulence conditions were taken from established flow conditions from a coarse initial mesh of the cryogenic condenser geometry (turbulence intensity = 6.45%; hydraulic diameter = 0.0224m; intermittency = 1). The outlet was set as a pressure outlet at atmospheric pressure. The numerical simulation was performed using the pressure based SIMPLE (semi-implicit method for pressure-linked equations) solver, with single precision. A second-order (upwind) advection scheme was applied to all variables.

The first ca. 200 iterations were completed using the realizable k-ε model before switching to the transition SST model. This aided the convergence of the transition SST model. Monotonic convergence was achieved for the simulations using the default convergence criteria (all residuals less than 1 x10$^{-3}$). The default under-relaxation factors were used in the coarse, medium and fine meshes, the very coarse mesh required the momentum and turbulent kinetic energy under-relaxation factors to be reduced to 0.5 and 0.6 respectively towards the end of the simulation.

### *3.5.5 Establishing qualitative grid independence*

In this work grid independence is first assessed qualitatively by plotting velocity profiles through the flow. This shows that the fluid flow simulations used in the grid independence study are broadly similar and in itself is good evidence for grid independence. Other data has also been sampled, to give this basic grid independence check further grounding. The pressure drop was sampled between baffles. The reattachment location for the jet have been extracted using the method described in Haque *et al.* (2007).

### *3.5.6 Establishing quantitative grid independence*

The procedure of Roache (1997) was applied to provide a quantitative estimate of grid independence. This method is based on an asymptotic approach of the solution result (f) to a hypothetical 'true value' with increasing grid refinement. The method requires three grid refinements, and a constant refinement ratio. The theoretical order of convergence for a grid refinement ratio r = 2 is p = 2. The first step of the method involves calculating the observed order of convergence as a test for the asymptotic range (see equation 3-9).

$$p = \frac{ln\left(\frac{f_3 - f_2}{f_2 - f_1}\right)}{\ln(r)} \tag{3-9}$$

The hypothetical value of the solution result for a very refined grid, $f_{h=0}$, can be calculated through Richardson extrapolation as shown in equation 3-10. Note that this value represents the result for an infinitesimally fine grid, but should not be interpreted as a 'perfect' or 'true' result.

It assumes monotone truncation error convergence, and magnifies machine round-off error and iteration error. It also does not obey conservation laws (Roache, 1997).

$$f_{h=0} = f_1 + \frac{(f_1 - f_2)}{r^p - 1} \tag{3-10}$$

The grid convergence index can be used to calculate error bands, as shown in equations 3-11 and 3-12. The safety factor Fs = 1.25 for studies using three meshes. The grid convergence index can also be used to test for asymptotic convergence using equation 3-13.

$$GCI_{12} = \frac{Fs\left|\frac{f_1 - f_2}{f_1}\right|}{r^p - 1} \tag{3-11}$$

$$GCI_{23} = \frac{Fs\left|\frac{f_2 - f_3}{f_2}\right|}{r^p - 1} \tag{3-12}$$

$$\frac{GCI_{23}}{r^p GCI_{12}} \approx 1 \tag{3-13}$$

The apparent convergence condition R* can be used as an alternative test for convergence with grid refinement (Almohammadi *et al.*, 2013). The Richardson extrapolation method is only valid when the convergence condition is monotonic. Oscillatory convergence is also possible and can be assessed using the apparent convergence condition, as shown in equation 3-14.

$$R^* = \frac{f_2 - f_1}{f_3 - f_2} \tag{3-14}$$

| | |
|---|---|
| $R^* > 1$ | monotonic divergence |
| $1 > R^* > 0$ | monotonic convergence |
| $0 > R^* > -1$ | oscillatory convergence |
| $R^* < -1$ | oscillatory divergence |

### *3.5.7 Quantification of other simulation errors*

Discretisation errors are typically the most important source of numerical error in CFD, and for this reason establishing grid independence is the vital verification practice in CFD. However, other errors, such as round-off errors, iteration errors and discretisation errors can also be assessed. The round-off error can be estimated by comparing single and double precision results. Iteration error can be estimated by comparing the result for different maximum residuals. The discretisation error, as an alternative to a grid independence study, may be estimated by increasing the order of accuracy of the discretisation scheme. These checks have also been performed as part of the grid independence study, and the results are given below in section 3.6.6.

### *3.5.8 Three dimensional mesh method*

As the three dimensional model geometry is a prism in the Z direction, it may be meshed using a swept mesh method in the Z direction. The boundaries of the model also represent physical surfaces inside the condenser, and therefore require similar grid refinements in the near-wall region in order to resolve the boundary layer. In the swept mesh method this can be controlled using two parameters: the number of divisions, $n_{sb}$, and the sweep bias, $S_b$. Figure 16 provides an illustration of a swept mesh method with a sweep bias applied to a cube. The relationship is given in equation 3-15.

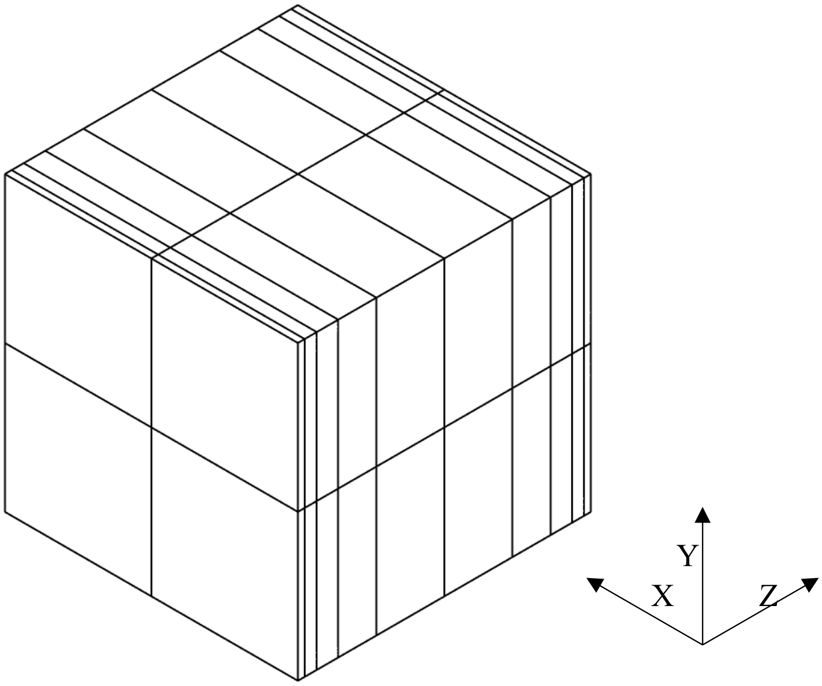

*Figure 16: Illustration of a swept mesh method.*

$$S_b = g^{n_{sb}-1} \qquad 3\text{-}15$$

## 3.6 Meshing and Grid Independence Study – Results

This section covers the results from the grid independence study, applying the methods described in the previous section. Figure 20 provides a visual demonstration that grid independence has been achieved. This is supported by the pressure drop and reattachment location results reported in Table 9. Some quantitative results indicate asymptotic convergence as is demonstrated in Figure 24. Those that do not however do fit the definition for oscillatory convergence given in equation 3-14. This demonstrates that grid independence has been achieved for the medium mesh with a growth rate of g = 1.2. The investigation of other simulation errors revealed that as expected, discretisation error makes the greatest contribution, and other errors are not significant in comparison. The method used to apply this mesh sizing in the 3rd dimension are covered below.

### *3.6.1 Geometry used in the grid independence study*

In this work, the grid independence study was conducted on a two-dimensional simplification of the full three-dimensional model geometry covered previously in section 3.3. This simplification was made to allow the simulations to be completed with a low computational load. As the baffle spacing reduces along the condenser length, the four closest baffles have been used in this two dimensional model, shown in Figure 17. This allowed the flow patterns, jet flow and recirculation present in the full three-dimensional simulations to become established whilst further simplifying the geometry for the grid independence study, reducing computational load. A constriction and a porous zone were added to the geometry at the outlet. The justification for this is as for the full three dimensional model: it prevented recirculation at the outlet that would otherwise hinder convergence.

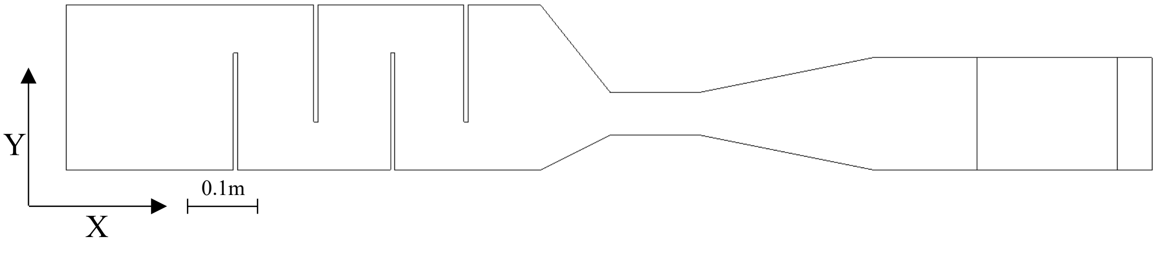

*Figure 17: 2D geometry used in grid-independence study.*

### *3.6.2 First layer (near-wall) cell height*

The transition SST model was used for the grid independence study using the appropriate mesh requirements (first layer cell height $y^+ = 1$, growth rate g = 1.1) for the initial "coarse" mesh. An estimate for shear velocity is required to find the height of the first cell $y_{1st\ cell}$. This may be estimated using an empirical correlation for skin friction such as the Blasius formula. For this study a value of wall shear stress $\tau_w$ = 1.91 Pa was extracted from a (pre-grid independence study) basic simulation. This gave a first cell height $y_{1st\ cell}$ = 11.2 μm, for the $y^+ = 1$ condition according to equation 3-4.

### *3.6.3 Mesh refinement*

The five conditions listed in section 3.5.2 above ((a) to (e)) cannot be met without compromise. The hypothetical closest integer value of $n_{cells}$ that satisfies condition (c) only according to equation 3-7 neglects condition (d) and (e). As a compromise, the number of cells in the inflation layer $n_{cells}$ was altered in order to satisfy conditions (c), (d) and (e) above. This resulted in the inflation layer sizing described in Table 7.

In addition to the inflation layer sizing, two other constraints were applied to the mesh sizing and were scaled with refinement ratio. The 'maximum bulk face size' controlled the mesh size away from the inflation layer. The 'number of divisions across the baffle edge' allowed a refinement in grid spacing around the baffle edges. This controlled the local mesh density in the area around the baffle edge, to capture the flow behaviour in this region. The baffle edge is highlighted by the red line in Figure 18, which shows the local increased mesh density in this area resulting from this mesh constraint.

Five meshes were generated for the grid independence study. The 'coarse' mesh was generated from the predicted first layer cell height of 11.2μm. From this mesh two refinements ('medium' and 'fine') and one coarsening ('very coarse') followed integer grid refinements. Based on this the medium mesh was found to give an appropriate level of refinement to capture the flow with acceptable accuracy. Applying these mesh sizing constraints to the 3D model resulted in a mesh size that was too large for the computer platform available. The 'medium' mesh was therefore repeated, increasing the growth rate to g = 1.2 in the near-wall region. This significantly reduced the number of elements in the 3D model. The meshes generated for the grid independence study are shown in the appendix 8.5. The size constraints applied to each mesh in the grid independence study are given in Table 7.

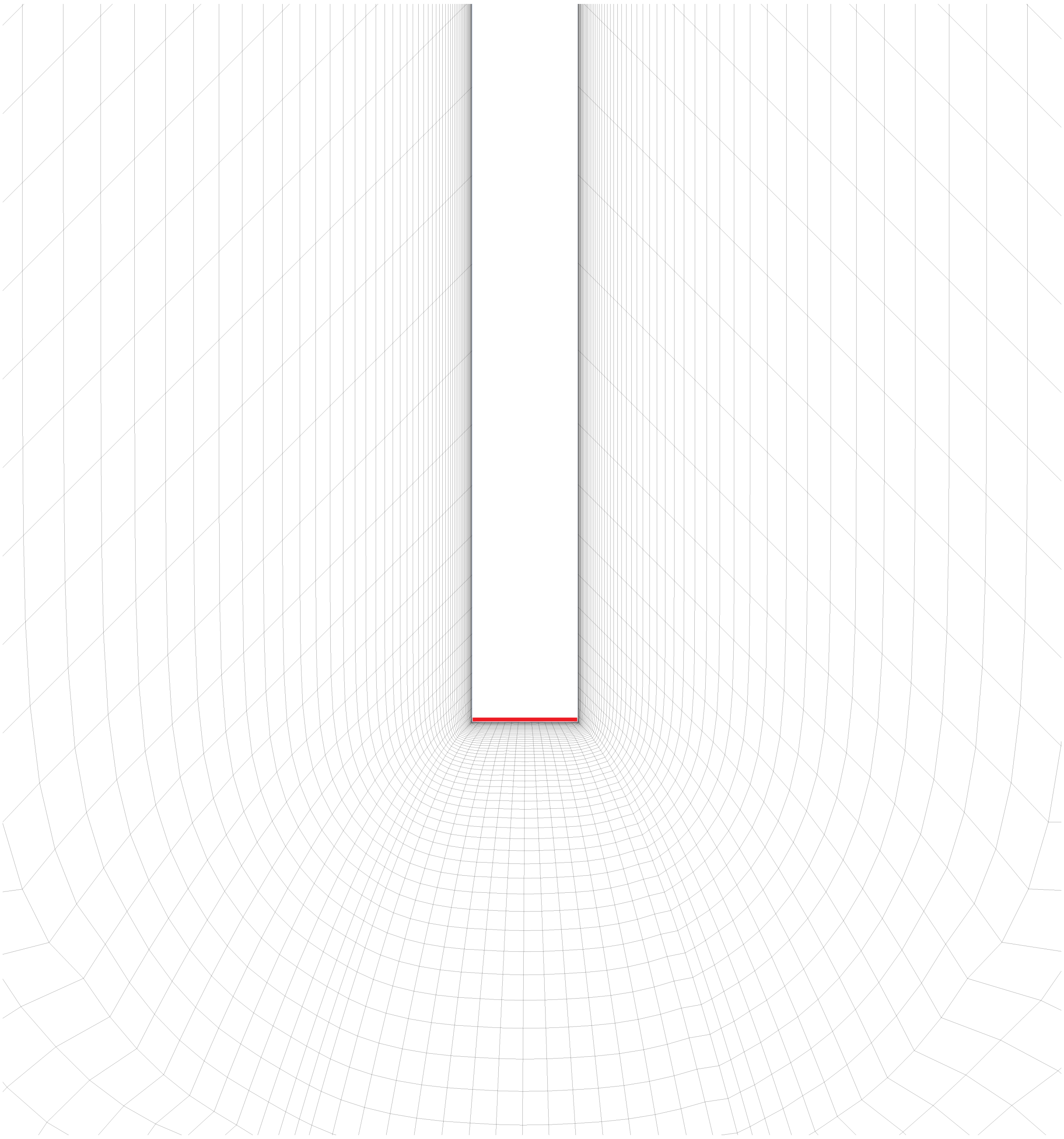

*Figure 18: Illustration of meshing around the baffle edge.*

| | very coarse | coarse | medium | fine | med, g = 1.2 |
|---|---|---|---|---|---|
| max bulk size (mm) | 10 | 5 | 2.5 | 1.25 | 2.5 |
| $y_{1st\ cell}$ (μm) | 22.4 | 11.2 | 5.6 | 2.8 | 5.6 |
| no. div'ns a/c baffle edge | 8 | 16 | 32 | 64 | 32 |
| baffle edge mesh size(mm) | 0.75 | 0.375 | 0.188 | 0.0938 | 0.188 |
| inflation layer characteristics | | | | | |
| number of cells $n_{cells}$ | 50 | 58 | 63 | 61 | 34 |
| $y_{total\ height}$ (mm) | 26.1 | 28.1 | 22.7 | 9.35 | 13.8 |
| $y_{last\ cell\ height}$ (mm) | 2.39 | 2.56 | 2.06 | 0.853 | 2.30 |

*Table 7: Mesh sizing for 2D grid independence study.*

The results shown in Table 8 indicate that these meshes are of comparable quality and satisfy the acceptance criteria given in appendix 8.3.

| | very coarse | coarse | medium | fine | med, g = 1.2 | acceptance criteria: |
|---|---|---|---|---|---|---|
| nodes | 30089 | 67734 | 159094 | 415404 | 108198 | |
| elements | 29704 | 67076 | 157927 | 413307 | 107090 | |
| skewness | | | | | | |
| max | 0.731 | 0.552 | 0.74 | 0.730 | 0.74 | < 0.9 |
| average | 0.272 | 0.241 | 0.207 | 0.175 | 0.182 | < 0.33 |
| aspect ratio | | | | | | less than five in bulk flow |
| all bulk flow > 5 ? | yes | yes | yes | yes | yes | |
| orthogonal quality | | | | | | |
| min | 0.116 | 0.116 | 0.116 | 0.116 | 0.116 | > 0.01 |
| average | 0.863 | 0.884 | 0.905 | 0.926 | 0.922 | |

*Table 8: Mesh quality metrics for 2D grid independence study.*

### *3.6.4 Results in grid independence study*

Results from the grid independence study established that the medium mesh with a growth rate of 1.2 introduced an acceptable level of discretisation error for the modelling work. These results were interpreted from velocity profiles and pressure data, extracted from the simulation.

Velocity profiles were taken from the sample lines shown in Figure 19. Samples were taken across baffle three (Figure 19 (i)), midway between three and four (Figure 19 (ii)), and across the fourth baffle cut (Figure 19 (iii)). The velocity profiles in these three locations are plotted in Figure 20. The velocity component orthogonal to the line is plotted in all three cases. The results approach the fine mesh velocity profile with refinement. The medium mesh with a growth rate of 1.2 (shown in red) is acceptable for use in the model, giving a close match to the medium mesh.

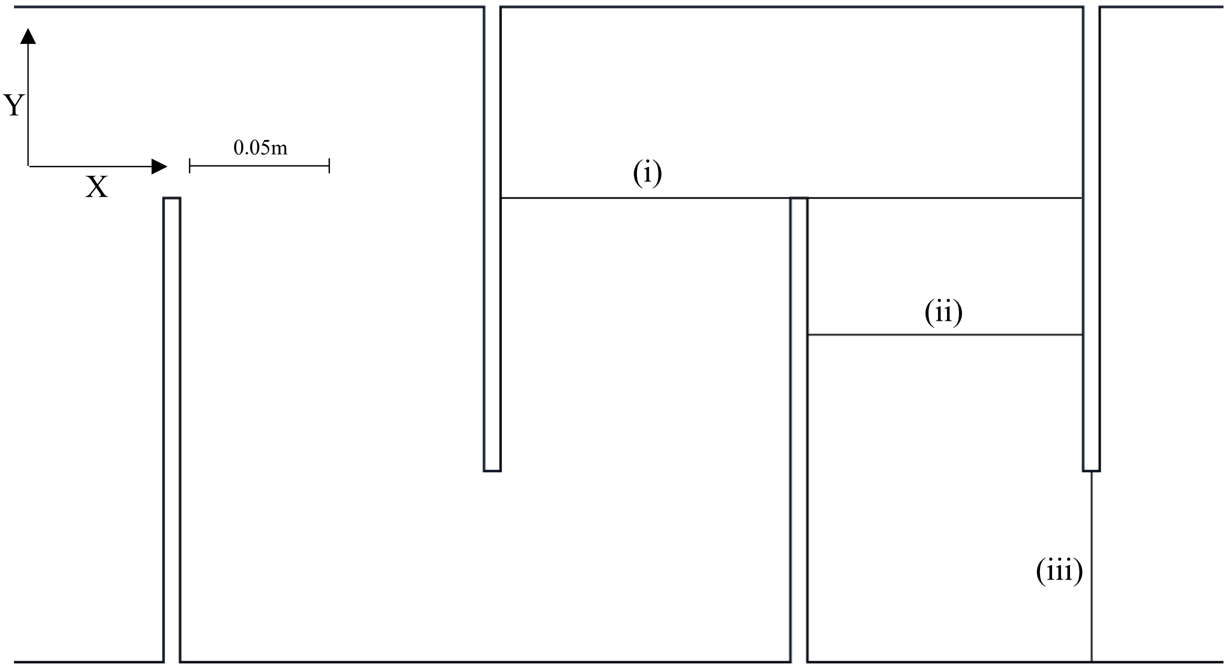

*Figure 19: Sampling locations for velocity profiles in grid independence study.*

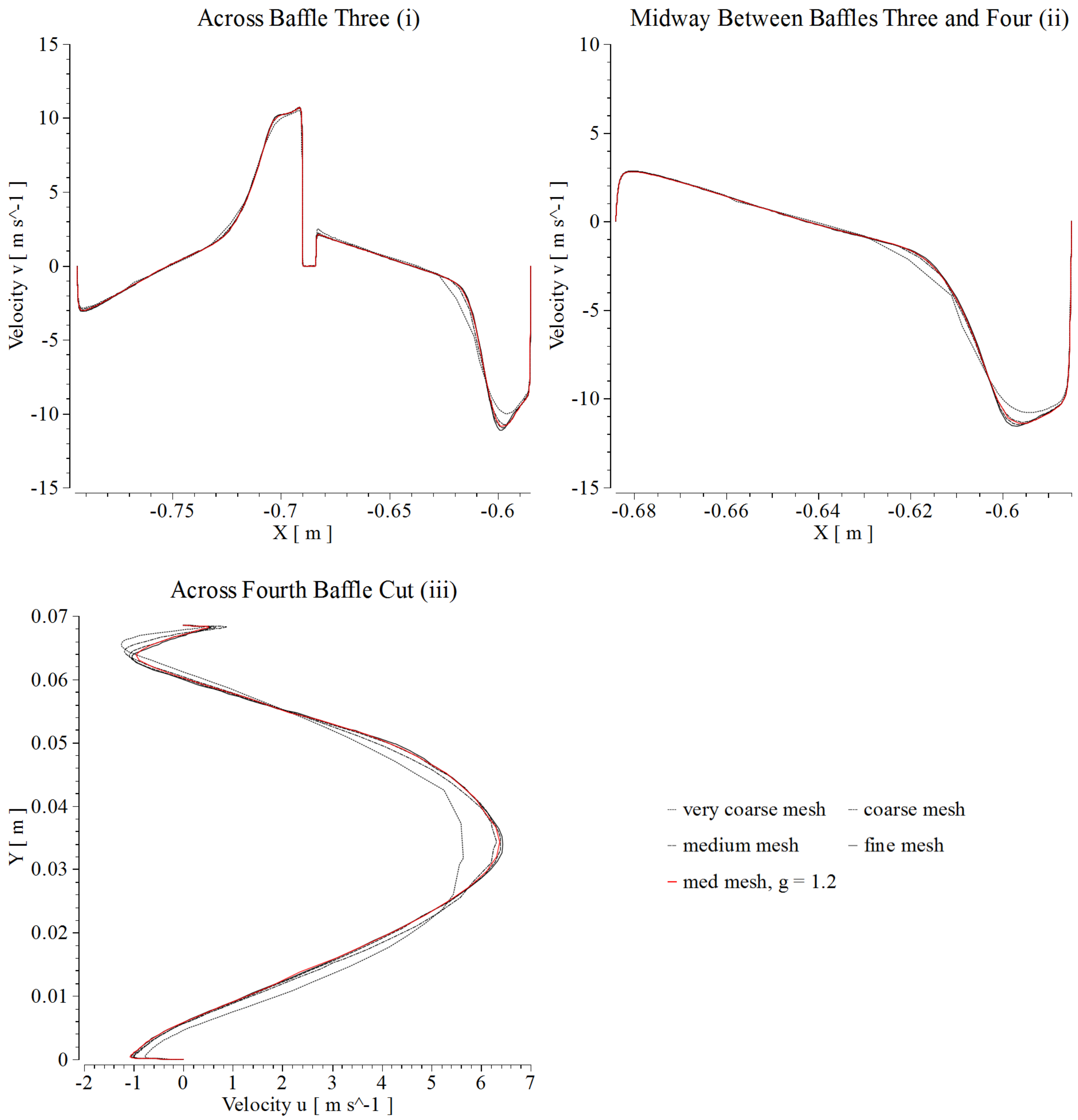

*Figure 20: Grid independence study results - velocity profiles.*

Flow detaches from the edge of baffle four and reattaches to the adjacent wall boundary (see Figure 21). The point marked in grey is a reattachment point. The reattachment plot is also shown in Figure 21. The plot is taken from within the laminar sublayer at the location where the jet reattaches to the wall. The velocity component is parallel to the wall. The point where the velocity is zero represents the reattachment point. These results show good agreement, the reattachment points lie within 1mm of the fine mesh result for every case except the very coarse mesh. The 1.2 growth rate result does not show the same convergence behaviour of the other grids. However it still gives a level of accuracy comparable to the original mesh, differing by less than 0.1 mm from the fine mesh result (Table 9, the x-coordinate is given relative to the 'fine' mesh result).

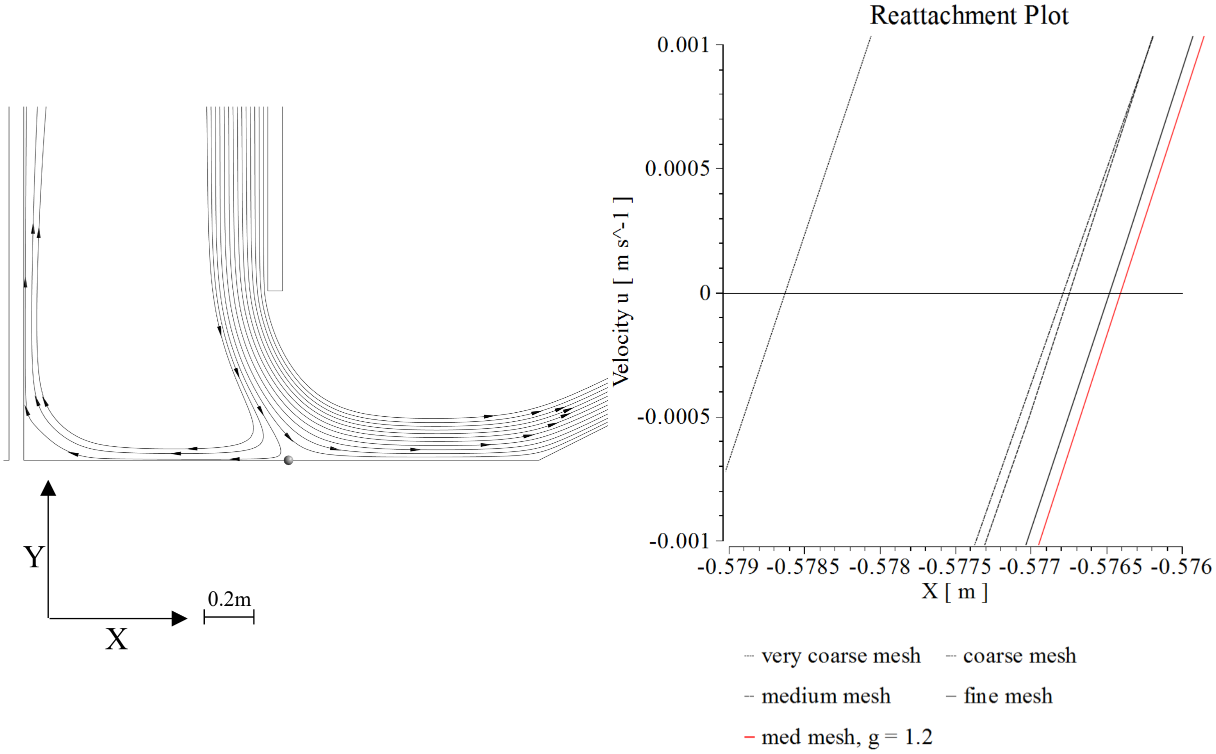

*Figure 21: Grid independence study results - reattachment plot.*

Pressure drop was sampled from lines across the cut of baffles two and four, as shown in Figure 22. Results are given in Table 9 for difference in static pressure between the two locations, as length weighted averages. Again the results indicate the mesh with a growth rate of 1.2 gives a result comparable to the original meshes.

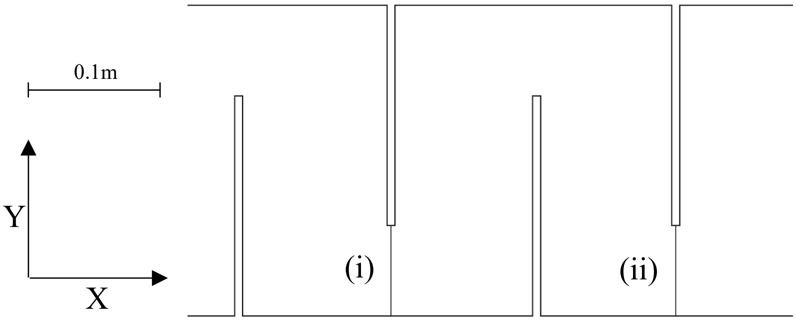

*Figure 22: Sampling locations for pressure drop in grid independence study.*

| | very coarse | coarse | medium | fine | medium, g = 1.2 |
|---|---|---|---|---|---|
| height of first cell (µm) | 22.4 | 11.2 | 5.6 | 2.8 | 5.6 |
| pressure drop (Pa) | 71.37 | 73.54 | 73.13 | 73.13 | 73.11 |
| reattachment (mm) | 2.04 | 0.29 | 0.26 | 0 | -0.083 |

*Table 9: Pressure drop and reattachment for 2D grid independence study.*

### 3.6.5 *Results in quantitative grid independence study*

The solution shown in Figure 20 (i) was analysed using the method described above (section 3.5.6). As shown in Figure 23 and Table 10, the result has been sampled at 20 equidistant positions on the sample line. Not all of the points meet the criteria necessary for asymptotic convergence testing. The points were put to qualitative tests, as follows:

Q1: is the difference between $f_1$ and $f_2$, and between $f_2$ and $f_3$, the same sign ?

Q2: is the difference between $f_1$ and $f_2$, smaller than the difference between $f_3$ and $f_2$ ?

Q3: is the difference between $f_1$ and $f_2$ less than half of the difference between $f_3$ and $f_2$ ?

Around half of the points satisfy all three criteria. Point 6 is excluded for the very coarse mesh as the value itself changes sign at this point. The observed order of convergence is expected to match the theoretical order of convergence (p = 2). Where the observed order of convergence is higher than two, this indicates the convergence is better than expected.

The penultimate row in Table 10 (test=1 ?), is the test condition given in equation 3-13. Points 10, 9, 7, 4 and 3 show that velocity at this location is within the asymptotic range across all four meshes. At fine mesh refinements, the contribution of other errors on the final result is greater, and the asymptotic range does not continue indefinitely with increasing mesh refinement due to the contribution of errors from other sources (eg: round-off errors and convergence errors). Given that good correlation between the results is clearly visible, this is the likely cause of these results being outside the asymptotic range.

The medium mesh with a growth rate of 1.2 cannot be included in this quantitative method because it is an *unrelated grid*. However Figure 24 below shows that the results from this mesh (shown in red) are comparable to the original ($g = 1.1$) medium mesh.

The results in Table 10 show variation in the observed order of convergence p. The observed order of convergence may differ from the theoretical $p = 2$. Super-convergence is common, (where the observed order is higher) due to cancellation of space truncation errors. Observed order of convergence between 1 and 0 is also common. This result was present for all points that did not pass question three above. The presence of switching functions in the turbulence model can also corrupt convergence rates.

The result shown in the bottom row of Table 10 give the apparent convergence condition $R^*$. This demonstrates that all nineteen points show convergence with grid refinement in at least one of the two groups (fine/medium/coarse mesh or medium/coarse/very coarse mesh).

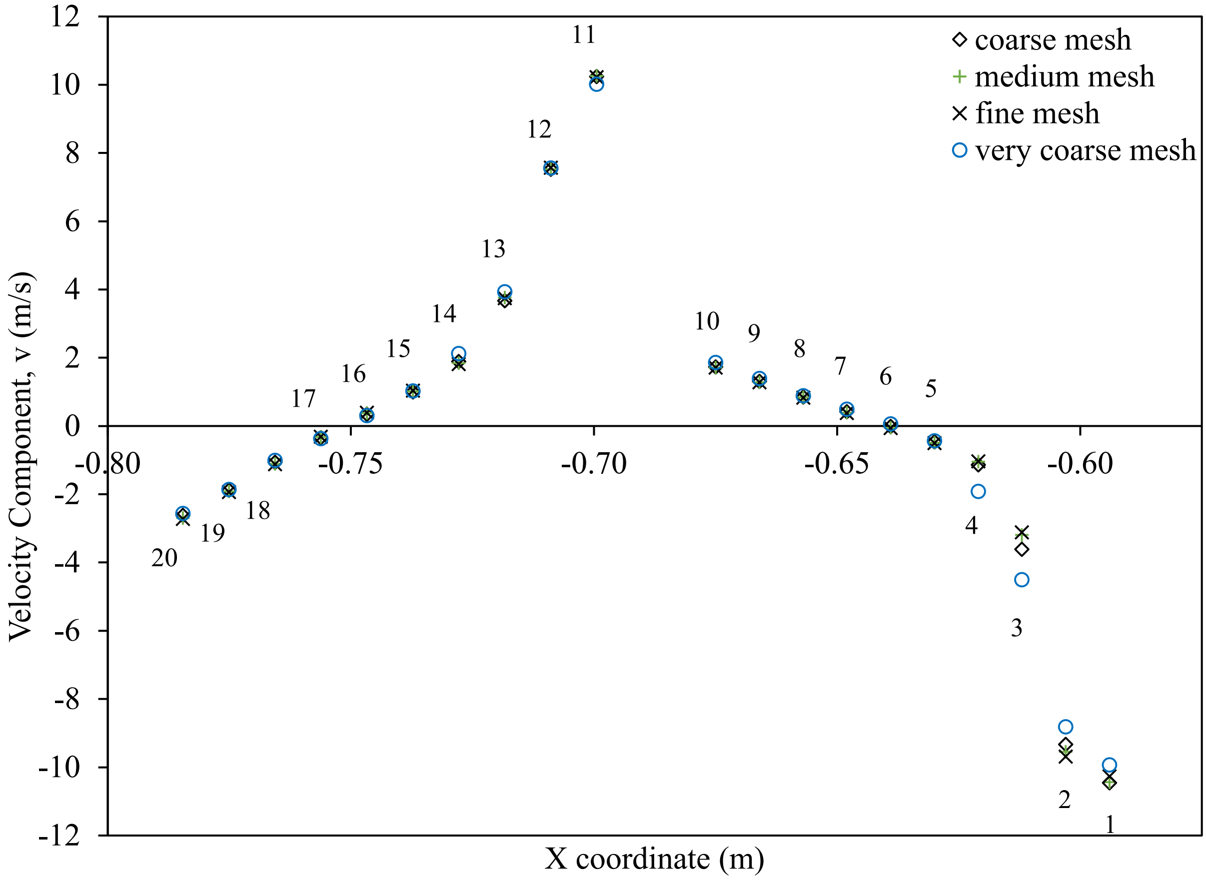

*Figure 23: Point-samples from the velocity profile across baffle three.*

| Across fine mesh, medium mesh and coarse mesh results: | | | | | | | | | | | | | | | | | | | | | |
|---|---|---|---|---|---|---|---|---|---|---|---|---|---|---|---|---|---|---|---|---|---|
| point | 20 | 19 | 18 | 17 | 16 | 15 | 14 | 13 | 12 | 11 | | 10 | 9 | 8 | 7 | 6 | 5 | 4 | 3 | 2 | 1 |
| Q1: | | | | | | | | 🟥 | | 🟥 | | | | | | | | | | | |
| Q2: | | | | | | | | | 🟥 | | | | | 🟥 | | | | | | | 🟥 |
| Q3: | | | | 🟥 | | 🟥 | 🟥 | | | | | | | | | | | | | 🟥 | |
| p observed | 1.4 | 1.1 | 3.4 | | 1.6 | | | | | | | 2.7 | 2.2 | | 1.5 | 2 | 3.4 | 4.3 | 2.5 | | |
| test =1 ? | 1.6 | 1.9 | 1.1 | | 1.5 | | | | | | | 1.2 | 1.3 | | 1.5 | 1.6 | 1.1 | 1.1 | 1.2 | | |
| R* | 🟩 0.4 | 🟩 0.5 | 🟩 0.1 | 🟩 0.5 | 🟩 0.3 | 🟩 0.6 | 🟩 0.6 | 🟩 -0.2 | 🟥 12 | 🟥 -3 | | 🟩 0.15 | 🟩 0.2 | 🟥 1.5 | 🟩 0.4 | 🟩 0.3 | 🟩 0.1 | 🟩 0.05 | 🟩 0.2 | 🟩 0.7 | 🟥 6.4 |
| Across medium mesh, coarse mesh and very coarse mesh results: | | | | | | | | | | | | | | | | | | | | | |
| Q1: | | | | | | 🟥 | | 🟥 | 🟥 | | | | | | | * | | | | | 🟥 |
| Q2: | 🟥 | 🟥 | | | | | | | | | | | | | | * | 🟥 | | | | |
| Q3: | | | 🟥 | 🟥 | 🟥 | | | | | | | | | | | * | | | | | |
| p observed | | | | | | | 2.5 | | | 4.2 | | 2.4 | 2 | 2.6 | 1.3 | * | | 3 | 1.1 | 1.3 | |
| test =1 ? | | | | | | | 1 | | | 1 | | 1 | 1 | 1 | 0.9 | * | | 0.9 | 0.9 | 1 | |
| R* | 🟥 1.3 | 🟥 1.7 | 🟩 0.9 | 🟩 0.5 | 🟩 0.7 | 🟩 -0.8 | 🟩 0.2 | 🟩 -0.4 | 🟩 -0.1 | 🟩 0.05 | | 🟩 0.2 | 🟩 0.2 | 🟩 0.2 | 🟩 0.4 | 🟩 * | 🟥 1.4 | 🟩 0.1 | 🟩 0.5 | 🟩 0.4 | 🟩 -0.05 |

*Table 10: Quantitative results for grid independence study.*

*Red colour signifies point has failed question given above (p. 78). For R*: green and red colours represent convergence or divergence respectively based on the conditions in equation 3-14, (p. 69)*

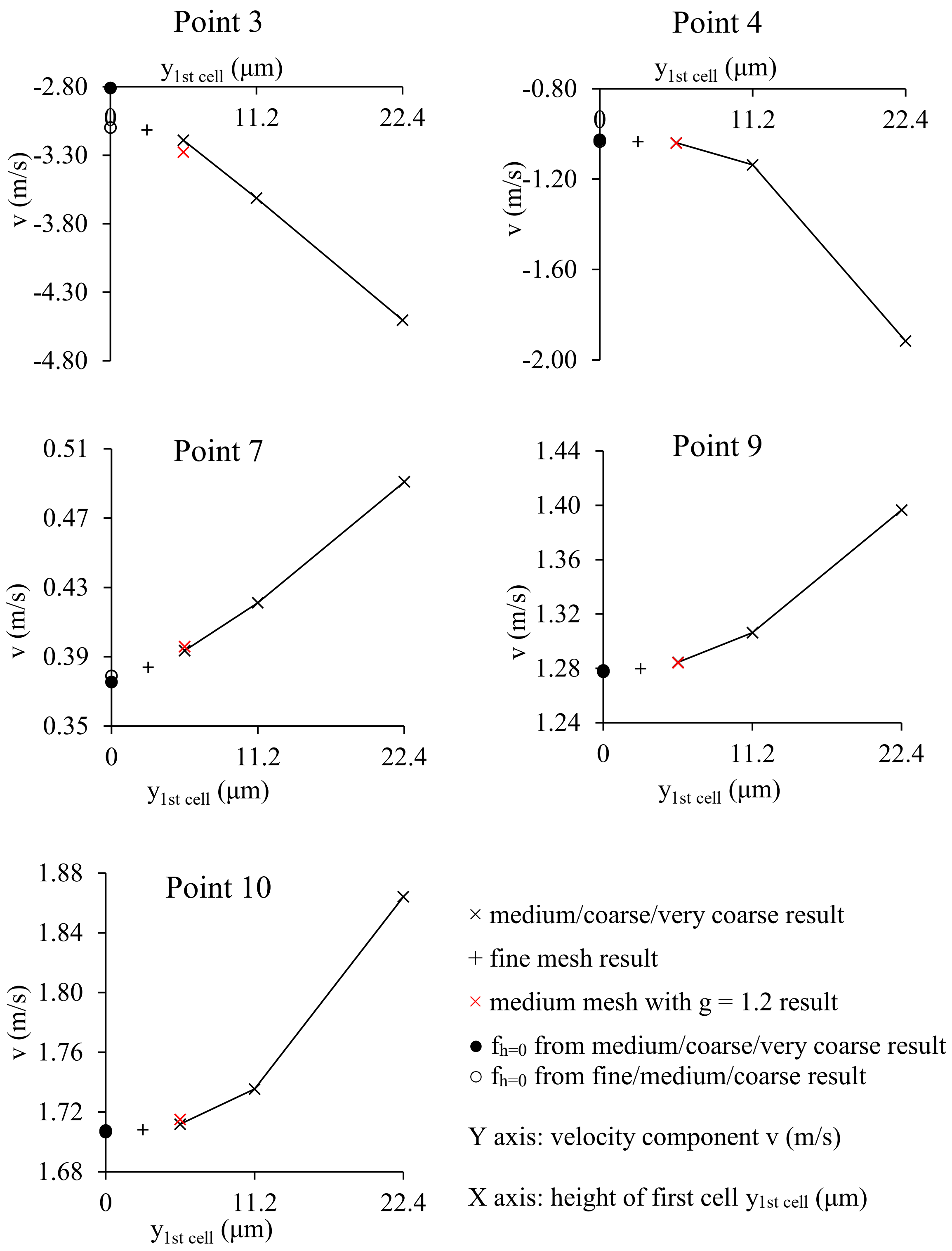

*Figure 24: Plots of asymptotic convergence.*

### 3.6.6 Quantification of other simulation errors

This section assesses round-off errors, iteration errors and discretisation errors using the 2D medium mesh with 1.2 growth rate as a base case. This simulation converged to a maximum continuity residual of 1.3x10$^{-4}$; as this value is well above the 1x10$^{-5}$ required for assessing these other errors, the simulation accuracy of this base case was increased by increasing the order of the discretisation scheme, and by using a local grid-doubling mesh refinement around the edges of the last two baffles. This suggests that discretisation error, mesh density and discretisation scheme, are still the biggest contributions to error. With these improvements the lowest attainable maximum residual using default under-relaxation factors was 1.7x10$^{-5}$, which was deemed acceptable for this purpose.

Six simulation runs were performed, these are summarised in Table 11.. The errors may be assessed by comparing the results of these simulations.

| simulation case | precision | max. residual at convergence (continuity) | discretisation scheme for transport variables |
|---|---|---|---|
| 1 | double | 1.0x10$^{-3}$ | 3rd order MUSCL |
| 2 | double | 1.0x10$^{-4}$ | 3rd order MUSCL |
| 3 | double | 1.7x10$^{-5}$ | 3rd order MUSCL |
| 4 | single | 2.4x10$^{-4}$ | 3rd order MUSCL |
| 5 | double | 1.0x10$^{-4}$ | 2nd order upwind |
| 6 | double | 1.0x10$^{-4}$ | 1st order upwind |

*Table 11: Simulations used to quantify other simulation errors. (MUSCL: monotonic upwind scheme for conservation laws).*

To compare the cases, the results were extracted for pressure drop between baffles two and four in the same manner as Figure 22 above. Velocities at point locations were also extracted in the same manner as Figure 23 above. Table 12 shows the result, where the error quoted is the largest percentage difference between the two cases for the extracted data. Both the round-off and iteration errors were ca. 0.1%. The discretisation error comparison demonstrates the fully first order accurate solution is not an accurate description of the flow. For the second order accurate solution, the discretisation error is confirmed as the most important error source, with a maximum value of 2.3% and an average value of < 1% for the extracted data.

|  | simulation case | comparison | error (%) |
|---|---|---|---|
| round-off error | two vs four | double vs single precision | 0.14% |
| iteration error | one vs two | 1x10$^{-3}$ vs 1x10$^{-4}$ | 0.11% |
|  | two vs three | 1x10$^{-4}$ vs 1x10$^{-5}$ | 0.14% |
| discretisation error | two vs five | 3rd order vs 2nd order | 2.3% |
|  | five vs six | 2nd order vs 1st order | >10% |

*Table 12: Quantification of other simulation errors.*

### 3.6.7 *Three dimensional mesh*

With grid independence established in the 2D model, the same mesh sizing constraints were applied to the full 3D cryogenic condenser geometry. Ideally the first cell height and growth rate would be identical to the two dimensional mesh. However the total cell height must be exactly half the domain extent in the Z-coordinate (11.75/2 = 5.875mm), and $n_{sb}$ must result in an integer number of mesh cells in the resulting model. Applying these sizing constraints creates a problem that is over-constrained (see equations 3-7 and 3-15).

To solve the problem a new value of g was calculated. A hypothetical $n_{cells}$ was first calculated from a rearrangement of equation 3-7. This was rounded down to the nearest unit giving a value of $n_{sb} = 29$. A new growth rate was found by iteration, $g = 1.203$. This value of g was then used to find the sweep bias $S_b = 178$. Table 13 indicates the resulting three dimensional mesh is of an acceptable quality based on skewness and orthogonal quality mesh metrics (see appendix 8.3). This establishes the mesh as appropriate for use in the CFD simulations of the cryogenic condenser and of the similitude model described in the results chapters that follow. The resulting mesh is shown in Figure 25 below.

| | 3D mesh (med, g = 1.2) | acceptance criteria |
|---|---|---|
| nodes | 7663032 | |
| elements | 6838625 | |
| skewness | | |
| max | 0.77 | < 0.9 |
| average | 0.23 | < 0.33 |
| orthogonal quality | | |
| min | 0.12 | > 0.01 |
| average | 0.87 | |

Table 13: Quality metrics for 3D mesh.

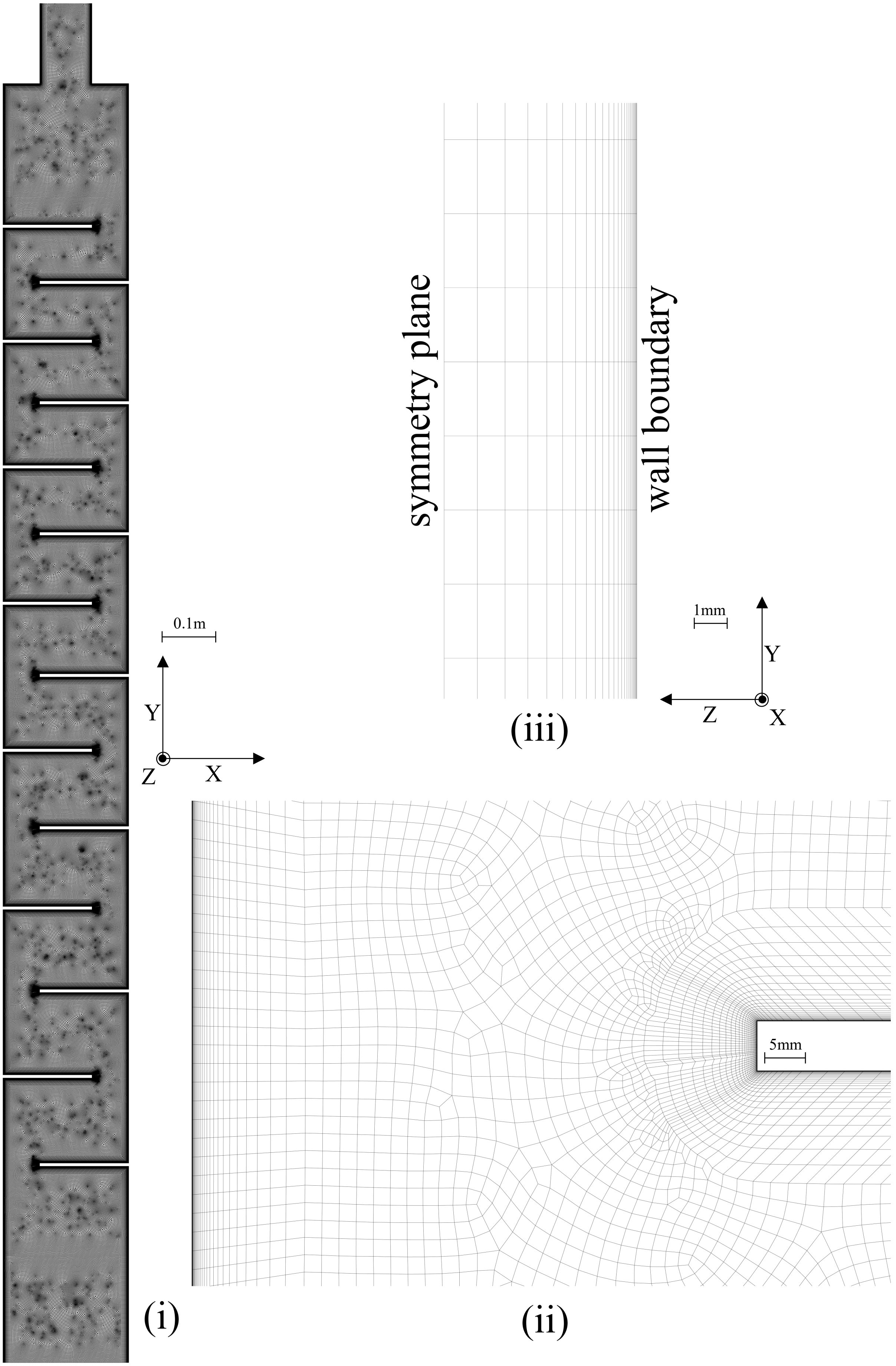

*Figure 25: Mesh used in the simulation. (i) view from z+ direction (ii) illustrating detail around baffle edge (iii) illustrating detail from side-on view, showing swept mesh.*

## 3.7 Numerical Simulation

The previous section has justified the meshing process applied to the CFD model. This section describes the numerical simulation conditions used in the modelling work. The numerical simulation work has been conducted at steady state. The second-order, pressure-based SIMPLE solver was used to solve the flow. Simulations used a double-precision floating point format. Second-order upwind schemes were applied to the transport variables unless otherwise stated. The iterative solver was considered converged when all of the residuals had dropped below 1 x$10^{-4}$ of their initial value. These choices were made based on standards for publishable quality CFD results according to ASME (2015), Zigh and Solis (2013, p. 25).

### *3.7.1 Material properties*

The fluid properties were approximated as pure nitrogen. Nitrogen is the main component of the vent gas, as the vent gases consists predominantly of nitrogen used for inertion of vessel headspace in the industrial process. These properties are temperature dependent over the operating range of the cryogenic condenser. Thermophysical properties of nitrogen (NIST, 2011) demonstrated that treating these properties as constant was appropriate for heat capacity but not for the other properties (density, thermal conductivity, and viscosity). A constant heat capacity of 1.043 kg/kJ-K was used in this work. Density was approximated using the ideal gas law. The Mach number is less than 0.3 at all conditions in the model, so the flow may be considered incompressible (Johnson, 1998, pp. 8-3). Thermal conductivity was approximated using a straight line, shown in equation 3-16. Viscosity was set using Sunderland's formula, given in equation 3-17, where the reference viscosity, reference temperature and Sunderland's temperature were $\mu_{ref} = 1.66$ x$10^{-5}$ kg/m.s, $T_{ref} = 273$ K, $S_{ref} = 107$ K respectively.

$$k_g(W/m.K) = 0.0000741T_g(K) + 0.00368 \tag{3-16}$$

$$\mu_g = \mu_{ref}\left(\frac{T_g}{T_{ref}}\right)^{3/2}\frac{\left(T_{ref} + S_{ref}\right)}{\left(T + S_{ref}\right)} \tag{3-17}$$

These temperature-dependent nitrogen properties deviate by a maximum of 1% from the values in literature (NIST, 2011) over the appropriate range (-100°C to +20°C at 1Atm). The PIV experiment used an isothermal air flow. For CFD modelling of the PIV experiment, constant air properties were used. An air density $\rho_g = 1.225$ kg/m$^3$, and a viscosity $\mu_g = 1.84$ x$10^{-5}$ kg/m.s were used in this case.

The properties of solid benzene were required for the Eulerian-Lagrangian modelling (discrete phase model, DPM) work. Constant physical properties were applied to the solid benzene phase (Density $\rho_p$ = 1016 kg/m$^3$; heat capacity $C_p$ = 1.246 kJ/kg-K (Maass and Waldbauer, 1925); thermal conductivity $k_p$ = 0.285 W/m.K (Purskii and Zholonko, 2003)). These values deviate significantly (by more than 10%) from the physically accurate values for the temperature range. However, the most important variable in the DPM modelling, solid density, does not vary significantly with temperature.

In order to model the desublimation process, the benzene vapour must be included in the fluid flow. This requires the diffusivity for all of the components of the gas phase. The concentration of benzene vapour in the system is sufficiently dilute for the diffusivity to be unaffected by concentration. Diffusivity is a strong function of temperature. In this work, this dependence was modelled using a straight line approximation. This has the advantages of low computational load and reasonable stability.

The straight line approximation required data in order for the line to be fitted. Two straight line approximations were required (the binary diffusivity of benzene in nitrogen, and the self-diffusivity of nitrogen) at one atmosphere, over the temperature range. In the first case, the data for the binary diffusivity of benzene in nitrogen is plotted in Figure 26 (i). The plotted curve is the result of the Chapman-Enskog equation, as described in Perry and Green (2008) with the characteristic length and energy parameters for benzene (Hirchfelder *et al.*, 1954) and nitrogen (taken from Fluent database). Crosses represent experimental data points, taken from Gustafson and Dickhut (1994) for benzene in air. In the second case, the data for nitrogen self-diffusivity is plotted in Figure 26 (ii). The plotted curve represents the self-diffusivity calculated from kinetic theory, using the equation in Kuhn *et al.* (2009, p. 417). The data point represents an experimental value (at 1 Bara) for nitrogen, taken from the same source. Based on this, linear best-fits to the curves in Figure 26 were made over the range of temperatures expected in the model. This is summarised in equation 3-18 and Table 14. The temperature at which the linear approximation turns negative is important for setting the limits during the iteration, the simulation solver can diverge or crash if this diffusivity becomes negative.

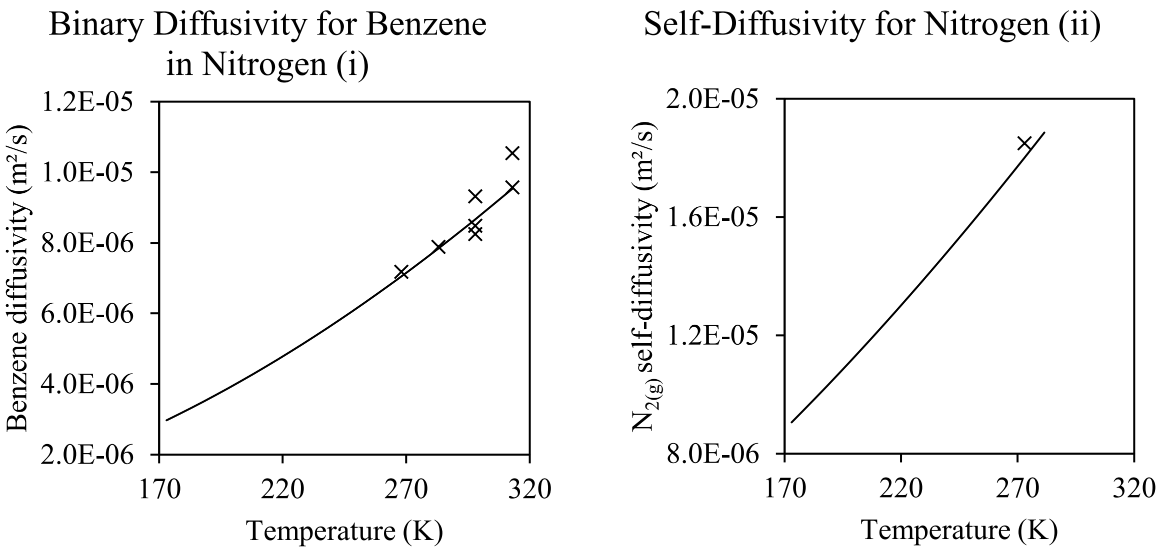

*Figure 26: Plots of diffusivity data, used as the basis for linear approximations.*

$$D_{AB} \approx A_0 + A_1 T \tag{3-18}$$

| | $A_0$ | $A_1$ | max deviation from expected values (%) | T(K) at which diffusivity turns negative |
|---|---|---|---|---|
| for binary benzene diffusivity in nitrogen | $-4.30 \times 10^{-6}$ | $4.15 \times 10^{-8}$ | 2.9% (173K to 250 K) | 103.5 |
| for nitrogen self-diffusivity | $-6.78 \times 10^{-6}$ | $9.05 \times 10^{-8}$ | 2% (173K to 281 K) | 74.9 |

*Table 14: Linear approximations of diffusivity.*

The equilibrium vapour pressure $P_e$ and the interfacial energy σ are two additional material properties that are needed to describe the nucleation process (in addition to the fluid properties already described), using the nucleation rate equation (2-68). To evaluate equilibrium vapour pressure, ideal behaviour was assumed. The equilibrium vapour pressure data for benzene was taken from the Cox equation in Ruzicka *et al.* (2014), shown in equation 3-19. Constants for benzene were as follows: $P_0 = 4785$ Pa; $T_0 = 279$ K; $A_0 = 3.06$; $A_1 = -1.91 \times 10^{-4}$; $A_2 = -5.47 \times 10^{-7}$. Validity covered a temperature range 150-278 K.

$$\ln\left(\frac{P_e(Pa)}{P_0}\right) = \left(\frac{1 - T_0}{1 - T(K)}\right) e^{(A_0 + A_1 T + A_2 T^2)} \tag{3-19}$$

A simple two-parameter August vapour pressure equation was fitted to this data, shown in equation 3-20. This simplification lowers the computational load. Exponentiation operations are computationally expensive in the code used to write the user-defined functions in fluent. Although they are mathematically the same, the operation $2^3$ (pow(2,3)) is computationally more expensive than 2 × 2 × 2, due to the algorithm used in the power function. The difference is negligible over a single calculation, but when the user-defined function is executed in every mesh cell at every flow iteration, the contribution can be significant. This simplified equation minimises this operation, and the resulting pressure deviates by a maximum of 4% from Ruzicka *et al.* (2014) over a temperature range 190-278K.

$$log_{10}(P_e) = 12.499 - \frac{2452.5}{T(K)} \qquad 3\text{-}20$$

The interfacial energy is an important factor in classical nucleation theory. It is cubed in the exponential term of the nucleation rate expression (2-68). The result of the rate expression has a strong dependence on the value of σ. This affects the accuracy of predictions made using the equation, such as the critical degree of supersaturation (Garmony and Mastorakos, 2008). Whilst benzene is a common material in laboratories, experimental measurement of the interfacial energy of solids is difficult. Conventional methods (such as the du Noüy ring tensiometer used to measure surface tension of liquids) cannot be applied to solids. It is possible to estimate interfacial energy using the Stefan-Skapski-Turnbull equation (Kashchiev, 2000, p. 183; Sauter *et al.*, 2012). This work, has used an average of three sources from literature. Narhe *et al.* (2009) quote a value of $\sigma_1$ = 30.32 mN/m for benzene at $T_1$ = 3°C. This value was extrapolated across the temperature range in the model using the equation 3-22. This is taken from Branan (2005, p. 397) and is known as the Guggenheim-Katayama formula. A linear equation (3-22) for the surface free energy of polystyrene was used for the second source (DataPhysics Instruments GmbH, 2007). The formula for liquid benzene interfacial energy from Katz *et al.* (1975) was used for the third source, shown in equation 3-23. The average is given in Table 15, the answer may be inaccurate due to extrapolation.

| temperature | interfacial energy σ (mN/m) | | | |
|---|---|---|---|---|
| T(K) | first source | second source | third source | average |
| 278.675 | 30.0 | 35.5 | 30.7 | 32.1 |
| 220 | 37.6 | 39.8 | 38.3 | 38.5 |
| 210 | 38.9 | 40.5 | 39.6 | 39.7 |
| 200 | 40.3 | 41.2 | 40.9 | 40.8 |
| 190 | 41.6 | 41.9 | 42.1 | 41.9 |

*Table 15: Estimate for interfacial energy of solid benzene.*

$$\sigma = \sigma_1 \left( \frac{T_c - T(K)}{T_c - T_1} \right)^{1.2} \tag{3-21}$$

$$\sigma\ (mN/m) = 34.5 + (0.072(293 - T(K)) \tag{3-22}$$

$$\sigma\ (mN/m) = 31.45 - 0.1286(T(K) - 273.15) \tag{3-23}$$

### *3.7.2 Wall boundary conditions*

A linear temperature profile was applied across the wall boundary representing the lamella surface. This was set to vary from -60°C to -100°C with increasing Y-coordinate, based on the operating conditions of the cryogenic condenser. The wall temperature profile was achieved via a user-defined function (Appendix 8.4.1). This temperature profile is intended to approximate counter-current sensible heat transfer to the coolant (cold nitrogen gas) flow that is not part of the CFD model. The effect of the user-defined function is illustrated in the Figure 27, which plots the temperature of the wall and the modelled flow, coloured over the temperature range (red: -60°C, blue: -100°C).

For Eulerian-Lagrangian modelling work, walls in the model should be set to respond in a specific way to particle collisions. There are many options for this: for example walls can be set to trap particles; reflect particles; cause the breakup of droplets or allow the particles to escape. In this work, collisions with the wall result in deposition of the benzene frost particle onto the internal surface of the cryogenic condenser. In the CFD simulation, collisions with the wall (in cases where there is mass exchanged between the particle and the vapour) can affect the mass balance. The deposited benzene particles are removed from the domain along with the benzene mass they represent. To do this in the Fluent software, all of the walls must be set to 'escape'. This is because the Fluent Eulerian-Lagrangian models are designed primarily to model evaporating sprays. If the walls are set to 'trap', the particle is modelled as an evaporating droplet following collision with the wall, and the mass is added back into the vapour in the system.

### *3.7.3 Inlet boundary conditions*

The inlet to the model consists of a uniform velocity profile normal to the boundary. The appropriate velocities were determined based on continuity for the three flowrates to be analysed (0.907 m/s, 0.605 m/s, and 0.302 m/s at 150 $Nm^3/hr$, 100 $Nm^3/hr$, 50 $Nm^3/hr$). The inlet turbulence conditions were set as in section 3.5.4. Inlet temperature was set to 281 K based on average ambient temperature at Aesica Cramlington (Climate-Data.org, 2014). In simulations which included nucleation and growth of the particles, the fluid is modelled as a binary mixture of two species: benzene and nitrogen, and the mixture is given the same physical properties as pure nitrogen. The inlet mass fraction of benzene in this case was set to 0.0148 to correspond with the mass balance above (Section 1.1.2, p.13).

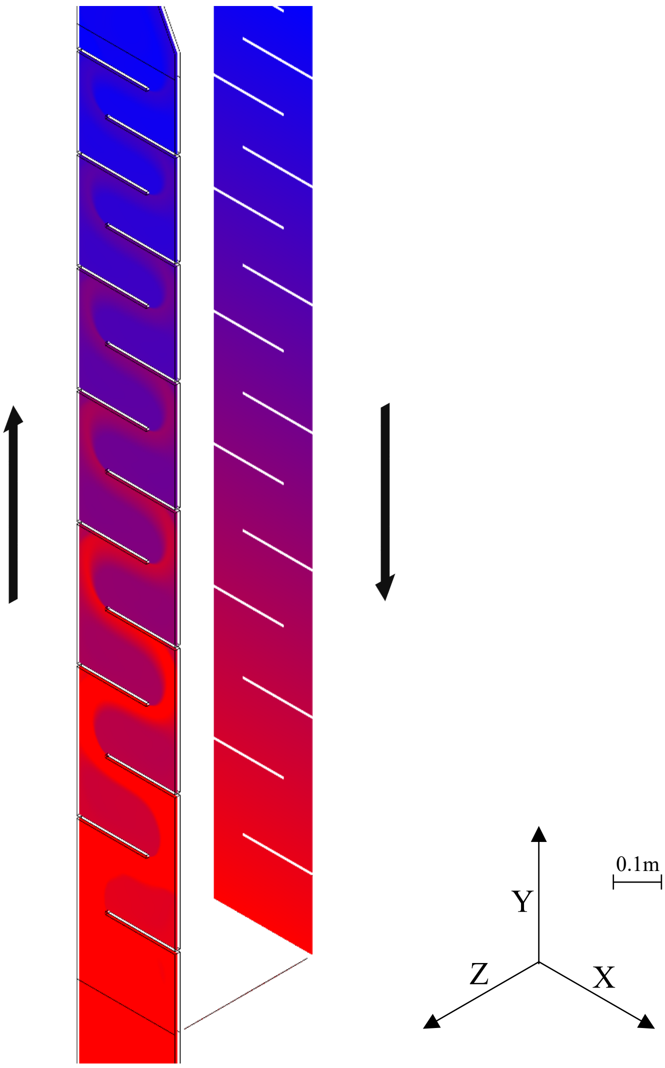

*Figure 27: Illustration of temperature profile on the condenser wall.*

### 3.7.4 Eulerian-Lagrangian modelling of inert particles

In addition to modelling the nucleation and growth of the particles through Eulerian-Lagrangian models, part of this study used inert particles that did not exchange mass with the flow. Eulerian-Lagrangian modelling of inert particles was used to explore the effect of particle diameter on entrainment in the gas flow. Particles were approximated as solid non-porous spheres of constant diameter. When compared to modelling the nucleation and growth rigorously, this simulation was easier to solve, taking far less computation time. Based on the results described in section 6.1 two planes were chosen to represent locations for homogeneous and heterogeneous nucleation, based on the temperature (and therefore, degree of supersaturation) at which nucleation was expected to occur. Heterogeneous nucleation occurring in the space between baffles two and three, homogeneous nucleation occurring in the space between baffles four and five. Each plane contains a uniform 1mm grid of injection locations, as illustrated in Figure 28. Each injection point was assigned a temperature and velocity vector appropriate to their location in the model. For expediency this was accomplished via a user-defined function, see appendix 8.4.2. The effect of turbulence on the particle was considered using the discrete random walk model.

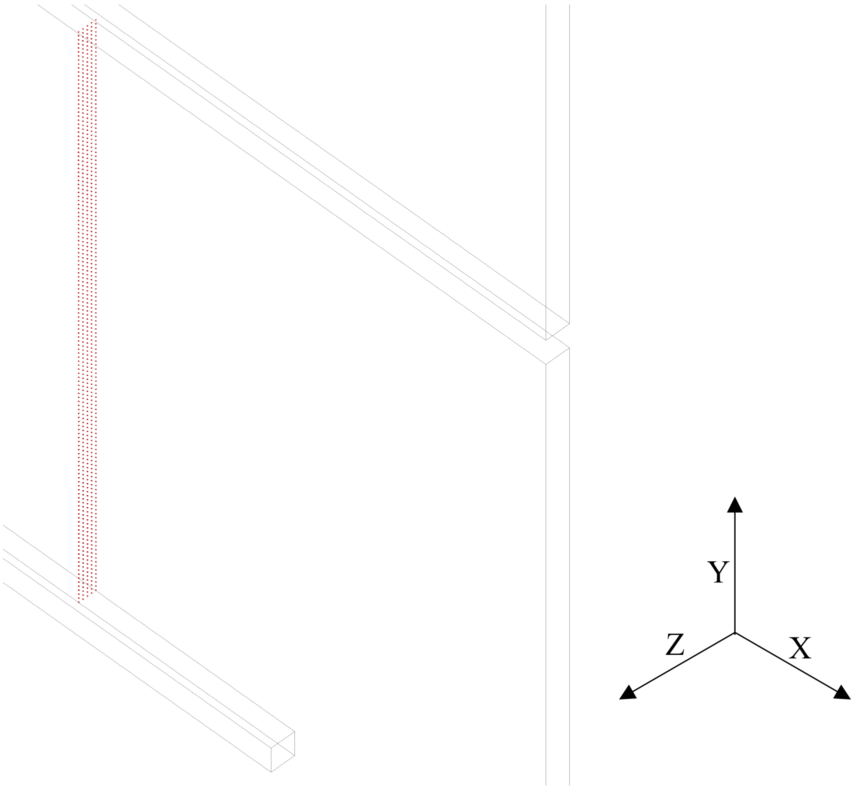

*Figure 28: Illustration of injection locations used in the inert Eulerian-Lagrangian study.*

### 3.7.5 Eulerian-Lagrangian modelling of nucleation

The nucleation and growth model creates particles that are initially very small. Small particles will be subject to the Cunningham slip correction factor as introduced in section 2.15.1. As well as being an issue for the accuracy of the CFD model, including the Cunningham slip factor avoids problems with the simulation that can be caused by small particles exchanging unphysical amounts of momentum with the fluid flow when Stokes drag is applied. The simulation environment allows for the inclusion of a constant Cunningham slip correction factor in DPM modelling. This is not satisfactory for the nucleation and growth model, because growth changes the particle size, and therefore the Cunningham slip correction factor. In this simulation, the Cunningham slip correction factor is applied using a user-defined function. The user-defined function returns the drag coefficient in the form of the dimensionless group shown in 3-24, the Cunningham slip correction factor $C_c$ is included with this as demonstrated.

$$drag\ term\ (dimensionless) = \frac{18 C_d Re_p}{24} \times \frac{1}{C_c} \qquad 3\text{-}24$$

The drag coefficient $C_d$ is calculated using a spherical drag law. To allow the user-defined function to be verified against the spherical drag law in the Fluent software, the same source (Morsi and Alexander, 1972) was used to define the spherical drag law using a simple polynomial. Constants for the polynomial are given in equation 3-25 below for particle Reynolds number ranges applicable to the CFD work. The user-defined function is given in Appendix 8.4.3.

$$\begin{gathered}
C_d = \frac{24}{Re_p} \quad Re_p < 0.1 \\
C_d = \frac{24.73}{Re_p} + \frac{0.0903}{Re_p^2} + 3.69 \quad 0.1 < Re_p < 1 \\
C_d = \frac{22.73}{Re_p} + \frac{3.8889}{Re_p^2} + 1.222 \quad 1 < Re_p < 10 \\
C_d = \frac{46.5}{Re_p} - \frac{116.67}{Re_p^2} + 1.6167 \quad 10 < Re_p < 100
\end{gathered} \qquad 3\text{-}25$$

Including nucleation in the CFD model was also accomplished through user-written computer code. The first step involved the use of Eulerian source terms for mass, species and energy to be exchanged with the fluid during nucleation. The nucleation rate and the critical diameter are both calculated at this stage, and this information is stored in every mesh cell using two user-defined memory slots. The second step involved using an execute-on-demand user-defined function, which converted this information into injection files. The third step involved a journal file which deletes the old injections and read the new injection files into Fluent.

The user-defined function used in the first step is given in Appendix 8.4.4. The nucleation rate is calculated from equation 2-68 and the critical diameter is calculated from equation 2-53 above. The simulation requires mass, energy and species source terms to make the mass and energy balances correct. This is covered in Appendices 8.4.5 and 8.4.6.

The second step generates the injection file. Calculation of the nucleation rate assigns each mesh cell where nucleation occurs with a non-zero value for the user-defined memory slot. The user-defined function in appendix 8.4.7 converts information from each mesh cell into a line in the injection file. This creates an injection point in the centre of a cell where nucleation occurs, and assigns it with an appropriate properties from that mesh cell.

The third step loads the injection file. As the fluid flow is iterated, so the DPM model is also iterated. Each DPM iteration is conducted after a set number of flow iterations has been calculated (by default, every ten iterations the DPM model undergoes one iteration). The DPM iteration corrects the DPM sources (momentum, energy and mass exchanged with the flow). In this work, it also requires an injection iteration to iterate the injection locations for the DPM as the flow converges. This was accomplished using a Fluent journal file, given in Appendix 8.4.8.

### *3.7.6 Eulerian-Lagrangian modelling of growth*

Following nucleation, particles grow via mass transfer of benzene to the surface. This process is modelled using the concatenated user-defined function given in Appendix 8.4.9. Both the growth function (Appendix 8.4.9) and the nucleation function (Appendix 8.4.4) require the partial pressure and the equilibrium vapour pressure. The same approach is applied in both, with different pressure units (mmHg, Pa). Fluent stores the benzene gas concentration in units of mass fraction: this is converted to partial pressure using Raoult's law, which is applied to a binary benzene-nitrogen gas mixture as shown in equation 3-26.

$$P_{Bz} = P_T * \mathrm{x}_{Bz} = \frac{P_T}{M_{Bz}} * \frac{mf_{Bz}}{\frac{mf_{Bz}}{M_{Bz}} + \frac{1 - mf_{Bz}}{M_{N_2}}} \qquad 3\text{-}26$$

According to Friedlander (2000) particle growth in aerosols changes as it crosses the Knudsen number transition. Initially, the stable nucleus grows by molecular bombardment. Growth in this regime can be modelled using the Hertz-Knudsen equation. As the particle grows it crosses the Knudsen number transition. The particle becomes larger than the mean free path of the gas molecules. The particle-gas interactions change from collisions with individual gas molecules described by kinetic theory, to behaviour as a particle in a continuum. Mass transfer becomes diffusion-limited, growth occurs via a concentration gradient and can be described as shown in equation 3-27.

$$\frac{dm_p}{dt} = \rho_p \frac{dv_p}{dt} = \rho_p \frac{2\pi D_{AB} d_p v_m (P_A - P_e)}{k_B T} \times F.S.correction \qquad 3\text{-}27$$

Growth in both the molecular-bombardment and the Knudsen number transition regime can be modelled by applying a correction factor to equation 3-27 (Friedlander, 2000; Garmony and

Mastorakos, 2008). There are several alternative correction factors, the correction from Flagan and Sienfield (1988, p. 318) is used in this work (referred to as the Flagan and Sienfeld correction hereon, also known as the Fuchs interpolation formula) given in equation 3-28.

$$F.S.correction = \frac{1 + Kn_{AB}}{1 + \left(\frac{4D_{AB}}{\bar{c}_A \lambda_{AB}}\right) Kn_{AB}(1 + Kn_{AB})} \qquad 3\text{-}28$$

The Knudsen number in equation 3-28 requires the mean free path for collision with the condensing (desublimating) species. The Knudsen number describing mass transfer $Kn_{AB}$ is not the same as the Knudsen number describing particle drag $Kn_p$. $Kn_{AB}$ requires the binary mean free path $\lambda_{AB}$, in place of the carrier gas mean free path $\lambda_g$ in equation 2-78. The binary mean free path can be calculated from the diffusivity of benzene in nitrogen, as shown in equation 3-29. The mean molecular speed $\bar{c}_A$ was calculated from kinetic theory using equation 3-30.

$$\lambda_{AB} = \frac{D_{AB}}{\frac{3\pi}{32}\left(1 + \frac{M_{Bz}}{M_{N_2}}\right)\bar{c}_A} \qquad 3\text{-}29$$

$$\bar{c}_A = \sqrt{\frac{8RT}{\pi M_{Bz}}} \qquad 3\text{-}30$$

The result of this correction factor is shown in Figure 29, for a benzene partial pressure of 543Pa at two temperatures (T = 173K (i) and T = 250K (ii)) across a size range applicable to the modelled conditions. The dotted line represents growth by molecular bombardment while the dashed line represents growth by diffusion. The solid line represents the Flagan and Sienfeld correction, demonstrating the fit the correction provides for the Knudsen-number transition.

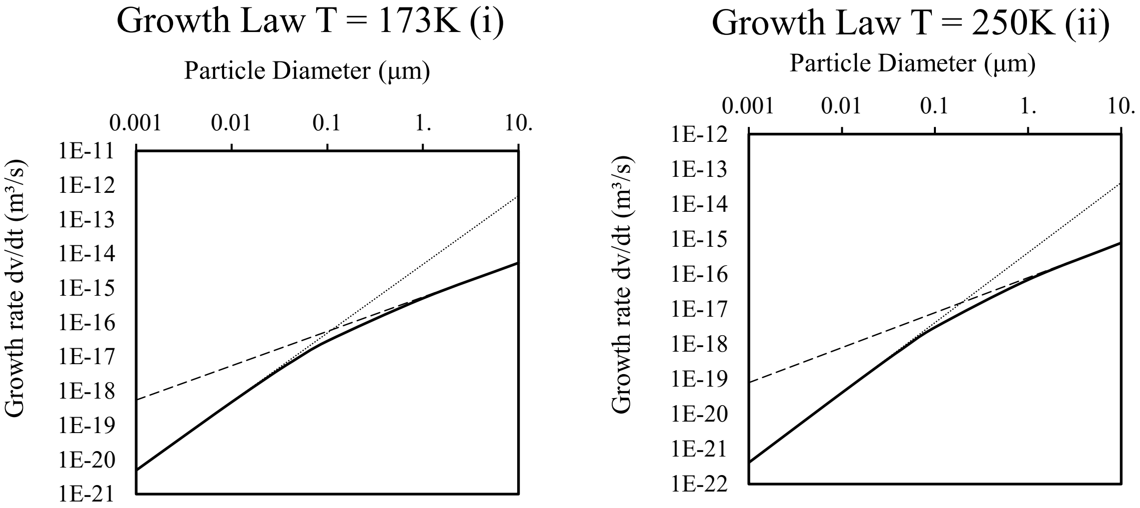

*Figure 29: Illustration of growth law.*

The code in Appendix 8.4.9 serves several functions, performing this calculation and applying the resulting source terms to the Lagrangian particle and to the Eulerian fluid flow. The switching law is included to override the Fluent default: the Fluent defaults are designed to model evaporation, and so typically switch from mass transfer (evaporation) to sensible heat exchange as temperature falls. For simplicity, isothermal conditions have been enforced in this work – the gas and particle temperature are forced to be equal. Also, the particles can only have positive growth or no growth at all: re-evaporation is not considered.

### *3.7.7 Numerical stiffness and the nucleation and growth model*

The nucleation and growth create a problem where equilibrium vapour pressure is obtained at a very fast rate. In numerical modelling, this type of problem is known as numerical stiffness or a ‘stiff chemistry’ problem. This can make the problem difficult to solve, causing problems such as divergence and other difficulties in obtaining a solution from the simulation.

The first approach to solving this problem involves reducing Under-Relaxation Factors (URF) to obtain a converging solution, and gradually increasing them once the solution is stable. In this work under-relaxation factors for species and DPM were reduced in this way. Reducing the species under-relaxation steadied the nucleation rate. The DPM under-relaxation factor (DPM URF) was set with an extremely low value initially ($1 \times 10^{-10}$ or less). Reaching a converged solution was found to be comparatively easy without the particles (with Eulerian nucleation sources only). This implied DPM particles were the main source of instability in the solver. However, particle growth changes the nucleation, and therefore particle injections, through removing benzene vapour from the flow domain. Reducing the DPM URF increases the number of flow iterations required to introduce the DPM source terms into the fluid flow. The default

(DPM URF = 0.5) introduces the DPM source term in ca. 10 iterations, but the approach is asymptotic for any URF less than unity.

The second approach involves changing the coupling of the DPM and Eulerian solution. Two approaches (stronger coupling or stronger decoupling) can work in different cases to increase stability. In this work, a stronger decoupling was found to be effective; the DPM URF is decreased and the number of flow iterations per DPM iteration was increased. This also benefits this solution speed, because the DPM iteration was the slowest part of the calculation.

Solver settings for the DPM itself can also be changed to provide increased stability and accuracy. In this work the ‘step length factor’ was changed from 5 to 50, this controls the number of discretisation steps performed in each mesh cell. The ‘maximum number of steps’ also must be increased to allow for the large model size and the increased number of discretisation steps. The ‘accuracy control’ overrides these settings however: in this work it was reduced to 1 x$10^{-9}$ in order to obtain a suitable solution. An implicit tracking scheme was used on the basis that it was unconditionally stable. Node-based averaging was applied to stabilise the solution.

## 3.8 **Simplifications to the Particle Model**

There are some phenomena that have not been included in the Eulerian-Lagrangian particle modelling in this thesis. The Saffman lift force affects particles in shear flows. Acting normal to the flow direction, the Saffman lift force can act to lift the particle typically towards the higher velocities (away from the wall), however when near-wall effects are considered the force can also act in the opposing direction (towards the wall) under some conditions (Finlay, 2001, p. 252). The Magnus lift force is the force on a rotating particle due to the Magnus effect. Unlike the Saffman lift force the Magnus lift force can occur in uniform flow conditions, but relies on particle rotation to create a velocity difference (and therefore pressure and force difference) between sides of the rotating particle rotating with and against the direction of flow. This of course requires a rotating particle, usually the result of collisions between particles or particles rebounding from walls (Norouzi, 2016, p. 302). Stefan flow describes the convective flow induced as a result of diffusing species. This creates an attractive force for particles, towards the walls of a condenser plate as benzene vapour is removed from the gas flow. Other than through the mass source term for benzene, this effect of Stefan flow on particle trajectories is not considered in the model. Particle concentration gradients create a net diffusion in the opposite direction due to the random Brownian diffusion. As stated in Zhao (2011) Lagrangian models that include Brownian diffusion account for these effects. This thesis does not consider

Brownian diffusion. The presence of particles at high concentrations also changes the effective viscosity of the continuous phase, which in-turn affects fluid-particle interactions. Increases in aerosol effective viscosity due to particles can be described by the well-known Einstein equation (Friedlander, 2000, p. 8). Drops in apparent viscosity with particle addition have also been reported (Chand, 1971). This was not considered in the thesis modelling work.

## 3.9 **Simplifications to the Cryogenic Condenser Model**

The most significant simplification in the model is that frost is not considered. Frost models are inherently transient as removed species freeze on the cold walls. The growing frost can have a low thermal conductivity due to porosity. For benzene, the solid has a true thermal conductivity of 0.285 W/m-K. In the absence of conductivity data for benzene frosts, Wintermantel *et al.* (1987) report a voidage (porosity) of 70% for benzene frosts; based on Lee's expression (Lee, 2003) for water frost, a water frost with a voidage of 70% would have an effective thermal conductivity that is 1/10th of the true thermal conductivity. The benzene frost layer will have a significant effect on the heat exchanger performance as it changes both the heat conduction and the flow geometry, and defines the cycle times of cryogenic condensers. The walls were considered smooth, no wall roughness was considered in the model. Roughness and interfacial energies can affect frost onset. Smooth, hydrophobic surfaces delay the time-onset of water frosting (Wang, 2015). Frost formation was not considered in this thesis. Surface roughness, which also affects fluid flow and particle deposition, was not considered.

The heat transfer problem has been simplified to a linear temperature profile. This is a simplification of the heat transfer problem that ignores the stainless steel and the coolant-side resistances. This is an appropriate simplification for the coolant side as there is no phase change for the coolant within this exchanger. Modelling the heat exchange between the process and coolant fluid is a straightforward CFD problem. But modelling this would dramatically increase computational load of the simulation for very little gained in understanding, as control systems maintain the temperatures in the condenser by controlling coolant flows (Richardson *et al.*, 2002, p. 198). Modelling this aspect of the flow was therefore not investigated in this thesis.

## 3.10 **Summary Table**

| | |
|---|---|
| Turbulence models: | Low Reynolds number shear stress transport model.<br>$\dfrac{\partial(\rho_g k)}{\partial t}+\dfrac{\partial}{\partial x_j}(\rho_g k u_j)=\dfrac{\partial}{\partial x_j}\left[\left(\mu_g+\dfrac{\mu_t}{\sigma_k}\right)\dfrac{\partial k}{\partial x_j}\right]+\mu_t\boldsymbol{S}^2-\beta^*\rho_g k\omega$ 2-22<br>$\dfrac{\partial(\rho_g \omega)}{\partial t}+\dfrac{\partial}{\partial x_j}(\rho_g \omega u_j)=\dfrac{\partial}{\partial x_j}\left[\left(\mu_g+\dfrac{\mu_t}{\sigma_\omega}\right)\dfrac{\partial \omega}{\partial x_j}\right]+\dfrac{\alpha\rho_g}{\mu_t}\mu_t\boldsymbol{S}^2-\beta^*\rho_g\beta\rho_g k\omega^2+D_\omega$ 2-23<br>Transition shear stress transport model, in addition to above:<br>$\dfrac{\partial(\rho_g \widetilde{Re}_{\theta t})}{\partial t}+\dfrac{\partial(\rho_g u_j \widetilde{Re}_{\theta t})}{\partial x_j}=\dfrac{\partial}{\partial x_j}\left(\sigma_{\theta t}(\mu_g+\mu_t)\dfrac{\partial \widetilde{Re}_{\theta t}}{\partial x_j}\right)+P_{\theta t}$ 3-31<br>$\dfrac{\partial(\rho_g \gamma)}{\partial t}+\dfrac{\partial(\rho_g u_j \gamma)}{\partial x_j}=\dfrac{\partial}{\partial x_j}\left(\left(\mu_g+\dfrac{\mu_t}{\sigma_\gamma}\right)\dfrac{\partial \gamma}{\partial x_j}\right)+P_{\gamma 1}-E_{\gamma 1}+P_{\gamma 2}-E_{\gamma 2}$ 3-32<br>Also used in the thesis:<br>Low Reynolds number k-ε model<br>Detached eddy simulation<br>Splarat Allmaras Model<br>Standard k-ε model<br>Laminar |
| Boundary conditions: | Walls: No-slip boundary conditions. No roughness.<br>Heat exchange: fixed temperature (Dirichlet) boundary condition, varying linearly with temperature on the wall representing the lamella plate. No heat exchange for all other walls.<br>Inlet: uniform velocity perpendicular to plane, at 0.907m/s representing 150Nm$^3$/hr, $^2/_3$$^{\text{rds}}$ and $^1/_3$$^{\text{rds}}$ for 100, 50Nm$^3$/hr.<br>Outlet: constant pressure, 1 atmosphere absolute. |
| Initial conditions: | Domain averaged values (hybrid initialisation (Ansys, 2009)) |
| Simplifications: | Uniform flow distribution between lamella plates of the cryogenic condenser. Entrance effects are not considered, instead established velocity profile at plate inlets.<br>Flow is symmetrical.<br>Linear temperature profile at heat exchanger surface.<br>Gas has the transport properties of pure nitrogen. For mass transfer, a binary benzene/nitrogen mixture without water vapour is considered in the modelling work.<br>Benzene inlet concentration is based on historical data from plant emissions studies. Steady state is assumed, this is not the case in reality.<br>Frost build-up is ignored. |
| Simplifications (Particle): | No Saffman lift force<br>No Magnus lift force<br>No Stefan flow<br>No effect of particle concentration gradients<br>No changes of gas viscosity due to particle concentrations. |

*Table 16: Methods in flow modelling – summary table.*

## 3.11 **Conclusions**

This chapter has provided a background for the simulation results presented in chapters 5 and 6. The mesh sizing used in the study has been established as appropriate for the simulation. Based on the results from the two-dimensional model, the graphical results presented for velocity profiles (Figure 20) demonstrate an acceptable result. The quantitative results in pressure drop and reattachment location (Table 9) also indicate an acceptable discretisation error results from the chosen mesh sizing. The Roache method was unsuccessful in showing asymptotic approach in all the point solution values for velocity component analysed in section 3.6.5. However, the data met the criteria for oscillatory convergence. The results in Figure 24 indicate the chosen mesh sizing compares favourably to the medium mesh using a growth rate of g = 1.1. Of the five results plotted, the maximum grid convergence index for the medium mesh occurs for point seven (1.7%), and for other points is much less (>1%). Quantification of other errors in the simulation confirmed that the discretisation error was the largest contribution to errors in the result.

The appropriate mesh sizing has been applied to the three-dimensional model, producing a mesh that is acceptable based on the mesh quality metric chosen for this study. The grid was therefore deemed acceptable for use in the numerical simulation. For the numerical simulation, the choices made in setting up the simulation have been discussed in detail. The fluid properties have been chosen to give a simple but accurate temperature dependency. Choices in boundary conditions have also been justified. The Eulerian-Lagrangian modelling, particularly of nucleation and growth, has been described in detail in this chapter. The nucleation creating injection locations for the particles within model, and the growth law controlling mass transfer to the resulting particle across the Knudsen number transition. The next chapter covers the experimental methods.

# Chapter 4. Experimental Methods

This chapter covers the experimental methods used in this study. A background is provided for the physical data obtained on the cryogenic condenser. The particle image velocimetry (PIV) experimental set up is also described, and some of the choices made in this design are covered. The main purpose of the PIV is to validate the fluid flow simulations.

## 4.1 On-Site Tests of the Cryogenic Condenser

On-site tests at Aesica were not the work of the author. On-site tests were completed by external contractors, and the resulting data taken from emissions reports was processed by the author. The cryogenic condenser is currently installed at Aesica Cramlington, and is used in process duties, controlling dichloromethane (DCM) emissions-to-atmosphere. Measurements (environmental monitoring) are required to qualify the equipment for this application. These measurements are typically conducted by specialist contractors external to the company (in this case: Exova Catalyst Ltd.). This data is available for different production campaigns using DCM. The data varies widely between campaigns, as different conditions were monitored and the process conditions upstream changed because of changes in the process. Due to the batch nature of the processes time-averaged readings of outlet concentration are typically the most important parameters obtained from these studies.

The measurements were conducted using a combination of instruments. Fourier transform infrared spectroscopy (FTIR) was used to measure the vapour concentrations of DCM (Protea ProtIR 204M). Total VOC (volatile organic compounds) as carbon was measured using flame ionisation (SICK AG, FID 3006). Flowrate was measured using a pitot tube and thermocouple, according to British Standards Institution (2002). This measurement was usually taken at the beginning; time-series data was taken from process data of in-line instrumentation upstream and was not used as part of this environmental testing. The data mining was completed using a software plugin (CPACT PreScreen 2.1) within MathWorks® matlab® 2011. This followed validated pre-processing methods (Input of raw data matrix, specification of variables, detection of missing information, graphical univariate information, outlier detection, statistical summary, elimination of noise, time realignment), as per standard practice in data mining.

## 4.2 Particle Image Velocimetry Validation Experiments

Particle image velocimetry (PIV) is a common technique for experimental validation of fluid flow. In this work it is used to validate the fluid flow simulations only, under isothermal conditions. This section describes the apparatus used in the PIV experiments. Aspects affecting the design of the experiment are discussed following this. The design was based on geometric and dynamic similarity between the PIV experiment and the full-size cryogenic condenser. The desired particle seeding rate, as well as the settings for laser pulse delay, are discussed following a description of this.

### *4.2.1 Apparatus*

An isometric sketch of the apparatus is shown in Figure 30. A similitude model was fabricated from clear acrylic plastic. Image capture was performed using a purpose-built CCD camera (TSI® powerview$^{TM}$ plus 4MP). A laser light sheet was generated using a Nd:YAG dual pulse laser head pair (Quantel laser twins BSL-200), and directed to the model using a laser light arm (TSI® laserpulse$^{TM}$ light arm 610015). The laser pair had two power supplies[‡] (Big Sky Laser Ultra) each serving one laser head. The power supplies and camera were connected using a synchroniser (TSI laserpulse$^{TM}$ synchroniser 610035). This was in turn controlled using commercial software (Insight 4G) installed on a laboratory PC. This software was also used to capture and process the image pairs. Flow consisted of an air flow seeded with water droplets. Compressed air was supplied via a filter-regulator (EMC® EM-EW4000), to a mass flow controller (Bronkhorst® F-202BB). Particle seeding was achieved using a household ultrasonic humidifier (Challenge 3L) inside a closed chamber, as illustrated in the Figure 31 below.

---

[‡] *The power supplies served the laser heads in three ways. They supplied power to the laser head. They triggered the laser pulse based on the signal from the synchroniser. They supplied the laser head with a chilled water supply which was recirculated between the power supply and the laser head (the lasers were water-cooled). This type of design is standard for PIV setups, and is commonly referred to as a 'coolant-power supply'.*

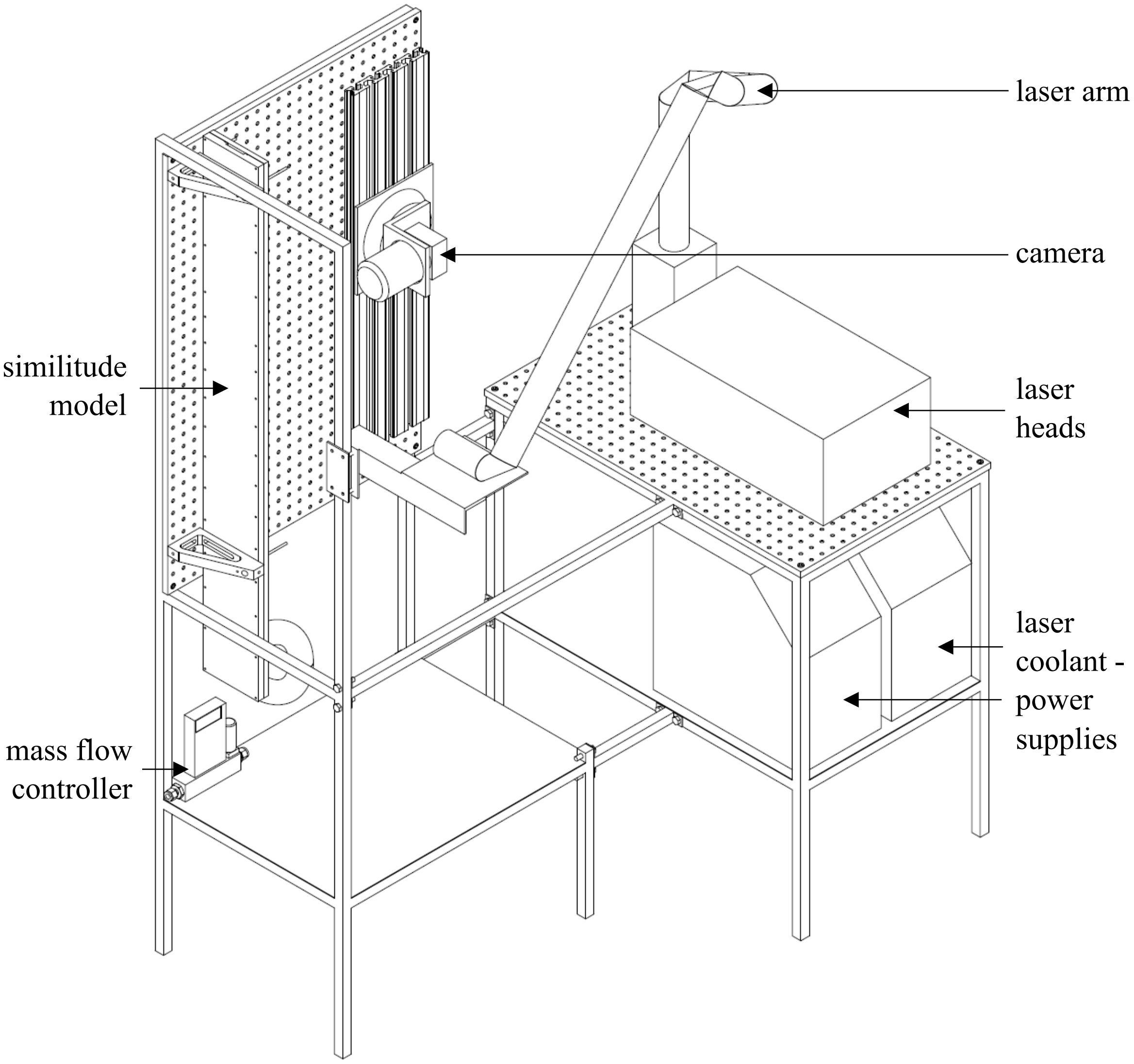

*Figure 30: Isometric drawing of the PIV apparatus.*

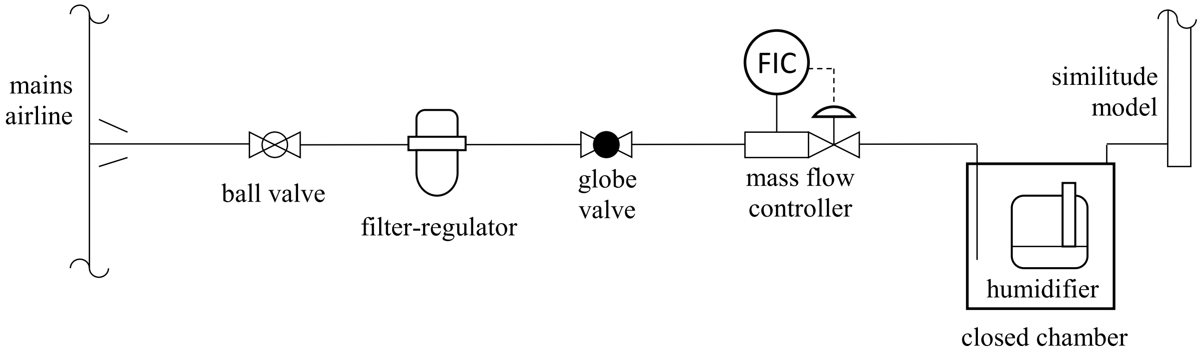

*Figure 31: Schematic of the air supply to the similitude model.*

### *4.2.2 Similitude model and Reynold's model law*

In engineering, the term 'similitude' usually refers to the relationship between a scale model of a system and the system itself (the prototype). The scale model is typically referred to as the 'model' only; in this thesis it is referred to as a 'similitude model' to distinguish it from the computational fluid dynamics (CFD) model. Similitude between the prototype and the similitude model allows the model to be tested experimentally, to gain information on how the prototype will behave. In fluid dynamics wind tunnels provide a familiar example: scale models of aircraft, cars, and so on may be tested to determine the characteristics of the full size prototype. Similitude also has applications outside of fluid dynamics which for conciseness will not be discussed here (see Murphy (1950) for more information).

The similitude model and the prototype share geometric similarity if one is a scaled reproduction of the other. It is possible to perform similitude studies without geometric similarity. For example, distorted similitude models can be used to study river hydraulics. However most similitude studies use geometric similarity. In this thesis, the similitude model is a 1:2.35 scale reproduction of the prototype (the flow domain used in the CFD model representing a single process side plate inside the cryogenic condenser). This is shown as an exploded isometric in Figure 32. The construction consisted of three acrylic sheets. The 10mm thick base and lid were machined with drilled holes and recesses. The main channel was cut from 5mm sheet using laser cutting to give a clear surface, and cemented to the base. The seal was made using an o-ring groove visible on the lid, and the compressive force of bolts through the model.

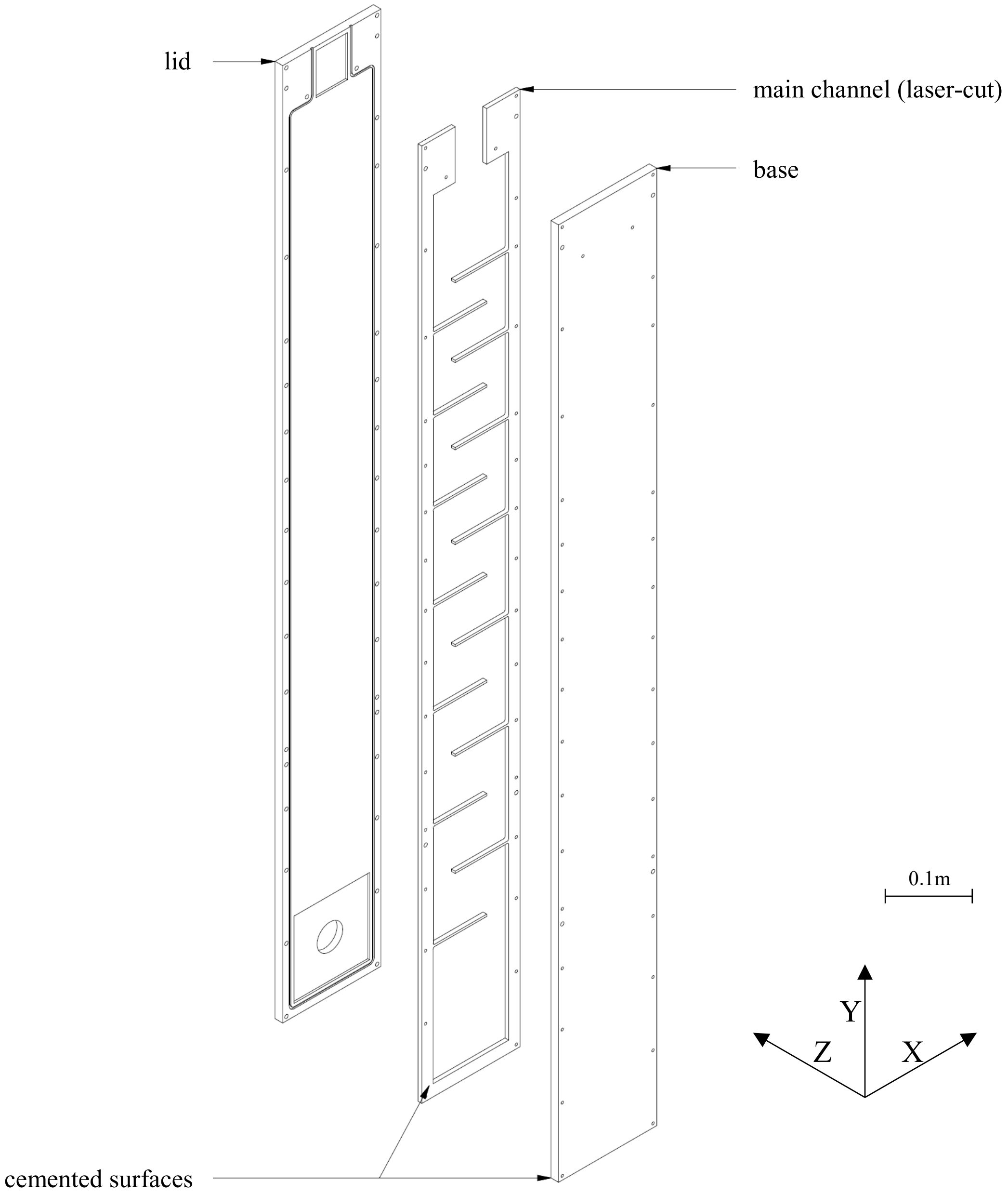

*Figure 32: Exploded isometric of similitude model.*

The similitude model and prototype share dynamic similarity if the magnitude and direction of forces scale between them. This can be tested by comparing velocity profiles between prototype and similitude model. In this work Reynolds model law applies and dynamic similarity is expected when the Reynolds numbers for the prototype and similitude model are equal (Sawhney, 2011, p. 291). Heat exchange affects this result, as discussed previously, by affecting temperature dependent fluid properties. As a result, an isothermal similitude model cannot obey the Reynolds model law if heat exchange is included in the prototype. To circumvent this, a flowrate in the similitude model was chosen by iteration that would minimise the total percentage error between the Reynolds number ($Re_{d\ \mathrm{hydraulic}}$) of the similitude model and the prototype (a CFD model incorporating heat transfer). The result for a flowrate of 0.00156 $m^3/s$ air in the similitude model is given in Figure 33, where ○ represents the similitude model results, × represents the result from section 3.4 above. Unlike the prototype, the similitude model has a constant Reynolds number across the baffle cut ($Re_{d\ hydraulic} = 6084$) because all of the variables in equation 3-2 are constant. The flowrate for the similitude model was therefore set to 0.00156 $m^3/s$ air at ambient pressure and temperature. Two additional flowrates were also included at 66% and 33% of the original flowrate, in both the CFD modelling and the similitude model. As is covered in section 6.1 the reduced flowrates show largely the same temperature profile in the flow. Therefore the reduced flowrates in the PIV study were also scaled proportionally (66%, 33%).

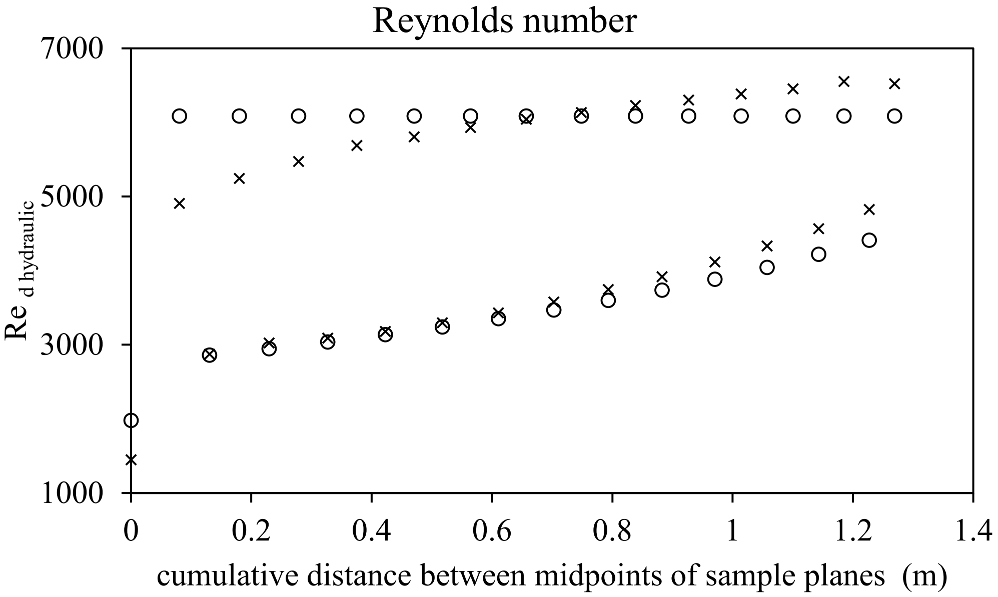

*Figure 33: Reynolds number of similitude model (○) versus prototype (×).*

The purpose of the similitude model in this study is to validate the fluid flow model in the CFD work. Heat transfer does play a role in this system, but it is not expected to dominate the fluid flow behaviour. The system has a low Richardson number, so mixed convection and fluid buoyancy are not expected to be significant. The CFD modelling can easily be repeated under isothermal conditions or at smaller domain size for comparison with the similitude model. This is covered in greater detail in the next chapter.

### 4.2.3 Sizing of particle seeding

Particle concentration is an important factor in the design of PIV experiments. This concentration is important as it controls the particle image density – the number of particles per interrogation area. Increasing the image density increases the valid detection probability. It also reduces measurement uncertainty (Raffel *et al.*, 2000). High concentrations can lead to undesirable effects, such as two-phase flow behaviour. Sources (Keane and Adrian, 1990; Omrane *et al.*, 2008; Cao *et al.*, 2014) recommend a particle concentration of between 10 and 20 particles per interrogation area. The interrogation area size is fixed by the choices in the experiment (field-of-view and the grid spacing used in the PIV). For a field-of-view of 100 x 100mm, the camera pixel resolution (2048 x 2048 pixels), giving a 1.6mm x 1.6 mm interrogation area for an interrogation area of 32 x 32 pixels. This is comparable to case studies given in Raffel *et al.* (2000). The laser light sheet thickness of 1mm requires a particle concentration of 7,800 particles/cm$^3$ to obtain 20 particles per interrogation area.

Typically, particles should not move more than a quarter of the way through the interrogation volume between the two pulses. This is known as the separation distance Δx, and must be between 0.05mm (one pixel) and 0.4mm (¼ of the interrogation area). The laser pulse delay Δt (the 'pair image interval time') is therefore set to give two images within this range. Two methods suggested by Cao *et al.* (2010) are given in Equations 4-1 and 4-2. This required $U_{max}$, which was taken from a CFD simulation of the similitude model ($u_{max}$ = 43.7 m/s, $v_{max}$ = 41.7 m/s) giving a laser pulse delay of Δt = 9.2µs from equation 4-1, and 1.14µs < Δt < 36.6µs from equation 4-2.

$$U_{max}(m/s)\ \Delta t(\mu s) = 250 \qquad 4\text{-}1$$

$$\frac{(size\ in\ image\ of\ 1\ pixel, mm)}{U_{max}} < \Delta t = \frac{\Delta x}{U_{max}} < \frac{d_{intwin}}{U_{max}} \qquad 4\text{-}2$$

In addition to concentration, particles must be the correct size. Two factors affect the selection of an appropriate particle size for seeding. The particles must be small enough to follow the fluid flow. Particles must also be large enough to be visible in the final PIV image. A particle image of at least two pixels is useful because it allows for sub-pixel resolution. By fitting a Gaussian curve to the particle image, the location can be found to ca. ± 0.1 pixels, increasing the accuracy of the PIV result. The particle image diameter $d_t$ can be estimated from the physical particle diameter $d_p$ using equations 4-3 and 4-4. The lateral magnification $M_0$ = 8.85 in the experiment. The diffraction limited spot diameter $d_s$ can be calculated from equation 4-4, in the experiment the lens f-number $f^{\#}$ is 2.8 and the wavelength λ = 0.532 µm for Nd:YAG lasers. The diameter of an aperrated image of a point source, $d_a$ is typically small compared to the other contributions in equation 4-3. A particle image diameter $d_t \approx$ 40µm satisfies the condition above.

$$d_t = \left(M_0^2 d_p^2 + d_s^2 + d_a^2\right)^{0.5} \tag{4-3}$$

$$d_s = 2.44(1 + M_0)f^{\#}\lambda \tag{4-4}$$

The ability for the seeded particles to follow the fluid flow was assessed using a CFD model of the PIV experiment. Particle were modelled using an inert Eulerian-Lagrangian model, in a manner identical to the results described in the next chapter (section 6.2). Particles of $\rho_p = 1000$ kg/m$^3$ were introduced into the CFD model of the PIV experiment, and the simulation was repeated with varying particle diameters. The effect of turbulence on the particle trajectories was modelled using a discrete random walk model. This CFD model indicated that water droplets of 1 to 2μm will give a successful particle tracking. Larger particles cause issues with concentration loss through deposition, as shown in Table 17.

| | particles reaching the outlet | av. dev. from flow vel. | Stokes number |
|---|---|---|---|
| massless | ~96% | - | - |
| 1μm | 90% | 0.379 m/s | 0.01 |
| 2μm | 50% | 0.431 m/s | 0.04 |
| 3μm | 30% | 0.624 m/s | 0.09 |
| 4μm | 0% | 0.707 m/s | 0.16 |

*Table 17: Test CFD Eulerian-Lagrangian model of PIV experiment.*

The average deviation from the flow velocity in Table 17 was calculated based on the difference between the particle velocity and the local fluid flow velocity, averaged over the length of the particle trajectory. The Stokes numbers in Table 17 used a fluid characteristic time $\tau_f = 33$ (m/s) / 0.01 (m). In this case the characteristic velocity is an average of the jet flow velocity, the characteristic length is twice the channel width. For acceptable Stokes numbers in PIV, Cao *et al.* (2014) and Ragni *et al.* (2011) recommend Stk less than 0.1. The particles generated by an ultrasonic humidifier method (section 4.2.1) are typically 1μm diameter. This section therefore demonstrates that the seeding method used in this work was appropriate to the PIV model.

## 4.3 **Conclusions**

This short chapter has covered the methods used for the PIV study. The PIV study provides validation for the fluid flow simulation. The PIV experimental set up has been described, and some of the choices made in this design have been covered. The chapter also briefly covered the data mining approach used to process data from on-site DCM tests of the cryogenic condenser. In the next chapter, the results from the PIV study are compared to fluid simulations in order to establish the accuracy of the latter.

# Chapter 5. Results and Discussion – Fluid flow and Experimental

This chapter covers the results obtained from computational fluid dynamics (CFD) modelling and particle image velocimetry (PIV) experiments and includes discussion of these results. These sections have been arranged in order of increasing complexity. The flow visualisation results introduce the section by describing flows within the condenser. Results from the PIV experiment provide a physical comparison to the CFD modelling. This allows the CFD modelling approaches to be compared to experimental results. The simplifications made in the flow modelling, such as using a symmetry plane to reduce computational load, and using a power-law discretisation for momentum transport, are compared to the PIV results. The model is also compared to different isotropic turbulence models and a time-averaged transient Discrete Eddy Simulation (DES) model result. This establishes that a RANS (Reynolds average Navier-Stokes) modelling approach is more appropriate for the problem than a DES modelling approach. The simulation result is then compared to the PIV in more detail. Results at three flowrates are covered in section 5.2.5, and the flows close to the baffle tip are discussed. Lastly, data mining of on-site data from Aesica Cramlington is considered. This shows that the cryogenic condenser achieves close to saturated vapour at the outlet in normal conditions for dichloromethane (DCM), and shows this performance falls with increased flowrate. The simulations described in the chapter consider fluid flows only: particles, nucleation and growth simulation are covered in chapter 6.

## 5.1 Flow Visualisation

A visualisation of the basic fluid flow, taken from the numerical simulation, is shown in Figure 34 below. The dominant feature in the model is the main jet flow. This travels upwards through the condenser, becoming attached to the undersides of baffles. The jet detaches at the edge of the baffle, and reattaches briefly at the vertical boundary of the model representing the condenser shell, before attaching to the next baffle surface. Secondary flow features in the model occur because of the main jet flow. Large recirculation patterns occupy most of the space between baffles.

Smaller recirculation patterns also form in the corners where the baffle meets the vertical boundary, and at the edge of the baffle. In the latter case, this recirculation pattern is also visible in the experimental results covered in section 5.2.6 (p. 136). These smaller recirculation patterns are illustrated in Figure 35 below.

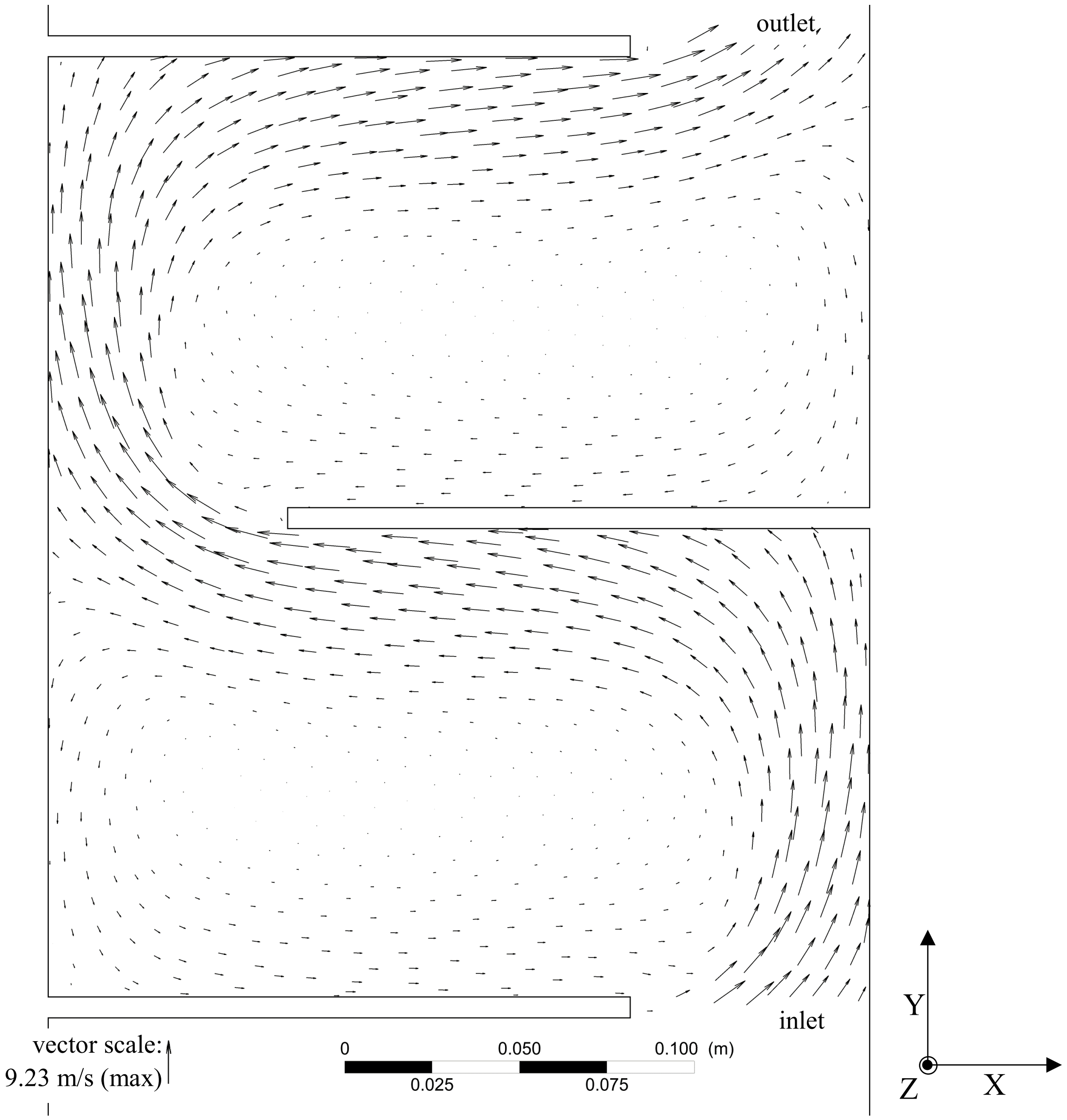

*Figure 34: Flow visualisation.*

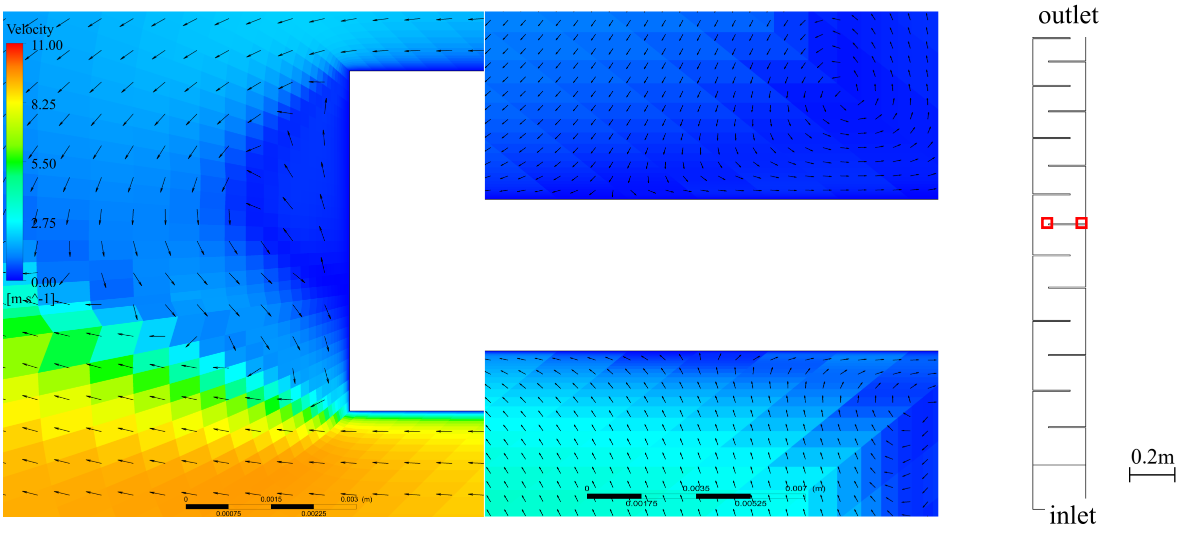

(i) (ii) (iii)

*Figure 35: Small recirculation patterns. (i) baffle tip, (ii) near baffle and wall joint (iii) location of images (around baffle 7). vectors are constant.*

The maximum flow velocity (illustrated in Figure 37 below) also occurs at the point where the main jet detaches from the baffle edge. Son *et al.* (2002) also observed this for a similar flow geometry, both in simulation and experiment. They explain this maximum in flow velocity magnitude at the smallest radius of curving flow as an affect that counter-balances centrifugal force in Euler momentum conservation.

### *5.1.1 Free vortex explanation for maximum velocity at the baffle tip*

In a free vortex flow, the tangential velocity is proportional to the inverse of vortex radius. The curvature of the main jet flow as it leaves the baffle edge can be approximated as a circle. If the x-component of the velocity is sampled on a vertical line, in-line with the point of maximum velocity, the resulting velocity profile is shown in Figure 36 (i). If the same data is plotted using the inverse, the region shown in grey is directly proportional. This region is also the region where the flow maximum occurs in Figure 37. Results in Figures 36 and 37 are taken from the flow simulation described in section 5.2.5 at 90l/min flowrate. This may explain the area of maximum velocity around the baffle tips: it is caused by a free-vortex type flow (constant angular momentum) in this region of the main jet as is curves around the baffle.

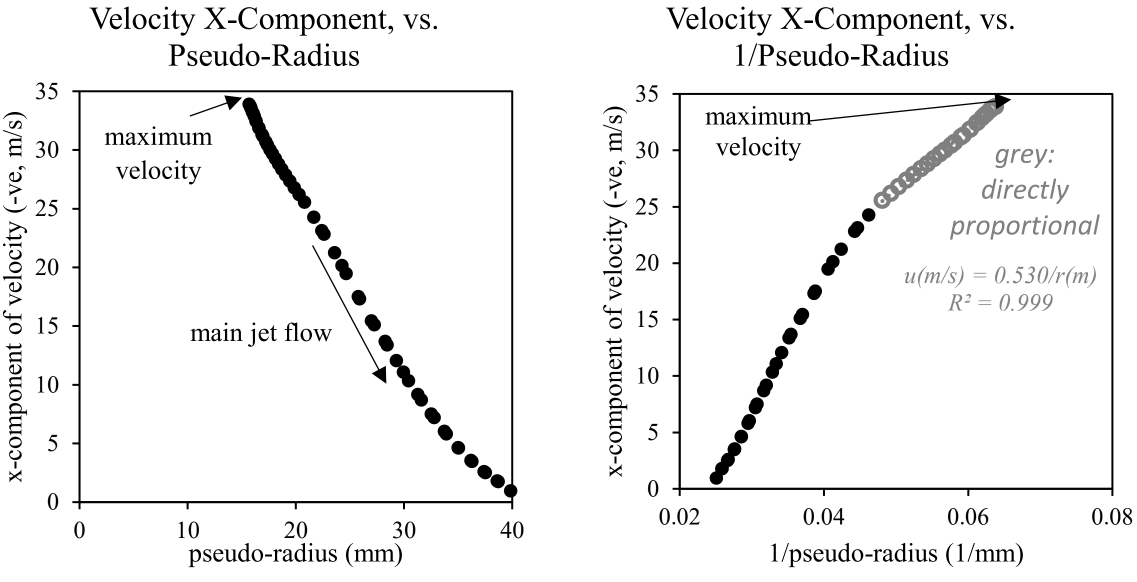

(i) (ii)

*Figure 36: Velocity profiles around the point of maximum velocity, vs. pseudo-radius.*

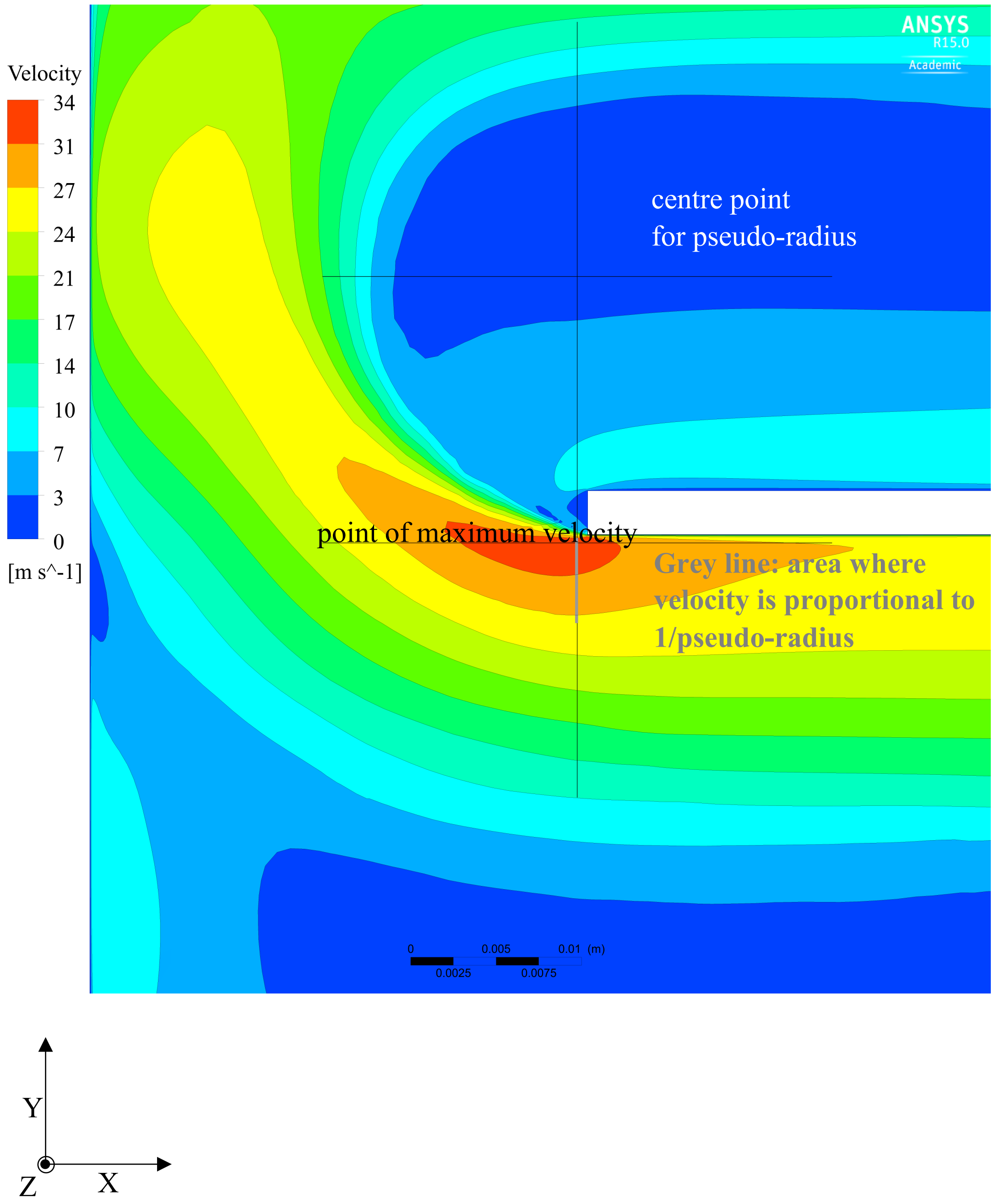

*Figure 37: Illustration of maximum velocity magnitude.*

### *5.1.2 Convergence*

The issue of reaching low residuals with a second order momentum discretisation was explored extensively. This revealed that the problem was:

1. Not due to buoyancy. Convergence was not improved with isothermal conditions or without gravity.
2. Not due to so-called “stuck residuals” from the gradient limiter. Changing the gradient limiter did not affect the result.
3. Not due to under-relaxation factor choice. This was explored through a design-of-experiment that examined the sensitivity of the convergence to changing under-relation factors inside recommended limits. However, these changes did not affect the result.
4. Not due to inherently transient flow. Transient flow simulations did not show characteristic periodic behaviour, as would be expected if the flow was inherently transient.
5. Not due to insufficient mesh refinement. Mesh refinements over both the full domain and localised around baffle tips did not improve the simulation result.
6. Not due to a requirement for increased solution order. Increasing the discretisation order (through MUSCL (monotonic upwind scheme for conservation laws) or QUICK (quadratic upstream interpolation for convective kinematics discretisation)) for individual transport variables did not improve the simulation.
7. Not due to improper initialisation. Initialising with a fully converged 1st order simulation (the best-case scenario) did not affect the simulation.

The issue could be related to resolving the jet. The k-ε model solves below $1\text{x}10^{-4}$ residuals, even when fully 2nd order. The 1st order, power law momentum and first-to-higher-order-blended discretisations solve with the SST (shear stress transport) type models. Both the k-ε model and the other discretisation schemes are more diffusive for jet flows, this would have a stabilising effect on the simulation.

In this work, the fluid flow simulations were solved to below $1\text{x}10^{-4}$ residuals with second order transport variables (unless otherwise stated explicitly). This is in-keeping with publishing standards for CFD simulation (Zigh and Solis, 2013, p. 25; Kuron, 2015). The flow simulation for the full-scale geometry did not reach this convergence with second-order momentum discretisation. However, this did solve with power-law momentum discretisation. The power-law discretisation is a compromise: it is not considered second order accurate (ASME, 2015). However, as is shown in section 5.2.2, power-law momentum discretisation provides a more accurate result, more in-keeping with the experimental results from PIV.

## 5.2 PIV Results

The PIV results were obtained at six locations in the similitude model. Figure 38 shows the locations of sampled images from the point-of-view of the camera in setup, the laser light-sheet enters from above. Flow around baffles 2 and 3 (baffles are numbered in order from the inlet to the outlet by convention for this thesis) could not be sampled easily as the supporting structure obscured the line of sight.

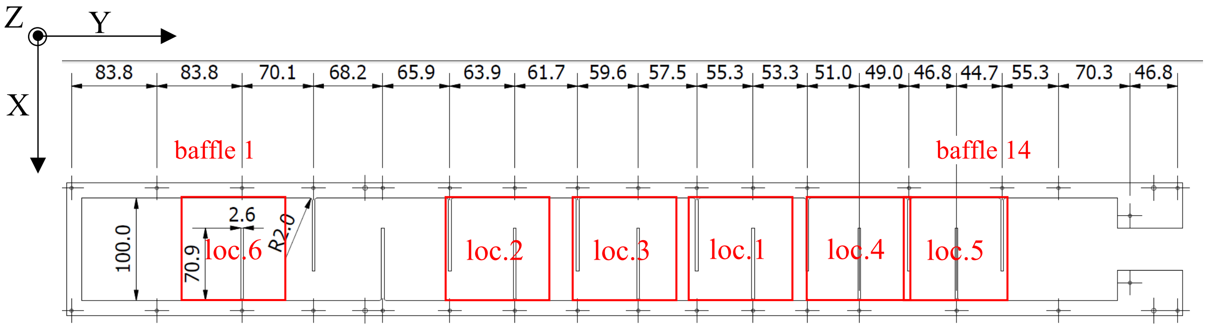

*Figure 38: Locations of sampled images.*

The vector field from each PIV result was averaged over 100 image pairs to account for the turbulent fluctuations. Composite images of the results are given in Figure 39 and Figure 40 for two experimental repeats at three flowrates. The deep blue areas on the right of these images are due to a combination of surface glare and seeding water droplets colliding with and forming condensation on the walls in this area, giving a false zero velocity in these areas. In the latter case, the location of this condensation is similar to the particle simulation results covered in section 6.2.6 (p. 155). Generally, the second experimental repeat results were an improvement and have been favoured for the comparisons with the simulation results that follow. Measurements around the baffle cuts shown in Figure 45, Figure 48 and Figure 55 below are much slower than the simulation, particularly around baffle 9. A combination of factors made obtaining results at the baffle cut especially difficult, issues with obtaining good PIV results are explored below.

There were some issues with the PIV results. The right-hand side of the image was typically subject to glare from the laser reflecting off of the opposite wall. Extremes of the images were often unreliable. Damaged pixels inside the camera (including a row of damaged pixels), the quality of the laser light sheet, and the shadows cast by the baffle edges contributed to this. Contamination of the window surface occurred with dust, (and fibres left behind from drying the model), which was attracted to the walls through static charge. Using anti-static wipes helped this. Cleaning could occasionally create tiny scratches in the acrylic and the PIV results were sensitive to these scratches. Seeding involved a compromise between getting enough droplets into the domain to obtain a good quality result whilst avoiding condensation forming on the walls obscuring the image. To get round this the seeder was turned on only when results were being obtained. A short (roughly 10 sec) delay between activating the seeder and activating the camera to obtain results allowed the domain to fill with particles. The seeder was turned off as soon as the images were obtained. If the room temperature was too high, there would not be enough particles in the domain to obtain a result, due to their evaporation. A makeshift bubbler was included on the air inlet inside the seeding chamber to help alleviate this. Another problem with the seeding was that droplets would leave a residue when dry, causing dirt on the window. This was thought to be due to hard water, and using deionised (DI) water exclusively improved this, but did not eliminate it – the water usually needed changed every 2-3 days.  The lasers on occasion could be unreliable, with one of the pair firing much weaker than the other. This affected results because the more similar each image in each pair is, the better the quality of the PIV result obtained – if one image is not properly illuminated, then a result is not obtained. The lasers usually warmed up with use giving better results in the afternoons.

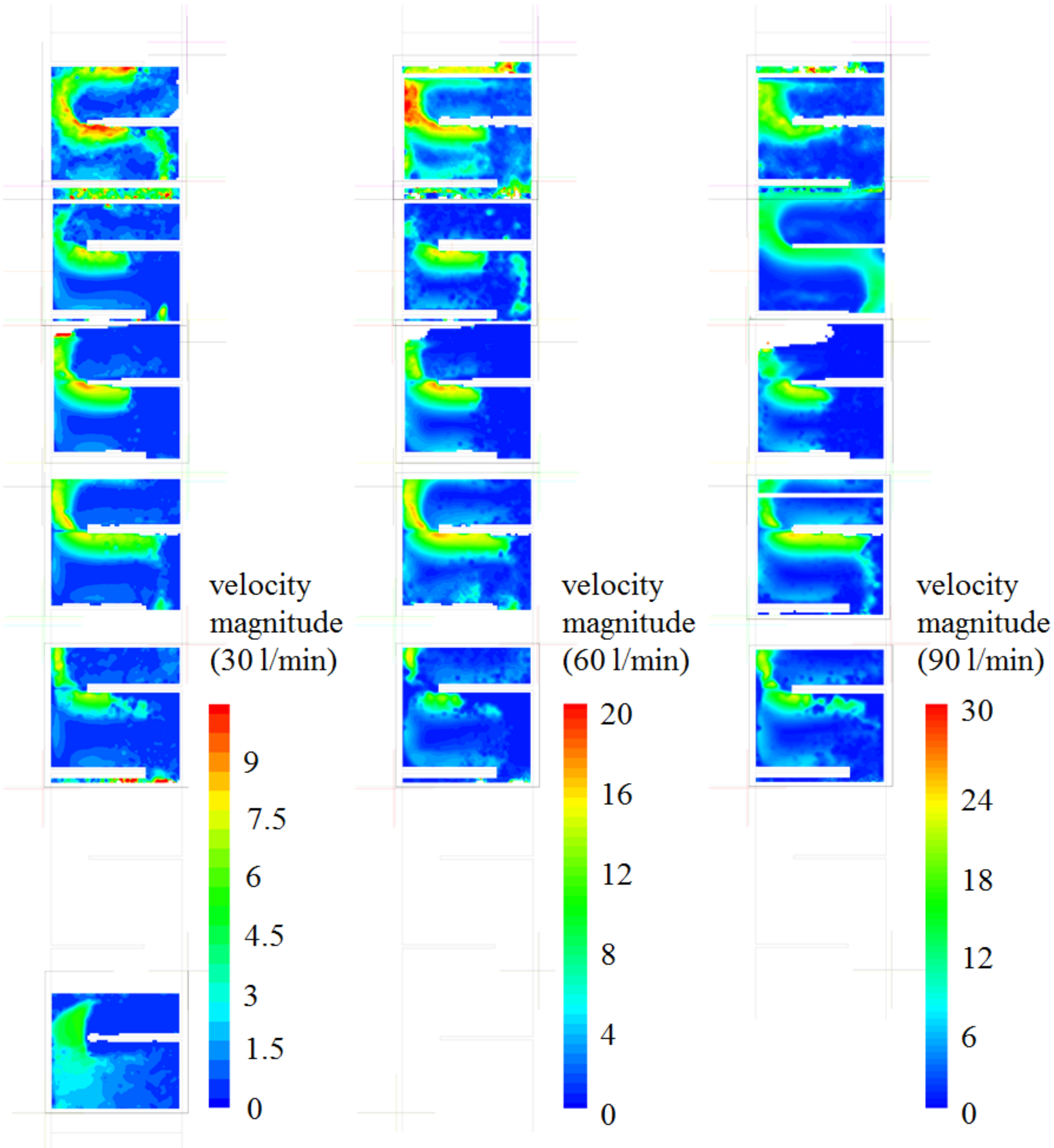

(i) (ii) (iii)

*Figure 39: First experimental repeat. (i) at 30l/min flowrate, (ii) at 60l/min flowrate, (iii) at 90l/min flowrate.*

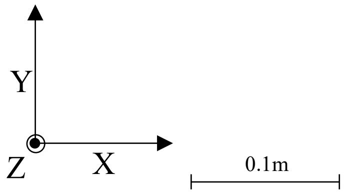

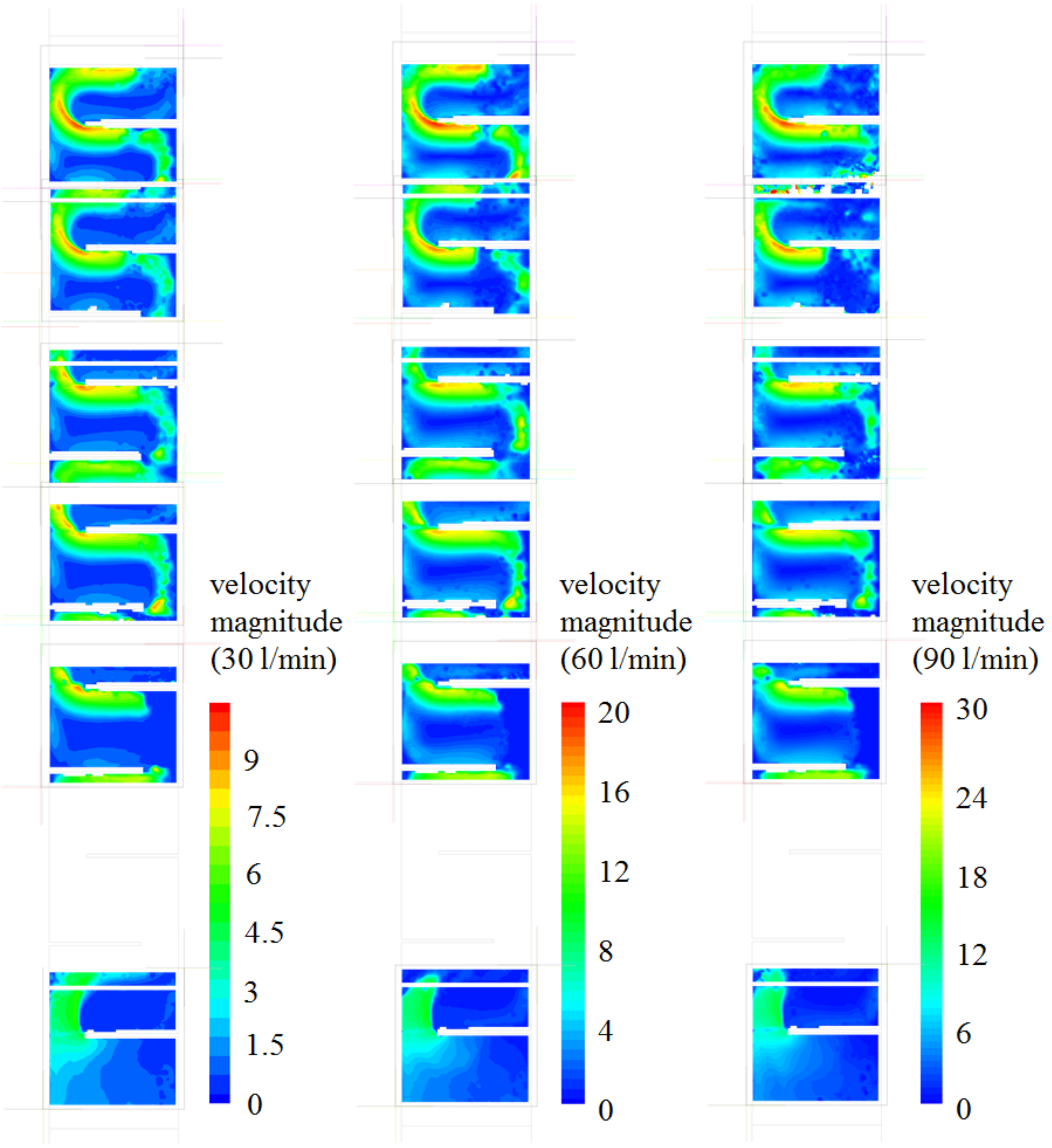

(i) (ii) (iii)

*Figure 40: Second experimental repeat. (i) at 30l/min flowrate, (ii) at 60l/min flowrate, (iii) at 90l/min flowrate.*

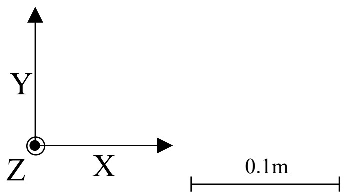

Sampling locations for comparison between the PIV and CFD results are shown in Figure 41 below. The boltholes in the model obscured PIV results on some baffle cuts: in these cases ((viii),(ix),(x),(xi) in Figure 41), the sample plane has been moved upwards 1cm so that it intersects an illuminated part of the main jet flow.

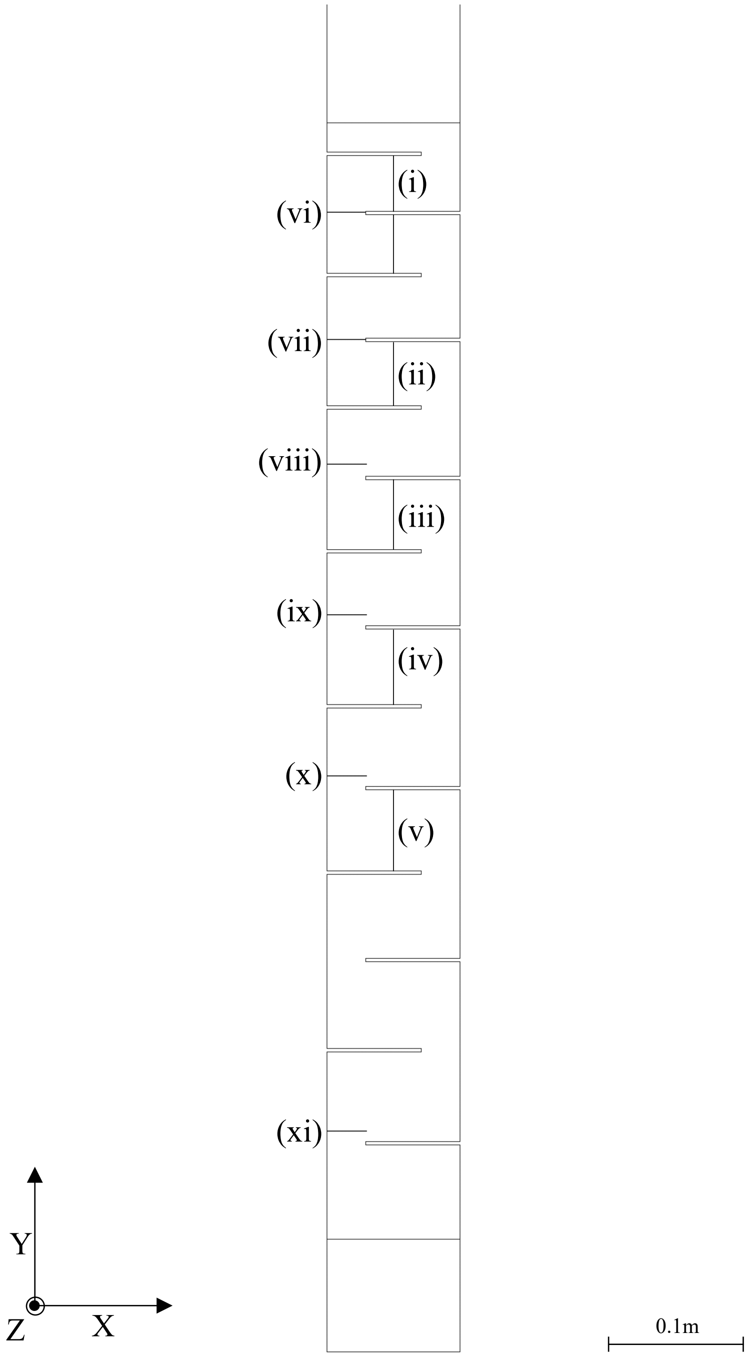

*Figure 41: Locations of profiles for PIV-CFD comparisons. Midway between: (i) baffles 12 and 14; (ii) baffles 10 and 11 (iii) baffles 8 and 9 (iv) baffles 6 and 7 (v) baffles 4 and 5. Across: (vi) baffle cut 13; (vii) baffle cut 11; (viii) baffle cut 9; (ix) baffle cut 7; (x) baffle cut 5; (xi) baffle cut 1.*

### *5.2.1 Comparing models with and without symmetry plane.*

The model symmetry plane needs to be justified as a potential source of deviation from the physical flow pattern. The symmetry plane improves the simulation by halving the mesh size and stabilising convergence. However, the symmetry plane is a simplification that assumes there is no net flow across the plane defined as a symmetric boundary (in this case, no flow in the Z-direction for a centreline plane in the XY direction).

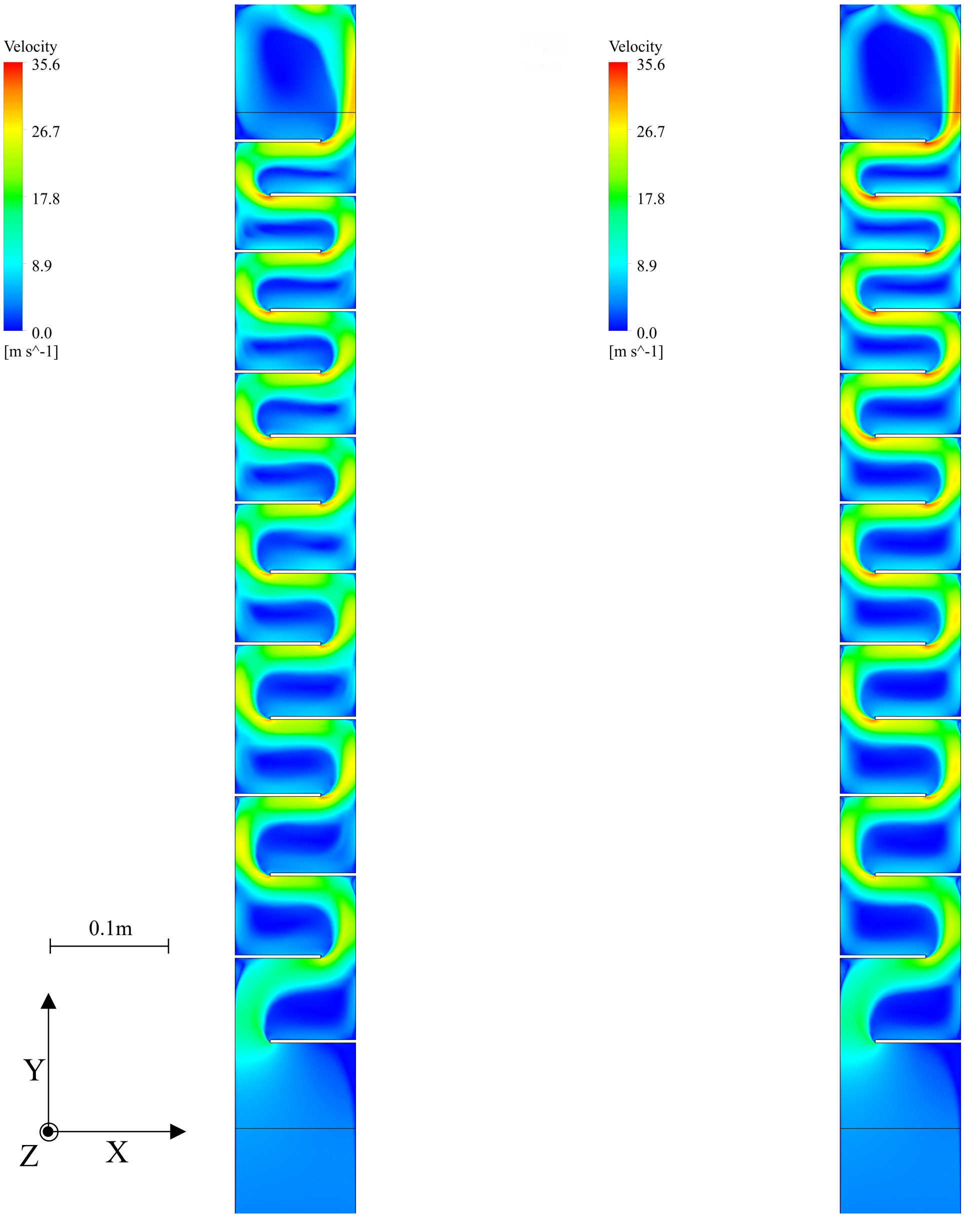

(i) (ii)

*Figure 42: Velocity contours on centre plane (i) non symmetrical (ii) symmetrical.*

For this comparison, the non-symmetric model was solved to $1\text{x}10^{-3}$ residuals, while the symmetric model was solved to $1\text{x}10^{-4}$ residuals. Both cases used a low-Re SST turbulence model with power law momentum discretisation on a similitude-scale CFD model at 90 l/min flowrate. Velocity contours at the centreline are shown in Figure 42 for (i) non-symmetrical and (ii) symmetrical cases.

There is a net z-component velocity that is ignored by the symmetrical model, shown in Figure 43 below. The secondary flow in the z-direction is caused by the jet impact onto the solid walls. However ignoring this z-component does not appear to have affected the simulation results significantly. Figure 44 compares the results to experimental data. The non-symmetric model seems to match the data better in the recirculation regions (positive velocities in Figure 44), but deviates from the relatively simple velocity profile shown in the experiment. The symmetric model over predicts the maximum velocity but has the same characteristic shape as the experiment. Figures 43 and 44 indicate that the simplification imposed by using the symmetry plane does not adversely affect the simulation accuracy compared to physical data.

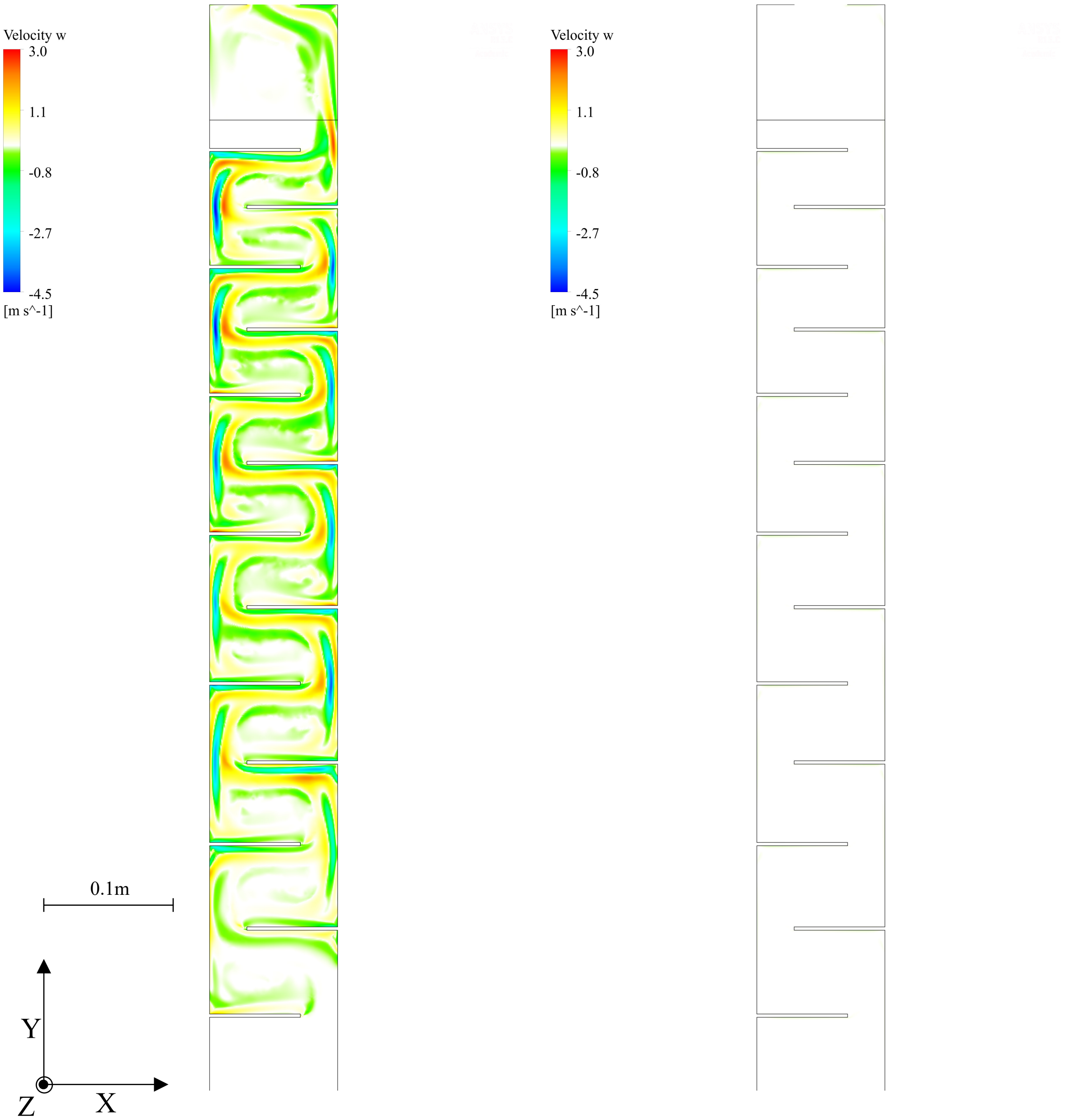

(i) (ii)

*Figure 43: Z-component (w) velocity contours on centre plane. (i) Non-symmetrical (ii) symmetrical.*

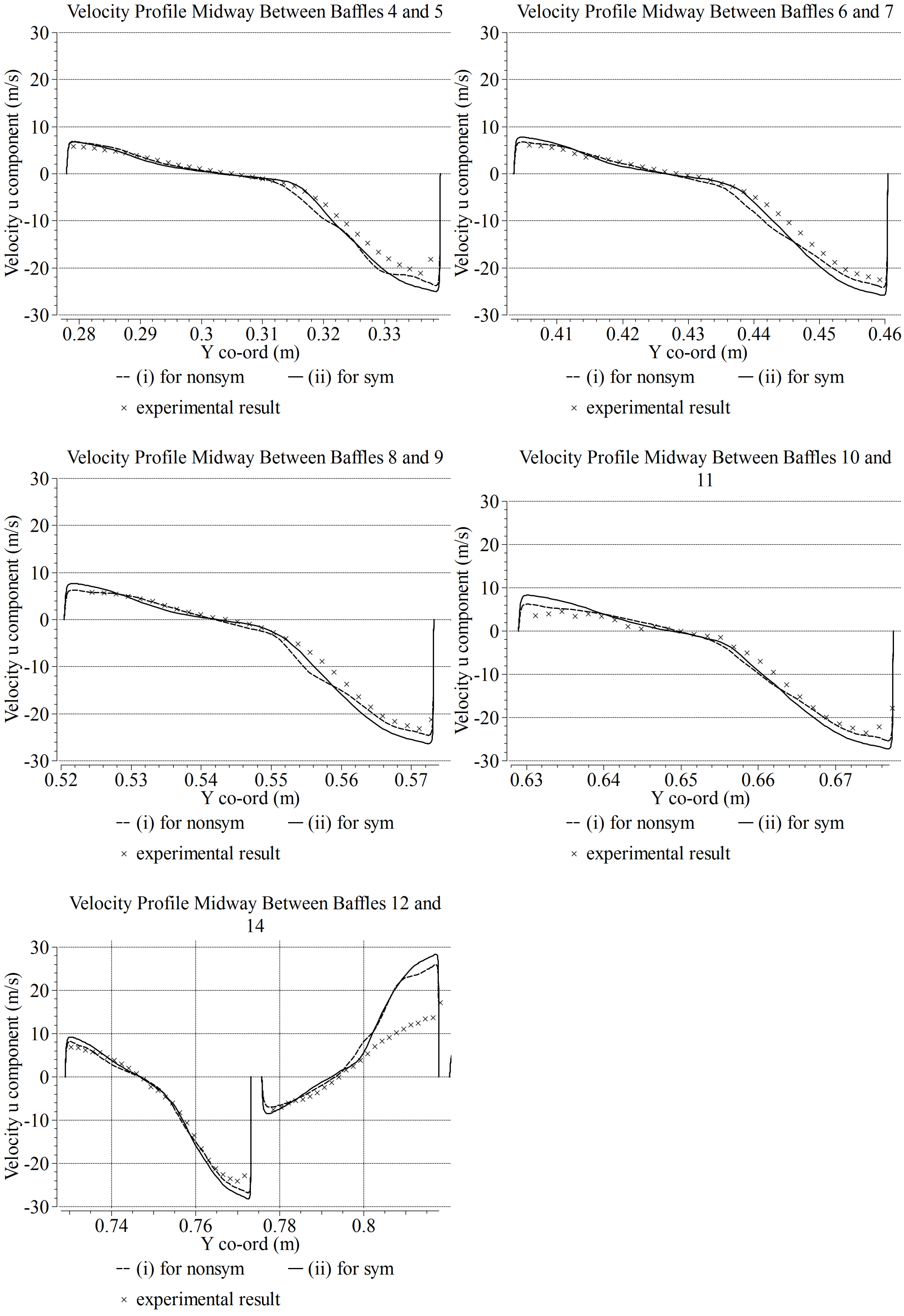

*Figure 44: Velocity profiles midway between baffles. Non-symmetrical vs. symmetrical comparison.*

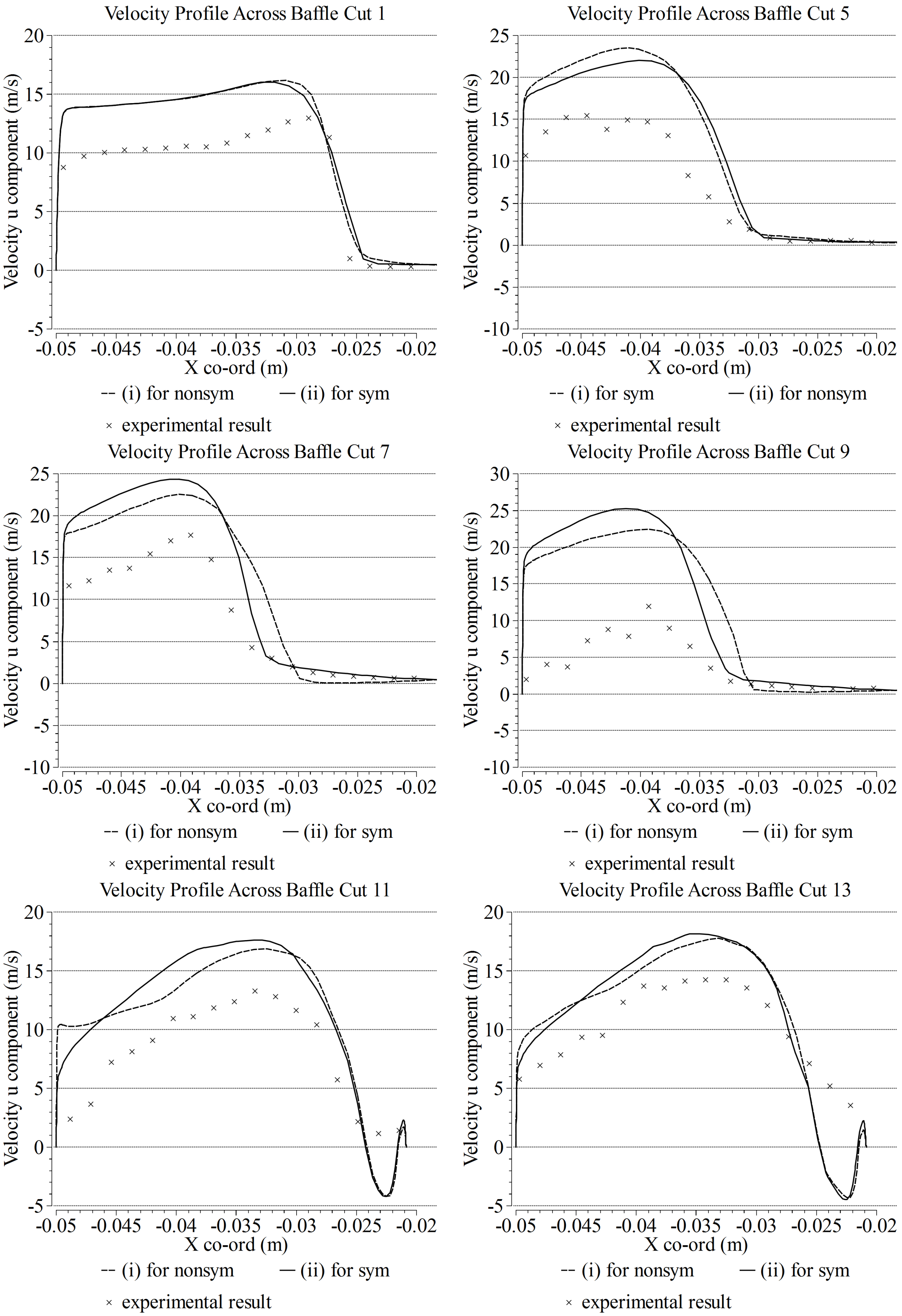

*Figure 45: Velocity profiles across baffle cuts. Non-symmetrical vs. symmetrical comparison.*

### *5.2.2 Comparing fully 2nd order momentum with power-law momentum solution.*

A fully second order solution is desirable as this is the benchmark for publishable-quality CFD. However, convergence was difficult to achieve with fully second order simulation, so a power-law momentum discretisation was used as a compromise. This converges much more easily, but is less numerically accurate.

For this comparison, the symmetric result from the previous subsection was compared to a fully second order solution on a symmetric mesh. Velocity contour plots given below in Figure 46 demonstrate that the main jet flow for the fully second order simulation is faster and is less spread-out than for the power-law momentum case. However comparison with experimental data in Figure 47 demonstrates that this doesn't conform to reality. The power-law momentum discretisation shows better agreement with the experimental results.

Figure 48 shows the results for velocity profiles across the baffle cuts. Both discretisation schemes predict a faster jet in this area than is obtained in the experiment. However, the power-law momentum discretisation again shows a better comparison with the overall shape of the velocity profile. The experimental flows were slower than the simulated flow, in every case. This could be due at least in part to experimental errors, such as uncontrolled gas temperature, upstream leakages and tolerances for the dimensions of the channel. Differences between experiment and simulation are more pronounced for results across baffle cuts. This area was subject to greater deposition of contaminants, for reasons explored in the next chapter (section 6.2.6). The PIV image quality (Figure 39 and Figure 40) contributed particularly around baffle 9. This image quality is subject to the effect of the nearby bolt holes on the laser light sheet and the damaged pixel line in the camera.

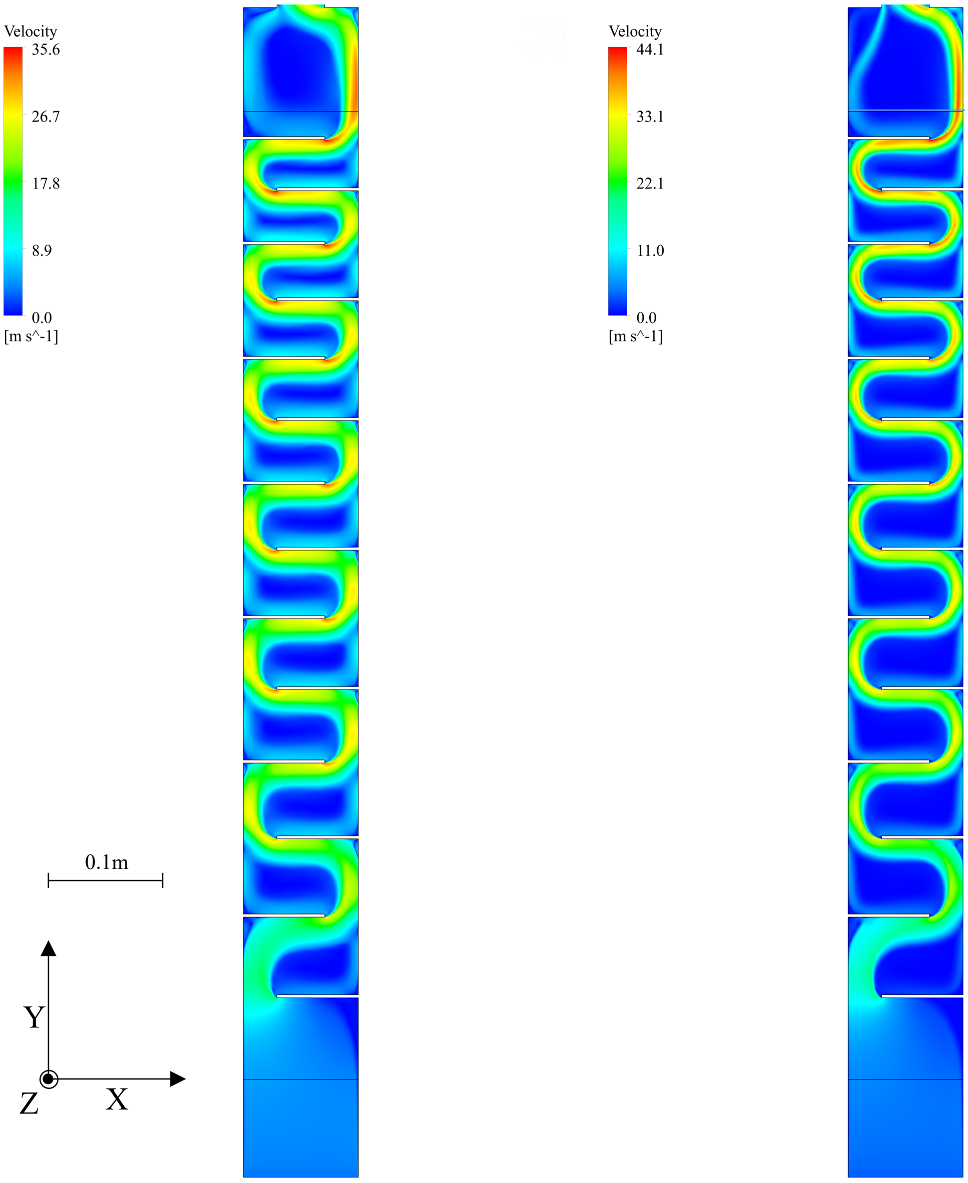

(i) (ii)

*Figure 46: Velocity contours on centre plane. (i) power-law momentum (ii) fully second order.*

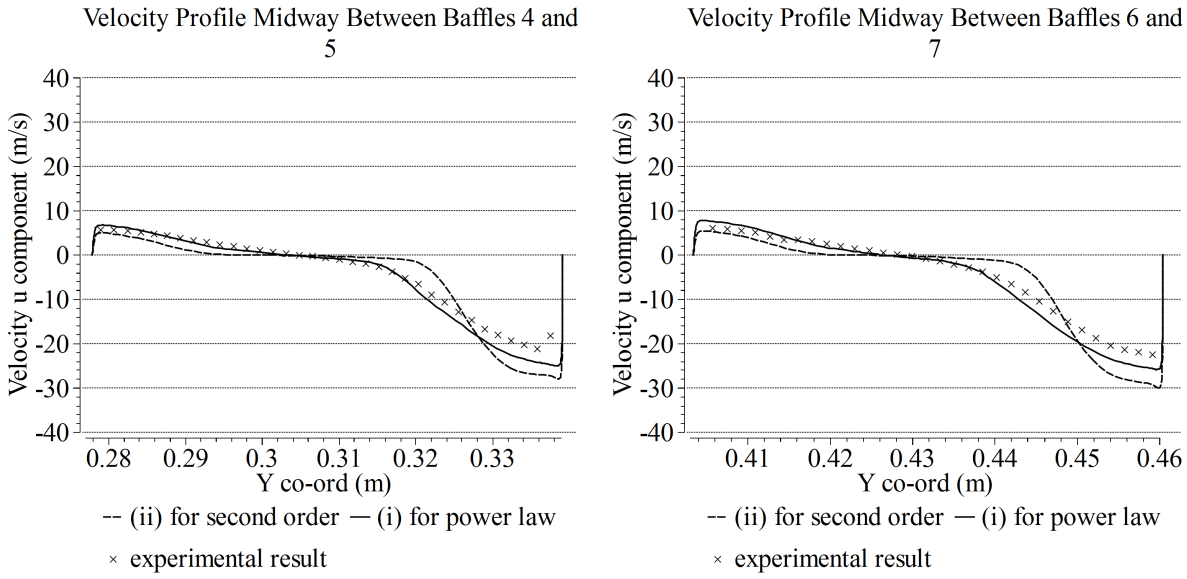

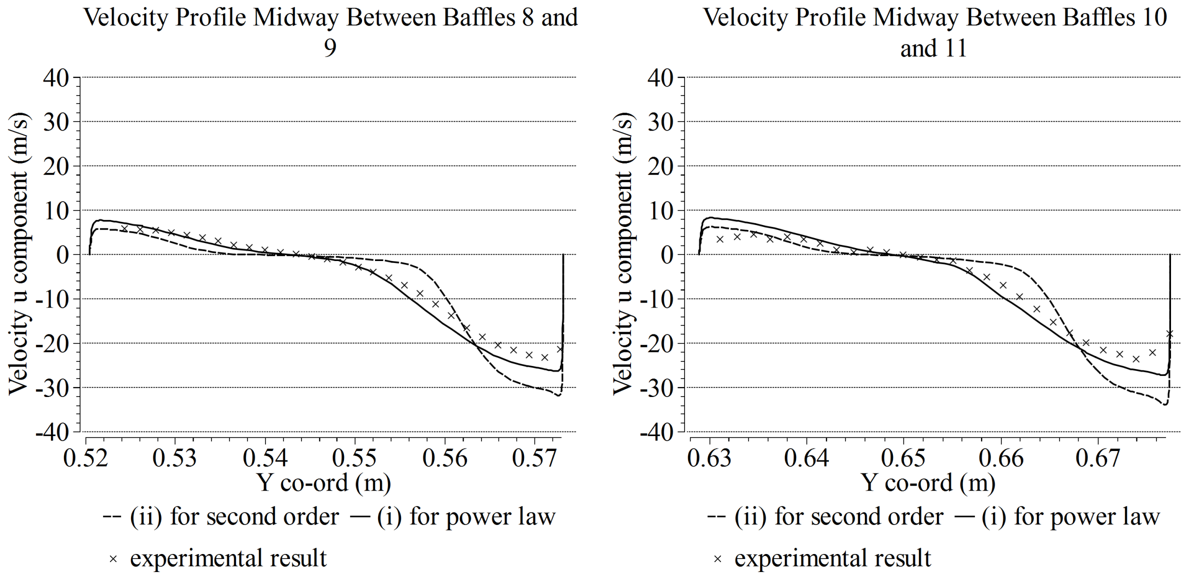

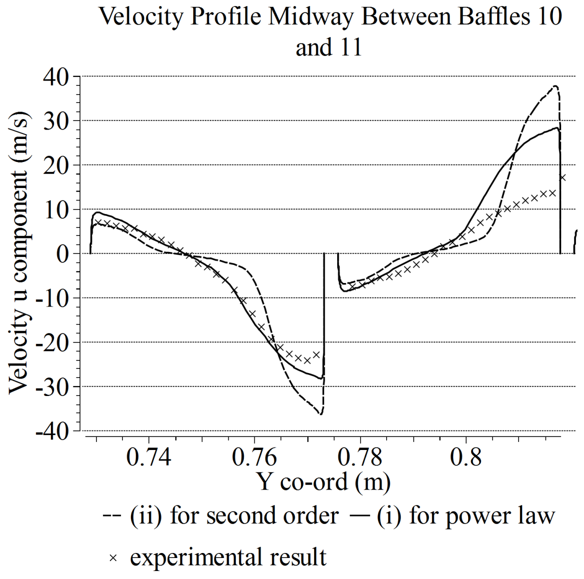

*Figure 47: Velocity profiles midway between baffles. Power-law momentum versus fully second order solution comparison.*

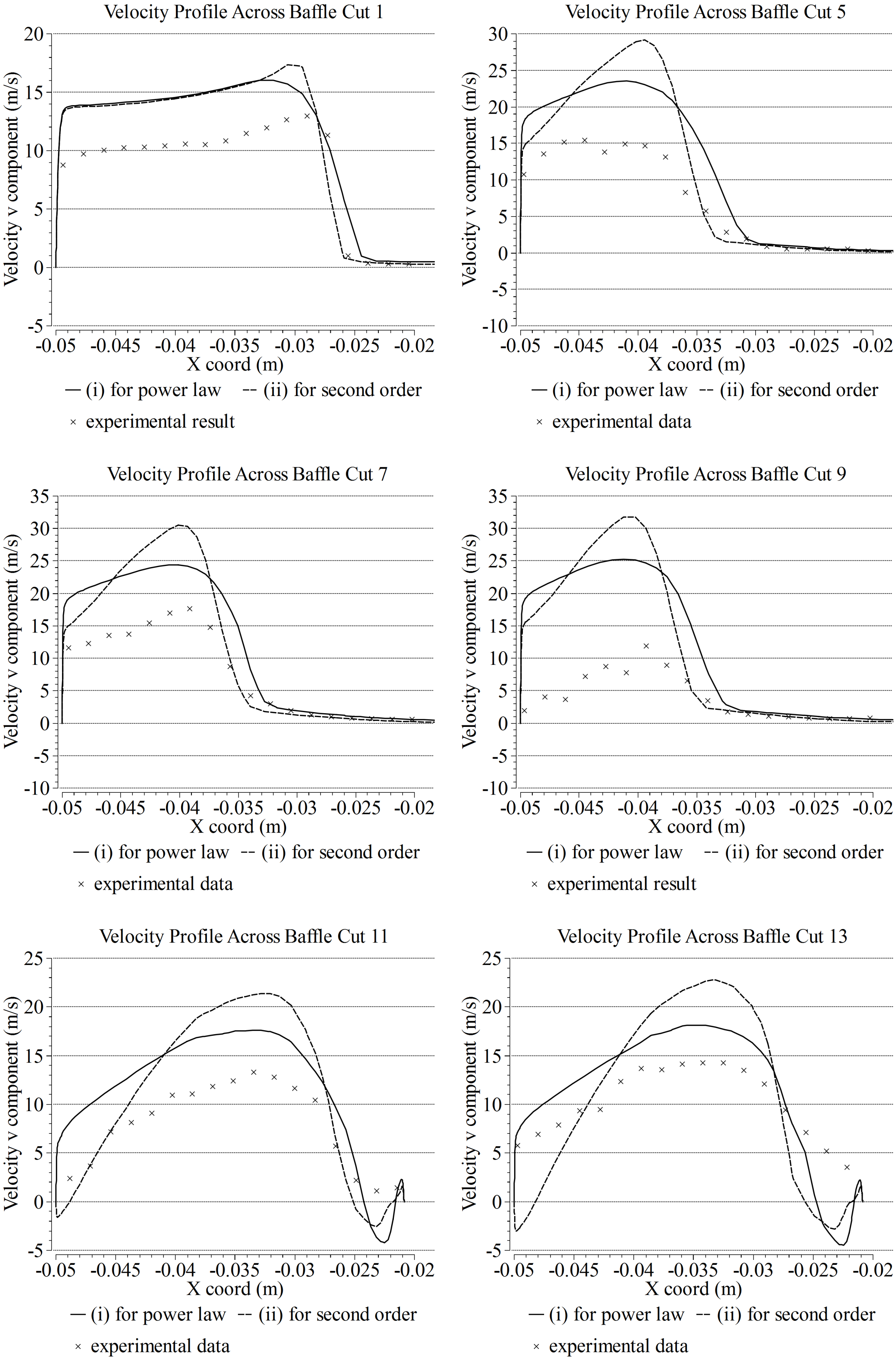

*Figure 48: Velocity profiles across baffle cuts. Power-law momentum versus fully second order solution comparison.*

### *5.2.3 Comparison of turbulence models*

For this comparison, the following simulation cases were investigated:

(i) "Low-Re" k-ε model. Standard k-ε model with boundary layer resolution. This used the 'enhanced-wall function' which, for meshes with appropriate near wall refinements as is the case here, resolves the boundary layer instead of using a wall function.

(ii) Standard k-ε model. Standard k-ε model with standard wall function. This used the 'scalable wall function' which allows the standard k-ε model with standard wall function to be applied even when the mesh is refined ($y^+ < 30$) as is the case here.

(iii) Spalart-Allmaras model. One equation turbulence model that also resolves the boundary layer for refined meshes.

(iv) Low-Re SST model. As explained previously. A two-equation k-ω model that resolves the boundary layer when the mesh is refined as is the case here.

The images below in Figure 49 show the differences between the fluid flow simulations are relatively minor. The velocity profiles in Figure 50 show that while all of the models give a good comparison to the experiment, the Low-Re SST model gives the best fit to the experimental data. This result supports the choice of Low-Re SST model for use in the thesis.

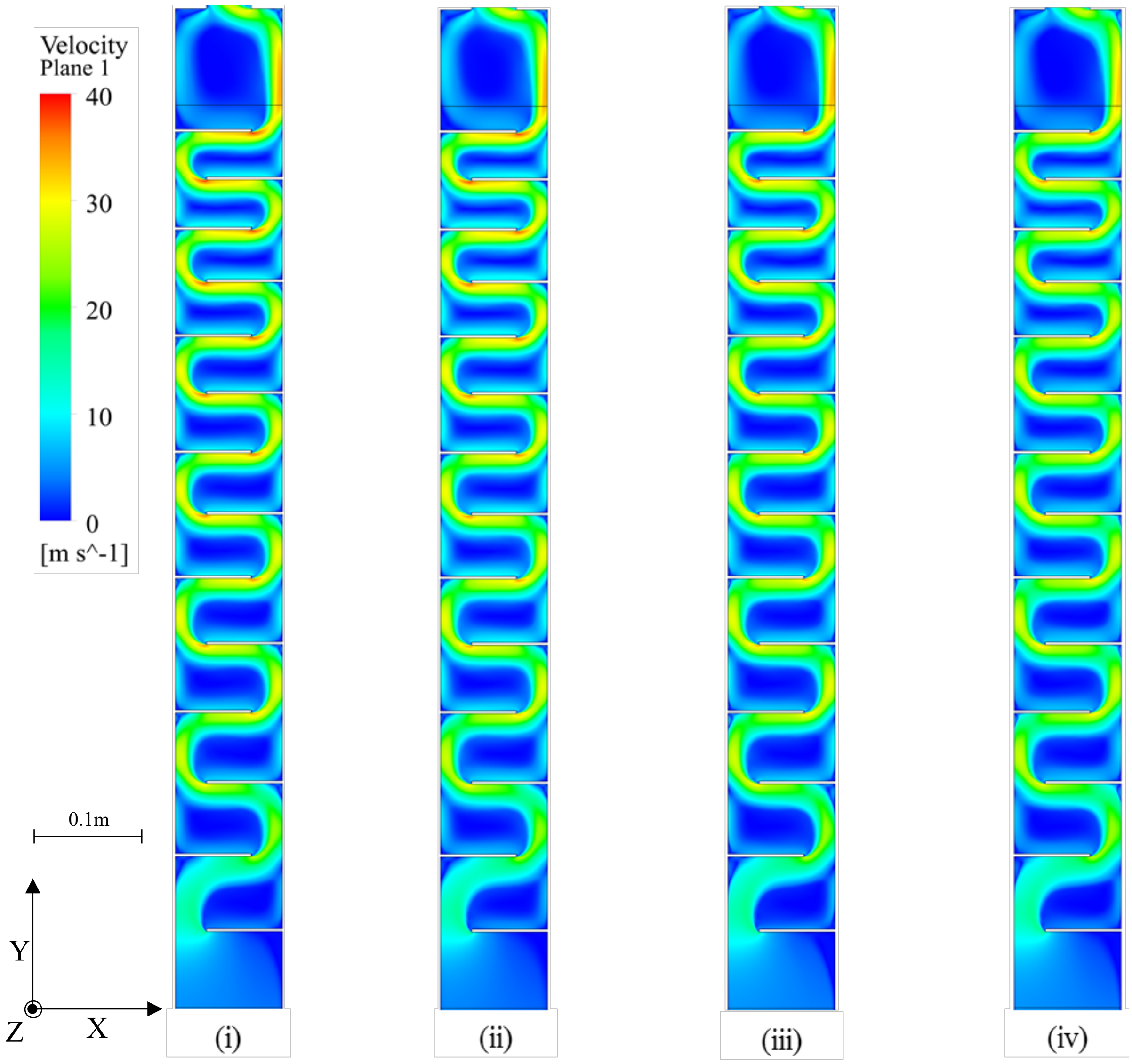

*Figure 49: Velocity contours on centre plane. (i) "low-Re" k-ε model (ii) standard k-ε model (iii) Spalart-Allmaras model (iv) Low-Re SST model.*

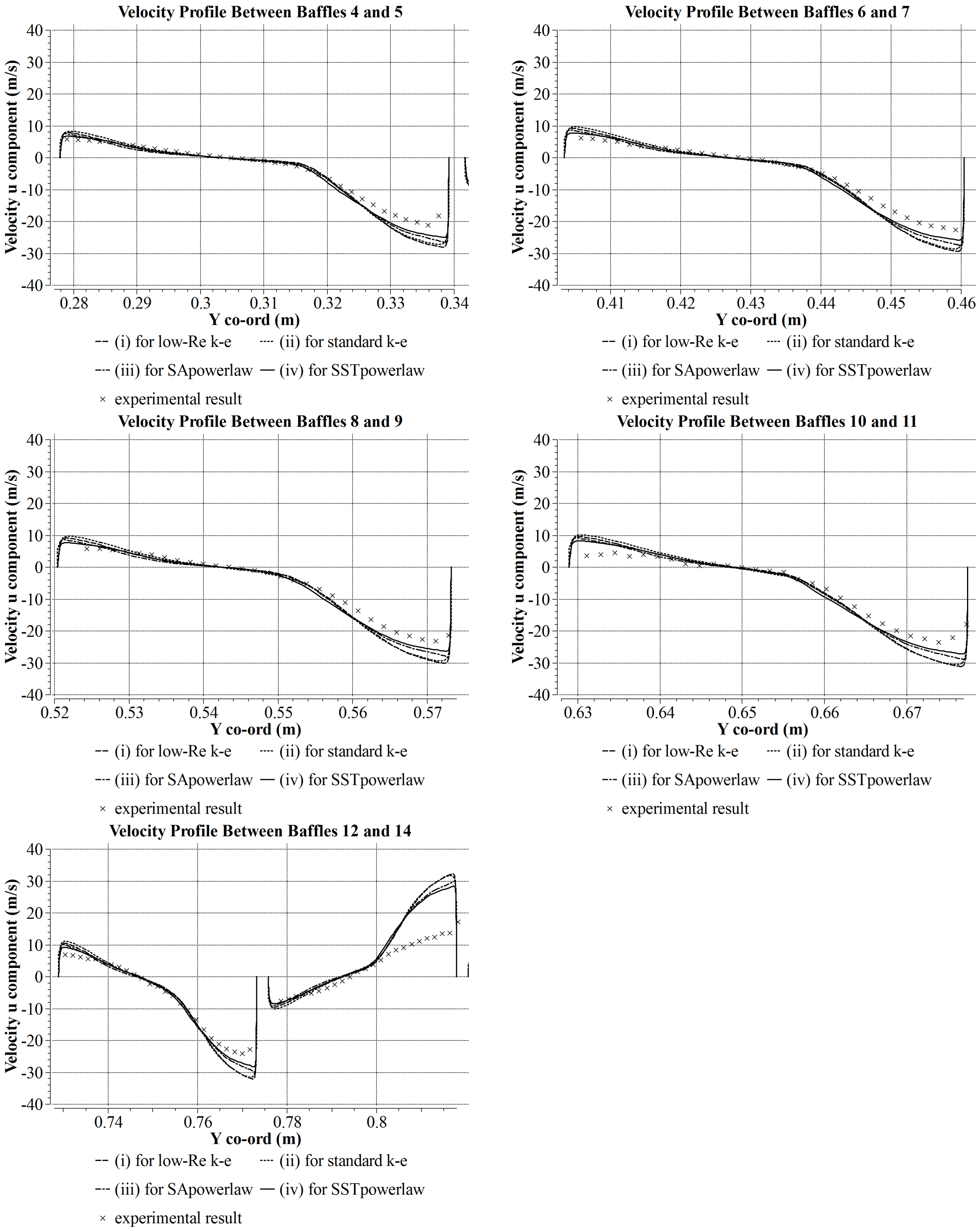
Velocity Profile Between Baffles 4 and 5

Velocity Profile Between Baffles 6 and 7

Velocity Profile Between Baffles 8 and 9

Velocity Profile Between Baffles 10 and 11

Velocity Profile Between Baffles 12 and 14

*Figure 50: Velocity profiles, comparison for different turbulence models.*

### 5.2.4 Comparison with Detached Eddy Simulation result

For this comparison, the previous result (SST model, power law, symmetric mesh) was compared to a detached eddy simulation (DES) result. The detached eddy simulation is a different approach to the isotropic RANS (Reynolds averaged Navier-Stokes) models described earlier. For the DES approach the simulation is transient (unsteady), not steady state. Large eddies in the bulk flow are simulated in transient flow while small eddies and near-wall behaviour are simulated using RANS turbulence models.

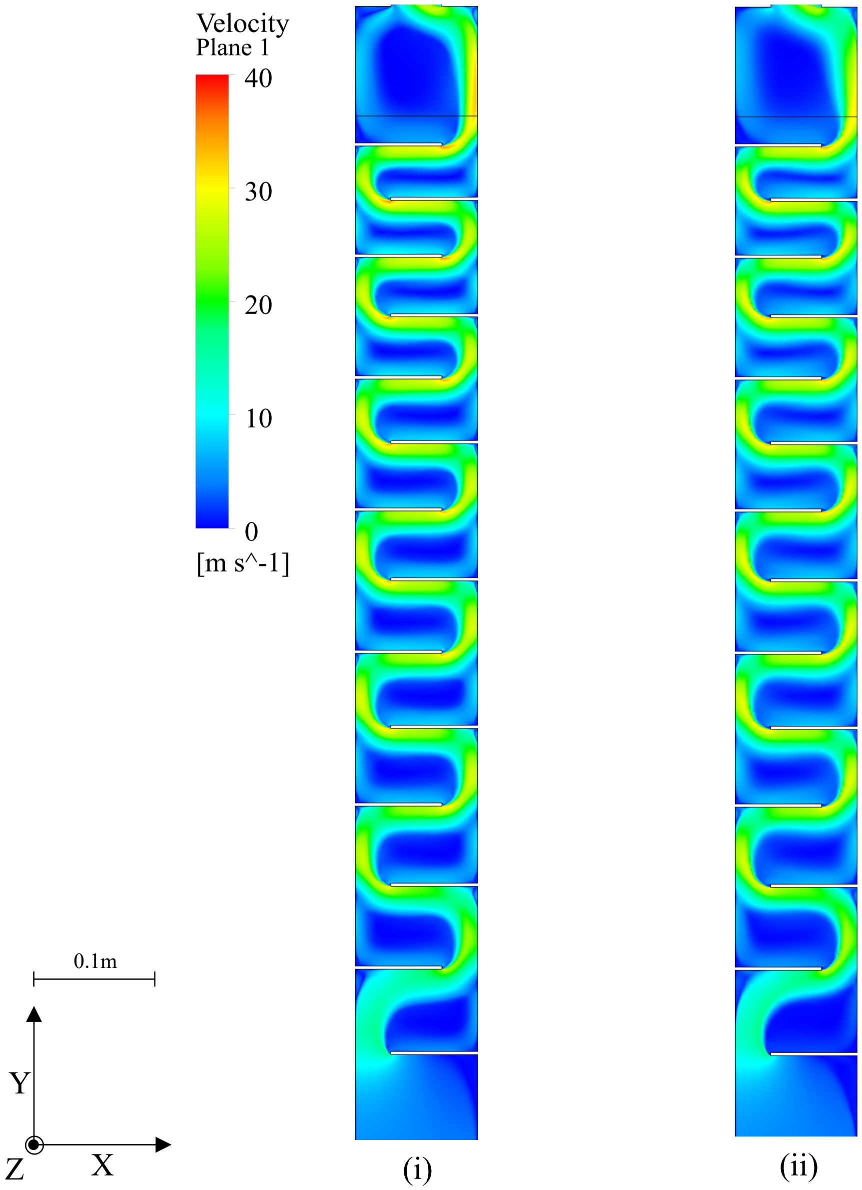

*Figure 51: Velocity contour comparison (i) SST models, (ii) unsteady DES model.*

The results below are shown for a 0.1s time-averaged result: this is roughly equal to the duration of sampling during the PIV experiment. The results in Figures 51 and 52 below indicate that despite the much higher computational load of the DES simulation, the accuracy of the results compared to experiments are similar. Using the DES does not improve the result significantly. This provides evidence that a steady state, isotropic RANS modelling approach is appropriate for this work.

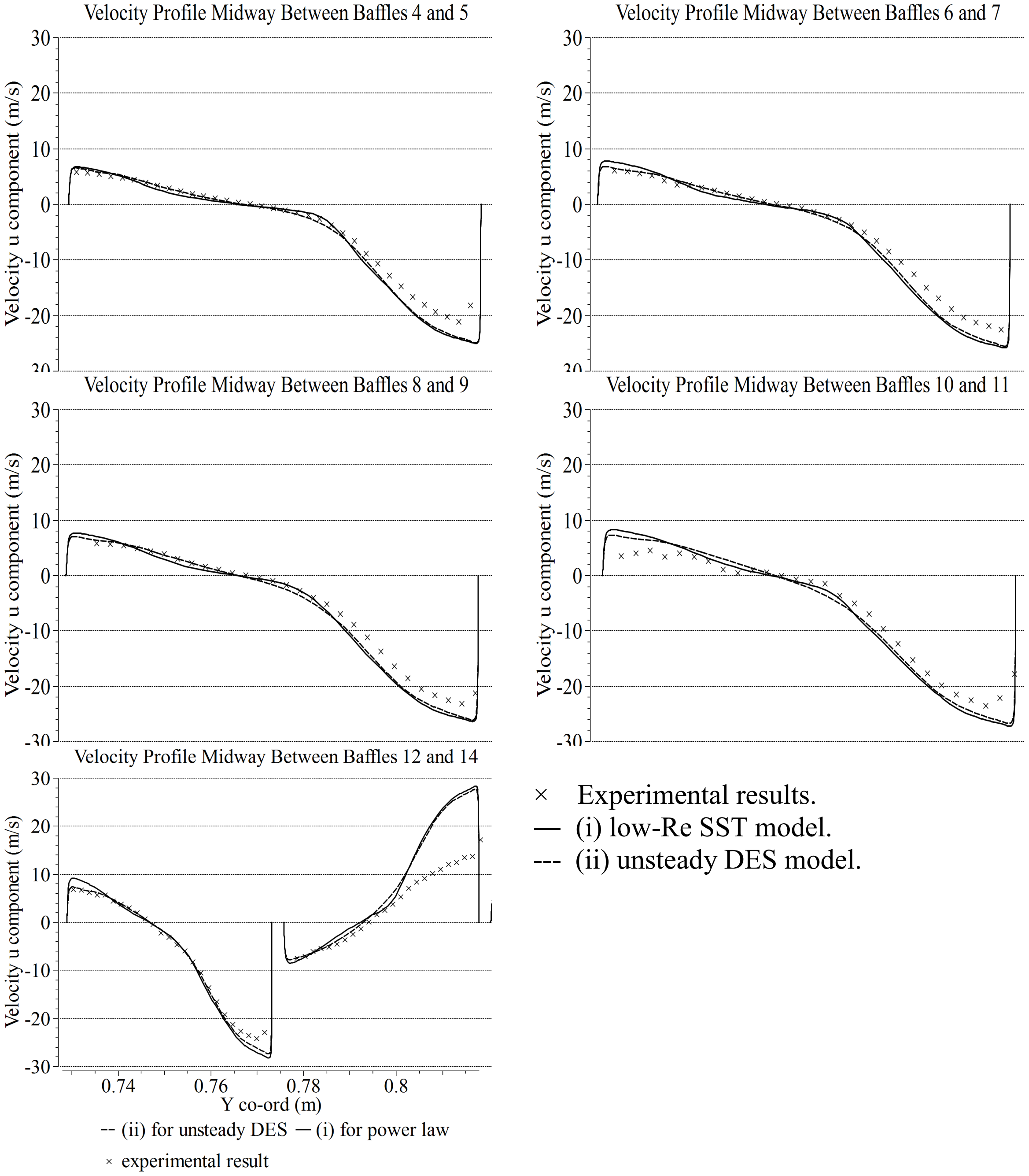

*Figure 52: Velocity profiles, comparison for unsteady DES.*

### *5.2.5 Comparison of simulation and PIV results*

The above comparisons have established the Low-Re SST model with power-law momentum discretisation on a symmetric mesh as an appropriate CFD model for the fluid flow. In this section, this will be compared with the PIV result taken at different flowrates. This comparison uses the following simulation results:

(i) 30 l/min transition SST model, symmetric mesh, power law momentum discretisation. Solved to below $1x10^{-4}$ residuals.

(ii) 60 l/min low-Re SST model, symmetric mesh, power law momentum discretisation. Solved to below $1x10^{-4}$ residuals.

(iii) 90 l/min low-Re SST model, symmetric mesh, power law momentum discretisation. Solved to below $1x10^{-4}$ residuals.

Velocity contour plots are shown in Figure 53. These have been limited to 0.5m/s increments and 0 to 10m/s (30l/min), 20m/s (60l/min) or 30m/s (90l/min) to compare with the composite images for the PIV above (Figure 40).

Velocity profiles midway between baffles are given in Figure 54. Overall these show good comparison between the simulations and experiment. Behaviour near the inlet and outlet shows the biggest discrepancy; this is to be expected as the conditions in the experiment and the flow simulation differ in these regions. The experiment had a bulkhead inlet and the outlet was open to air whilst the flow simulation used a developed flow at inlet and an outlet through an additional porous domain. Velocity profiles along the baffles cuts are given in Figure 55. The PIV data at baffle cuts 5, 7 and 9 is clearly problematic: this is probably due to the quality of the PIV result. The results across baffle cuts 1, 11 and 13 show a reasonable comparison to the simulation. The maximum velocity in the simulations exceeds the experimental velocity in every case. Recirculation at the baffles tip (negative velocities along baffle cuts 11 and 13) are not represented in the experimental data in Figure 55. This is discussed in more detail in the next section (5.2.6).

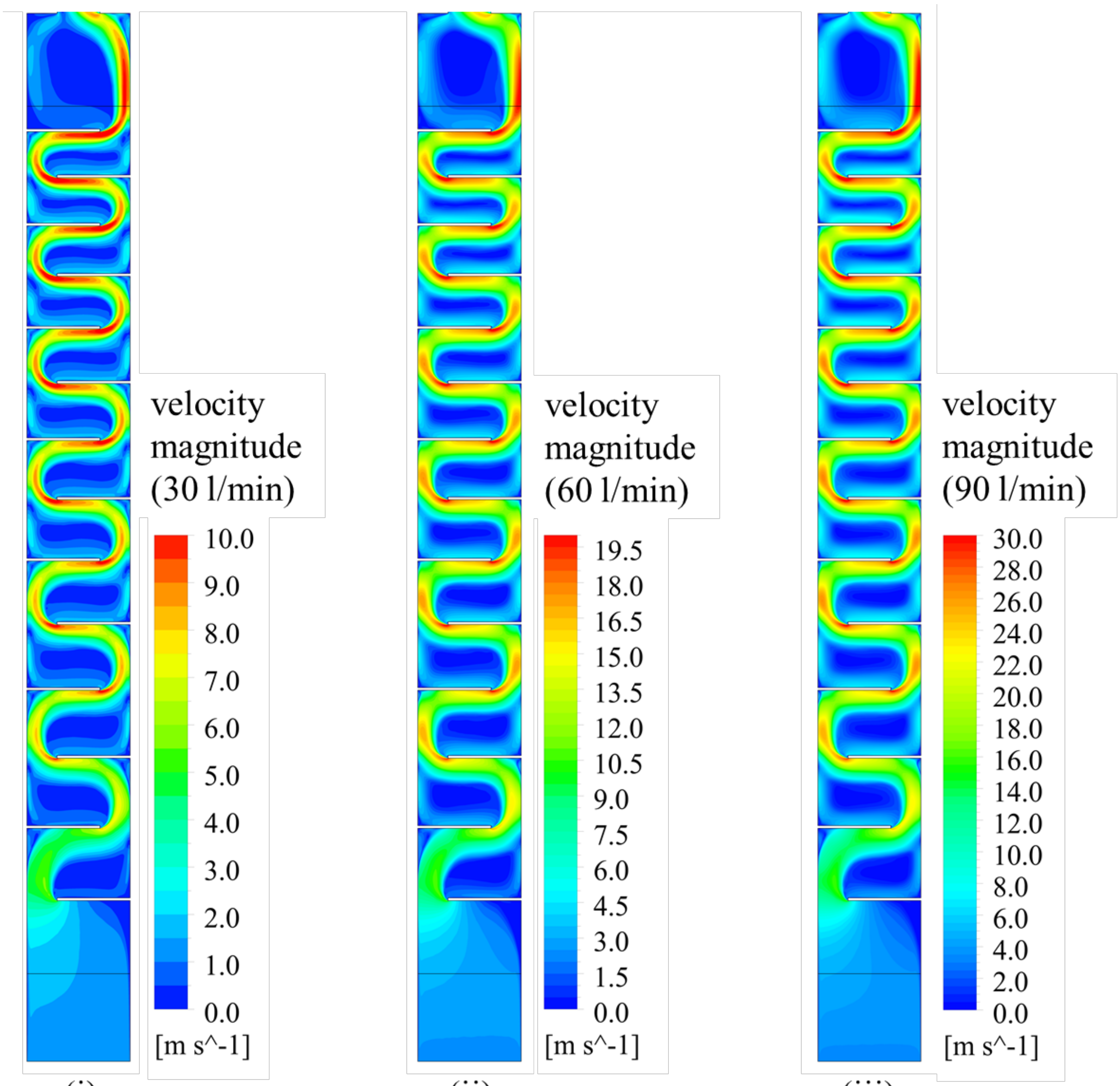

(i) (ii) (iii)

*Figure 53: Velocity contours plots at centre plane (i) 30l/min, (ii) 60l/min (iii) 90 l/min SST simulations.*

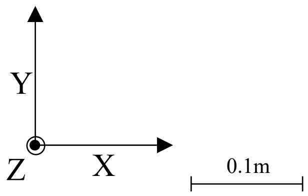

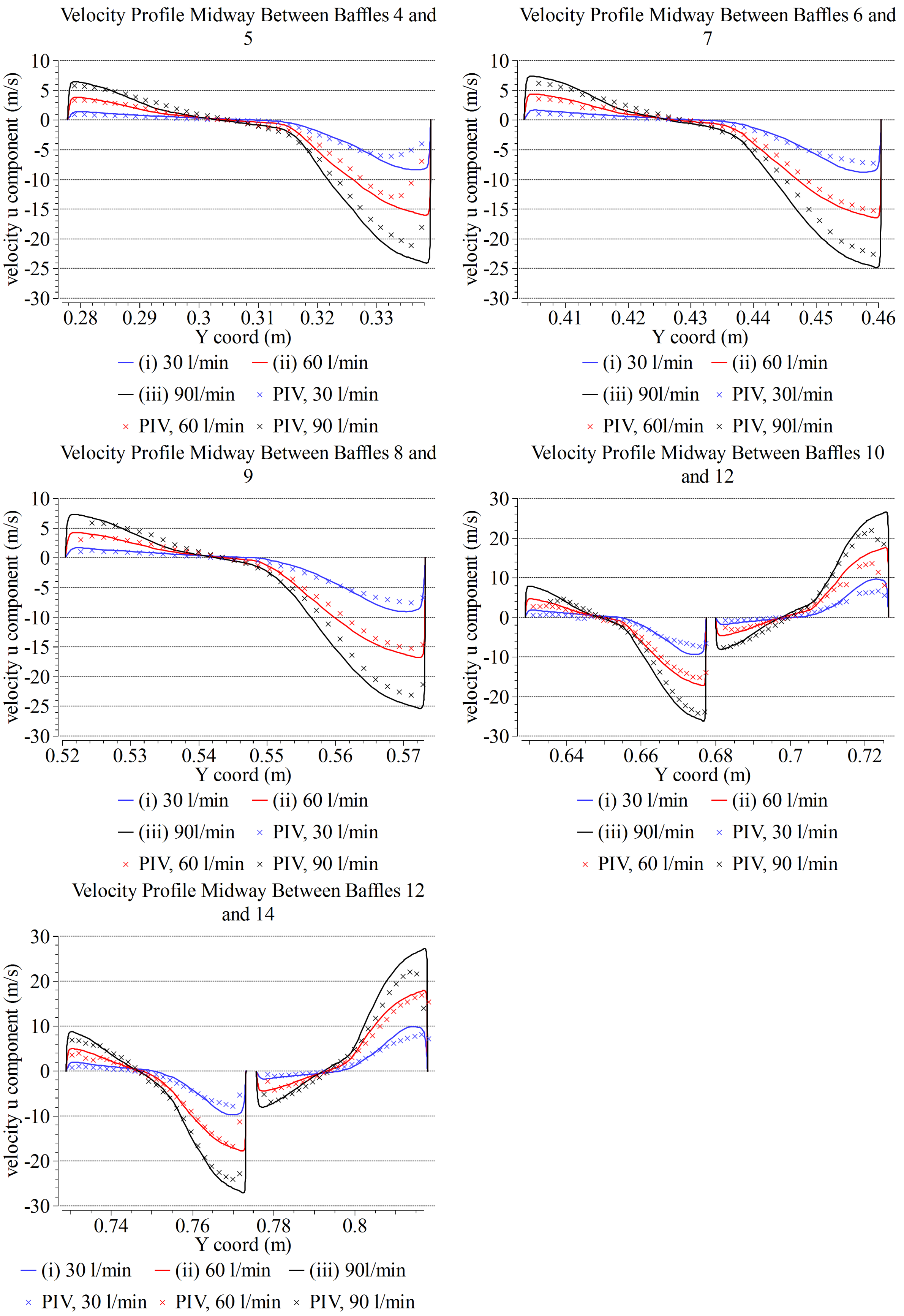

*Figure 54: Velocity profiles midway between baffles. At (i) 30l/min, (ii) 60l/min, (iii) 90l/min flowrates.*

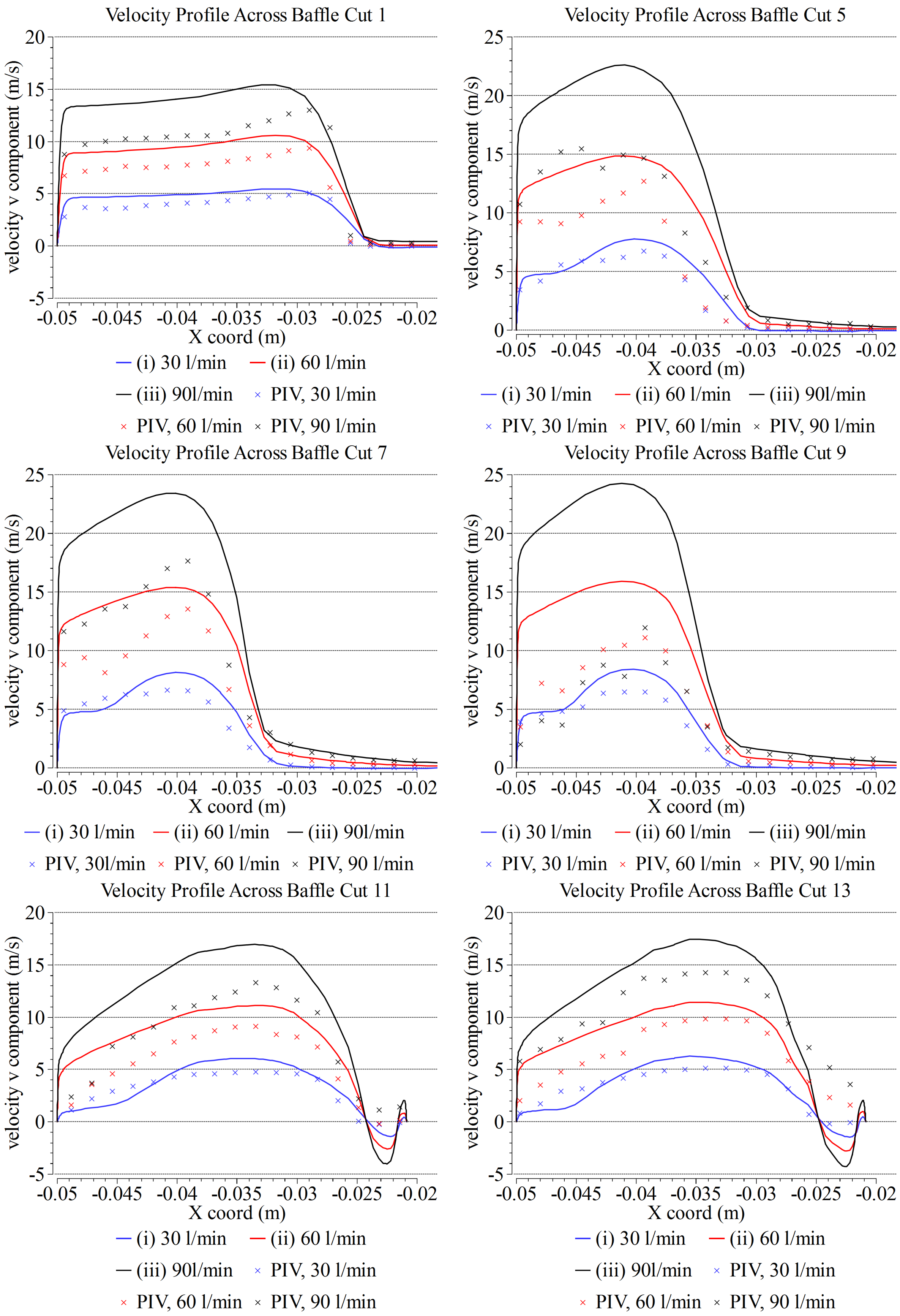

*Figure 55: Velocity profiles across baffle cuts. At (i) 30l/min, (ii) 60l/min, (iii) 90l/min flowrates.*

### *5.2.6 Close-up repeats around baffle 11 tip*

A more detailed PIV result can be obtained by moving the camera closer to the model. Flow around the tip of baffle 11 was examined with two repeats using close-ups in this way. The disadvantage of the smaller field-of-view is that a denser particle seeding is required to obtain a result: experimental repeats were conducted at 30 l/min and 60 l/min but not at 90 l/min due to insufficient particle seeding.

The results are shown below as contour plots (Figure 56) and vector plots (Figure 57), with CFD results included for comparison. The effect of the line of dead pixels can be seen in these contour plots, causing the line of low velocity at x = 37mm. The simulation at 60 l/min compares better to the experimental result than the result at 30 l/min. Particularly, the area of low velocity near the reattachment of the jet observed in the 30 l/min simulation is not present in the experimental result. The PIV result is similar for both flowrates suggesting the characteristics of the flow are similar over the range studied. Both CFD models predict a faster main jet flow than is observed in the PIV experiment. The experimental jet flow also decelerates faster than the CFD results predict. The 30 l/min appears to give a slightly better prediction of the general shape of the jet in the right-hand side of the image (PIV image x coordinate 30mm and above).

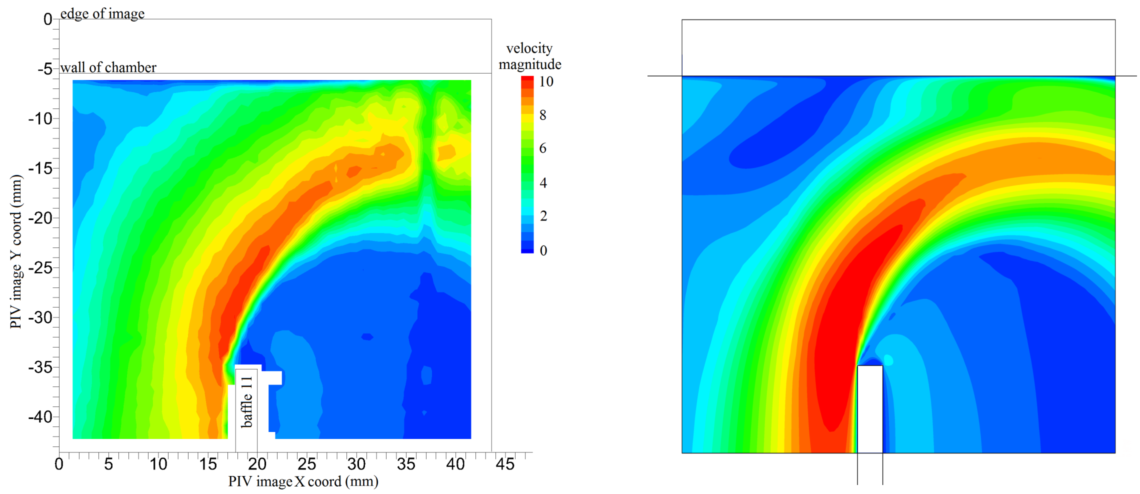

PIV Velocity Contour at Baffle 11, 30 l/min

CFD Velocity Contour at Baffle 11, 30 l/min

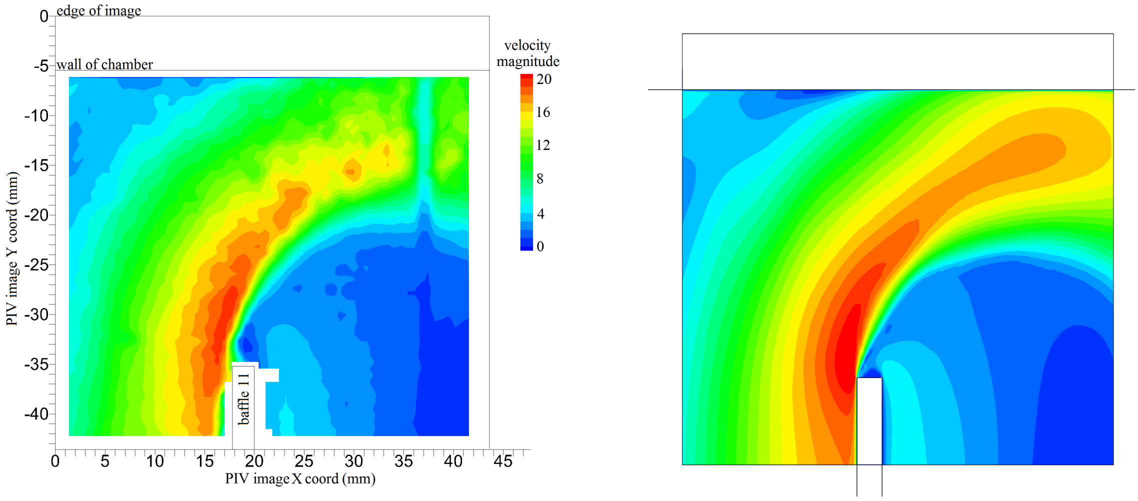

PIV Velocity Contour at Baffle 11, 60 l/min

CFD Velocity Contour at Baffle 11, 60 l/min

*Figure 56: Velocity contour plots from PIV result at baffle 11, compared to CFD results.*

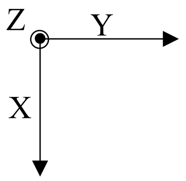

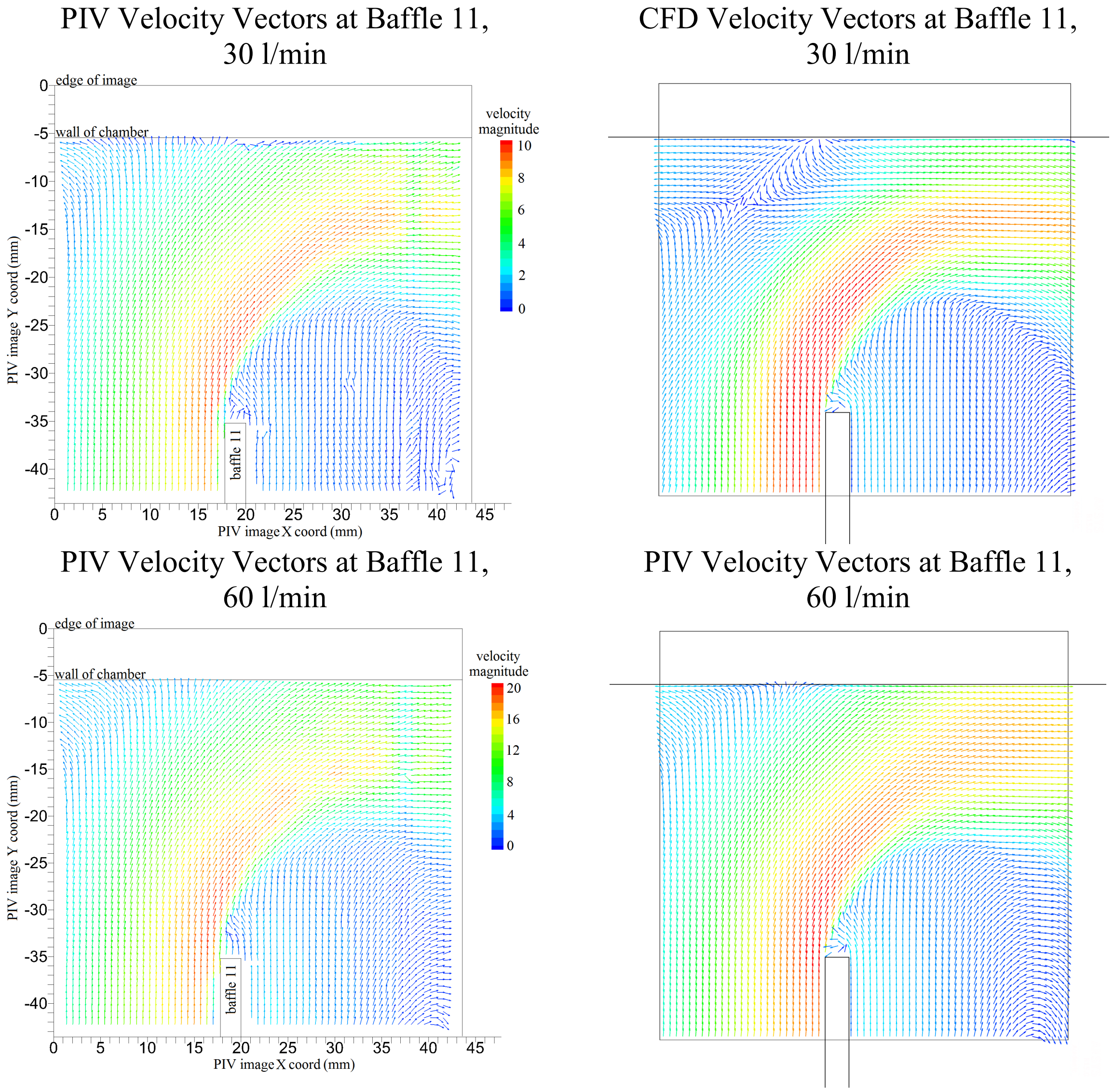

*Figure 57: Velocity vector plots from PIV result at baffle 11, compared to CFD results.*

The reattachment locations were determined using a method similar to that described in section 3.6.4. As the PIV result does not reliably give the velocity near the wall, this was extrapolated. Data was extracted from the first three rows of vectors in the PIV image (PIV image y coord = -5 to -8mm), the location where the velocity x-component (PIV coords) equals zero in these rows was determined. A straight line of best fit was put through these three data points and extrapolated to the wall. The reattachment locations are shown in Table 19. This reaffirms what is visible in Figure 56: the area of low velocity in the CFD model at 30 l/min affecting jet reattachment is not present in the experiment. Otherwise, there is good comparison between the PIV and CFD at 60 l/min.

| result | reattachment location, PIV image x coord |
|---|---|
| PIV, 30 l/min | x = 12.4 mm |
| PIV, 60 l/min | x = 14.3 mm |
| CFD, 30 l/min | x = 17.3 mm |
| CFD, 60 l/min | x = 14.1 mm |

*Table 18: Reattachment locations for PIV result.*

The velocity profiles across the baffle cuts can be obtained with greater detail using these close-up results. These show similar behaviour to the results shown in Figure 55 above. The experimental result broadly resembles the simulation in profile shape, but at a slightly lower velocity. Recirculation around the baffle tip (negative velocities in Figure 58) are visible in the experimental result, due to the improved resolution in comparison to Figure 55. However, this recirculation is less pronounced than predicted by the CFD.

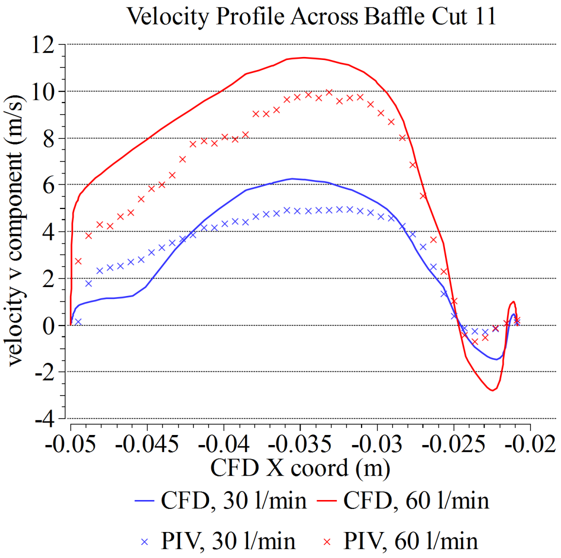

*Figure 58: velocity profile across baffle cut 11, for close-up repeats.*

## 5.3 **Data Mining of On-Site Process Data**

Performing full-scale tests on the cryogenic condenser installed at Aesica Cramlington using benzene carried prohibitive cost and risk. Operating data was however available in the form of several on-site tests, completed for environmental monitoring purposes by Aesica. The current use of the cryogenic condenser involves controlling vent emissions of another volatile organic compound (VOC): dichloromethane (DCM). The aim of the data mining process was to obtain useable data from these reports, that could potentially be compared to simulation. The main aims were to quantify the residual DCM concentration at the outlet of the cryogenic condenser, and to determine whether this varied with inlet conditions such as flowrate and inlet concentration.

Data mining was conducted with emissions monitoring reports. These reports were available for DCM abatement using the cryogenic condenser. The batch nature of the processes leads to results at transient conditions that are difficult to interpret with any certainty. The bivariate relationships between treated variables did not reveal any statistically significant correlations (Pearson correlation coefficients less than 0.9). This is shown in the rank correlation matrix in Figure 59 below, where the variables are numbered as shown in Table 19. The strongest correlation was observed between two measurements of DCM outlet concentration, this is shown in Figure 60 below. The discrepancy between a units conversion of these two measures (total VOC as Carbon, vs DCM by Fourier-transform infra-red FTIR) and the line of best fit may be due to a presence of other solvents in addition to DCM. Although this suggests there may be correlations between inlet and outlet concentrations (one of the original aims of the data mining was to determine this relationship) the plots show there is no visible trend between them.

| | |
|---|---|
| 1 | Time |
| 2 | DCM at outlet |
| 3 | Flowrate |
| 4 | Temperature |
| 5 | VOC as C at inlet |
| 6 | VOC as C at outlet |
| 7 | Water vapour at outlet |

*Table 19: Variables numbering for rank correlation matrix.*

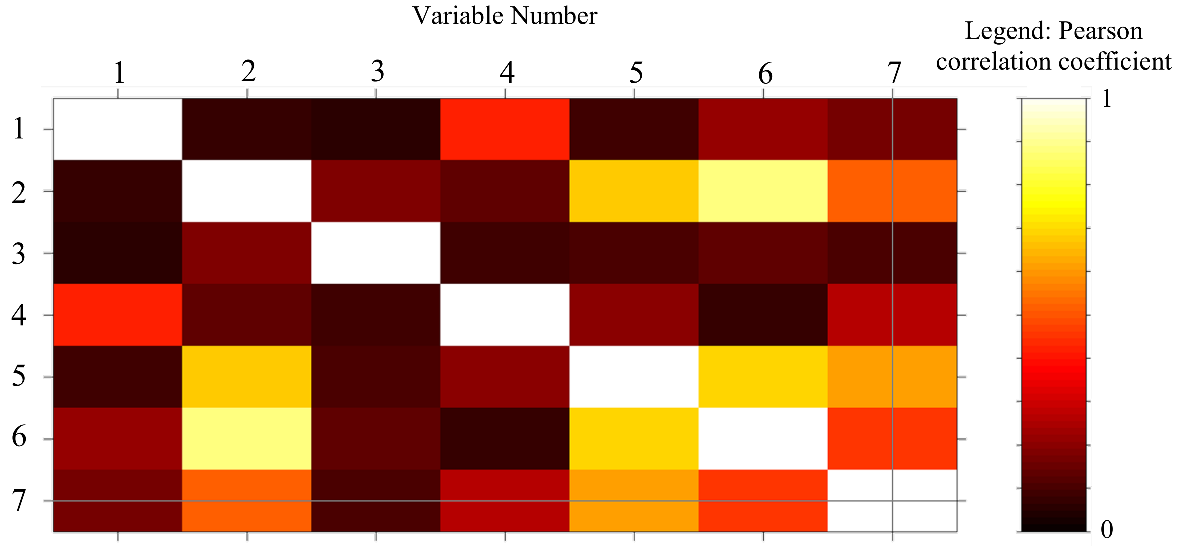

*Figure 59: Rank correlation matrix*

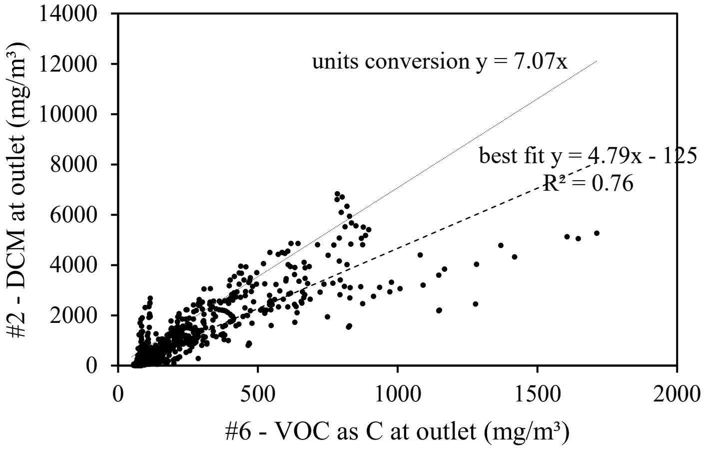

*Figure 60: DCM at outlet by FTIR and VOC as C.*

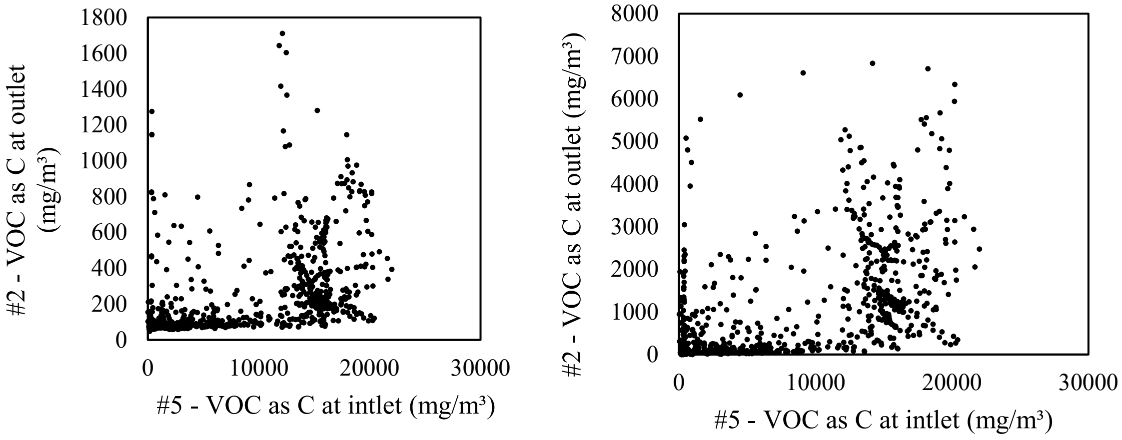

*Figure 61: Scatter plots of inlet vs outlet vapour concentrations of DCM.*

Data from one campaign was treated to remove all values between peaks, as these are likely to represent low or no flow conditions in the cryogenic condenser, which are not useful for our purposes. The resulting changes removed 80% of the data. There was no correlation between inlet and outlet concentrations of DCM. However, the resulting statistical summary data suggested a mean value that was close to saturation conditions for the outlet data. Lines shown in Figure 62 represent DCM vapour pressure from various sources: (Perry, 1927; Lide, 1993; NIST, 2016). Crosses in Figure 62 indicate mean concentrations, with error bars representing standard deviations.

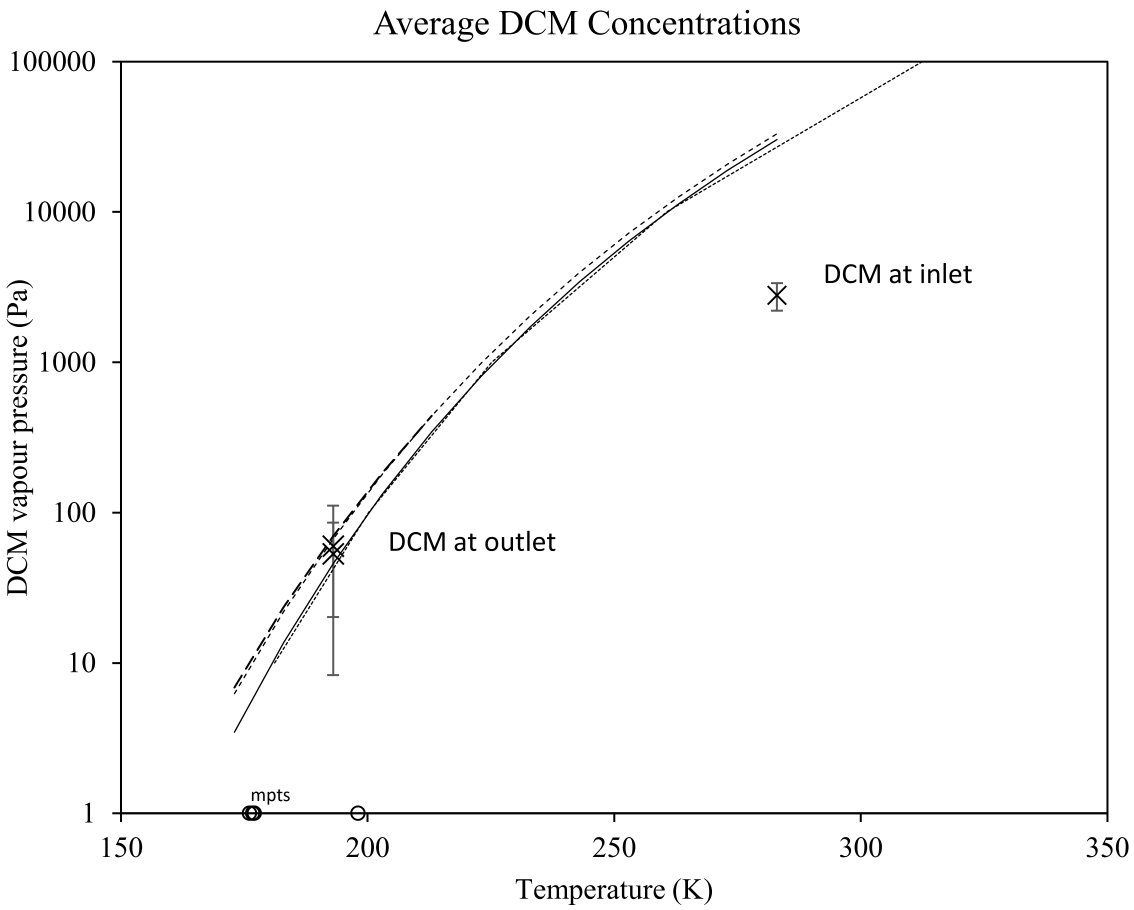

*Figure 62: Average DCM concentration. Lines indicate DCM vapour pressure curves.*

An output close to saturation indicates very good performance of the cryogenic condenser when capturing DCM. This is only suggestive however, it can't be used for validation due to the large error band in the data. The results show good comparison between FTIR and VOC as carbon measurements for the reported DCM concentration at the outlet.

No correlation was observed between outlet DCM concentration and flowrate data. The expected trend (better capture with reduced gas flowrate) was observed between average values from two campaigns: this is shown in Figure 63, where error bars represent a standard deviation. However, the high flowrate campaign data is also well above the designed operating conditions of the cryogenic condenser (150Nm$^3$/hr).

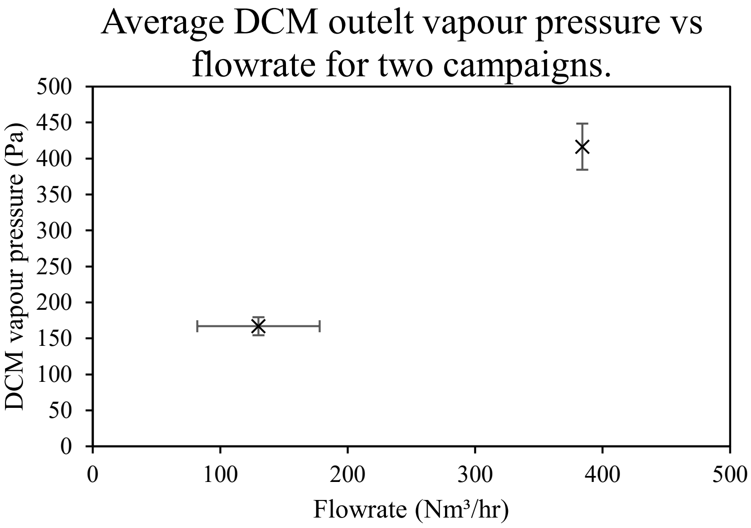

*Figure 63: Average DCM concentrations vs. flowrate.*

## 5.4 **Conclusions**

The data mining of the on-site test data indicates two main outcomes. The outlet vent gas is at near-saturation indicating very good performance when condensing DCM. The DCM outlet concentration increases with flowrate, although this flowrate range is well above the design range of the condenser.

Comparison of the PIV experiment and simulation has validated the CFD model of the similitude-scale experiment. This in turn provides confidence in the full scale model result. The results demonstrate reasonable agreement between simulation and experiment. Use of a symmetry plane does ignore a predicted z-component of the flow along the centreline. The ignored z-component may explain some of the deviation between simulation and experiment visible around the baffle cuts (Figure 45 shows the non-symmetrical agrees slightly better around baffles 7 and 11). Use of fully second order discretisation, whilst recommended in principle, actually leads to unphysical results. Turbulence model comparisons indicate there is no real substantial differences between the models, the low-Re SST model performing most favourably in comparison to experiment. Similarly, DES simulations, whilst being very high computational load, do not result in a more accurate answer. The transition-SST model was used for solving the flow at 30 l/min flowrate, but the low-Re SST model appears to better predict the jet attachment and velocity profile at the baffle cut. Overall, although a low-Re SST model is simple, it gives a reasonable prediction of the flow. Improvements in order of accuracy and turbulence modelling (through the use of different turbulence models, DES approaches, transition modelling) do not actually lead to better comparison with the experimental results obtained by PIV.

# Chapter 6. Results and Discussion – Particle Formation and Transport

The previous chapter has established that the fluid flow model simulates the basic flow in the geometry of the cryogenic condenser, with a reasonable comparison to experimental data obtained by particle image velocimetry (PIV). In this chapter, the fluid flow model is built upon to simulate the more complex phenomena occurring in the cryogenic condenser using computational fluid dynamics (CFD). Firstly, the heat transfer modelling is described in detail. This shows the effect of gas flowrate on the temperature profile of the gas to be relatively mild, and gives some indication of where critical temperatures for nucleation will be achieved inside the condenser. Next, inert Eulerian-Lagrangian modelling was then used to gain insight into the particle behaviour inside the condenser, and determine what phenomena are important in modelling the particle trajectories. Particle trajectories lead to particle collisions with walls in the CFD model. This represents deposition of the benzene particle onto internal surface of the condenser: the point at which benzene is separated and removed from the gas. Massless inert Eulerian-Lagrangian modelling can also be used to find residence time distributions in the fluid flow, and is therefore also covered in this section.

A full model of nucleation and growth was developed firstly for a 2D parallel plate model of the condenser. This allows the results of the model to be interpreted clearly, illustrating a nucleation front in the model and the effects of particle growth. A full 3D model of nucleation and growth was also completed on a high-performance computing cluster and this is covered in the final section of this chapter.

## 6.1 Temperature Profile

Cooling of the gas flow through heat exchange was simulated using a linear wall temperature profile, as illustrated in Figure 27 (section 3.7.2, p. 90). The linear wall surface temperature profile varied from -60 near the inlet to -100°C at the top of the condenser. This was based on the operating conditions for the cryogenic condenser.

Figure 64 (i) is a contour plot of the predicted nitrogen temperature, showing the effect this wall temperature profile has on the bulk gas temperature for a pure nitrogen flow. The recirculation regions between the baffles are cooled to a lower temperature than the main jet flow. This is due to a longer contact time with the cold wall.

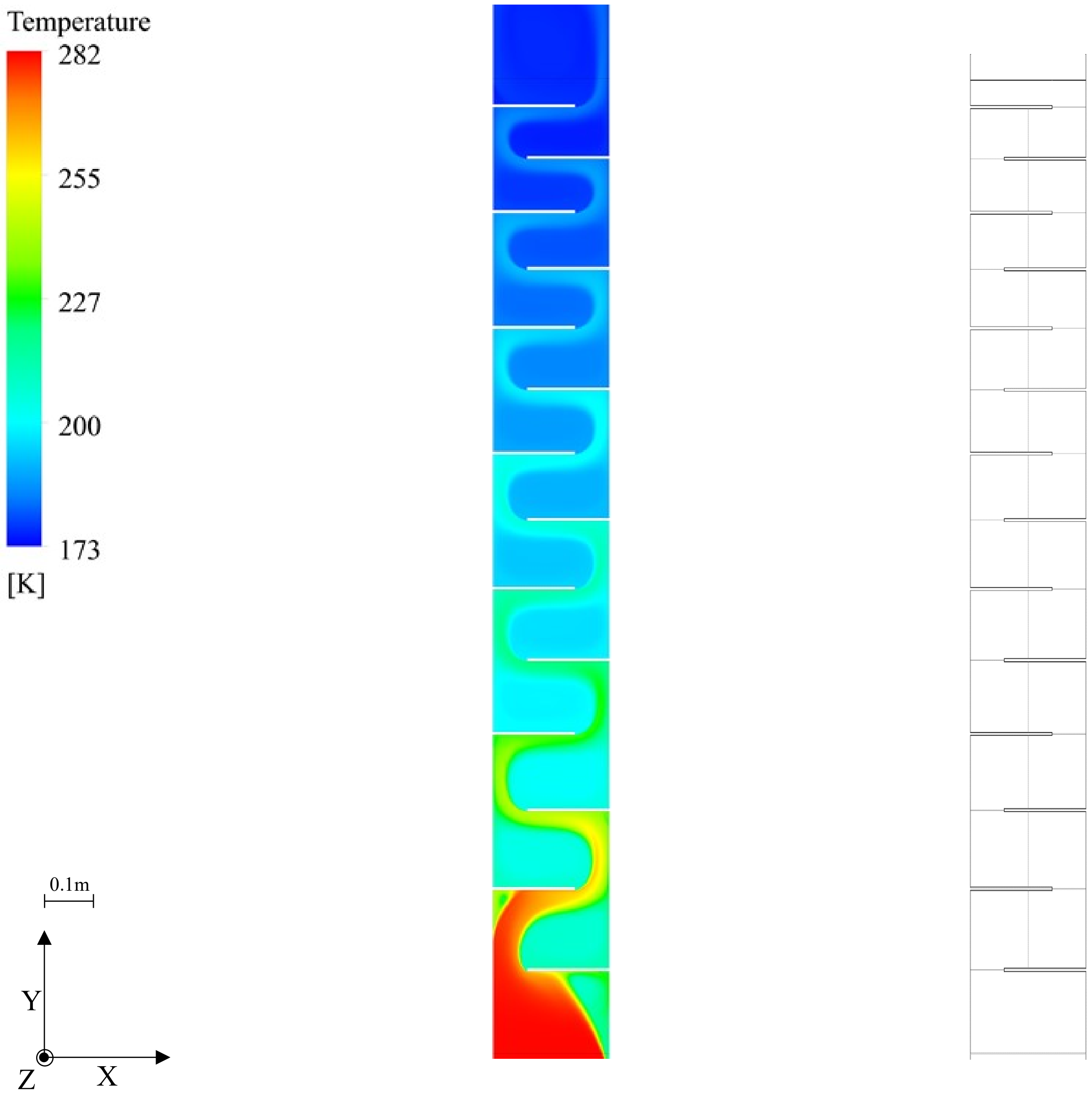

(i) (ii)

*Figure 64: (i) Contour plot of temperature profile for cooled gas-only flow, (ii) Sample plane locations in the CFD model.*

Temperature profiles were collected using sampling planes, located across the baffle cut and between the baffle spaces as illustrated in Figure 64 (ii). The resulting temperature profiles are shown in Figure 65 below. The x-axis represents the distance the gas has travelled into the condenser. Error bars represent a standard deviation. The dashed line shows the maximum temperature: this represents the temperature of the main jet flow. Planes down the centreline of the model, in the spaces between baffles, consist predominantly of recirculation flow and are therefore cooler than the sample planes in line with the baffles (at the baffle cuts), which are dominated by the main jet flow. In Figure 65 the two solid lines show this distinction.

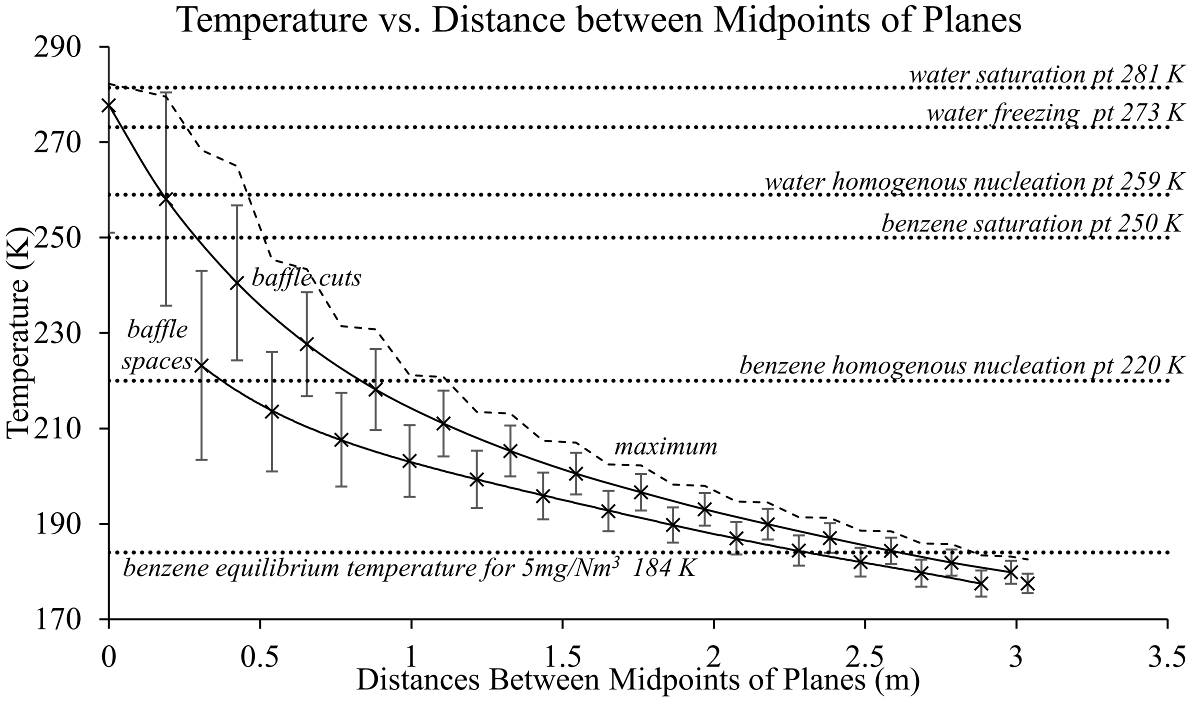

*Figure 65: Temperature profile, 150 Nm$^3$/hr. Points ✕ : area-weighted average temperature of sample planes; solid lines —: data fit; dashed line --: maximum temperature at sample plane; error bars: standard deviation.*

The point at which homogeneous nucleation can be predicted using classical nucleation theory. The critical degree of supersaturation and the critical temperature at which homogeneous nucleation occurs can be found from iteratively solving equation 2-68. As covered in section 2.13.5, the heterogeneous nucleation can be predicted from the saturation temperature, or, the point at which the gas flow becomes supersaturated.

In the industrial process under study (flurbiprofen manufacture), upstream of the cryogenic condenser the vent gas flow is first treated through an aqueous scrubber. The inlet to the cryogenic condenser is expected to be saturated with water, and (heterogeneous) condensation of this species will occur immediately in the condenser. Homogeneous nucleation of water was calculated to occur under the same conditions at 259 K, less than 0.5m into the condenser. Benzene will desublimate at the gas moves further into the condenser, with heterogeneous nucleation occurring at 250 K, roughly 0.5m into the condenser. Homogeneous nucleation was predicted at a temperature of 220 K, 1.1m into the condenser.

Figure 66 below illustrates the same result as Figure 65, for varying flowrates. As the flow rate decreases, differences between the main jet temperature and the temperature of the recirculation regions are reduced. However the flow rate variation does not cause a significant change in the temperature profile of the gas. Comparing 150 Nm$^3$/hr to 50 Nm$^3$/hr, heterogeneous (saturation) conditions for benzene move 0.04m upstream under the lower flow rate, while homogeneous nucleation conditions move 0.2m upstream. As this difference is small, for inert Eulerian-Lagrangian modelling the locations were not changed at different flowrates when modelling nucleation (section 6.2). The closeness of the three lowest lines in Figure 66 indicate that the temperature of the recirculation regions between baffles does not change with flowrate.

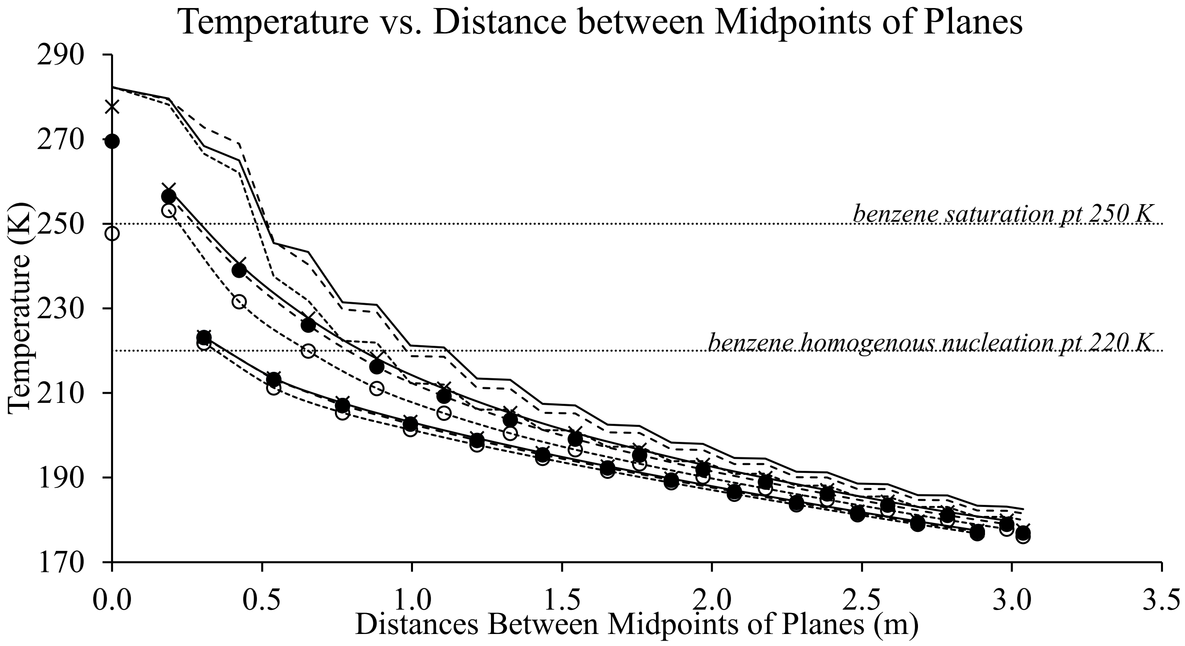

*Figure 66: Variation in temperature profile with flow rate. Solid line/crosses –X– 150 Nm$^3$/hr; Long dashes/filled dots --●-- : 100 Nm$^3$/hr; short dashes/unfilled dots ··○·· : 50 Nm$^3$/hr.*

Figure 67 shows a flow visualisation of the result plotted in Figure 65 (150Nm$^3$/hr flowrate, −100°C exit plate temperature). The figure shows the temperature profile in the centre plane. Above the contour at 250 K, heterogeneous nucleation of benzene is possible. Above the contour at 220 K, homogeneous nucleation of benzene is possible. Above the contour at 184K, meeting the environmental regulation limits is possible.

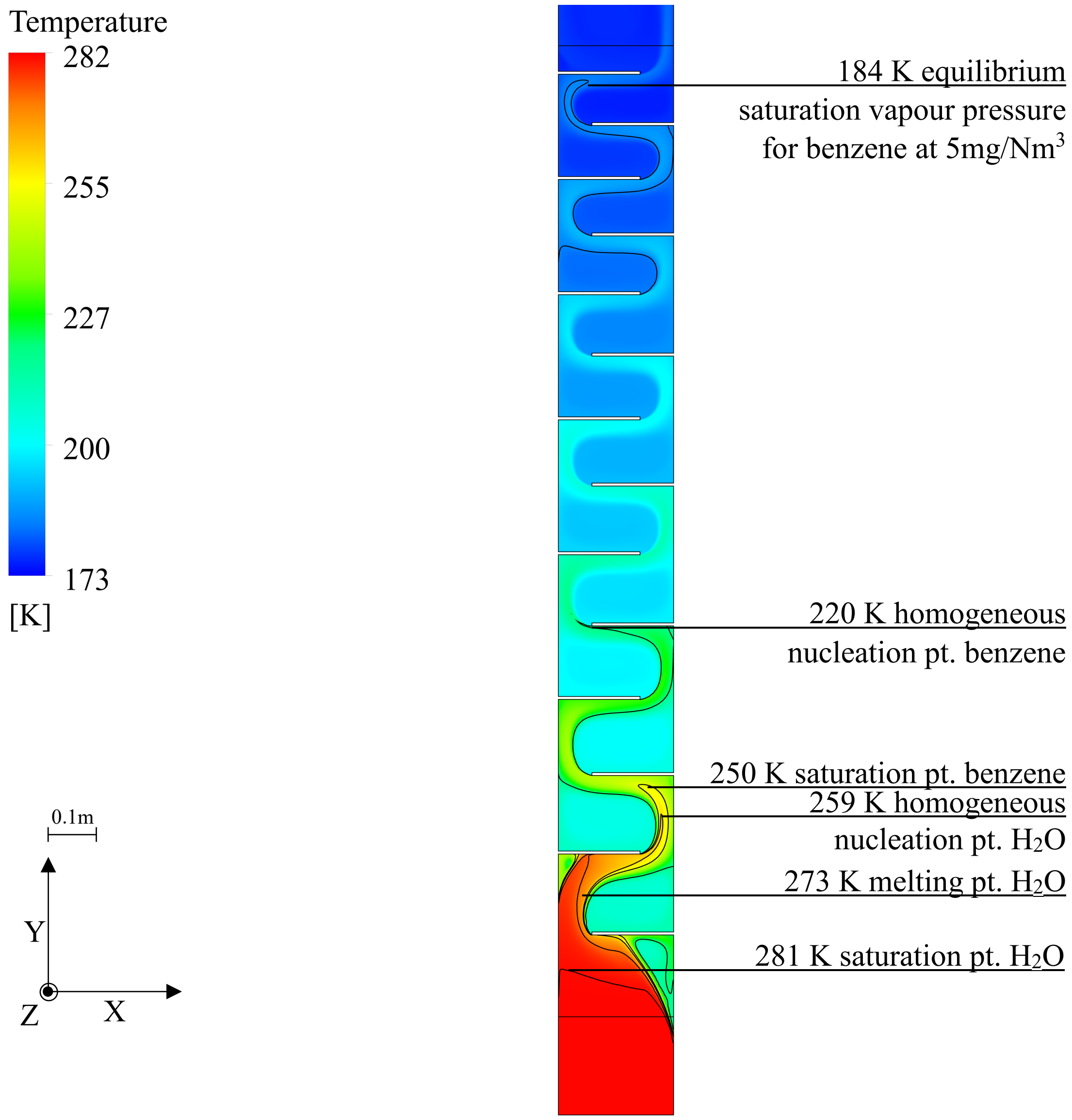

*Figure 67: Annotated temperature contours on centre plane.*

### 6.1.1 *Enthalpy profile*

The temperature profile may presented as a change in enthalpy of the stream, as shown in Figure 68 and Figure 69 below. This is shown for the stream enthalpy of the heat exchanger as a whole. Assuming benzene is removed from the stream to vapour/solid equilibrium, releasing heat of desublimation into the stream. This provides the thermal duty of the cryogenic condenser along its length.

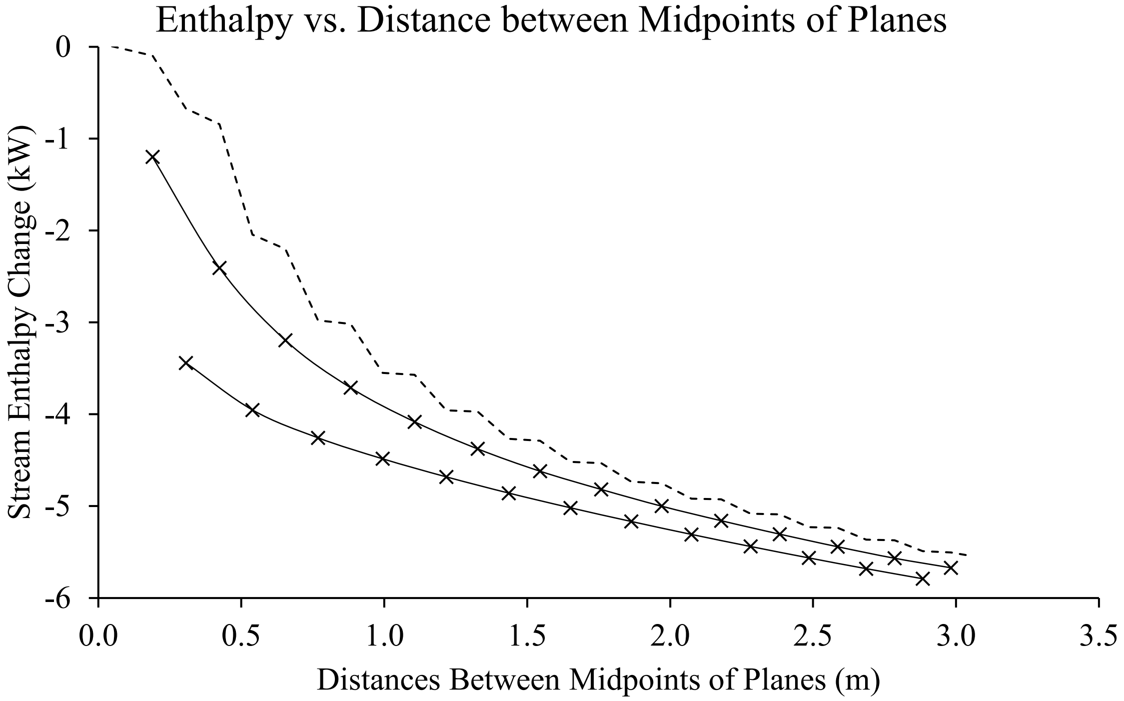

*Figure 68: Stream enthalpy profile, 150Nm$^3$/hr. Points: × : area-weighted average enthalpy of sample planes; solid lines —: data fit; dashed line --: maximum temperature at sample plane.*

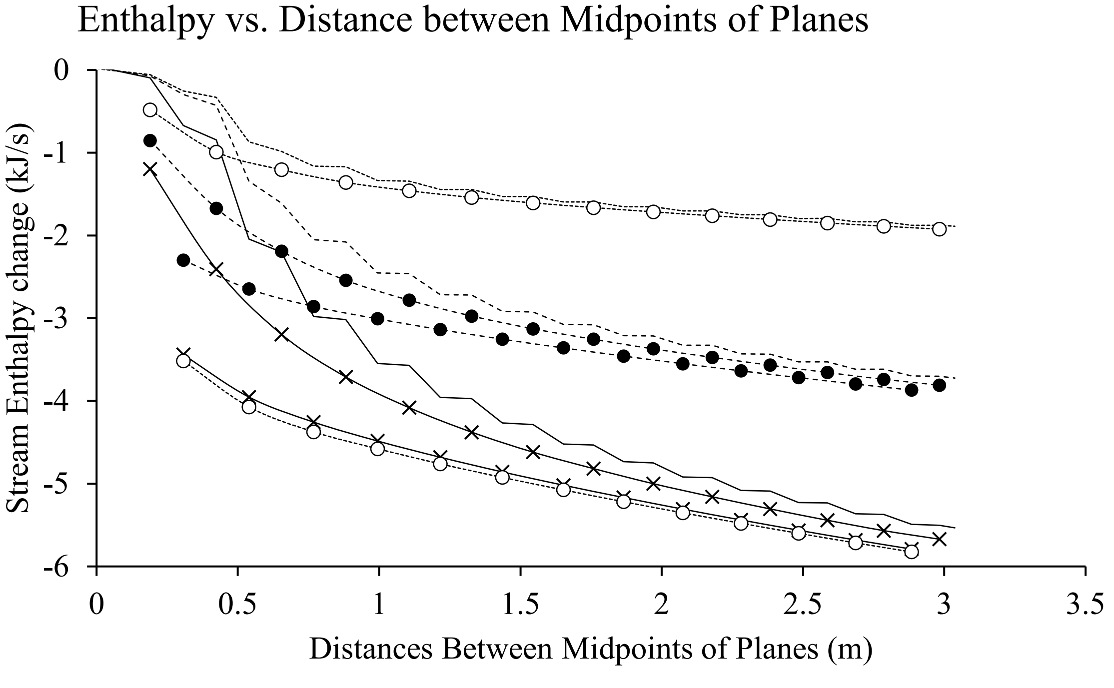

*Figure 69: Variation in enthalpy profile with flow rate. Solid line/crosses –×– 150 Nm$^3$/hr; long dashes/filled dots --●-- : 100 Nm$^3$/hr; short dashes/unfilled dots ··○·· : 50 Nm$^3$/hr.*

## 6.2 Inert Eulerian-Lagrangian Particle Modelling

This section covers inert Eulerian-Lagrangian particle modelling. The behaviour of benzene particles formed by desublimation was initially simulated by injecting inert particles. The injection locations were chosen as a plane of injections based on the expected nucleation conditions from section 6.1. The simulation was repeated for increments of particle diameter. The figures below show capture efficiency, as a percentage of particles which were deposited on the flow domain walls. Benzene must be captured at very low levels in the cryogenic condenser. A figure of over 99% particle capture $d_{p(99\%)}$ was chosen to be indicative of good particle capture. Particle larger than this size has a very high likelihood of becoming captured inside the condenser.

### *6.2.1 Effect of turbulence*

The effect of turbulence is illustrated in Figure 70 (i). This compares the result without turbulence modelling in the particle streams to a result modelling turbulent diffusion of the particles with discrete random walks. Turbulence promotes particle deposition by moving the particles on random trajectories. This increases the likelihood of particles depositing on the walls. To meet the extremely low levels of benzene in the outlet vent gas, total (>99%) removal of these particle is desired. This occurs at $d_{p\,(99\%)} = 12\mu m$ when turbulence is included.

### *6.2.2 Effect of thermophoresis*

Thermophoresis affects particles of small radii (typ. >10µm) in flows under large temperature gradients (typ. 50K/cm or more (Srikanth and Jayaraj, 1995). Thermophoresis creates an attractive force towards the cold plates, improving the deposition for small particles as can be seen in Figure 70 (ii). Thermophoresis does not affect large particles, so the diameter for capture $d_{p\,(99\%)} = 12\mu m$ is not affected by thermophoresis. For particles less than 10µm, thermophoresis improves the particle capture substantially: capture of 5µm particles for example, doubles from 18% to 37% as a result of including thermophoresis in the model.

### *6.2.3 Effect of Cunningham slip*

Cunningham slip only affects particles in the Knudsen number transition or with large Knudsen numbers. This occurs for particles of less than ca. 1µm, as covered in section 2.15.1 above. Figure 70 (iii) below confirms that this deviation affects this region only. Deposition increases slightly due to the effect that the Cunningham slip correction factor has on particle drag in comparison to a spherical drag law: reducing drag, therefore increasing deviation from the fluid flow.

### *6.2.4 Effect of heterogeneous vs homogeneous nucleation*

The plots are continued in Figure 71 (iv), which shows the difference between homogeneous and heterogeneous nucleation locations. Particles were injected in a 1mm square grid, between baffles 2 and 3 to represent heterogeneous injection, and between baffles 4 and 5 to represent homogeneous injection. Heterogeneous nucleation shows a slightly higher capture efficiency. As the heterogeneous nucleation occurs earlier in the condenser, particles must navigate a more tortuous path. Also, as the temperature gradient is higher, the effect of thermophoresis on particle capture is slightly more pronounced. However the differences are not substantial, and $d_{p(99\%)} = 12\mu m$ in both cases.

### *6.2.5 Effect of flowrate*

Reducing the gas flowrate increases the size of particles that are required for complete capture. The effect of flowrate is covered in Figure 71 (v). Lower flowrates lead to less particle deposition due mostly to lower Stokes numbers at equivalent particle diameters. Thermophoretic force is also reduced at lower flowrates, as the average gas flow is cooler, reducing the temperature gradient and therefore the thermophoretic force. The reduced flowrate has a large impact on the diameter for capture as shown in Table 20. The diameter for capture can be expressed as Stokes numbers, also shown in Table 20. Inertial deposition is dependent on Stokes number, the ratio of momentum response time to fluid characteristic time. These Stokes numbers are close to one and are not a strong function of flowrate, indicating that inertial deposition is the dominant mechanism for particle capture.

| Gas flowrate | Diameter for capture $d_{p(99\%)}$ | Stokes number Stk |
|---|---|---|
| 150 $Nm^3/hr$ | 12 μm | 0.18 |
| 100 $Nm^3/hr$ | 16 μm | 0.22 |
| 50 $Nm^3/hr$ | 23 μm | 0.23 |

*Table 20: effect of flowrate on diameter for capture.*

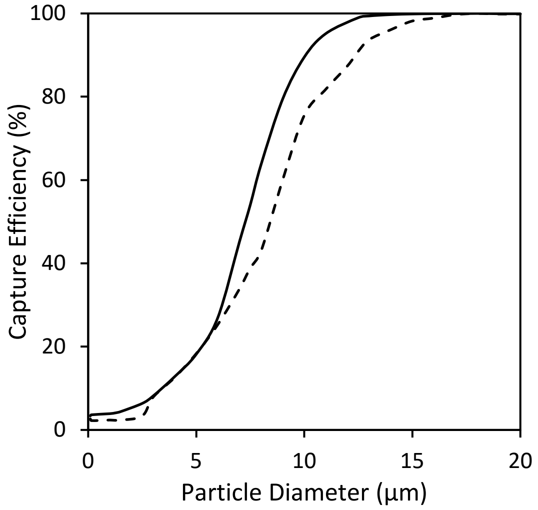

(i) Comparing the effect of turbulent particle diffusion on particle capture. Homogeneous nucleation, 150Nm$^3$/hr.

Solid line: — including turbulence

Dashed line: --- neglecting turbulence

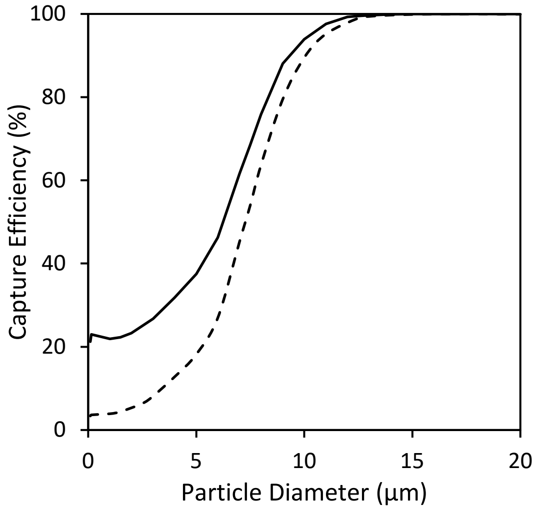

(ii) Comparing the effect of thermophoresis on particle capture. Homogeneous nucleation, 150Nm$^3$/hr.

Solid line: — including thermophoresis

Dashed line: --- neglecting thermophoresis

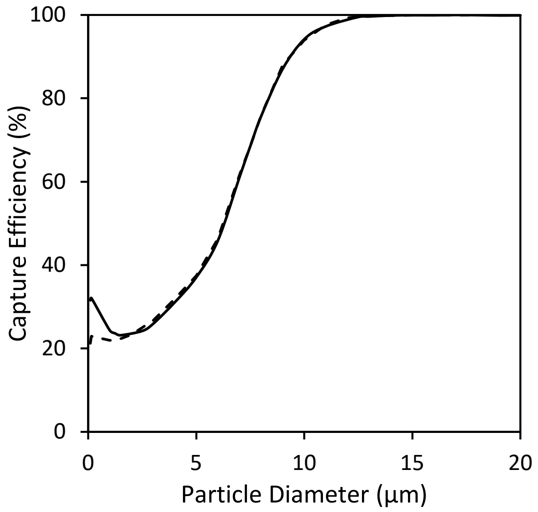

(iii) Comparing the effect of including Cunningham slip on particle capture. Homogeneous nucleation, 150Nm$^3$/hr.

Solid line: — including Cunningham slip correction factor.

Dashed line: --- spherical drag law

*Figure 70: Capture efficiency plots.*

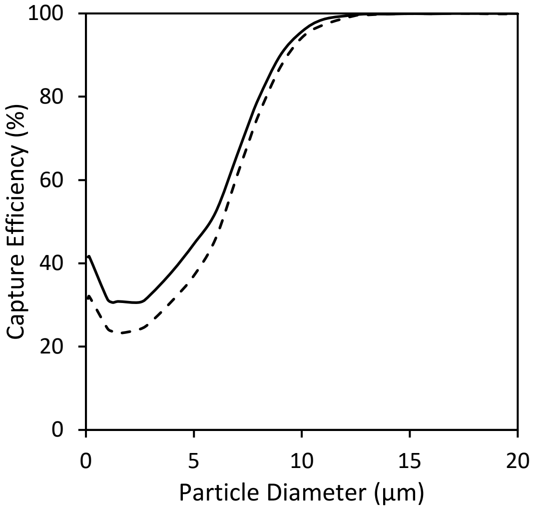

(iv) Comparing the effect of heterogeneous vs homogeneous nucleation locations on particle capture, 150 Nm$^3$/hr.

Solid line: — heterogeneous nucleation

Dashed line: --- homogenous nucleation

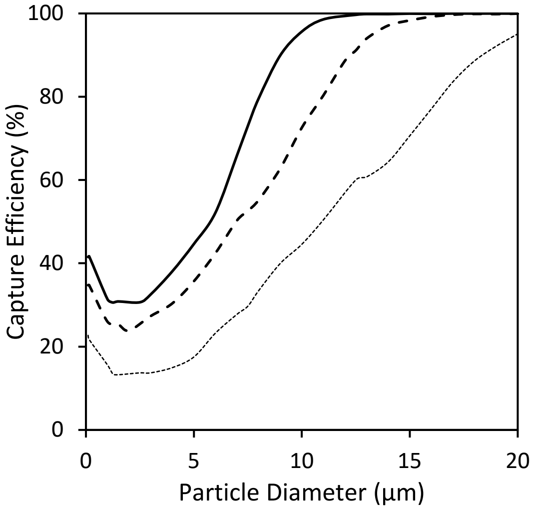

(v) Comparing the effect of flowrate on particle capture, heterogeneous nucleation.

Solid line: — 150 Nm$^3$/hr

Long dashes: --- 100 Nm$^3$/hr

Short Dashes: --- 50Nm$^3$/hr

*Figure 71: Capture efficiency plots (continued).*

### *6.2.6 Accretion areas for particle deposition.*

This section covers results showing the areas in the model where particles accumulate as they are deposited. The simulation results are shown in Figure 73. These are compared to a small cardboard scale-model shown in Figure 72.

Particles accumulate through deposition on the internal surfaces of the cryogenic condenser. Figure 73 shows the results from a flow simulation at 150Nm$^3$/hr, and an injection of inert 10μm particles at the entrance to the condenser plates. As the flow moves through the model, specific areas where particles deposit are:

(a) On the condenser shell,

(b) On the surface of the lamella plate, where the main jet flow changes direction,

(c) On the underside of the baffle.

The colour scale in Figure 73 represents the mass flowrate of particles to these locations following their release. Particles concentrate on the condenser shell (a) opposite the baffle. As the jet turns round the baffle, the particles struggle to follow the flow trajectory. Particles deviate from the curving fluid flow and deposit on the condenser shell (a) opposite the baffles. The flow simulation shown in Figure 73 includes the effect of turbulence on the particle trajectories, through a discrete random walk model. Particles concentrate on the surface of the lamella plate (b). This is due to a combination of deviation from the flow trajectory and the randomness imposed on the particle direction due to turbulence. Particles also concentrate on the undersides of the baffles (c): this is a result of deviation from the fluid flow. This result demonstrates that particle deposition is driven by an inability to follow the curvature of the flow stream.

The simulation result is compared to a 1:4 basic cardboard scale-model shown in Figure 72. This experiment was performed with unmeasured air flowrate, and particle seeding was accomplished with black spray paint. The experimental setup was otherwise similar to Figure 31 (section 4.2.1, p. 102). Some notable differences from the simulation are the noticeable increase in deposition for flow immediately around the baffle tip. The particle size and flowrate were not controlled in this experiment, the deviation may also be due to the simplified Z-component of the velocity of the symmetric simulation geometry, discussed in section 5.2.1, p. 118).

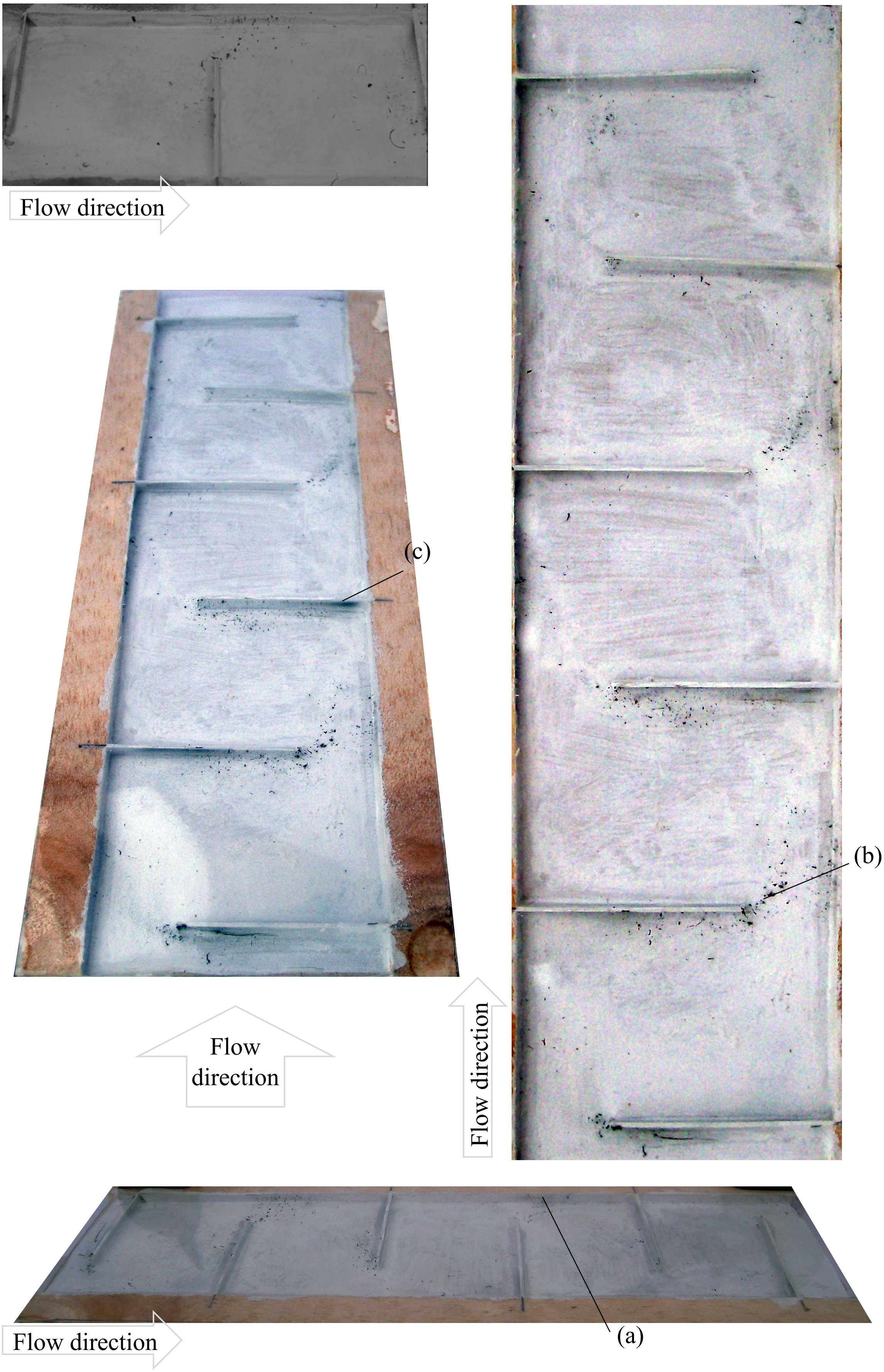

*Figure 72: Experimental basic scale-model flow.*

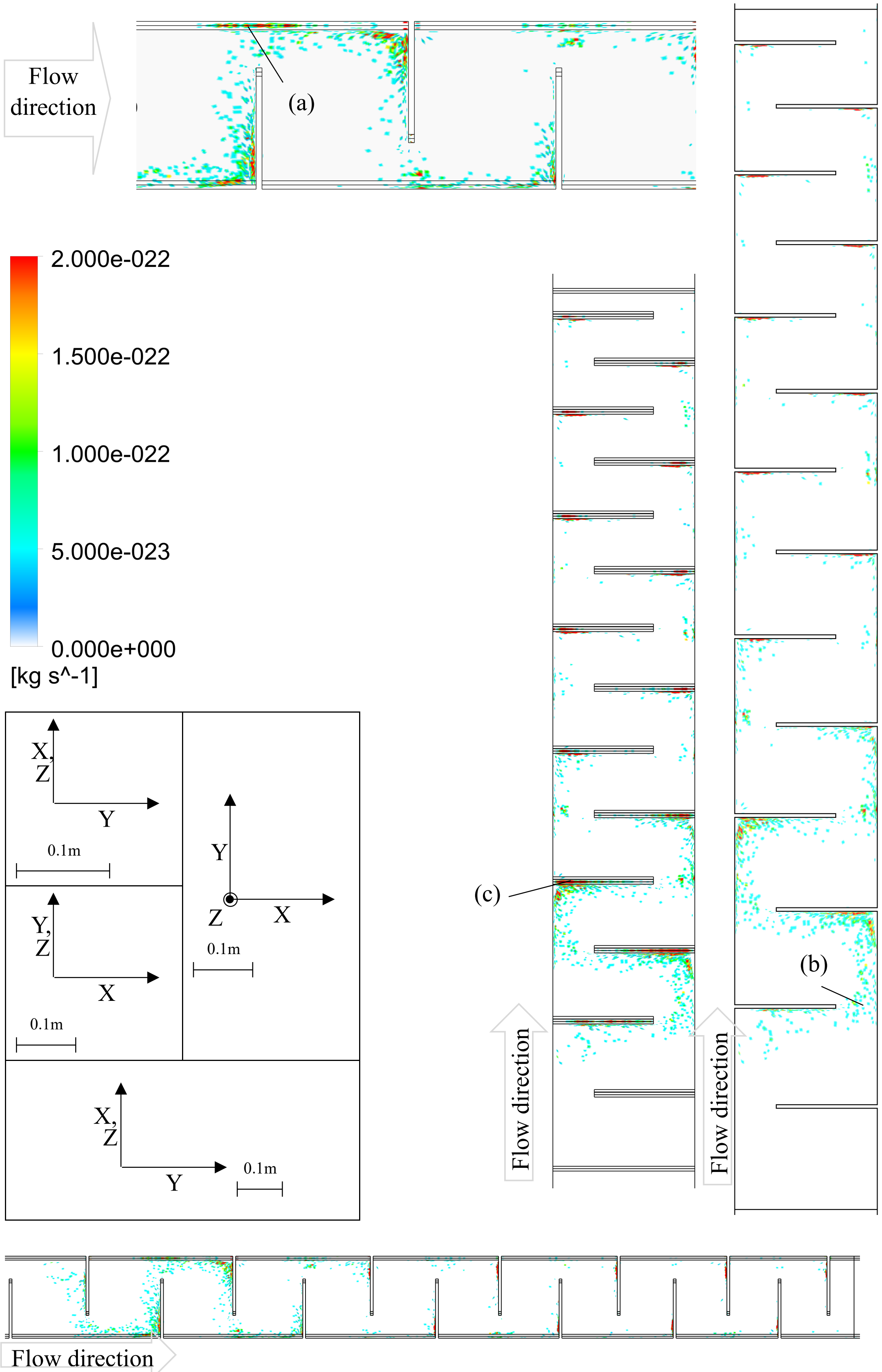

*Figure 73: DPM accretion areas.*

### 6.2.7 Residence time distribution

Massless particle tracking was used to find the residence time distribution resulting from the CFD flow domain. An equally spaced grid of 4200 injection locations was created at the entrance to the plates in the symmetry model (ca. 0.5mm grid spacing). The particles were sampled at the outlet to obtain the exit age of every massless particle. The maximum exit age was 140s, however these old particles have an unrepresentative impact on the mean (The massless particles in this simulation represent tiny elements of tracer that would be used in an impulse response experiment. Each massless particle has a concentration of 1/4200 of the total tracer, for the elements of tracer they represent this concentration would be infinitesimal). The data was sampled from 1.03s to 31.03s with 100 size bins, which captured 99.9% of the massless particles. The resulting residence time distribution (exit age distribution function, E) is given in Figure 74.

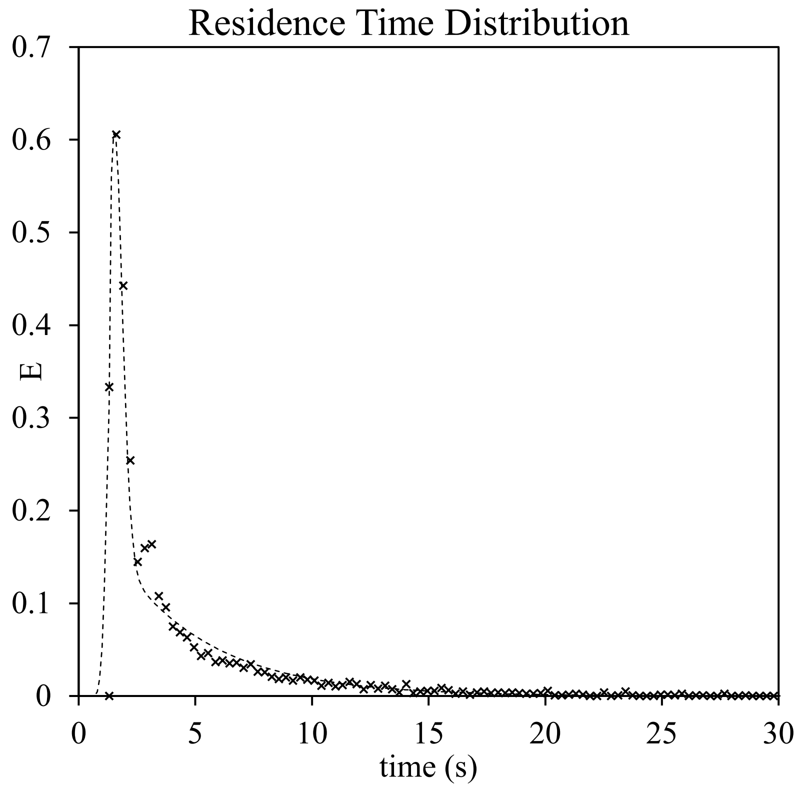

*Figure 74: Residence time distribution obtained by massless particle tracking.*

The resulting average residence time was 4.03s and the variance was 15.4s$^2$. This compares well to the calculated residence time $\tau_{ideal}$ = 4.04s based on the domain volume and volume-average density. The distribution shows a positive skew and a high kurtosis at 1.6s. The maximum (kurtosis peak) is earlier than the mean residence time: this is characteristic of bypass flow. Bypass flow may be approximated by a continuous stirred tank reactor in parallel with a plug flow reactor. The dotted line shown in Figure 74 shows an arbitrary curve of this type, fitted to give similar average residence time and variance.

The bypass flow is caused by the main jet flow in the model, which carries massless particles to the outlet at a fast rate. The recirculation regions create the tail of the distribution by delaying the massless particles from reaching the outlet. The data from Figure 74 implies a second peak at 3s, this is below the expected 4s, and so must also represent a bypass flow. Inspection of individual particle tracks revealed that, other than staying in the main jet flow completely, the second most popular particle trajectory is to complete a single recirculation before re-entering the jet. This causes the second peak. The geometry of the cryogenic condenser cannot be expected to produce perfect backmixing. If the recirculation regions created well mixed zones, then the flow could be expected to fit a tanks-in-series model. However a tanks-in-series system would create a clear peak at the mean residence time. This is not seen here, which suggests incomplete mixing is created by the recirculation regions.

### 6.3 Dynamic Eulerian-Lagrangian Model of Nucleation and Growth – 2D

To reduce computational load, initial results were obtained using a two-dimensional model. This consisted of a rectangular domain 1980 x 11.75mm. This is a parallel plate model, representing the space between two lamellae in the condenser, viewed end-on and ignoring baffles. The results from this work demonstrate a clear nucleation front that also enables clearer interpretation of the nucleation and growth behaviours inside the model. As the flow domain is extreme in its aspect ratio, the images of the flow domain are shown stretched in the y-direction by a factor of ten.

At inlet velocities that represent the condenser during operation, the flow in this 2D domain is predominantly laminar under simulation conditions. Figure 75 shows the results for a simulation using a transition SST (shear stress transport) model including the effects of heat transfer through a linear wall temperature profile. The data is sampled from a line three-quarters of the way into the condenser (x coordinate = 1.5m). The red cross represents the design point, equivalent to a 150Nm$^3$/hr flowrate through the condenser. As the velocity is increased from this point (shown by black crosses) the flow moves from laminar to turbulent flow. This is modelled in the transition SST model as a shift from an intermittency of zero (laminar) to one (turbulent). Inspection of contour plots (not shown) revealed the intended intermittency conditions (=1 in the core flow) were not achieved until inlet velocities were above 8m/s. Figure 75 (ii) shows a comparison with literature data taken from Whan and Rothus (1959) for transition flow between parallel plates (shown in grey). This author defines laminar flow as below $Re_{d\ hydraulic} = 2700$. The ratio of area-average velocity to maximum velocity is essentially an estimate of whether the velocity profile is laminar (plane Poiseuille flow, av.vel.:max.vel. = 2/3) or a fully turbulent velocity profile. Illustrated by the dotted line, this demonstrates that at the design flowrate, flow is laminar in the 2D parallel plates CFD model. The 3D model is turbulent while the 2D parallel plate model is laminar implying that the baffles are important for turbulent flow in the 3D model. The 2D model here shows a good fit to data for parallel plates, which suggests that buoyancy and other heat transfer effects do not affect flow significantly.

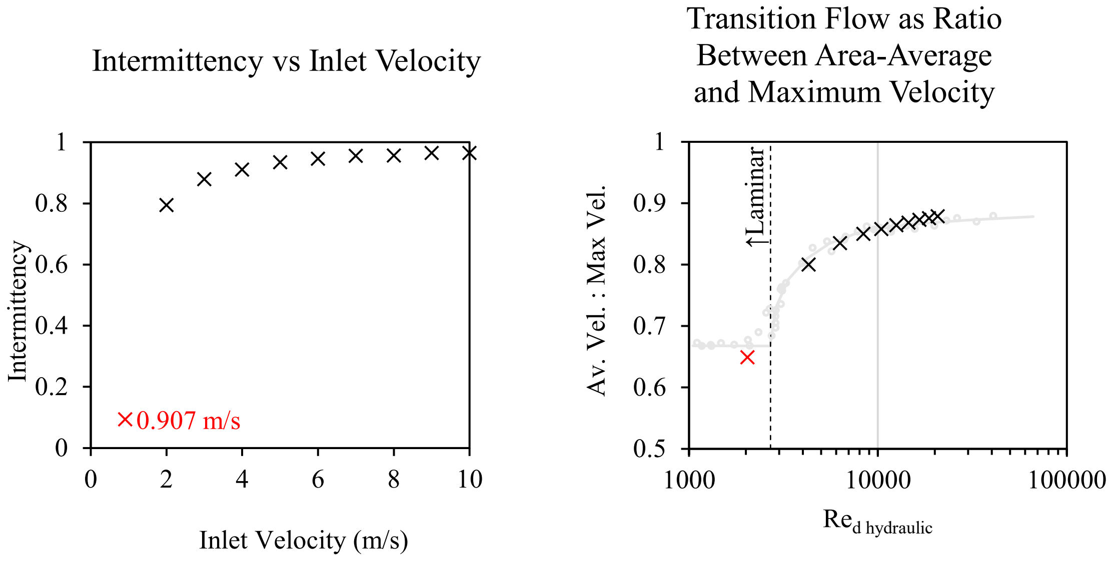

(i) (ii)

*Figure 75: Transition vs flowrate for 2D parallel plate model with heat exchange.*

Laminar and turbulent flows provide different challenges for modelling nucleation and growth in the 2D CFD model. In both cases, a stable solution of the basic fluid flow is necessary as a starting point for introducing the particles. As the transition flows are difficult to predict correctly (and flow solutions with the transition SST model can be challenging), the 2D nucleation and growth model was repeated under laminar conditions for the design flowrate (0.907 m/s), and with an increased flowrate (10m/s) to model turbulent flow. The results from the different turbulence models are compared in Figure 76 below. There are some differences between the two approaches as can be seen in the velocity profiles. Particularly for the turbulent cases. However for the turbulent case, this flowrate is significantly higher than the operating range of the equipment, and is intended only as a test case for the effect of turbulence on the growth and nucleation.

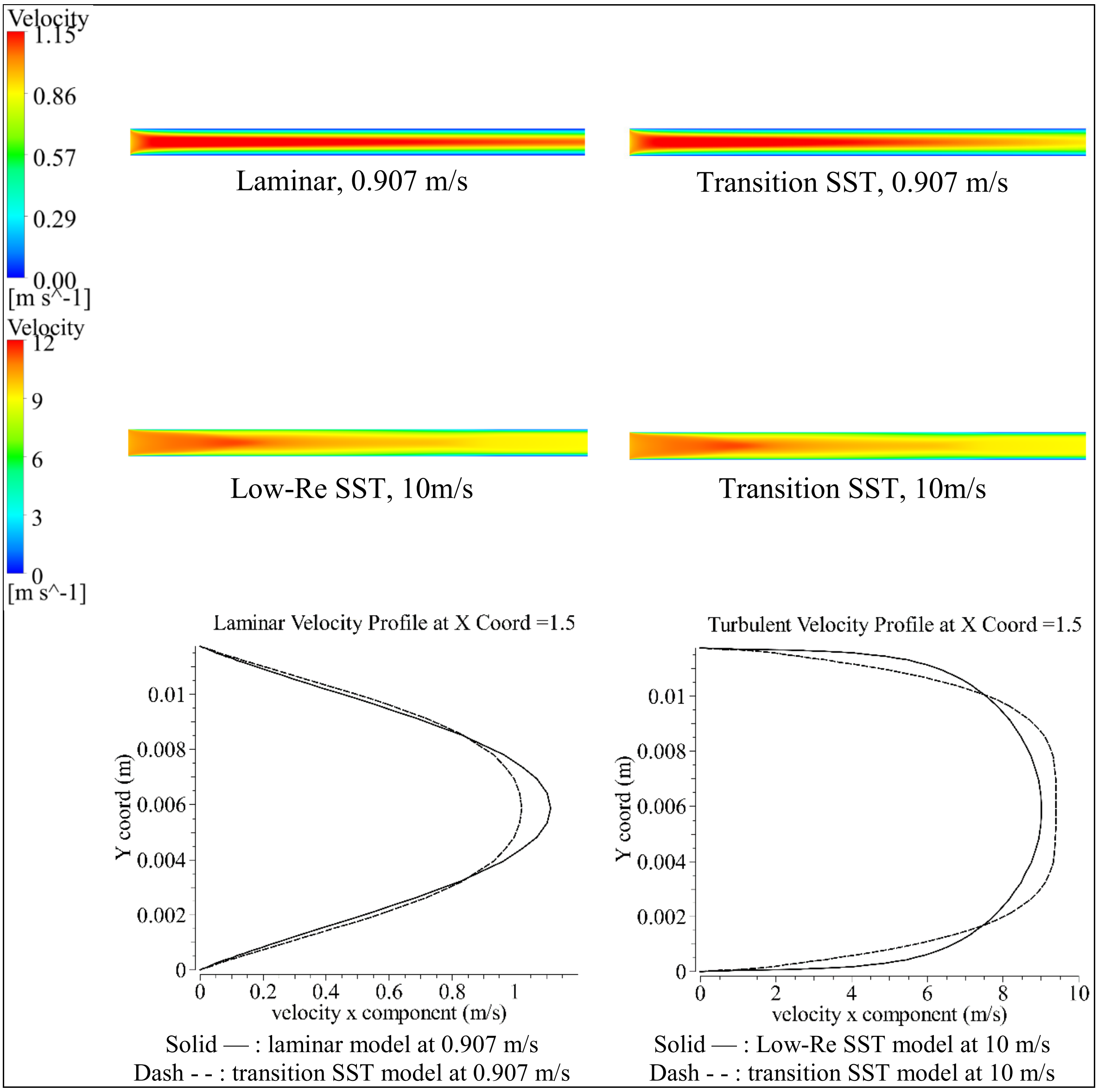

*Figure 76: Comparing turbulence models for the 2D parallel plates models with heat transfer only.*

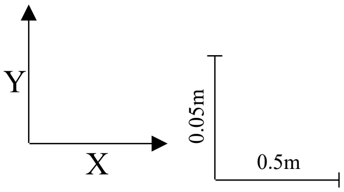

### *6.3.1 Laminar two dimensional model, Eulerian nucleation sources only.*

Eulerian sources are used in the model to define the nucleation. These remove benzene and add latent heat to cells where nucleation occurs. Mass flowrates extracted from the solution demonstrate the mass sources are functioning correctly: the sum of the mass source equals the mass removed, and this mass is entirely benzene. The mass balance is given in Table 21. The outlet benzene mass fraction is 0.0104; as this simulation predicts homogeneous nucleation only and not the particle growth, mass exchange stops below supersaturation. Similarly, an enthalpy balance demonstrates that the latent heat generation due to nucleation (33.4 W) is accounted for in the model.

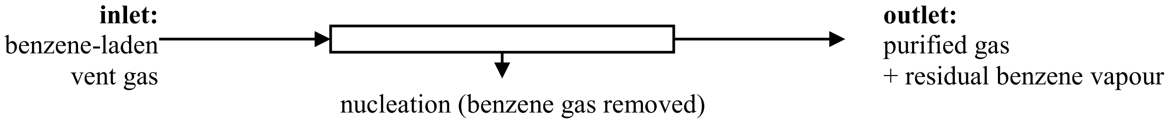

| | Benzene (kg/s) | Nitrogen (kg/s) | Total (kg/s) | Enthalpy (W) |
|---|---|---|---|---|
| Inlet | 1.93x10-4 | 1.28x10-2 | 1.30x10-2 | -218 W |
| Outlet | 1.36x10-4 | 1.28x10-2 | 1.30x10-2 | -1302 W |
| Nucleation | 5.71x10-5 | - | 5.71x10-5 | 33.4 W |
| | | | Wall cooling | 1116 W |

*Table 21: Mass-energy balance for laminar 2D nucleation-only model.*

A plot of the nucleation rate in each cell demonstrates that most of the nucleation occurs next to the wall. Figure 77 shows a plot of this. Note that tessellation in Figure 77 is due to the mesh and not the image quality. A maximum nucleation rate[§] of 0.0952 kg/m$^3$s (J = 1.07x10$^{16}$ nuclei/cm$^3$s) occurs in the near-wall region, compared to 3.96x10$^{-5}$ kg/m$^3$s (J = 2.31x10$^{12}$ nuclei/cm$^3$s) in the centreline. The temperature for supersaturation agrees with the calculated critical temperature shown earlier in section 6.1. Figure 78 shows the temperature profile, where the black line represents 220K, which coincides with the edge of the blue area in Figure 77.

---

[§] Calculated using cell-based values from fluent.

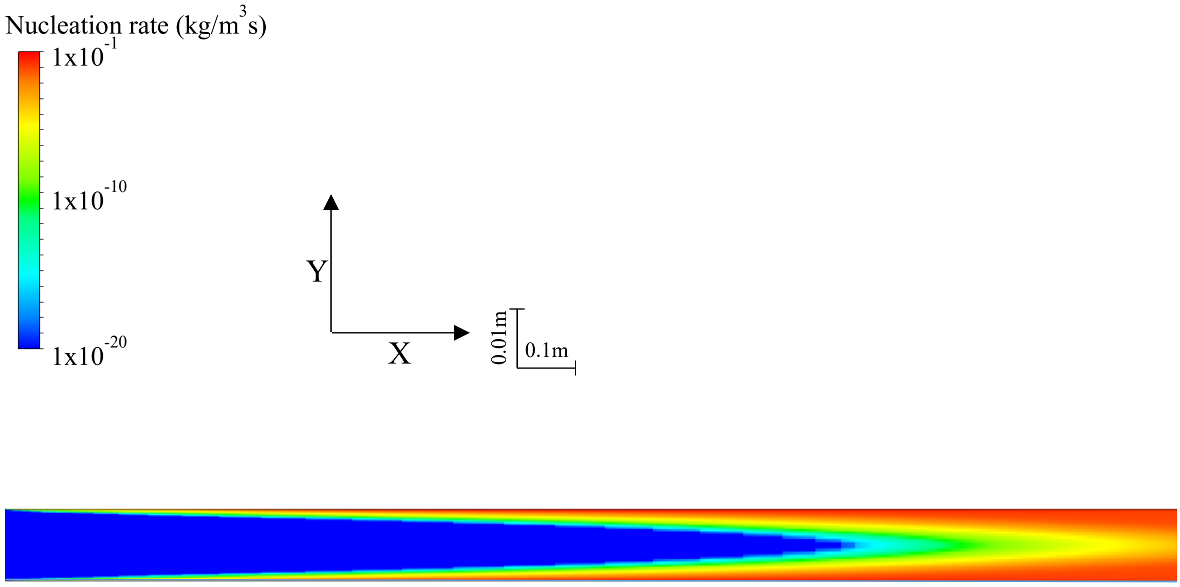

*Figure 77: Nucleation rate for 2D laminar nucleation only model.*

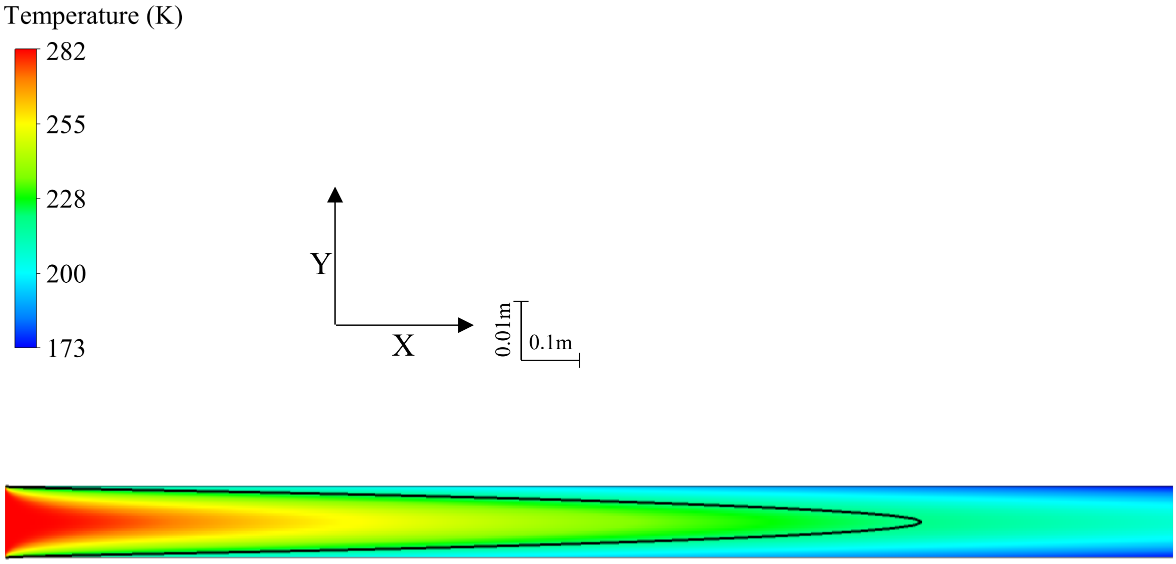

*Figure 78 Temperature profile for 2D laminar nucleation only model.*

### 6.3.2 *Laminar two dimensional model, nucleation and inert particles*

The laminar result with inert particle injections is shown below in Figures 79 and 80. This generates particles without applying any growth to them. Figure 80 illustrates the creation of the particles tracks in the domain. The largest particles form early-on in the flow, nucleation rate and critical particle size are both controlled by degree of supersaturation. This result demonstrates how the particles are generated inside the flow geometry.

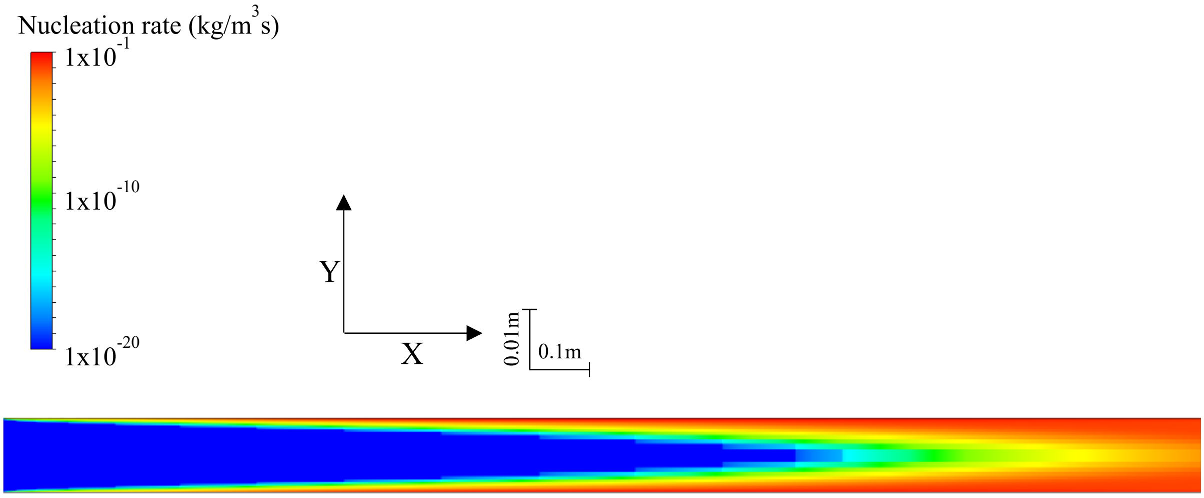

*Figure 79: Nucleation rate profile, nucleation with inert particles.*

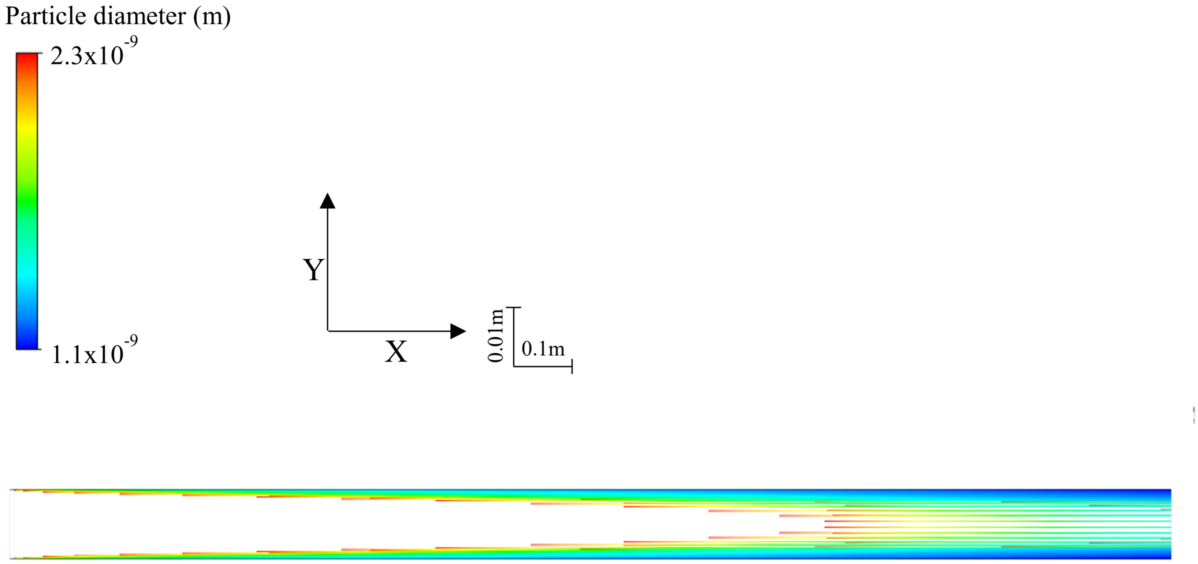

*Figure 80: Particle tracks, nucleation with inert particles.*

### *6.3.3 Laminar two dimensional model Eulerian nucleation and growth.*

Once the Eulerian sources for nucleation had been established, this information was used to generate particle injection locations at each cell centre. The particles are carried by the fluid flow. As they progress, the growth function removes benzene from the fluid cell and increases the particle diameter. The removal of benzene alters the nucleation locations in the fluid flow, the main difference being less nucleation downstream of the nucleation front as growth can remove benzene down to saturation ($S = 1$), while homogeneous nucleation requires a critical degree of supersaturation ($S_{crit,} > 1$). There is also far less nucleation overall, as the rapid particle growth depletes the gas-phase of benzene rapidly once nucleation occurs. The mass balance indicates that nucleation removes benzene from the system. The gas mass fraction at the outlet is $2.02 \times 10^{-3}$, or a partial pressure of 73 Pa, or a benzene concentration of 2.47g/Nm$^3$. However a significant amount of benzene escapes as particles at the outlet.

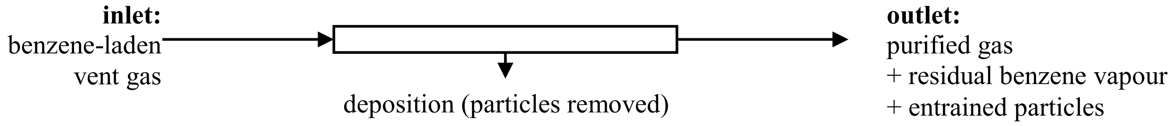

| | Benzene (kg/s) | Nitrogen (kg/s) | Total (kg/s) |
|---|---|---|---|
| Inlet | $1.93 \times 10^{-4}$ | $1.28 \times 10^{-2}$ | $1.30 \times 10^{-2}$ |
| Outlet | $2.59 \times 10^{-5}$ | $1.28 \times 10^{-2}$ | $1.28 \times 10^{-2}$ |
| Nucleation | $8.28 \times 10^{-16}$ | - | $8.28 \times 10^{-16}$ |
| Growth | $1.67 \times 10^{-4}$ | - | $1.67 \times 10^{-4}$ |

| Particle massflows: | Benzene (kg/s) |
|---|---|
| Outlet | $9.61 \times 10^{-5}$ |
| Base wall | $3.55 \times 10^{-5}$ |
| Top wall | $3.55 \times 10^{-5}$ |

*Table 22: Mass balance for 2D laminar nucleation and growth model.*

The energy balance is shown in Table 23 shows that the growth source is a combination of latent heat, plus an enthalpy balance based on the flow of mass to the particle surface (calculated from the particle heat capacity using a Hess' law type calculation).

| | |
|---|---|
| Inlet stream enthalpy | -219 W |
| Outlet stream enthalpy | -1288 W |
| Wall cooling | 1185 W |
| Growth source | 115 W |
| Latent heat, nucleation | $4.7 \times 10^{-10}$ W |

*Table 23: Energy balance for 2D laminar nucleation and growth model*

The resulting nucleation front in Figure 81 differs to the result shown in Figure 79. As growth depletes the surrounding fluid of benzene vapour, the nucleation rate lowers ($1.33 \times 10^{-6}$ maximum) and the nucleation front becomes a narrow band within the flow where particles are generated. Particle tracks are shown in Figure 82. These demonstrate the particles are generated at the onset of nucleation. The highest concentration of particles is in the near-wall region.

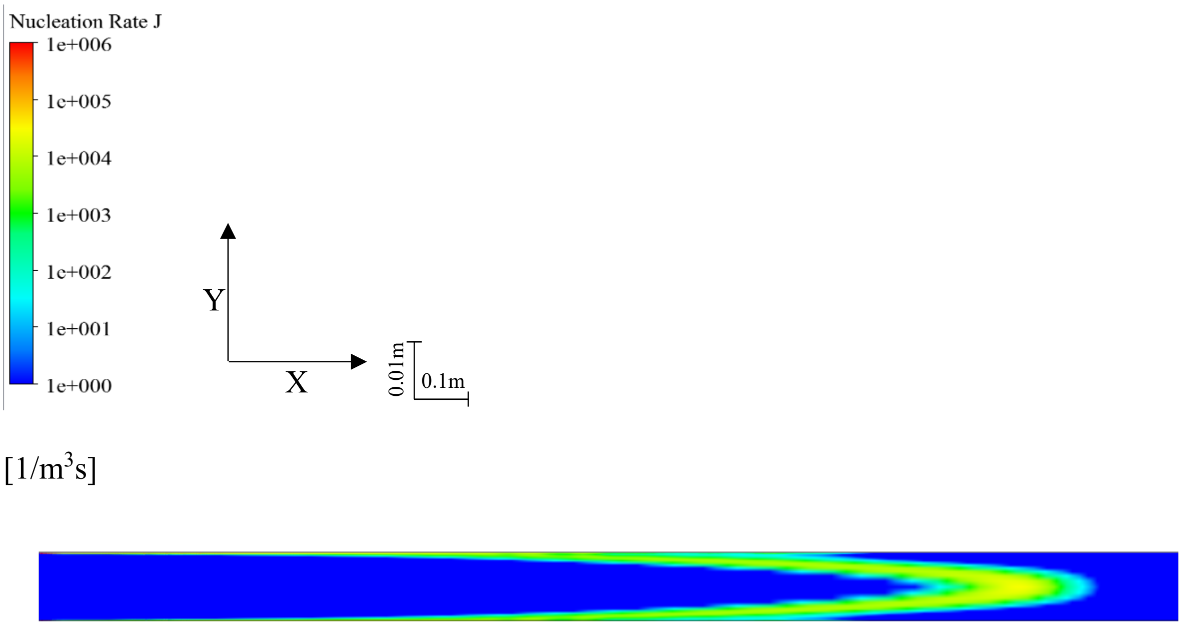

*Figure 81: Nucleation front.*

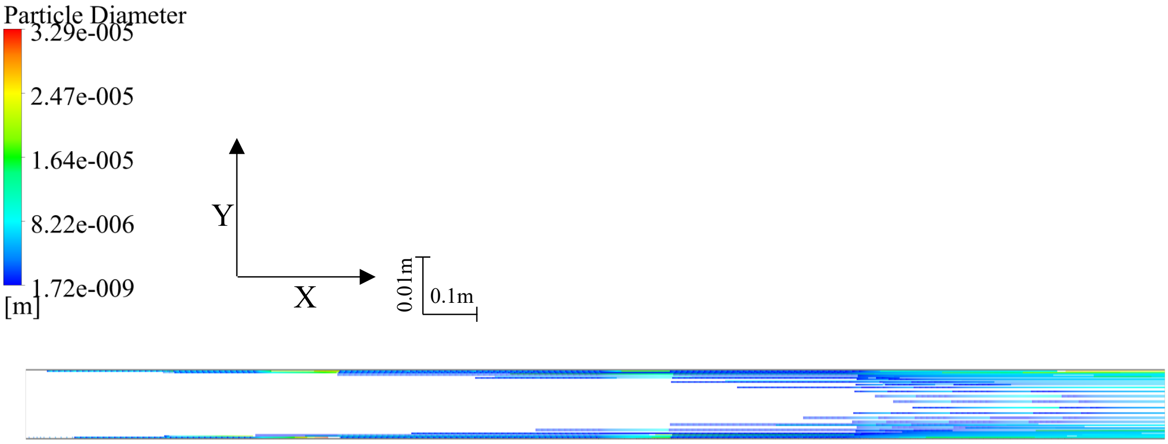

*Figure 82: Generation of particles in domain.*

Figure 83 demonstrates the nucleation and growth profiles along the centreline of the 2D model. The concentration of benzene vapour falls slowly initially, as a result of diffusion processes toward particle tracks in the near-wall cells. Through the first three-quarters of the model (x coord = 0 to 1.6m) the degree of supersaturation increases steadily as the gas is cooled. When the critical degree of supersaturation is reached, nucleation is rapid but removes very little mass from the gas phase. Particle growth follows nucleation and is responsible for removing most of the benzene vapour from the gas phase. This causes the degree of supersaturation to fall back down, asymptotically approaching saturation (S = 1).

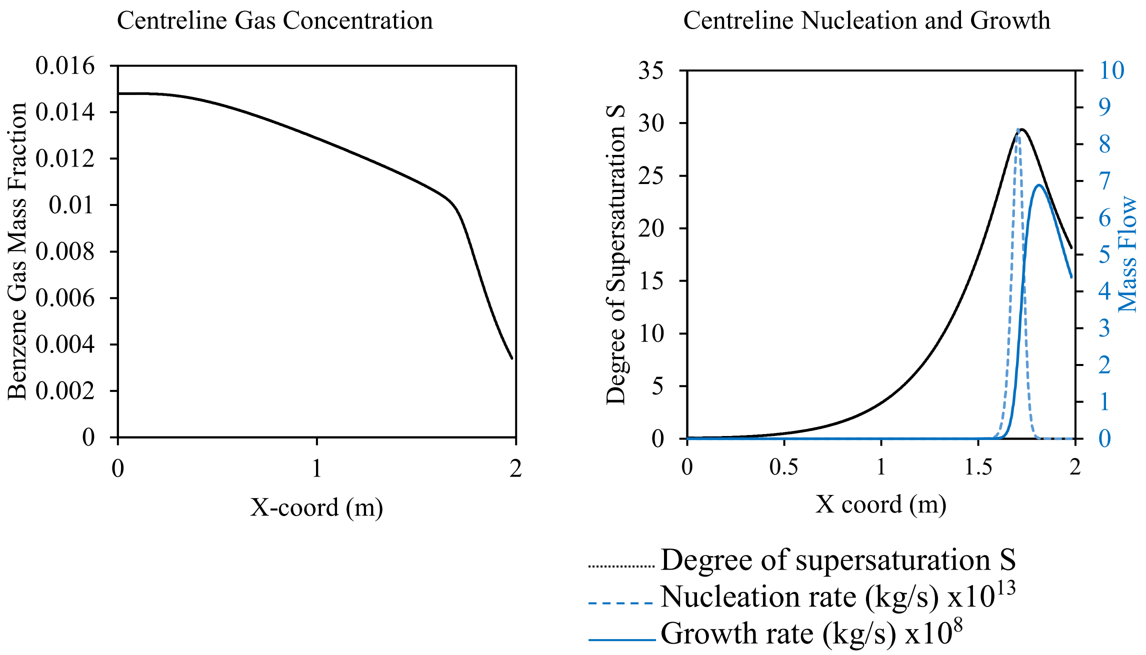

*Figure 83: Nucleation and growth behaviour along centreline.*

Particle histograms are shown in Figure 84. The average size of the nucleus is between 1-2 nanometers. This then grows to an average particle size of 5μm.

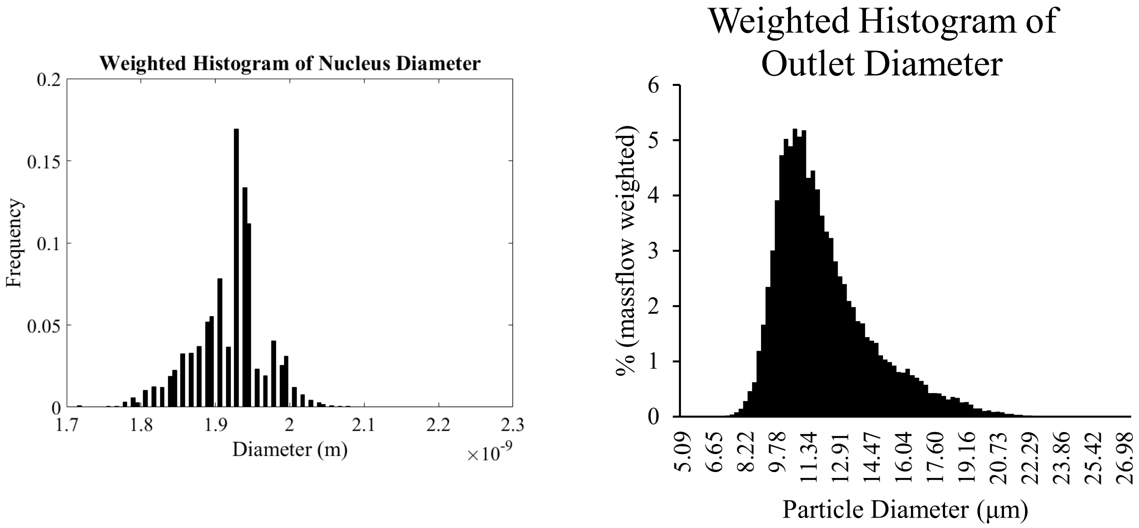

(i) (ii)

*Figure 84: Particle statistics for laminar 2D model.*

### *6.3.4 Turbulent case two dimensional model, Eulerian nucleation sources only.*

The simulation described in section 6.3.1 was repeated at an inlet velocity of 10m/s, using the low-Re SST model. The mass balance in Table 24 shows an increase in massflow, but an otherwise similar result to Table 21 above. Nucleation rate and temperature profiles are shown in Figure 85 and Figure 86, respectively. A maximum nucleation rate of 4.01 kg/m$^3$s (J = 7.07x10$^{17}$ nuclei/cm$^3$s) occurs in the near-wall region, compared to 5.55x10$^{-7}$ kg/m$^3$s (J = 2.63x10$^{10}$ nuclei/cm$^3$s) in the centreline. Cooling is delayed when compared to the laminar case, due to the increased flowrate. In comparison to the laminar case, more nucleation occurs at the walls, while less occurs in the centre. This is due to the increased effective diffusion that results from turbulent flow.

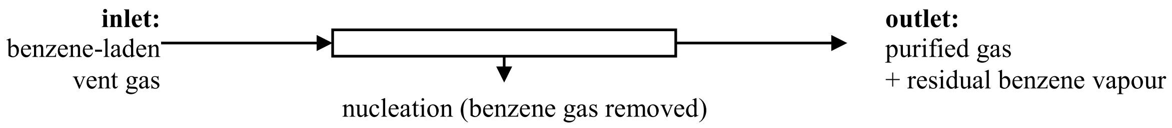

| | Benzene (kg/s) | Nitrogen (kg/s) | Total (kg/s) | Enthalpy (W) |
|---|---|---|---|---|
| Inlet | 2.13x10$^{-3}$ | 0.141 | 0.144 | -2418 W |
| Outlet | 1.17x10$^{-3}$ | 0.141 | 0.144 | -13563 W |
| Nucleation | 4.46x10$^{-4}$ | - | 4.46x10$^{-4}$ | 254 W |
| | | | Wall cooling | 11398 W |

*Table 24: Mass-energy balance for turbulent 2D nucleation-only model.*

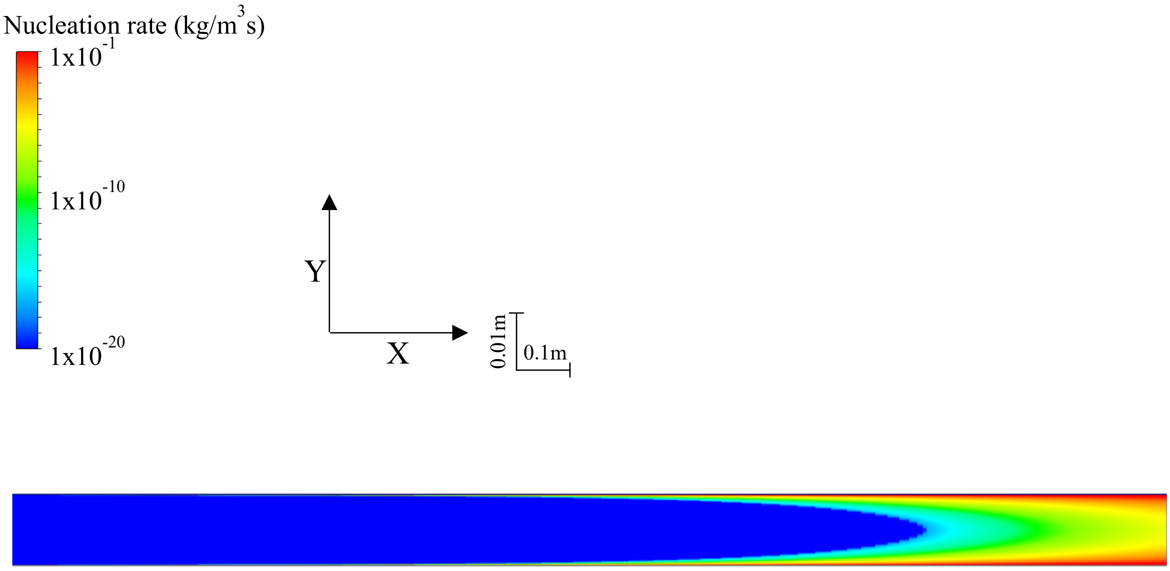

*Figure 85: Nucleation rate for 2D turbulent nucleation only model.*

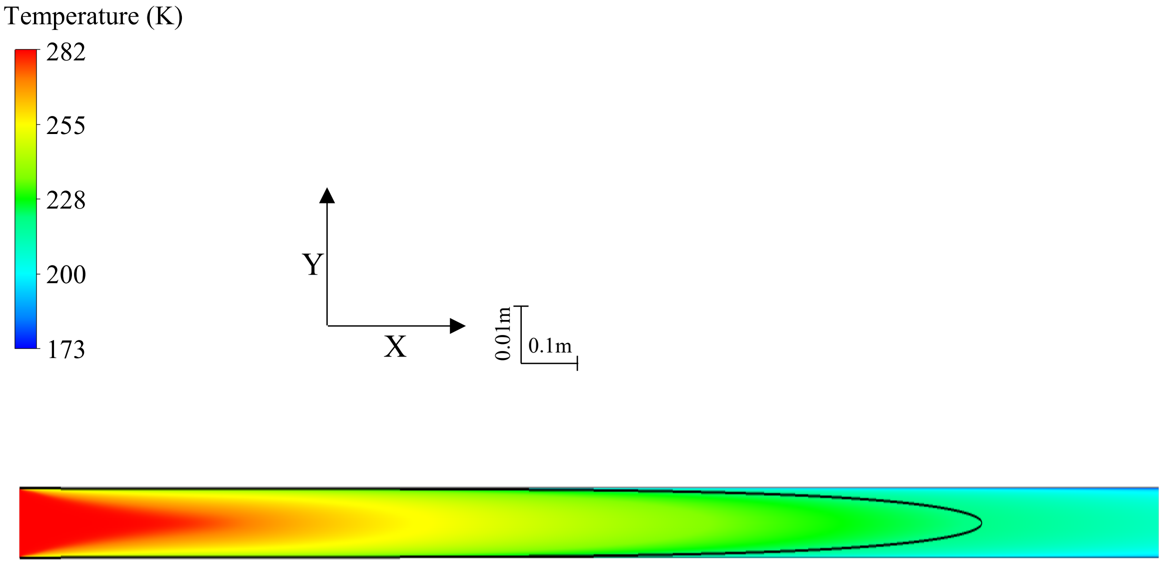

*Figure 86: Temperature for 2D turbulent nucleation only model.*

### 6.3.5 *Turbulent two dimensional model, nucleation and growth.*

Results for the 2D turbulent simulation are shown below. The mass balance (Table 25) indicates that again most of the benzene is removed from the system by growth. The gas mass fraction at the outlet is $2.7\text{x}10^{-3}$, corresponding to a partial pressure of 100 Pa, or a gas concentration of 3.4 g/Nm$^3$. A significant amount (41%) of particles escape at the exit, however this is an improvement on the laminar result.

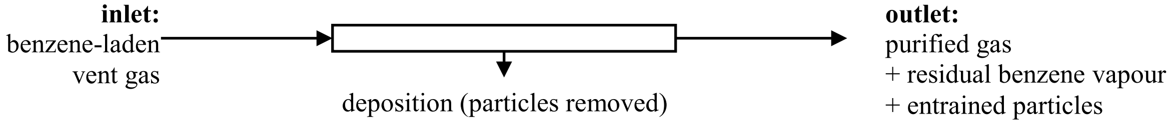

| | Benzene (kg/s) | Nitrogen (kg/s) | Total (kg/s) |
|---|---|---|---|
| Inlet | $2.13\text{x}10^{-3}$ | 0.141 | 0.144 |
| Outlet | $3.88\text{x}10^{-4}$ | 0.141 | 0.142 |
| Nucleation | $5.32\text{x}10^{-9}$ | - | $5.32\ \text{x}10^{-9}$ |
| Growth | $1.74\text{x}10^{-3}$ | - | $1.74\text{x}10^{-3}$ |

| Particle massflows: | Benzene (kg/s) |
|---|---|
| Outlet | $7.11\text{x}10^{-4}$ |
| Base wall | $4.97\text{x}10^{-4}$ |
| Top wall | $5.12\text{x}10^{-4}$ |

*Table 25: Mass balance for 2D turbulent case.*

| | |
|---|---|
| Inlet stream enthalpy | -8998 W |
| Outlet stream enthalpy | -15955 W |
| Wall cooling | 13555 W |
| Growth source | 6659 W |
| Latent heat, nucleation | $2.98\text{x}10^{-3}$ W |

*Table 26: Energy balance for 2D turbulent case.*

In the turbulent model, the effect of turbulence on the particle trajectories is modelled using a discrete random walk model. The result of this can be seen in Figure 88. Particles that form in the laminar sublayer are not affected by the turbulent mixing. However, particles that form outside of the laminar sublayer are mixed with the flow. Turbulent mixing increases the effective diffusivity of benzene vapour. As a result mass transfer is improved, concentration gradients are not as steep. Therefore, in comparison to the laminar flow model, less bulk nucleation is observed, as more mass-removal occurs for the near-wall cells. This is observable when comparing Figure 83 to Figure 89. However, in the turbulent model, due to the 10m/s flowrate the gas is not fully cooled, so the nucleation profile is not fully captured by the model.

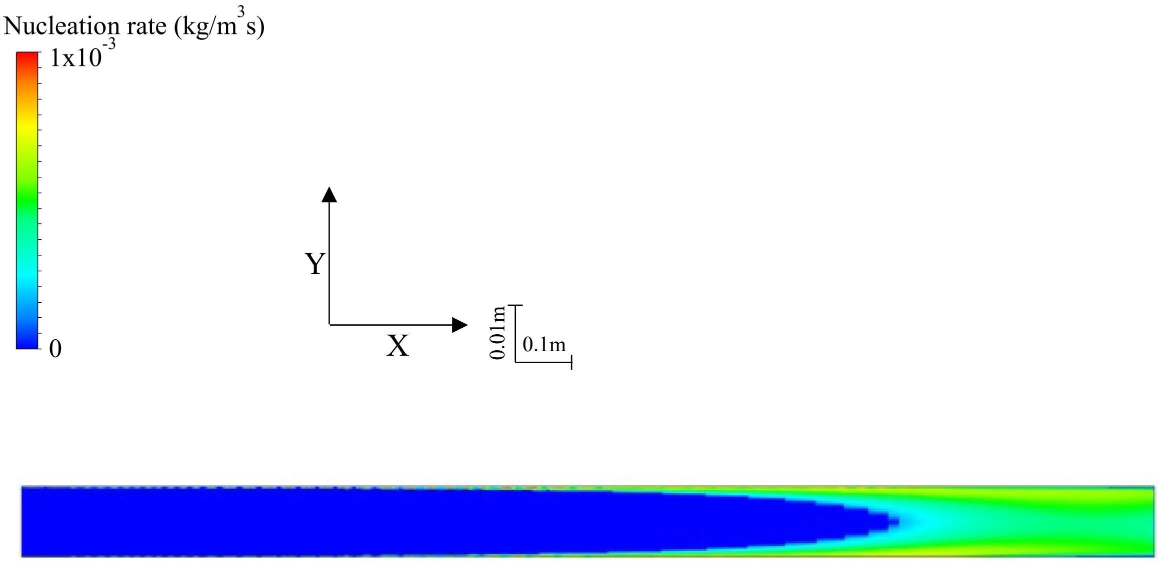

*Figure 87: Nucleation rate for turbulent 2D case.*

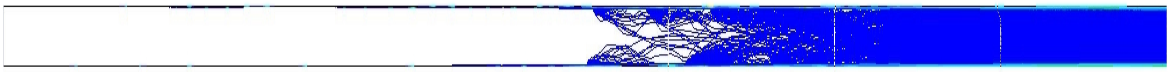

*Figure 88: Particle tracks for turbulent 2D result.*

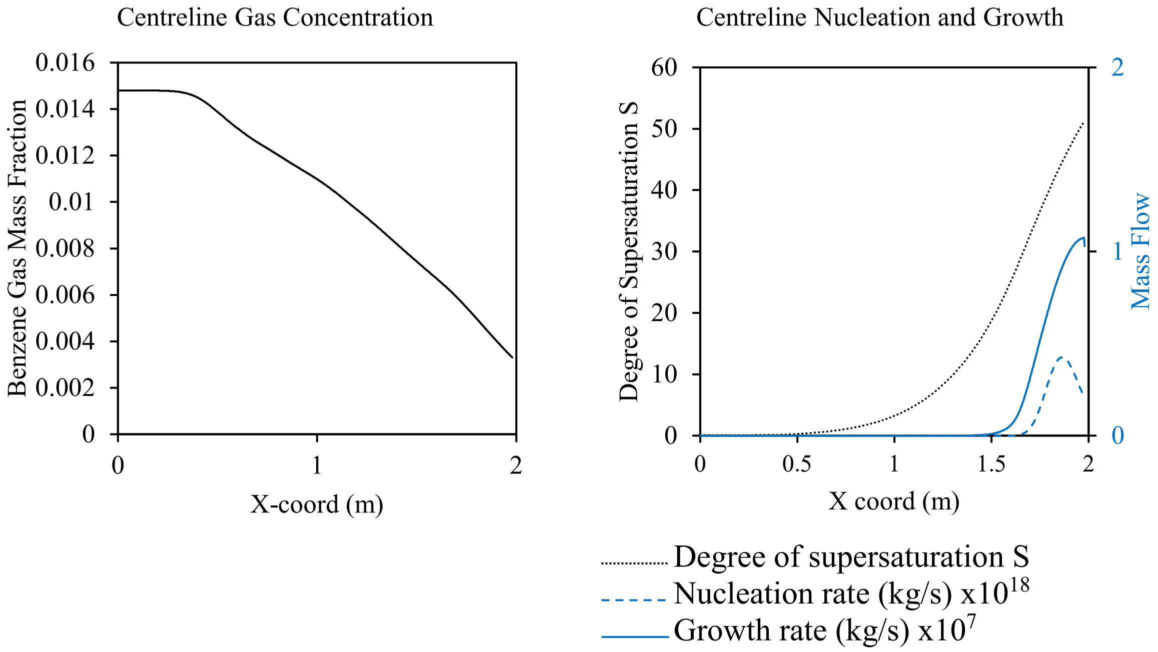

*Figure 89: Turbulent 2D parallel plates model nucleation and growth along centreline.*

The histograms in Figure 90 show that the nucleation occurs at a similar critical nucleus diameter in both the laminar and turbulent cases is due to the reduction in nucleation rate in comparison to the laminar result, as a lower initial concentration of nuclei would result in more growth before they obtain equilibrium with the gas phase., which is the expected result. Particles grow to a larger diameter for the turbulent flow.

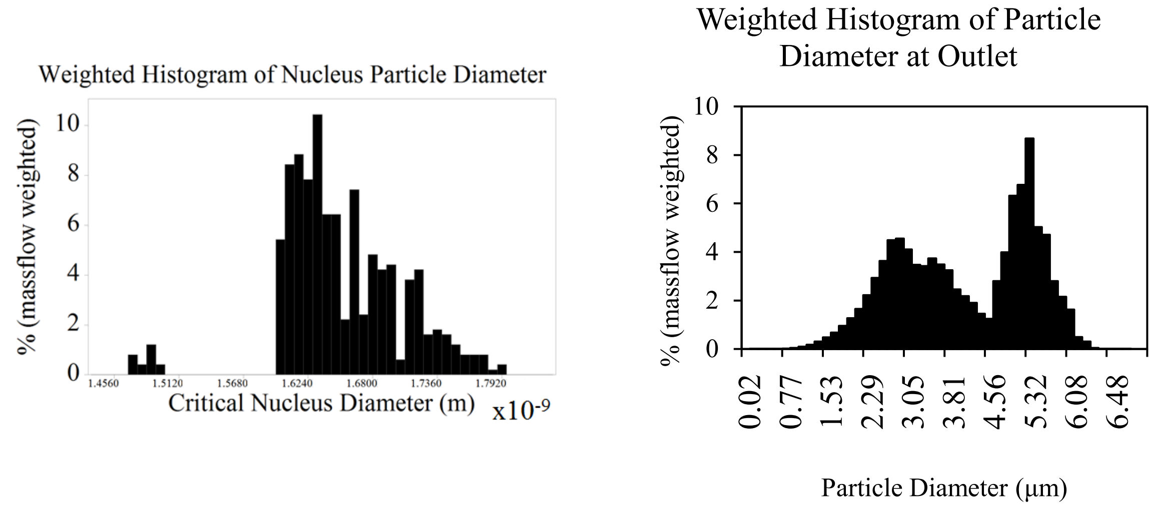

*Figure 90: Particle statistics for turbulent 2D parallel plates model.*

## 6.4 Full Three Dimensional Nucleation and Growth Model

The nucleation and growth model is numerically stiff and so requires many iterations to reach a converged solution. The addition of the mesh requirements of the model and the high computational load of particle simulation leads to a very computationally expensive model. The full model result reported below was completed with a k-ε type model. This was chosen instead of an SST model because the solution convergence of the k-ε type models in flow-only simulations of the cryogenic condenser tended to be more reliable than the SST-type models. The flow simulation should converge in a predictable manner before the introduction of particles with two-way coupling into the model. This is because when the Eulerian-Lagrangian model is iterated, the fluid flow simulation must be solved between the discrete phase model (DPM) iterations. Therefore, a realizable k-ε model with enhanced wall treatment (a low-Re approach) was chosen for the turbulence model for this result. The simulation was second order accurate.

### *6.4.1 Comparison for change in the turbulence model*

The full nucleation and growth result used a Low-Re k-e model with fully second order discretisation, while the flows reported elsewhere in the thesis used a Low-Re SST model with power-law momentum discretisation. This change in turbulence model requires a check on the accuracy to the flow. A comparison is provided in Figure 91, for modelled flow inside the similitude model. With reference to the results from the previous chapter (sections 5.2.2 and 5.2.3), it is clear that the differences between the two models are a result of using a fully second order momentum discretisation rather than difference from the turbulence modelling approach.

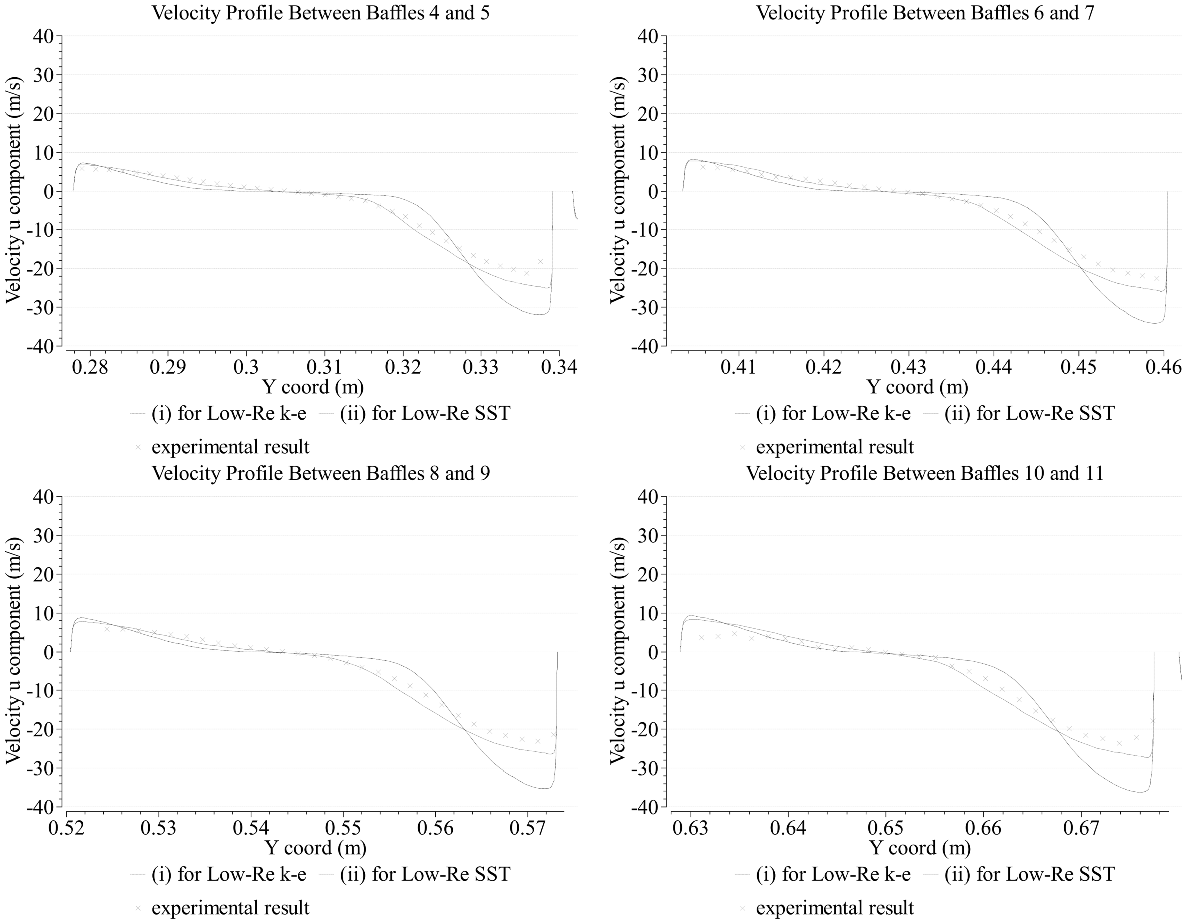

*Figure 91: comparison of turbulence model used in the full 3D nucleation and growth result (Low-Re k-ε model) with that used elsewhere in the thesis (Low-Re SST model).*

### *6.4.2 Results*

Figure 92 gives an indication of the nucleation front inside the model. Note that Figure 92 is coloured by distance from the cooled wall (in the Z-direction): White areas represent no nucleation, blue areas represent near-wall nucleation, and other colours represent nucleation in the bulk gas flow. As with the 2D result, most nucleation occurs near the cooled surface (blue areas). Areas of other colours are of most interest for generating particles that become entrained in the gas phase. Figure 92 predicts these will form in the space between baffle 4 and 5. This compares well to the temperature boundary covered earlier (Figure 67 p.149). Areas are also observable where bulk nucleation occurs. Recirculation, particularly above baffles 1,2,3 and 12, shows bulk nucleation occurring, most likely due to cooling in these areas. The surface of the jet also shows nucleation locations, where the jet flow mixes with colder fluid in the recirculation regions. Nucleation by mixing is a common mechanism by which supersaturation is reached and mists can form in real-life scenarios (for example: in rising steam condensation clouds above hot water). However, the resulting isolated cells of nucleation locations in the model may be problematic when solving the simulation.

Particle trajectories are shown in Figure 93 below. This result has not included the effects of turbulence on particle trajectories as the resulting computational load would be unacceptable. Most of the large particles are present between baffles 1 to 7. In this area the vapour concentration is still high, providing a driving force for growth. These particles exit the fluid domain by collisions with the wall surfaces, removing benzene from the system. Towards the top of the condenser, (between baffles 8 and 14), there is clearly a greater quantity of fine particles.

The mass balance reveals an outlet mass fraction of $3.66\text{x}10^{-4}$, corresponding to a partial pressure of 13 Pa, and a gas concentration of 427mg/Nm$^3$. This shows the condenser will not be capable of obtaining the required 5mg/Nm$^3$ emission limit for benzene vapour according to these simulations. The outlet gas is significantly supersaturated (S = 160).

| | Benzene (kg/s) | Nitrogen (kg/s) | Total (kg/s) |
|---|---|---|---|
| Inlet | $2.27\text{x}10^{-5}$ | 0.00151 | 0.00153 |
| Outlet | $5.54\text{x}10^{-7}$ | 0.00151 | 0.00151 |
| Nucleation | $6.14\text{x}10^{-15}$ | - | $6.14\text{x}10^{-15}$ |
| Growth | $2.20\text{x}10^{-5}$ | - | $2.20\text{x}10^{-5}$ |

| Particle massflows: | Benzene (kg/s) |
|---|---|
| Outlet | $1.83\text{x}10^{-7}$ |
| Walls | $1.09\text{x}10^{-5}$ |

*Table 27: Mass balance: 3D model of nucleation and growth.*

| | |
|---|---|
| Inlet stream enthalpy | -26.7W |
| Outlet stream enthalpy | -185W |
| Wall cooling | 173W |
| Growth source | 15.3W |
| Latent heat, nucleation | $3.49\text{x}10^{-9}$W |

*Table 28: Energy balance for 3D model of nucleation and growth.*

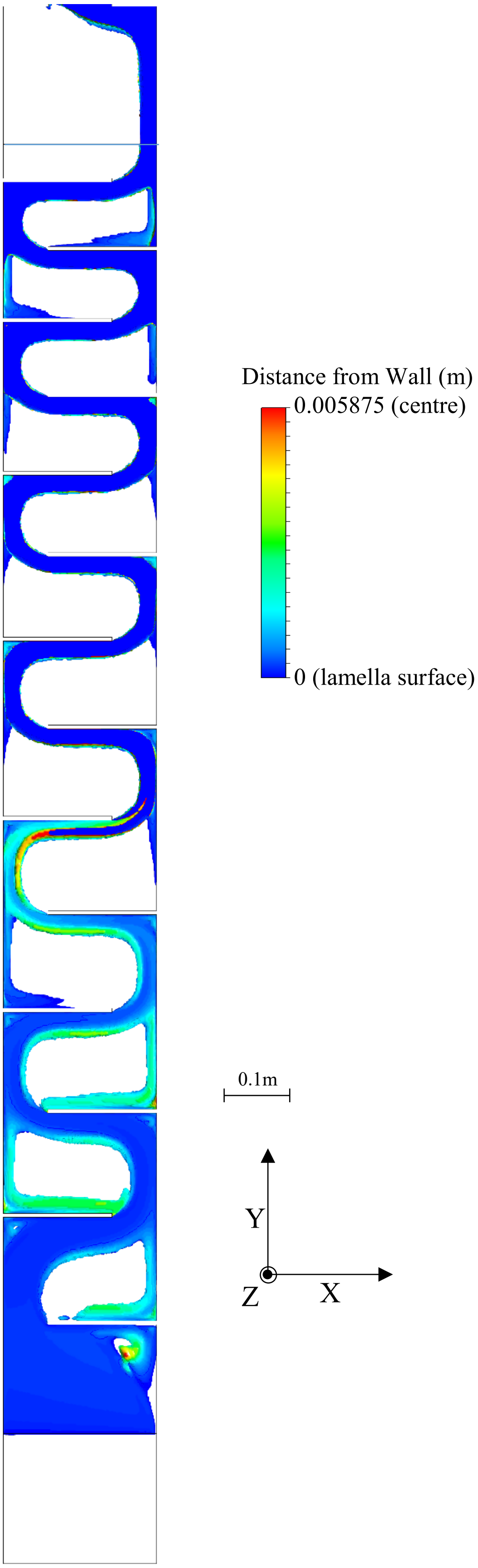

Figure 92: Nucleation locations, coloured by distance from wall.

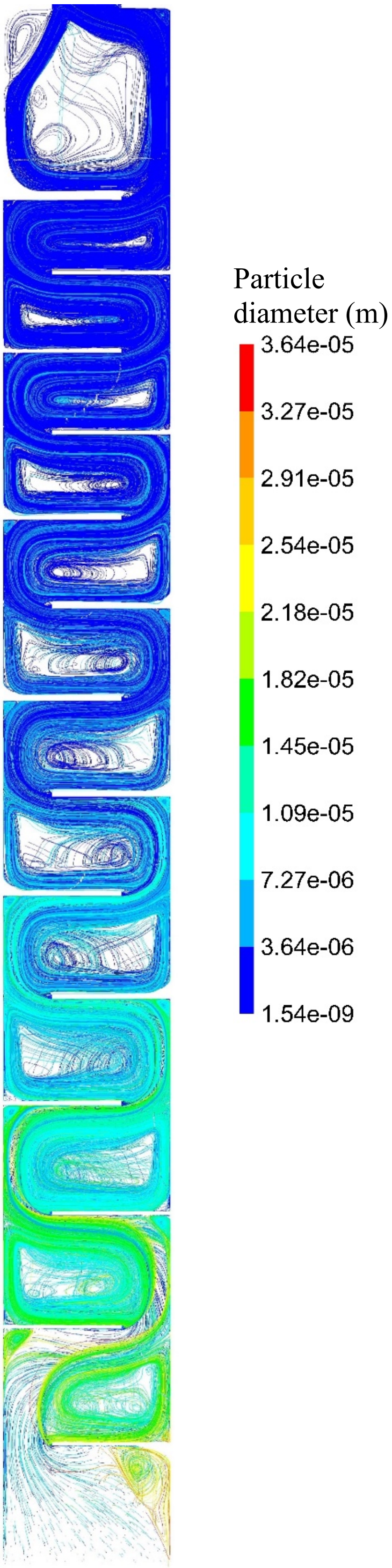

Figure 93: Particle tracks, coloured by particle diameter.

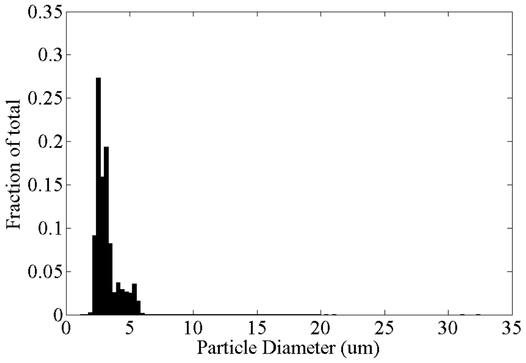

*Figure 94: Mass flow-weighted histogram of particle escaping model at the outlet, for full nucleation and growth model.*

A concentration profile for the full 3D model is shown in Figure 95 below. This has been prepared in a manner similar to the temperature profiles shown earlier. The overall profile is similar to the temperature profile. The recirculation regions have lower benzene gas concentrations due to the colder flow and longer residence times the recirculation offers. The standard deviations (represented by the error bars) support the conclusion that most of the dynamics of nucleation and growth occur in the first half of the condenser.

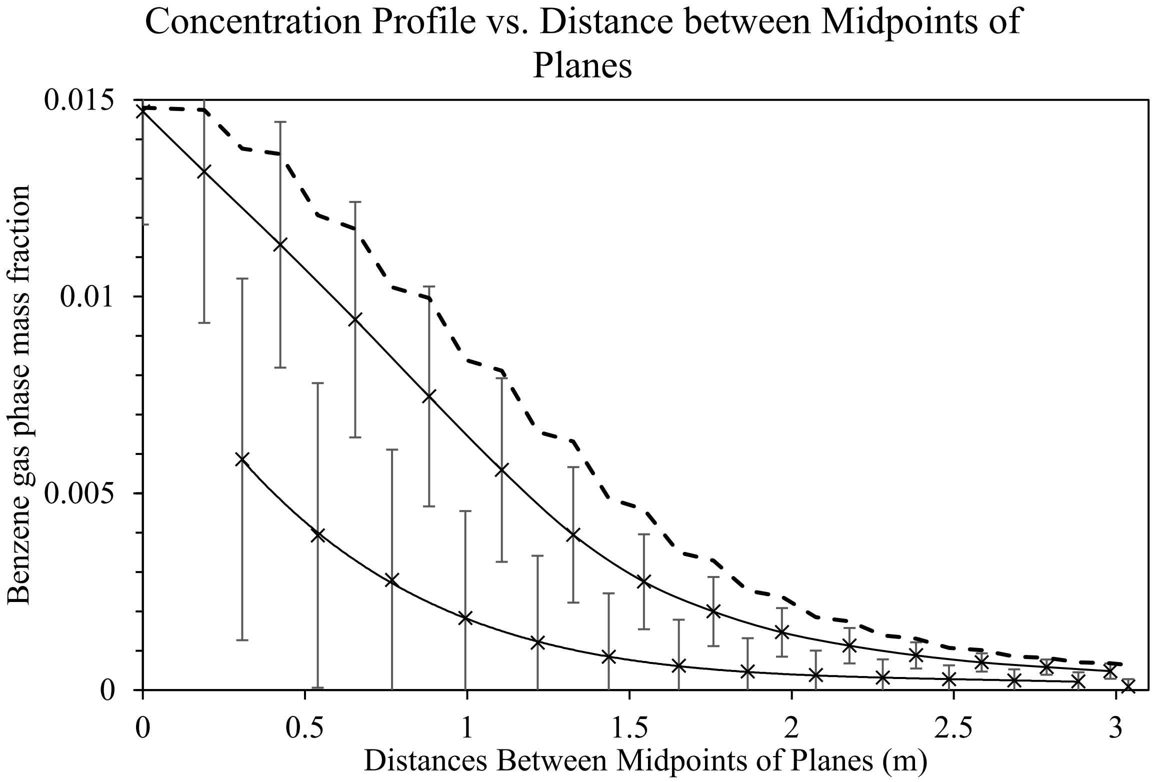

*Figure 95: Gas-phase concentration profile for the full 3D model including nucleation and growth. crosses X : area-weighted average concentrations; dashed line - - : maximum concentrations; error bars: standard deviation. .*

## 6.5 **Conclusions**

This chapter has focussed on expanding the basic CFD fluid flow simulation to model particle behaviour in the gas. The temperature profile demonstrated that the fast cooling achieved inside the condenser leads to water vapour nucleating a very short distance into the condenser. Benzene desublimation occurred later in the condenser: between baffles 2 and 3 for heterogeneous nucleation and between baffles 4 and 5 for homogeneous nucleation. These locations did not change significantly with flowrate.

The inert Eulerian-Lagrangian modelling investigated several phenomena and their influence on particle capture. Turbulence has a noticeable effect on particle capture, improving particle capture by directing particles towards the walls by random motion. Thermophoresis is an important capture mechanism for small particles, the diameter for capture ($d_{p99\%}$ ,= 12 μm) was not affected by the inclusion of thermophoresis in the model. The Cunningham slip factor increased the particle capture slightly for small particles below the Knudsen number transition, but otherwise modelled particle drag identically to the spherical drag model. The location of homogeneous vs heterogeneous nucleation did not significantly affect the capture efficiency. At lower flowrates, the diameter for capture increased, this indicated that inertial deposition is the dominant mechanism for particle capture at this particle diameter. The particle accretion study provided further understanding of this. The massless particle tracking showed the residence time distribution was affected by bypass transition from the main jet and incomplete mixing in the recirculation regions.

The nucleation and growth modelling was first applied to a 2D parallel plate geometry. Nucleation produced a concentrated particle stream in the near wall region and a nucleation front across the flow domain. Homogenous nucleation produced a particulate in the gas flow. Turbulent flow was modelled by increasing the velocity. This showed a reduced amount of particulate in the bulk because of turbulent diffusion. The full 3D model provided information on the outlet vapour and particle concentrations.

# Chapter 7. Conclusions

In reference to the research question outlined in the introduction, The Eulerian-Lagrangian model has been successfully developed and applied, in a computational fluid dynamics (CFD) context, to model nucleation and growth in the case under study. This model predicts that the cryogenic condensation will reduce the benzene vapour concentration significantly but will not reach the emissions limit required by environmental regulators. In this case the author recommends the use of an adsorption polishing step following cryogenic condensation. This was also suggested by Gupta and Verma (2002). This may appear futile at face value, however the cryogenic condenser will produce a cold, de-humidified gasflow of low initial volatile organic compounds VOC concentration, which is ideal for treatment using adsorption. As a polishing step, hydrophobic zeolite may be used to eliminate the bed-fire hazard posed by activated carbon. A smaller unit size will dramatically reduce many of the impacts a larger adsorption process would carry, such as sorbent replacement, financial costs, energy demand and safety hazards.

Currently, cryogenic condenser design strategies focus on achieving working designs that can operate in practice. Comparatively little information is available to allow for more detailed design procedures for cryogenic condensation processes. Currently site trails at full scale (where the equipment is leased to the customer) play a significant role in equipment specification. Every chemical process is different, and assessing applications *in-silico* could substantially reduce the real-world cost of these site trials. This thesis has aimed to take a first step in this direction, but it is clearly an unexplored area for future potential research.

## 7.1 Summary of Findings

The results of simulation have determined an outlet vapour concentration of 427mg/Nm$^3$. This is above the 5mg/m$^3$ limit required by environmental regulation. Particle entrainment is expected to result in 1% of incoming benzene leaving the condenser as aerosol, in the absence of any capture methods used downstream (such as a mist eliminator).

The results of the fluid flow simulations inside the condenser geometry shows a characteristic flow pattern, consisting of a main jet flow with recirculating patterns forming between the baffle spaces. Comparison with particle image velocimetry (PIV) measurements indicated this was a good physical description of the flow. Many of the simplifications used in the modelling, actually improved the fit to the experimental data from the PIV. In the CFD results, massless particle tracking gave information on residence time distribution showing a strong tendency for bypass flow as a result of the main jet. The temperature profiles were obtained using the sampling planes. This indicated that the recirculation patterns were significantly colder than the main gas flow, due to the slower velocities, and therefore longer timespans spent in contact with the wall. This gas temperature profile could not have been predicted by simpler flow modelling methods, such as a one-dimensional model.

The temperature profile led to insights into temperature dependent phenomena in the condenser. A close approach temperature (ca. 5°C) is achieved at the outlet. For the vapour concentrations analysed in this work, the fast cooling of the process gases means that water nucleation occurs a short distance into the condenser. Benzene desublimation occurs later in the exchanger: between baffles 2 and 3 for heterogeneous particle formation and between 4 and 5 for homogeneous nucleation. These locations do not change significantly with flowrate.

The inert Eulerian-Lagrangian model results indicated that thermophoresis is an important capture mechanism for small particles. The smallest diameter with a capture efficiency of >99% ($d_{p>99\%} = 12\ \mu m$) was not significantly affected by the inclusion of thermophoresis in the model. The location of homogeneous nucleation was also found not to significantly affect capture. Particle tracking results indicated that inertial deposition based on flow curvature was an important mechanism in the deposition of these larger particles.

## 7.2 Original Contribution to Knowledge

This study has developed a Eulerian-Lagrangian model of nucleation and growth of an aerosol in CFD. As was discussed in the literature review chapter (section 2.8), this does not have any direct parallels in work relating to cryogenic condensation. Modelling of a cryogenic condenser in CFD as a separation process has also not been addressed previously in open literature. The fluid flow modelling in itself should also not be overlooked as an original contribution. Although heat exchanger modelling in CFD is a well-studied field, the geometry and the transitional flow modelling in this work represent an original contribution. Flows in heat exchangers are often weakly turbulent ($Re_{dh} < 10{,}000$), because the high heat transfer coefficients in turbulent flow must be balanced against other practicalities, such as pressure drop. Heat exchanger modelling typically requires boundary layer mesh refinement, to properly model heat transfer in the boundary layer. Relatively few publications deal with condensation from inert carrier gases in CFD, and literature review reveals fog formation inside such condensers is still far from completely understood.

## 7.3 Importance of the Research in the Wider Field

Cryogenic condensation is a relatively new abatement technology. Through making use of the cooling effect of liquid nitrogen, the energy demand and plant footprint required for VOC abatement can be significantly reduced. Developing better models of cryogenic condensation processes could encourage uptake in the industry, by providing a method to assess the applicability of cryogenic condensation to specific industrial processes. Frost formation is often the main issue when applying cryogenic condensation in practice. This thesis has chosen to focus on a specific aspect of frost formation: modelling nucleation, growth and subsequent deposition of benzene frost particles in the flow. By modelling the frost formation process in CFD, this could lead to improvements in early-stage design of cryogenic condensers themselves. This could equally apply to desublimation as a separation technique in other industries or at less extreme temperatures.

## 7.4 Recommendations for Future Research

This section covers areas in which the research could be extended in the future.

### *7.4.1 Modelling different condensing species*

The model could be expanded to include the effect of different condensing species on the condensation process. In most practical cases, including the case under study, water vapour is also present in the untreated gas. This is significant to the problem definition, condensed water particles can serve as foreign nuclei for the heterogeneous condensation of other components. It is possible to model this using a multicomponent DPM model in Fluent (Benini and Ponza, 2011). The main barrier to using the multicomponent DPM model in Fluent is that it deletes all particles less than 0.1μm, because it assumes they have evaporated completely. Though in the process of conducting this study a solution to this wasn't found, it could be pursued in future work. Additionally, other species could be modelled instead of benzene. Organohalides and carbon dioxide being two industrially important examples.

### *7.4.2 Modelling different geometries*

The effect of geometry changes could be investigated further. The position of the baffles could be investigated. The flow pattern in the current geometry is not optimal: in heat exchangers typically the baffles should direct the flow without forming the significant recirculation patterns visible in the simulation. This should be remedied by increasing baffle cut (shortening baffles) or narrowing the baffle spacing. The effect on nucleation, growth and deposition could be assessed.

### *7.4.3 Modelling frost formation*

The effects of frost build-up have not been included in the scope of this study. Frost formation is a major problem in cryogenic condensation processes affecting cycle times of units. Industrial vent emissions often contain significant amounts of water vapour. The effects of frost build-up could be investigated initially using fixed geometry changes. A full frost model could be developed following this and added to the current CFD simulation. A fluid-structure interaction model may be appropriate for the turbulent flows encountered in the system.

### *7.4.4 Modelling the effect of turbulence on nucleation*

In turbulent flows conditions fluctuate with time (see Figure 6, p36). The factors controlling nucleation (concentration and temperature) also fluctuate due to turbulence. The effect of these fluctuations on the nucleation rate is that the critical degree of supersaturation is reached further upstream. Compared to mean quantities, turbulent fluctuations result in a lower peak nucleation rate, that is effective over a greater area. These effects have been modelled previously using probability density functions (Lesniewski and Friedlander, 1995; Garmony and Mastorakos, 2008). A similar approach may be applicable to the model in this work, given that the nucleation source terms are Eulerian.

### *7.4.5 Including corrections or alternatives to classical nucleation theory*

The limitations of classical nucleation theory are well-known. Various corrections to classical nucleation theory exist. In addition to the non-isothermal and heterogeneous corrections mentioned earlier, there are self-consistency corrections (Nadykto and Yu, 2005) and corrections for size-dependency of properties (such as the Tolman length for interfacial energy). Alternatives to classical nucleation theory also exist, such as the Hale's scaling model (Barrett and Baldwin, 2000) or Ruckenstein-Narsimhan-Nowakowski theory (Ruckenstien *et al.*, 2015). These could be attempted in place of classical nucleation in the CFD model. The practicality of some of these improvements is debateable however: the self-consistency factor for example often creates further deviations between classical nucleation theory and experimental results.

### *7.4.6 Modelling the effect of Brownian motion on particles*

For low stokes number particles, the particle inertia is insufficient to drive the particle through the laminar sublayer to deposit onto the surface. Deposition is instead driven by Brownian diffusion in the laminar sublayer. Brownian motion can be included in DPM models in Fluent but the built-in model is only applicable to laminar flow simulations. This model takes an approach similar to the discrete random walk turbulence model: a random number is applied to multiple trajectories for each particle injection. Aside from thermophoretic force, Brownian motion was not considered in this work. However it may be possible in future: for example, through a user-defined discrete random walk model. This would however increase the computational load of the simulation.

### *7.4.7 Including vapour film diffusion to the plate surface*

In the current model, a high concentration of nucleation and growing particles in the near-wall location acts to exhaust the benzene mass fraction to equilibrium in the near wall cells. This can instead be modelled as a boundary condition as covered by Dehbi *et al.* (2013). In future work this may serve to reduce computational load by reducing the number of particles.

### *7.4.8 Experimental validation of the nucleation and growth model*

This thesis restricted validation efforts to flow field validation using PIV. Validation of the nucleation and growth model has not been pursued. The process of nucleation is not yet fully understood. Currently a significant problem in studying nucleation stems from poor correspondence between theory and experiment. Experiment and theory often deviate by orders of magnitude, and different apparatus often show significant inconsistencies. Apparatus such as diffusion chambers require transport process modelling in order to obtain results. In aerosol nucleation, the effect of carrier gases is not fully understood, and the proposed benchmark system (n-pentanol in helium) has failed to produce results that can be repeated independently (Anisimov *et al.*, 2009).

Bench-scale experiments representing a cryogenic VOC condenser need to obtain low temperatures in the laboratory, this has been another barrier to experimental work in the area. The necessary temperatures could be reached in a laboratory environment in future without using liquid nitrogen: for example, using a laboratory cold trap (essentially two-stage refrigeration to -100°C) or through cooling mixtures (for example, Thilorier's mixture: $CO_{2(s)}$ and ether at -100°C).

Validation against published experimental data is another option. This was not pursued in the current work due to concerns with the completeness of experimental descriptions in available published work. Laminar aerosol flow tubes are a standard apparatus for aerosol experiments. Typically used in meteorology-related research, laminar aerosol flow tubes often use cooling of a gas flow through heat exchange to generate aerosol, giving them some parallels with this study (Khalizov *et al.*, 2006). Laminar aerosol flow tubes could be one route to pursue experimental work in future, either through independent research or validation against published experiments.

## 7.5 Recommendations for Practitioners in CFD

In this work, some barriers were encountered when trying to obtain full convergence from the model. The transition SST (shear stress transport) model is recognised by other authors as being difficult to solve (Benini and Ponza, 2011). Convergence to very low residuals is required for the species solution to reach a meaningful result; in order to reach a low species residual, often the other residuals must also fall to low values.

Problems were encountered also involving the numerically stiff DPM problem. The DPM iterations were the limiting factor in simulation running speed. Efforts to reduce the computational load and tackle the stiffness problem may be worthy of further investigation. The Eulerian-Lagrangian approach is effective for modelling of inertial particle deposition. This deposition mode is relevant to large particles, but much of the behaviour of aerosol particles during nucleation and growth occurs for small particles. There may be ways to simplify modelling of these particles in early stages of growth. The number of particle injection locations could be reduced in future by applying a coarse grid of static injection points, independent of the fluid mesh, that activate based on the conditions in the surrounding fluid.

## 7.6 Final Thoughts

The research has developed a CFD model of nucleation and growth of benzene particulate inside a cryogenic condenser. This has predicted an outlet vapour concentration of benzene and the entrainment of benzene particles in the outlet gas, providing an answer to the research question. This work represents an original contribution to knowledge in the form of a Eulerian-Lagrangian simulation of particle nucleation and growth during cryogenic condensation. The ability to simulate cryogenic condensation processes in CFD could be of substantial benefit to the design and application of the technology in the future. This thesis has aimed to take a first step in this direction. It is clearly a challenging academic problem as the long history of modelling in areas such as aircraft ice accretion demonstrates. It is a relatively unexplored area for potential research in a chemical engineering context. The development of better modelling in this area could also have importance in a wider context than is explored in this thesis, encompassing many industrial processes that involve desublimation, condensation and nucleation, as well as other problems outside the discipline of chemical engineering where these phenomena are important. There is a clear need for better modelling of these processes generally. This thesis provides a contribution to knowledge in this area.

# References

Adams, S., Armitage, B. and Nicholson, J. (1976) *2-(substituted biphenylyl) propionic acids*. United States Patent Office Patent no. US3932499. [Online]. Available at: http://www.google.com/patents/US3932499 (Accessed: 10 June 2015).

Adamson, A. and Gast, A. (1997) *Physical chemistry of surfaces*. 6th edn. Hoboken: Wiley.

Almohammadi, K., Ingham, D., Ma, L. and Pourkashan, M. (2013) 'Computational fluid dynamics (CFD) mesh independency techniques for a straight blade vertical axis wind turbine', *Energy*, 58, pp. 483-493.

Andersson, B., Andersson, R., Hakansson, L., Mortensen, M., Sudiyo, R. and Van Wachem, B. (2011) *Computational fluid dynamics for engineers*. Chambridge: Chambridge University Press.

Anisimov, M., Fominyku, E., Akimov, S. and Hopke, P. (2009) 'Vapor-gas/liquid nucleation experiments: a review of the challenges', *Journal of Aerosol Science*, 40(9), pp. 733-746.

Ansys (2009) *Ansys fluent 12.0 users guide*. Pennsylvania Ansys Inc.

ASHRAE (2009) *ASHRAE handbook of fundamentals*. Atlanta: American Society of Heating, Refrigerating and Air-Conditioning Engineers Inc.

ASME (2015) *Journal of Fluids Engineering Editorial Policy Statement on the Control of Numerical Accuracy* Available at: http://journaltool.asme.org/Content/AuthorResources.cfm (Accessed: 27 July 2015).

Bakhtar, F., Young, J., White, A. and Simpson, D. (2004) 'Classical nucleation theory and its application to condensing steam flows', *Proceedings of the Institution of Mechanical Engineers, Part C: Journal of Mechanical Engineering Science*, 219(12), pp. 1315-1333.

Barrett, J. and Baldwin, T. (2000) 'Aerosol nucleation and growth during laminar tube flow: maximum saturations and nucleation rates', *Journal of Aerosol Science*, 31(6), pp. 633-650.

BAuA (2006) *Benzene: strategy for limiting risks (environment)*. Available at: http://www.baua.de/ (Accessed: 22 October 2015).

Baxter, L. (2014) *Methods and systems for separating condensable vapors from gases*. United States Patent Office Patent no. US8715401. [Online]. Available at: https://www.google.com/patents/US8715401 (Accessed: 16 February 2015).

Beaugendre, H., Morency, F. and Habashi, W. (2006) 'Development of a second generation in-flight icing simulation code', *Journal of Fluids Engineering*, 128(2), pp. 378-387.

Belaissaoui, B., Moullec, Y. and Favre, E. (2016) 'Energy efficiency of a hybrid membrane/condensation process for VOC recovery from air: a generic approach', *Energy*, 95, pp. 291-302.

Benini, E. and Ponza, R. (2011) 'Assessment of gamma-theta transitional model for laminar-turbulent transition prediction in supercritical fluids ', *8th International Conference on Heat Transfer, Fluid Mechanics and Thermodynamics (HEFAT)*. Pointe Aux Piments, 11-13 July. pp. 525-532.

Berstad, D., Anantharaman, R. and Neksa, P. (2013) 'Low-temperature $CO_2$ capture technologies - applications and potential', *International Journal of Refrigeration* 36(5), pp. 1403-1416.

Bott, T. (1995) *Fouling of heat exchangers*. Amsterdam: Elsevier.

Branan, C. (2005) *Rules of thumb for chemical engineers*. 2nd edn. Amsterdam: Elsevier.

Brandon, D. and Aggarwal, S. (2001) 'A numerical investigation of particle deposition on a square cylinder placed in a channel flow', *Aerosol Science and Technology*, 34(4), pp. 340-352.

Breuer, M., Baytekin, H. and Matilda, E. (2006) 'Prediction of aerosol deposition in 90 bends using LES and an efficient lagrangian tracking method', *Journal of Aerosol Science*, 37(11), pp. 1407-1428.

British Standards Institution (2002) *BS EN 13284-1: Stationary source emmissions - determination of low range mass concentration of dust - part 1: manual gravimetric method*. London: British Standards Institution.

Brouwers, H. (1992) 'A film model for heat and mass transfer with fog formation', *Chemical Engineering Science*, 47(12), pp. 3023-3036.

Cao, G., Sivukari, M., Kurnitski, J. and Ruponen, M. (2010) 'PIV measurement of the attached plane jet velocity field at a high turbulence intensity level in a room', *International Journal of Heat and Fluid Flow*, 31(5), pp. 897-908.

Cao, X., Liu, J., Jaing, N. and Chen, Q. (2014) 'Particle image velocimetry measurement of indoor airflow field: a review of the technologies and applications', *Energy and Buildings*, 69, pp. 367-380.

Cao, y., Chen, K. and Sheridan, J. (2008a) 'Flowfield simulation and aerodynamic performance analysis of complex iced aerofoils with hybrid multi-block grid', *Journal of Aerospace Engineering*, 222(3), pp. 417-422.

Cao, Y., Wu, Z., Su, Y. and Xu, Z. (2015) 'Aircraft flight characteristics in icing conditions', *Progress in Aerospace Science*, 74, pp. 62-80.

Cao, Y., Zhang, Q. and Sheridan, J. (2008b) 'Numerical simulation of rime ice accretions on an aerofoil using an Eulerian method', *Aeronautical Journal*, 112(1131), pp. 243-249.

Cao, Y., Zhang, Q. and Sheridan, J. (2012) 'Numerical simulation of ice accretions on an aircraft wing', *Aerospace Science and Technology*, 23(1), pp. 296-304.

Chand, P. (1971) 'Viscosity of dusty gases', Chemical Engineering Science, 26(7), pp. 1019-1024.

Chang, H., Chung, M. and Park, S. (2009a) 'Cryogenic heat-exchanger design for freeze-out removal of carbon dioxide from landfill gas', *Journal of Thermal Science and Technology*, 4(3), pp. 362-371.

Chang, H., Chung, M. and Park, S. (2009b) 'Integrated cryogenic system for $CO_2$ separation and LNG production from landfill gas', *Joint Cryogenic Engineering and International Cryogenic Materials Conferences*. Tuscon, 28 June pp. 278-285.

Chang, H. and Smith, J. (1990) 'Mass transfer of supersaturated contaminants in cryogenic helium heat exchangers', *International Journal of Heat and Mass Transfer*, 33(6), pp. 1299-1306.

Chara, Z., Horak, V. and Rozehnal, D. (2009) 'Aerodynamic degration of iced aerofoils: experiments and CFD simulations', *3rd international symposium on flow applications in aerospace.* Vail, 2-6 August 2009. American Society of Mechanical Engineers.

Cheng, A. (1995) *Volatile organic compounds recovery from vent gas streams*. United States Patent Office Patent no. 5540057. [Online] Available at: http://www.google.com/patents/US5540057 (Accessed:11 March 2016).

Cheng, A. Devack, D. (1999) *Nonfreezing heat exchanger*. United States of America Patent Office Patent no. 5937656 [Online] Available at: http://www.google.com/patents/US5937656 (Accessed: 1st December 2014).

Cheng, Y., He, H., Yang, C., Zeng, G., Li, X., Chen, H. and Yu, G. (2016) 'Challenges and solutions for biofiltration of hydrophobic volatile organic compounds', *Biotechnology Advances*, 34(6), pp. 1091-1102.

Cheremissinoff, N. (2002) *Handbook of air pollution prevention and control*. Oxford: Butterworth-Hienemann.

Chilcott, R. (2013) *HPA compendium of chemical hazards - benzene*. Available at: www.gov.uk/government/publications/benzene-general-information-incident-management-and-toxicology (Accessed: 09 June 2015).

Choi, D., Devinny, J. and Deshusses, M. (2004) 'Behaviour of field-scale biotrickling filter under nonsteady state conditions', *Journal of Environmental Engineering*, 130(3), pp. 322-328.

Chuang, W., Cao, X., Yang, Y. and Jing, Z. (2012) 'Evaluation of natural gas dehydration in supersonic swirling separators applying the discrete particle model', *Advanced Powder Technology*, 23(2), pp. 228-233.

Clark, M. (2011) *Transport modeling for environmental engineers and scientists*. Hoboken: Wiley.

Climate-Data.org (2014) *Climate Cramlington*. Available at: http://en.climate-data.org/location/29540/# (Accessed: 13 August 2016).

Clodic, D., El Hitti, R., Younes, M., Bill, A. and Casier, F. (2005) '$CO_2$ capture by anti-sublimation thermo-economic process evaluation', *4th Annual Conference on Carbon Capture & Sequestration*. Alexandria Virginia, 2-5 May. pp.1-11.

Clodic, D. and Younes, M. (2002) 'A new method for $CO_2$ capture: frosting $CO_2$ at atmospheric pressure', *6th International Conference on Greenhouse Gas Control Techologies*. Kyoto, 1 October. . pp. 155-160.

Clodic, D., Younes, M. and Bill, A. (2004) 'Test results of $CO_2$ capture by anti-sublimation capture efficiency and energy consumption for boiler plants', *7th International Conference on Greenhouse Gas Control Technologies* Vancouver, 5 September. pp. 1774-1780.

Colburn, A. and Edison, A. (1941) 'Prevention of fog in cooler-condensers', *Industrial and Engineering Chemistry*, 33(4), pp. 457-458.

Couper, J., Penney, W., Fair, J. and Walas, S. (2010) *Chemical process equipment selection and design*. 2nd edn. Amsterdam: Elsevier.

CPCB (2007) *Proposed national emission standards for petrochemical plants*. Delhi: Central Pollution Control Board.

Craft, T. (2011) *Review of basic finite volume methods*. University of Manchester.

Cui, J., Li, W., Liu, Y. and Jiang, Z. (2011a) 'A new time- and space-dependent model for predicting frost formation', *Applied Thermal Engineering*, 31(4), pp. 447-457.

Cui, J., Li, W. and Zhao, Y. (2011b) 'A new model for predicting performance of fin-and-tube heat exchanger under frost condition', *International Journal of Heat and Fluid Flow*, 32(1), pp. 249-260.

DataPhysics Instruments GmbH (2007) *Solid surface energy data (SFE) for common polymers*. Available at: http://www.surface-tension.de/solid-surface-energy.htm (Accessed: 04 July 2015).

Date, A. (2005) *Introduction to computational fluid dynamics*. Chambridge: Chambridge University Press.

Davis, E. and Schweiger, G. (2002) *The airbourne microparticle*. Berlin: Springer.

Davis, R. and Zeiss, R. (2002) 'Cryogenic condensation: a cost-effective technology for controlling VOC emissions', *Environmental Progress*, 21(2), pp. 111-115.

Dawson, D., Willson, E., Hill, P. and Russell, K. (1969) 'Nucleation of supersaturated vapors in nozzles II C6H6,CHCl3, CCl3F and C2H5OH', *Journal of Chemical Physics*, 51(12), pp. 5389-5397.

De-Kruif, C. (1980) 'Enthalpies of sublimation and vapour pressures of 11 polycyclic hydrocarbons', *Journal of Chemical Thermodynamics*, 12(3), pp. 243-248.

DEFRA (2012) *Non-Automatic Hydrocarbon Network*. Available at: http://uk-air.defra.gov.uk/networks/ (Accessed: 22 October 2015).

Dehbi, A., Janasz, F. and Bell, B. (2013) 'Prediction of steam condensation in the presence of noncondensable gases using a CFD-based approach', *Nuclear Engineering and Design*, 258, pp. 199-210.

Dimier, P. (2012) *Introduction to ansys meshing: mesh quality*. Available at: www.ansys.com (Accessed: 14 June 2015).

Ding, H., Wang, C. and Zhao, Y. (2014) 'An analytical method for Wilson point in nozzle flow with homogeneous nucleating', *International Journal of Heat and Mass Transfer*, 73, pp. 586-594.

Drabble, J. (2015) 'Air pollutant deposition and effects', *Environment Special Interest Group Webinar Programme* London, 18 November 2015. Institution of Chemical Engineers.

Dunn, R. and El-Halwagi, M. (1994a) 'Optimal design of Multicomponent VOC condensation systems', *Journal of Hazardous Materials*, 38(1), pp. 187-206.

Dunn, R. and El-Halwagi, M. (1994b) 'Selection of optimal VOC-condensation systems', *Waste Management*, 14(2), pp. 103-113.

Dwivedi, P., Gaur, V., Sharma, A. and Verma, N. (2004) 'Comparative study of removal of volatile organic compounds by cryogenic condensation and adsorption by activated carbon', *Separation and Purification Technology*, 39(1), pp. 23-37.

Dykas, S. and Wroblewski, W. (2012) 'Numerical modelling of steam condensing flow in low and high-pressure nozzles', *International Journal of Heat and Mass Transfer*, 55(21), pp. 6191-6199.

EPA (2010) *Indicators: non-methane volatile organic compounds (NMVOC) emissions*. Copenhagen: European Environment Agency.

Fernandez, F. and Priesto, M. (2016) 'Study of aerosol behaviour in filmwise condensation processes with the presence of inert gas', *International Journal of Heat and Mass Transfer*, 93, pp. 1059-1071.

Finlay, W. (2001) The mechanics of inhaled pharmaceutical aerosols. Amsterdam: Elsevier.

Flagan, R. and Sienfield, J. (1988) *Fundamentals of air pollution engineering*. New Jersey: Prentice-Hall.

Flagan, R. and Sienfield, J. (2012) *Fundamentals of air pollution engineering*. 2nd edn. Mineloa: Dover Publications.

Fletcher, N. (1959) 'On ice-crystal production by aerosol particles', *Journal of Meteorology*, 16(2), pp. 173-180.

Friedlander, S. (2000) *Smoke, dust, and haze: fundementals of aerosol particle dynamics*. 2nd edn. Oxford: Oxford University Press.

Fu, P. and Farzaneh, M. (2010) 'A CFD approach for modeling the rime-ice accretion process on a horizontal-axis wind turbine', *Journal of Wind Engineering and Industrial Aerodynamics*, 98(4-5), pp. 181-188.

Fu, P., Farzaneh, M. and Bouchard, G. (2006) 'Two-dimensional modelling of the ice accretion process on transmission line wires and conductors', *Cold Regions Science and Technology*, 46(3), pp. 285-330.

Galletti, C., Brunazzi, E. and Tognotti, L. (2008) 'A numerical model for gas flow and droplet motion in wave-plate mist eliminators with drainage channels', *Chemical Engineering Science*, 63(23), pp. 5639-5652.

Garde, R. (1997) *Fluid mechanics through problems* New Dehli: New Age International.

Garmony, A. and Mastorakos, E. (2008) 'Aerosol nucleation and growth in a turbulent jet using the stochastic fields method', *Chemical Engineering Science*, 63(16), pp. 4078-4089.

Gerber, A. (2002) 'Two-phase Eulerian-Lagrangian model for nucleating steam flow', *Journal of Fluids Engineering*, 124(2), pp. 465-475.

Ghiaasiaan, S. (2007) *Two phase flow, boiling and condensation in conventional and minature systems*. New York: Chambridge University Press.

Gupta, V. and Verma, N. (2002) 'Removal of volatile organic compounds by cryogenic condensation followed by adsorption', *Chemical Engineering Science*, 57(14), pp. 2679-2696.

Gustafson, K. and Dickhut, R. (1994) 'Molecular diffusivity of aromatic hydrocarbons in air', *Journal of Chemical Engineering Data.*, 39(2), pp. 286-289.

Haghighi, M., Hawboldt, K. and Abdi, M. (2015) 'Supersonic gas separators: review of recent developments', *Journal of Natural Gas Science and Engineering*, 27(1), pp. 109-121.

Haque, A., Ahmad, F., Yamada, S. and Chaudhry, S. (2007) 'Assessment of turbulence models for turbulent flow over backward facing step', *Proceedings of the World Congress on Engineering*. London, 02 July IAENG, pp. 1340-1345.

Hart, A. and Gnanendran, N. (2009) 'Cryogenic $CO_2$ capture in natural gas', *Energy Procedia*, 1(1), pp. 697-706.
Hart, D. (2012) *Near-wall modelling and transition modelling*. Available at: www.ansys.com (Accessed: 05 November 2014).
Hefter, G. (1986) *Solubility system benzene with water*. Available at: http://srdata.nist.gov/solubility/sol_detail.aspx?sysID=37_51 (Accessed: 24 February).
Hermes, C., Piucco, R., Barbosa, J. and Melo, C. (2009) 'A study of frost growth and densification on flat surfaces', *Experimental Thermal and Fluid Science*, 33(2), pp. 371-379.
Herzog, F. (1994) 'Solvent recovery and waste gas purification with cryogenic processes', *Proceedings of the Second International Symposium on Characterisation and Control of Odours and VOC in the Process industries*. Louvain-la-Neuve, 3 November 1993. Amsterdam: Elsevier, pp. 309-319.
Hewitt, GF. Shires, GL. Bott, TR. (1994) *Process heat transfer*. Boca Raton: CRC Press.
Hirchfelder, J., Curtis, C. and Bird, R. (1954) *Molecular theory of gases and liquids*. New York: Wiley.
Housiadas, C., Schrader, K. and Drossinos, Y. (1998) 'Dehumidifation of air flow through cooling at sub-freezing temperatures', *International Journal of Heat and Mass Transfer*, 41(12), pp. 1821-1831.
IARC (1982) 'Benzene', *IARC Monographs on the Evaluation of the Carcinogenic Risks of Chemicals to Humans*, 29, pp. 93-148.
IARC (2012) 'Benzene', *IARC Monographs on the Evaluation of Carcinogenic Risks to Humans*, 100F, pp. 249-294.
Ingham, D., Hildyard, L. and Hildyard, M. (1990) 'On the critical Stokes number for particle transport in potential and viscous flows near bluff bodies', *Journal of Aerosol Science*, 21(7), pp. 935-946.
IPCS (1993) *Environmental health criteria 150: benzene*. Available at: http://www.inchem.org/documents/ehc/ehc/ehc150.htm (Accessed: 22 October 2015).
James, D. (2011) *Falling drop $CO_2$ deposition (desublimation) heat exchanger for the cryogenic carbon capture process*. Brigham Young University.
Jansen, R., Gimelshein, N., Gimelshein, S. and Wysong, I. (2011) 'A Lagrangian-Eulerian approach to modeling homogeneous condensation in high-density flows', *Journal of Chemical Physics*, 134(10), p. 104105.
Jassim, E. (2008) *Locating hydrate deposition in multiphase compressed natural gas flow lines using computational fluid dynamics techniques*. Memorial University of Newfoundland.
Jassim, E., Abdi, M. and Muzychka, Y. (2010) 'A new approach to investigate hydrate deposition in gas-dominated flowlines', *Journal of Natural Gas Science and Engineering*, 2(4), pp. 163-177.
Johnson, R. (1998) *Handbook of Fluid Dynamics*. Boca Raton: CRC Press.
Jonsson, S. and Westman, J. (2011) *Cryogenic biogas upgrading using plate heat exchangers*. Master's thesis. Chalmers University of Technology.
Kamrin, M. (1988) *Toxicology: a primer on toxicology principles and applications*. Chelsea: Lewis Publishers inc.
Kantrowitz, A. (1951) 'Nucleation in very rapid vapor expansions', *Journal of Chemical Physics*, 19(9), pp. 1097-1100.
Karl, J. (2000) 'Spontaneous condensation in boundary layers', *Heat and Mass Transfer*, 36(1), pp. 37-44.
Kashchiev, D. (2000) *Nucleation: basic theory and applications*. Amsterdam: Elsevier.
Katz, J. and Ostermier, B. (1967) 'Diffusion cloud-chamber investigation of homogeneous nucleation', *Journal of Chemical Physics*, 47(2), pp. 478-487.
Katz, J., Scoppa, C., Kumar, N. and Mirabel, P. (1975) 'Condensation of a supersaturated vapor II The homogeneous nucleation of the n-alkyl benzenes', *Journal of Chemical Physics*, 62, pp. 448-465.

Keane, R. and Adrian, R. (1990) 'Optimization of particle image velocimeters part 1: double pulsed systems', *Measurement Science and Technology*, 1(11), pp. 1202-1215.
Kelley, B., Valencia, P., Northrop, P. and Mart, C. (2011) 'Controlled freeze zone for developing sour gas reserves', *Energy Procedia*, 4, pp. 824-829.
Kennes, C. and Veiga, N. (2002) *Bioreactors for waste gas treatment*. Dordrecht: Kluwer Acedemic.
Khalizov, A., Earle, M., Johnson, W., Stubley, G. and Sloan, J. (2006) 'Modelling of flow dynamics in aerosol flow tubes', *Journal of Aerosol Science*, 37(10), pp. 1174-1187.
Khan, F. and Ghoshal, A. (2000) 'Removal of volatile organic compounds from polluted air', *Journal of Loss Prevention in the Process Industries*, 13(6), pp. 527-545.
Khvorostyanov, V. and Curry, J. (2014) *Thermodynamics, kinetics and microphysics of clouds*. Chambridge: Chambridge University Press.
Kim, D., Kim, C. and Lee, K. (2015) 'Frosting model for predicting macroscopic and local frost behaviours on a cold plate', *International Journal of Heat and Mass Transfer*, 82, pp. 135-142.
Kind, R. (2001) *Ice accretion simulation evaluation test*. Neully-sur-Seine: NATO.
Kosteltz, A., Finkelstien, A. and Sears, G. (1996) 'What are the real opportunities in biological gas cleaning for North America', *Proceedings of the 89th Annual Meeting & Exhibition of Air & Waste Management Association*. Nashville, 23-28 June. A&WMA.
Kreith, F. (2000) *CRC handbook of thermal engineering*. Boca Raton: CRC Press.
Krupiczka, R. and Pyschny, J. (1990) 'Mathematical modelling of the desublimation of phthalic anhydride', *Chemical Engineering and Processing: Process Intensification*, 28(1), pp. 29-34.
Kuhn, H., Fosterling, H. and Waldeck, D. (2009) *Principles of physical chemistry*. 2nd edn. New York: Wiley.
Kuron, M. (2015) *Three criteria for assessing CFD convergence*. Available at: http://www.engineering.com/DesignSoftware/DesignSoftwareArticles/ArticleID/9296/3-Criteria-for-Assessing-CFD-Convergence.aspx (Accessed: 07 July 2015).
Lam, H. and Peng, H. (2016) 'Study of wake characteristics of a vertical axis wind turbine by two- and three-dimensional computational fluid dynamics simulations', *Renewable Energy*, 90, pp. 386-398.
Langtry, R. (2006) *A correlation-based transition model using local variables for unstructured parallelized CFD codes*. University of Stuttgart.
Lee, K.J., S. Yang, DK. (2003) 'Prediction of the frost formation on a cold flat surface', International Journal of Heat and Mass Transfer, 46(20), pp. 3789-3796.
Lee, R. et al. (1996) *Cryogenic vapour recovery process and system*. United States of America Patent Office Patent no. 5533338. [Online] Available at: http://www.google.com/patents/US5937656 (Accessed: 1st December 2014).
Lenic, K., Trp, A. and Frankovic, B. (2009) 'Transient two-dimensional model of frost formation on a fin-and-tube heat exchanger', *international Journal of Heat and Mass Transfer*, 52(1), pp. 22-32.
Lesniewski, T. and Friedlander, S. (1995) 'The effect of turbulence on rates of particle formation by homogeneous nucleation', *Aerosol Science and Technology*, 23(2), pp. 174-182.
Lewandowski, D. (1999) *Design of thermal oxidation systems for volatile organic compounds*. Boca Raton: CRC Press.
Li, J. (2013) 'CFD simulation of water vapour condensation in the presence of non-condensable gas in vertical cylindrical condensers', *International Journal of Heat and Mass Transfer*, 57(2), pp. 708-721.
Li, J. (2014) *Name reactions: a collection of detailed mechanisms and synthetic applications*. 5th edn. Berlin: Springer.
Lide, D. (1993) *CRC Handbook of Chemistry and Physics* 74th edn. Boca Raton: CRC Press.

Lively, R., Koros, W. and Johnson, J. (2012) 'Enhanced cryogenic $CO_2$ capture using dynamically operated low-cost fiber beds', *Chemical Engineering Science*, 71, pp. 97-103.

LoPinto, L. (1982) 'Fog formation in low-temperature condensers', *Chemical Engineering*, 89(10), pp. 111-113.

Lu, G., Frazen, R., Yu, X. and Xu, Y. (2006) 'Synthesis of flurbiprofen via Suzuki reaction catalyzed by palladium charcoal in water', *Chinese Chemical Letters*, 17(4), pp. 461-464.

Luliano, E. and Perez, E. (2016) *Application of surrogate-based global optimisation to aerodynamic design*. Berlin: Springer.

Ma, Q. (2012) 'Location selection of extra nuclei injecting for inner-core SGS device with droplet enlargement measure', *Advanced Materials Research*, 516, pp. 931-934.

Maass, O. and Waldbauer, L. (1925) 'The specific heats and latent heats of fusion of ice and of several organic compounds', *Journal of the Amecian Chemical Society*, 47(1), pp. 1-9.

Maliyekkal, S., Rene, E., Philip, L. and Swaminathan, T. (2004) 'Performance of BTX degraders under substrate versatility conditions', *Journal of Hazardous Materials B*, 109(1), pp. 201-211.

Manthey, A. and Schaber, K. (2000) 'The formation and behaviour of fog in a tube bundle condenser', *International Journal of Thermal Sciences*, 39(9), pp. 1004-1014.

Markov, I. (2003) *Crystal growth for beginners: fundamentals of nucleation, crystal growth and epitaxy*. 2nd edn. Singapore: World Scientific.

Matar, M., Mirbach, M. and Tayim, H. (1989) *Catalysis in petrochemical processes*. Berlin: Springer.

Mayle, R. (1991) 'The role of laminar-turbulent transition in gas turbine engines', *Journal of Turbomachinery*, 113(4), pp. 509-536.

McFarland, A., Gong, H., Muyshondt, A., Wente, W. and Anand, N. (1997) 'Aerosol deposition in bends with turbulent flow', *Environmental Science and Technology* 31(12), pp. 3371-3377.

McGraw, R. (2007) 'Description of aerosol dynamics by the quadrature method of moments', *Aerosol Science and Technology*, 27(2), pp. 255-265.

McKetta, J. (1991) *Encyclopedia of chemical processing and design*. Boca Raton: CRC Press.

Meisen, A.S., X. (1997) 'Research and development issues in $CO_2$ capture', *Energy Conversion and Management*, 38(1), pp. 37-42.

Menter, F. (1993) 'Zonal two-equation k-w turbulence models for aerodynamic flows', *24th AIAA Fluids Dynamics Conference*. Orlando, 09 July 1993. NASA pp. 1-21.

Mills, A. (1992) *Heat transfer*. Boca Raton: CRC Press.

Mitani, T. and Takashima, Y. (1981) 'Consideration of the removal of desublimated matter in an annular-tube cold trap', *Journal of Chemical Engineering of Japan*, 14(4), pp. 282-288.

Morsi, S. and Alexander, A. (1972) 'An investigation of particle trajectories in two-phase flow systems', *Journal of Fluid Mechanics*, 55(2), pp. 193-208.

Mudlair, S., Giri, B., Padoley, K., Satpute, D., Dixit, R., Bhatt, P., Pandey, R., Juwarkar, A. and Vaidya, A. (2010) 'Bioreactors for treatment of VOCs and odours', *Journal of Environmental Management*, 91(5), pp. 1039-1054.

Mullin, J. (2003) 'Sublimation', in Grolig, J. and Wagner, R. (eds.) *Ullmann's Encyclopedia of Industrial Chemistry*. Hoboken: Wiley.

Murphy, G. (1950) *Similitude in engineering*. New York: Ronald Press Co.

Nadykto, A. and Yu, F. (2005) 'Simple correction to the classical theory of homogeneous nucleation', *Journal of Chemical Physics* 122, p. 104511.

Naletov, V., Gordeev, L., Gledov, M. and Naletov, A. (2014a) 'Mathematical modelng of desublimation of carbon dioxide from flue gases of heat power systems', *Theoretical Foundations of Chemical Engineering*, 48(1), pp. 27-33.

Naletov, V., Lukyanov, V., Kulov, N., Naletov, A. and Glebov, M. (2014b) 'An experimental study of desublimation of carbon dioxide from a gas mixture', *Theoretical Foundations of Chemical Engineering*, 48(3), pp. 312-319.

Narhe, R., Khandkar, M., Shelke, P., Limaye, A. and Beysens, D. (2009) 'Condensation-induced jumping of water drops', *Physics Review E*, 80(3), p. 031604.
Nielson, B. (2013) *Cryogenic carbon capture using a desublimating spray tower*. Master's thesis. Brigham Young University.
NIST (2011) *Thermophysical properties of fluid systems*. Available at: webbook.nist.gov/chemistry/fluid (Accessed: 01 Aug 2014).
NIST (2016) *Methylene Chloride*. Available at: http://webbook.nist.gov/cgi/inchi/InChI%3D1S/CH2Cl2/c2-1-3/h1H2 (Accessed: 31 Oct 2016).
Noordally, E., Richmond, J. and Drumm, K. (1994) 'Catalytic oxidation processes for odour and VOC control', *Proceedings of the Second International Symposium on Characterisation and Control of Odours and VOC in the Process Industries*. Louvain-la-Neuve, 3 November 1993. Amsterdam: Elsevier, pp. 459-468.
Norouzi, H.Z., R. Gharebagh, RS. Mostoufi, N. (2016) Coupled CFD-DEM Modeling. Hoboken: Wiley.
Ojala, S., Koivikko, N., Laitinen, T., Mouammine, A., Seelam, P., Laassiri, S., Ainassaari, K., Brahmi, R. and Keiski, R. (2015) 'Utilisation of volatile organic compounds as an alternative for destructive abatement', *Catalysts*, 5(3), pp. 1092-1151.
Omrane, A., Petersson, P., Alden, M. and Linne, M. (2008) 'Simultaneous 2D flow velocity and gas temperature measurements using thermographic phosphors', *Applied Physics B*, 92(1), pp. 99-102.
Overcamp, T. and Scarlett, S. (1993) 'Effect of Reynold's number on the Stokes number of cyclones', *Aerosol Science and Technology*, 19(3), pp. 362-370.
Ozturk, B. and Yilmaz, D. (2006) 'Absorptive removal of volatile organic compounds from flue gas streams', *Process Safety and Environmental Protection*, 84(5), pp. 391-398.
Perry, J. (1927) 'Vapour pressures of methylene chloride', *Journal of Physical Chemistry*, 31(11), pp. 1737-1741.
Perry, R. and Green, D. (2008) *Perry's chemical engineering handbook*. 8th edn. New York: McGraw-Hill.
Pohanish, R. (2011) 'Sittig's handbook of toxic and hazardous chemicals and carcinogens', 6th edn. Amsterdam: Elsevier.
Potter, M., Wiggert, D. and Ramadan, B. (2011) *Mechanics of fluids*. Boston: Cengage Learning.
Purskii, O. and Zholonko, N. (2003) 'Influence of rotational motion of molecules on the thermal conductivity of solid SF6, CHCL3, C6H6 and CCL4', *Low Temperature Physics*, 29(9), pp. 771-775.
Rada, E., Raboni, M., Torretta, V., Copelli, S., Ragazzi, M., Caruson, P. and Istrate, I. (2014) 'Removal of benzene from oil refinery wastewater treatment plant exhausted gases with a multi-stage biofiltration pilot plant', *Revista de Chimie*, 65(1), pp. 68-70.
Raffel, M., Willert, C. and Kompenhans, J. (2000) *Particle image velocimetry a practical guide*. Berlin: Springer.
Ragni, D., Schrijer, F., Van Oudheusden, B. and Scarano, F. (2011) 'Particle tracer response across shocks measured by PIV', *Experiments in Fluids*, 50(1), pp. 53-64.
Ramkrishna, D. (2000) *Population balances: theory and applications to particulate systems engineering*. Waltham: Academic Press.
Raoux, S. and Wuttig, M. (2009) *Phase change materials*. Berlin: Springer.
Remsburg, R. (1998) *Advanced thermal design of electronic equipment*. Berlin: Springer.
Richardson, J., Harker, J. and Backhurst, J. (2002) *Coulson and Richardson's chemical engineering volume 2 particle technology and separation processes*. 5th edn. Amsterdam: Elsevier.
Rigopoulos, S. (2010) 'Population balance modelling of polydispersed particles in reactive flows', *Progress in Energy and Combustion Science*, 36(4), pp. 412-443.

Rijneek, L. (2005) 'Environment cryogenics for cleaner air', *Process Engineering*, 86(5), pp. 20-21.
Roache, P. (1997) 'Quantification of uncertainty in computational fluid dynamics', *Annual Review of Fluid Mechanics*, 29(1), pp. 123-160.
Ruckenstien, E., Berim, G. and Narismhan, G. (2015) 'A novel approach to the theory of homogeneous and heterogeneous nucleation', *Advances in Colloid and Interface Science*, 215, pp. 13-27.
Ruzicka, K., Fulem, M. and Cervinka, C. (2014) 'Recommended sublimation pressure and enthalpy of benzene', *Journal of Chemical Thermodynamics*, 68, pp. 40-47.
Sasao, Y., Miyake, S., Okazaki, K., Yamamoto, S. and Ooyama, H. (2013) 'Eulerian-Lagrangian numerical simulation of wet steam flow through multi-stage steam turbine', *Turbine Technical Conference and Exposition*. San Antonio, 3-7 June. New York: ASME
Sauter, C., Lorber, B. and Giege, R. (2012) 'Predicting protien crystallizability and nucleation', *Protien and Peptide Letters*, 19, pp. 725-731.
Sawhney, G. (2011) *Fundamentals of fluid mechanics*. IK International Publishing House Pvt Ltd: New Dehli.
Schetz, J. and Fuhs, A. (1999) *Fundamentals of fluid mechanics*. Hoboken: Wiley.
Schillaci, W. (2014) *Top US manufactured chemicals*. Available at: https://enviro.blr.com/whitepapers (Accessed: 20 October 2015).
Schlosser, M. and Geneste, H. (1998) 'The superbase approach to flurbiprofen: an exercise in optionally site-selective metalation', *Chemistry - A European Journal*, 4(10), pp. 1969-1973.
SES (2015) *Sustainable energy solutions*. Available at: http://sesinnovation.com (Accessed: 19 January 2016).
Silves, S. (2010) *Introduction to Ansys meshing: appendix meshing quality*. Available at: www.ansys.com (Accessed: 6 January 2014).
Simmons, A. (2009) *Guidance for the speciality chemicals sector*. Bristol: Environment Agency.
Slaughter, C. (2006) *Options and incentives to rebuild or replace VOC oxidation equipment* Available at: www.icac.com (Accessed: 22 February 2016).
Smolkin, P., Buynovskiy, A., Lazarchuk, V., Matveev, A., Sofronov, V. and Brendakov, V. (2007) 'Mathematical model of determining heat condition in desublimation process of volatile metal fluorides', *Bulletin of the Tomsk Polytechnic University*, 310(3), pp. 72-76.
Smolkin, P., Buynovskiy, A. and Sofronov, V. (2011) 'Determining the opimal process conditions for volatile metal flouride desublimation', *Chemistry of Sustainable Development*, 19(4), pp. 417-421.
Son, S., Kihm, K. and JC., H. (2002) 'PIV flow measurements for heat transfer characterization in two-pass square channels with smooth and 90 ribbed walls', *International Journal of Heat and Mass Transfer*, 45(24), pp. 4809-4822.
Song, C., Kitamura, Y., Li, S. and Ogasawara, K. (2012) 'Design of a cryogenic $CO_2$ capture system based on Stirling coolers', *International Journal of Greenhouse Gas Control*, 7, pp. 107-114.
Srikanth, R. and Jayaraj, S. (1995) 'Computational analysis of thermophoretic flow over cold inclined plates: effect of variable properties', *International Conference on Computational Engineering Science*. Hawaii, 30 July. Berlin: Springer, p. 1077.
Steigman, F. (1988) *Abatement of vapors from gas streams by solidifcation*. United States Patent Office Patent no. US4769054. [Online]. Available at: https://www.google.co.uk/patents/US4769054 (Accessed: 16 February 2016).
Sun, K., Lu, L., Jiang, H. and Hanhui, J. (2013) 'Experimental study of solid particle deposition in 90 ventilated bends of rectangular cross section with turbulent flow', *Aerosol Science and Technology*, 47(2), pp. 115-124.

Surovtseva, D., Amin, R. and Barifcani, A. (2011) 'Design and operation of pilot plant $CO_2$ capture from IGCC flue gases by combined cryogenic and hydrate method', *Chemical Engineering Research and Design*, 89(9), pp. 1752-1757.

Talbot, L., Cheng, R., Schefer, R. and Willis, D. (1980) 'Thermophoresis of particle in a heated boundary layer', *Journal of Fluid Mechanics*, 101(4), pp. 737-758.

Theunissen, T., Golombok, M., Brouwers, J., Bansal, G. and Van Benthum, R. (2011) 'Liquid $CO_2$ droplet extraction from gases', *Energy*, 36(5), pp. 2961-2967.

Thulukkanam, K. (2013) *Heat exchanger design handbook*. 2nd Edn. Boca Raton: CRC Press.

Tien, C. and Ramarao, B. (2007) *Granular filtration of aerosols and hydrosols*. 2nd edn. Amsterdam: Elsevier.

Tsai, Y., Liu, F. and Shen, P. (2009) 'Investigations of the pressure drop and flow distribution in a chevron-type plate heat exchanger', *International Communications in Heat and Mass Transfer*, 36(6), pp. 574-578.

Tuinier, M. and Annaland, M. (2012) 'Biogas purification using cryogenic packed-bed technology', *Industrial and Engineering Chemistry Research*, 51(15), pp. 5552-5558.

Tuinier, M., Annaland, M. and Kuipers, J. (2011) 'A novel process for cryogenic $CO_2$ capture using dynamically operated packed beds - an experimental and numerical study', *International Journal of Greenhouse Gas Control*, 5(4), pp. 694-701.

Ueda, H. and Takashima, Y. (1976) 'The local growth rate of desublimation on the surface of an annular-tube cold trap', *Journal of Chemical Engineering of Japan*, 9(2), pp. 121-129.

Ueda, H. and Takashima, Y. (1977) 'Desublimation of two-component vapors on the surface of an annular-tube cold trap', *Journal of Chemical Engineering of Japan*, 10(1), pp. 6-13.

UN Environment Programme (1998) *Pollution prevention and abatement handbook*. Washington DC: World Bank Publications.

Van Benthum, R., Van Kemenade, H., Brouwers, J. and Golombok, M. (2012) 'Condensed rotational separation of $CO_2$', *Applied Energy*, 93, pp. 457-465.

Vehkamaki, H., Maattanen, A., Lauri, A., Napari, I. and Kulmala, M. (2007) 'Technical note: the heterogeneous Zeldovich factor', *Atmospheric Chemistry and Physics*, 7(2), pp. 309-313.

Verspoor, P. (2007) *Guidance on the interpretation of the solvents emissions directive*. Brussels: European Solvents Industry Group.

Versteeg, H. and Malalasekera, W. (2007) *An introduction to computational fluid dynamics*. 2nd edn. New Jersey: Prentice Hall.

Walas, S. (1990) *Chemical process equipment selection and design*. Amsterdam: Elsevier.

Wang, Z.K., DJ. DeVries, L. Park, JM. (2015) 'Frost formation and anti-icing performance of a hydrophobic coating on aluminium', Experimental Thermal and Fluid Science, 60, pp. 132-137.

Wexler, A. (1977) 'Vapour pressure formulation for ice', *Journal of Research of the National Bureau of Standards*, 81A(1), pp. 5-20.

Whan, A. and Rothus, R. (1959) 'Characteristics of transition flow between parallel plates', *AICHE Journal*, 5(2), pp. 204-208.

Wilcox, D. (2006) *Turbulence modeling for CFD*. Lake Arrowhead: DCW industries.

Wintermantel, K., Holzknecht, B. and Thoma, P. (1987) 'Density of desublimated layers', *Chemical Engineering & Technology*, 10(1), pp. 405-410.

Wu, X., Ma, Q., Chu, F. and Hu, S. (2016) 'Phase change mass transfer model for frost growth and densification', *International Journal of Heat and Mass Transfer*, 96, pp. 11-19.

Xingwei, L., Zhongliang, L. and Yanxia, L. (2014) 'Investigation on separation efficiency in supersonic separator with gas-droplet flow based on DPM approach', *Separation Science and Technology*, 49(17), pp. 2603-2612.

Yang, D., Lee, K. and Cha, D. (2006) 'Frost formation on a cold surface under turbulent flow', *International Journal of Refrigeration*, 29(2), pp. 164-169.

Yennigalla, E. and Hetian, M. (2015) *The changing dynamics of global benzene supply*. Available at: http://blogs.platts.com/ (Accessed: 20 October 2015).
Yu, C., Ke, P., Yu, G. and Yang, C. (2015) 'Investigation of water impingement on a multi-element high-lift airfoil by Lagrangian and Eulerian approach', *Propulsion and Power Research*, 4(3), pp. 161-168.
Zhang, L., Jia, Y., Zhang, H. and Yang, T. (2010) 'Pilot study on removal of benzene by using high efficient biotrickling filter', *Bioinformatics and Biomedical Engineering (iCBBE) 4th International Conference* Chengdu,18-20 June.Piscataway: IEEE, pp. 1-4.
Zhao, B.C., C. Lai, ACK. (2011) 'Lagrangian stochastic particle tracking: further discussion', Aerosol Science and Technology, 45(8), pp. 901-902.
Zhao, G., Zhao, Q. and Chen, X. (2016) 'New 3-D ice accretion method of hovering rotor including effects of centrifugal force', *Aerospace Science and Technology*, 48, pp. 122-130.
Zigh, G. and Solis, J. (2013) *Computational fluid dynamics best practice guidelines for dry cask applications*. Washington: US Nuclear Regulatory Commission.
Zschaeck, G., Frank, T. and Burns, A. (2014) 'CFD modelling and validation of wall condensation in the presence of non-condensable gases', *Nuclear Engineering and Design*, 279(137-146).

# Chapter 8. Appendices

## 8.1 Personal Communication

correspondence.section@defra.gsi.gov.uk on behalf of Ministerial Contact Unit

Dear Mr Hendry,

Thank you for your email of 20 September about the National Emission Ceilings Directive.

In response to your question, the UK has a strong track record on protecting our environment and we will safeguard and improve this. The Withdrawal Bill will make sure the whole body of existing EU environmental law continues to have effect in UK law, providing businesses and stakeholders with maximum certainty as we leave the EU. As the UK negotiates its exit from the EU, we will continue to ensure that the right policies are in place for a cleaner, healthier environment for everyone. It will remain the role of Parliament, and ultimately the electorate, to hold the Government to account.

The UK has ambitious targets in place to reduce emissions of five damaging air pollutants (ammonia, nitrogen oxides, non-methane volatile organic compounds, fine particulate matter and sulphur dioxide) by 2020 and 2030; aiming to cut early deaths from air pollution by half. We will publish a Clean Air Strategy, setting out how we will work towards these goals, for consultation in 2018.

Kind regards,

MARK PLOWRIGHT

Ministerial Contact Unit

## 8.2 **Computational Platform**

Topsy was accessed using a combination of SSH secure shell (ver. 3.2.9) and MobaXTerm (ver. personal 8.6). SSH secure shell allowed for easy file transfer, while MobaXTerm allowed for GUI access to Topsy through X-Server, running Fluent on Topsy's 'frontend' (a.k.a. Topsy host). This meant that case files could be checked and edited easily before sending them to Topsy nodes as batch files for computing. SSH secure shell was installed on campus network PCs, MobaXterm was installed on a personal laptop. Topsy can only be accessed via the campus network, or via RAS. The software in the Topsy was a slightly earlier version of Fluent (14.5.7).

| Workstation | Dell Precision T1600 | ceamansys01 | Topsy |
|---|---|---|---|
| Operating system | Windows 7 enterprise 64 bit | Windows Server 2012 Standard | Rocks 6.2 |
| CPU | Intel® Xeon® E31270 @ 3.40GHz | Intel® Xeon® E5-2620 v2 @ 2.10GHz | 20 x 3.00GHz (typ) |
| RAM | 16GB | 32GB | 128GB (typ) |
| Geometry software | ANSYS® DesignModeller™ 15.0.7 | - | - |
| Meshing software | ANSYS® Meshing™ 15.0.7 | - | - |
| Numerical simulation software | ANSYS® FLUENT® 15.0.7 | ANSYS® FLUENT® 15.0.0 | ANSYS® FLUENT® 14.5.7 |
| Post processing software | ANSYS® FLUENT® 15.0.7;<br>ANSYS® CFD-Post 15.0.7 | - | - |

*Table 29: computing platform specifications.*

During parallel computing in Fluent, the simulation is run using a host and various nodes. The host partitions the mesh, and sends each mesh partition to a node for computation. When running Fluent in parallel on a single machine, such as a desktop PC, the hosts and nodes are processed by cores in a multicore processor.

Topsy also has a host (Topsy's 'frontend') and nodes. But each Topsy node contains multiple (typically 20) processors. When running Fluent on Topsy, the whole Fluent simulation is sent to a Topsy node for computation. For a typical Topsy node of 20 cores, Fluent can run in parallel with 19 Fluent nodes and 1 Fluent host processor. Currently Topsy is only able to run in this manner (sending individual simulations to individual Topsy nodes) it is not possible to use multiple Topsy nodes for a single Fluent simulation, so this places an upper limit on computational load. The simulation time can take a maximum of 48hrs – to circumvent this, the journal file for the simulation included instructions to automatically save the case and data files, and the simulations were restarted on a 48hr basis.

To submit a job to Topsy, the necessary files (Fluent case file, with data file, user-defined function (UDF) files and library, and other code such as injection files, as appropriate) was first transferred to the domain /share/nobackup/b2054056/. This directory is necessary for the large file sizes (larger than the 2GB limit on /home/b2054056) used in the simulations. Running the Fluent file requires two short code files. Topsy frontend requires a qsub code, in order to queue the job for processing on a Topsy node, and to open Fluent. Fluent requires a journal file to run the simulation. Qsub code typically takes the form:

```
#!/bin/bash # run this script in bash
#
#$ -cwd # use the current working directory
#$ -S /bin/bash # parse all scripts in specified shell
#$ -pe threaded 19    # use 19 cores on 1 Topsy node

# load the ansys module
module load ansys
# run fluent in 3D with 19 fluent nodes in batch using journal file
fluent 3ddp –t19 -g < startup.JOU
```

The qsub file must be saved as Linux code in order to be read by Topsy. This was done using the MobaTextEditor (clicking the linux icon before saving). The qsub file was saved in the same directory as the fluent code. The job was started by entering the commands into SSH or MobaXTerm:

```
[b2054056@topsy ~]$ cd /share/nobackup/b2054056/

[b2054056@topsy ~]$ qsub script.qsub
```

## 8.3 Mesh Quality Metrics

Data for the mesh metrics were extracted directly from the meshing software (ANSYS® Meshing$^{TM}$ 15.0.7). Skewness is calculated based on normalised angle deviation for hexahedral meshes (Dimier, 2012). Orthogonal quality is the cosine of the angle between the face-normal vector **A**ᵢ and a vector between the centroid of the cell and the centroid of the neighbouring cell **C**ᵢ. These are illustrated in Figure 96 below, and in equations 8-1 and 8-2. The acceptance criteria used in Table 8, (p. 74) and Table 13, (p. 83) are taken from Silves (2010) and Ansys (2009).

$$skewness = max\left[\frac{\theta_{max} - 90°}{180° - 90°} \; \frac{90° - \theta_{max}}{90°}\right] \tag{8-1}$$

$$orthogonal\ quality = \frac{\boldsymbol{A_i} \cdot \boldsymbol{C_i}}{|\boldsymbol{A_i}||\boldsymbol{C_i}|}\ (= cos\ \theta) \tag{8-2}$$

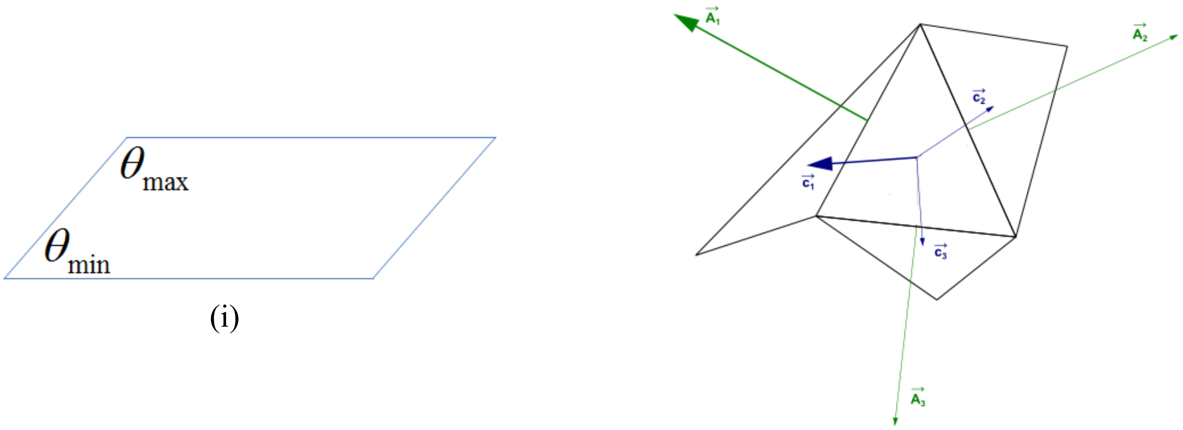

(i)

(ii)

*Figure 96: Illustrations for mesh quality metrics. (i) Skewness (ii) Orthogonal quality.*

## 8.4 Computer Code

### *8.4.1 User-defined function for linear wall temperature profile*

```
/*UDF generates linear T profile a/c boundary*/
/*James Hendry 29.04.15*/
#include "udf.h"
DEFINE_PROFILE(temperature_profile_100, thread, position)
{
   real r[3]; /* this will hold the position vector */
   real y;
   face_t f;
   begin_f_loop(f, thread)
   {
     F_CENTROID(r,f,thread);
     y = r[1];
     F_PROFILE(f, thread, position) = -20.20*y+213.;
   }
   end_f_loop(f, thread)
}
```

### *8.4.2 User-defined function for inert particle injections*

```
/*injection by properties in cell*/
/*James Hendry 22.05.15*/
#include "udf.h"
#include "surf.h" /* For RP_Cell & RP_THREAD*/
DEFINE_DPM_INJECTION_INIT(injbycell, I)
{
       Particle *p;
       cell_t cell;
       Thread *cthread;
       loop(p, I->p)
       {
             cell = P_CELL(p); /*get the cell and thread that the particle is
currently in*/
             cthread = P_CELL_THREAD(p); /*set up arrays...*/
             P_VEL(p)[0] = C_U(cell, cthread);
             P_VEL(p)[1] = C_V(cell, cthread);
             P_VEL(p)[2] = C_W(cell, cthread);
             P_T(p) = C_T(cell, cthread);
       }
}
```

### 8.4.3 User-defined function for diameter dependent Cunningham slip

```
/*the following implements a diameter-dependent Cunningham slip correction
factor*/
/*James Hendry 09.10.15 */
#include "udf.h"
#include "math.h"
DEFINE_DPM_DRAG(cunningham_drag_force, Re, p)
{
 cell_t c = P_CELL(p);
 Thread *t = P_CELL_THREAD(p);
 real lambda;
 lambda = 0.0002135166*C_MU_L(c, t)*sqrt(C_T(c, t));
 real Cc;
 Cc = 1 + (2 * lambda / P_DIAM(p))*(1.257 + 0.4*exp(-1.1*P_DIAM(p) / (2 *
lambda)));
 real Cd, drag_force;
 if (Re < 0.1)
 {
      Cd = 24 / Re;
      drag_force = 18*Cd*Re/(24*Cc);
      return (drag_force);
 }
 else if (Re < 1)
 {
      Cd = 22.73 / Re + 0.0903 / (Re*Re) + 3.69;
      drag_force = 18 * Cd*Re / (24*Cc);
      return (drag_force);
 }
 else if (Re < 10)
 {
      Cd = 29.1667 / Re - 3.8889 / (Re*Re) + 1.222;
      drag_force = 18 * Cd*Re / (24*Cc);
      return (drag_force);
 }
 else
 {
      Cd = 46.5 / Re - 116.67 / (Re*Re) + 1.6167;
      drag_force = 18 * Cd*Re / (24*Cc);
      return (drag_force);
 }
}
```

### 8.4.4 User-defined function Eulerian species source term due to nucleation.

```
/*defines injection Eulerian source for nucleation rate*/
/*James Hendry 24.08.15*/
#include "udf.h"
#include "math.h"
DEFINE_SOURCE(inj_source8, cell, thread, dS, eqn)
{
/*declarations*/
real J;
real mf;
real P;
real lgPe;
real Pe;
real r;
real S;
real T;
real tothepw;
real source;
/*extracting data from cells*/
mf = C_YI(cell, thread, 0);
T = C_T(cell, thread);
/*calculation */
lgPe = -2452.5 / T + 10.374;
Pe = pow(10, lgPe);
P = 9.73*mf / (mf / 78.11 + (1 - mf) / 28.014);
S = P / Pe;
if (S > 1)
	{
		tothepw = (-4.434e14)*(pow(T, -5.085)) / (log(S)*log(S));
		J = (3.23e32)*Pe / T*Pe / T*S*S*exp(tothepw);
		r = ((1.163e-6) - (2.043e-9)*T) / (T*log(S));
	}
else
	{
		J = 0;
		r = 0;
	}
if (J < 1) /*homogeneous nucleation conditions. If everywhere T <250 nucleates,
then e-100+ mass sources (<1 atom) occur.*/
	{
		J = 0;
		r = 0;
	}
	/*defining the source*/
	source = -(4.256e9)*J*r*r*r; /*treat source (kg/m3s) as a units conversion
of J (nucleii/cm3s)*/
	/*defining the user defined memory*/
	C_UDMI(cell, thread, 0) = source; /*(kg/m3s)*/
	C_UDMI(cell, thread, 1) = r * 2; /*diameter*/
	return source;
}
```

### 8.4.5 User-defined function for Eulerian mass source term due to nucleation

```
/*defines Eulerian source for mass removed due to nucleation*/
/*James Hendry 24.08.15*/
#include "udf.h"
#include "math.h"
DEFINE_SOURCE(inj_source8mass, cell, thread, dS, eqn)
{
	real source;
	source = C_UDMI(cell, thread, 0); /*(kg/m3s)*/
	return source;
}
```

### 8.4.6 User-defined function for Eulerian energy source term due to nucleation

```
/*defines Eulerian source for heat released due to nucleation*/
/*James Hendry 24.08.15*/
#include "udf.h"
#include "math.h"
DEFINE_SOURCE(inj_source8latent, cell, thread, dS, eqn)
{
	real source;
	source = C_UDMI(cell, thread, 0) * -568429; /*(J/m3s)*/
	return source;
}
```

### *8.4.7 User-defined function for generating injection files*

This define-on-demand user-defined function creates injection files. Each mesh partition in parallel computing is assigned an injection file. Each mesh cell (with a non-zero nucleation rate) is assigned a line in that injection file, and that line defines a point injection in the centre of the cell.

```
/*define-on-demand fcn for creating an injection in parallel, James Hendry
13.04.16 */
#include "udf.h"
#include "para.h"
#define ZONE_ID 22 /* this is the cell zone in fluent - THIS MAY CHANGE IN FINAL
MODEL*/
DEFINE_ON_DEMAND(definj_parallel_3D)
{
FILE* fp;
Domain *d = Get_Domain(1);
Thread *t = Lookup_Thread(d,ZONE_ID);
cell_t c;
double cell_center[ND_ND];
int cell_counter = 1;
real massflow;
real T;
real cellu;
real cellv;
real cellw;
real dia;
#if !RP_HOST /*if the CPU is not the host*/
if (I_AM_NODE_SAME_P(0))
{
	fp = fopen("idef0.inj", "w"); /*fopen is C code for writing text file
automatically. "w" mode is overwrite mode -  whatever is in that textfile
beforehand gets scrubbed when this function is called*/
}
else if (I_AM_NODE_SAME_P(1))
{
	fp = fopen("idef1.inj", "w");
}
else if (I_AM_NODE_SAME_P(2))
{
	fp = fopen("idef2.inj", "w");
}
else if (I_AM_NODE_SAME_P(3))
{
	fp = fopen("idef3.inj", "w");
}
… and so on…

else if (I_AM_NODE_SAME_P(17))
{
	fp = fopen("idef17.inj", "w");
}
else if (I_AM_NODE_SAME_P(18)) /*20 cores on bogstandard topsy machine minus
hostnode 19 */
{
	fp = fopen("idef18.inj", "w");
}
else if (I_AM_NODE_SAME_P(1000000))
```

```
{
	fp = fopen("idef_serial.inj", "w");
	Message("\n parallel inj UDF computing serial injection \n");
}
thread_loop_c(t, d)
{
begin_c_loop_int(c, t)
{
	massflow = -C_UDMI(c, t, 0) * C_VOLUME(c, t); /*the first UDM slot stores
the mass source (-ve)kg/m3s. I want it in (+ve)kg/s to define the DPM*/
	if (massflow > 0)
{
	C_CENTROID(cell_center, c, t);
	T = C_T(c, t);
	cellu = C_U(c, t);
	cellv = C_V(c, t);
	cellw = C_W(c, t);
	dia = C_UDMI(c, t, 1); /*inj_source UDF stores diameter in second UDM
slot*/
	/* functional part of the code - fprintf. From FLUENT guide:
	(( x y z u v w diameter temperature mass-flow) name ) is the form of
interest*/
	fprintf(fp, "(( ");
	fprintf(fp, "%e %e %e %e %e %e %e %e %e ", cell_center[0], cell_center[1],
cell_center[2], cellu, cellv, cellw, dia, T, massflow);
	fprintf(fp, ") ");
	fprintf(fp, "%d ", cell_counter);
	fprintf(fp, ")");
	fprintf(fp, "\n");
	cell_counter++;
}
}
end_c_loop_int(c, t)
}
fclose(fp);
Message("\n injection definition completed in node %d\n",myid);
#endif /*end compiler directive !RP_HOST*/

}
```

### *8.4.8 Journal file for injection iterations*

Journal file (.jou) for injection iterations. In this example, the injection is iterated once every 100 iterations. To line-up with the DPM iteration this was started one flow iteration before the DPM iteration – (eg: flow iteration _ _ 99). The code from the 4th line onwards was repeated (copy-and-paste method) for the required number of iterations.

A copy-and-paste method was used to repeat each injection iteration: this is not recommended coding practice. It is preferable to perform repeats using loops, this is not possible using Fluent journal files but is possible using Fluent scheme files. The alternative (automation using scheme code) was found to cause issues when the programme closed unexpectedly, for example from running out of computation time.

```
;;READ THE FILES
/file/read-case "TEST8.cas"
/file/read-data "TEST8.dat"
;; DELETE THE OLD INJS
/define/injections/delete-injection injection-0
/define/injections/delete-injection injection-1
/define/injections/delete-injection injection-2
/define/injections/delete-injection injection-3
… and so on …

/define/injections/delete-injection injection-18
;; CREATE NEW INJ FILES
/define/user-defined/execute-on-demand "definj_parallel_3D::libudf"
;; CREATE NEW INJS
/define/injections/create-injection injection-0 no yes file no "idef0.inj" no yes
yes custom "flagan_1::libudf" no no no no no no no no no "cond_allways_on::libudf"
no no
/define/injections/create-injection injection-1 no yes file no "idef1.inj" no yes
yes custom "flagan_1::libudf" no no no no no no no no no "cond_allways_on::libudf"
no no
/define/injections/create-injection injection-2 no yes file no "idef2.inj" no yes
yes custom "flagan_1::libudf" no no no no no no no no no "cond_allways_on::libudf"
no no
/define/injections/create-injection injection-3 no yes file no "idef3.inj" no yes
yes custom "flagan_1::libudf" no no no no no no no no no "cond_allways_on::libudf"
no no
… and so on …

/define/injections/create-injection injection-18 no yes file no "idef18.inj" no
yes yes custom "flagan_1::libudf" no no no no no no no no no
"cond_allways_on::libudf" no no
;;RUN FOR 100 ITERS
```

```
solve/iterate 100
;;WRITE FILE
/file/write-case-data "TEST8.cas" y
```

### *8.4.9 Concatenated user-defined function for growth law*

```
/*diffusion limited growth with Flagan correction James Hendry 11.09.15*/
#include "udf.h" /*necessary in any UDF, defines code as a fluent UDF*/
#include "math.h" /*include maths header. May be needed for powers */
#include "mem.h" /*include mem.h header. may be needed for C_DIFF_L */
DEFINE_DPM_LAW(flagan_1, p, ci) /*macro for dynamic DPM sources*/
{
       real Tp = P_T(p); /*particle temperature */
       real dp = P_DIAM(p); /*particle diameter */
       cell_t c = P_CELL(p); /*cell and thread of current particle */
       Thread *t = P_CELL_THREAD(p);
       real Pone; /*partial pressure of benzene in the gas (Pa)*/
       real Pd; /*equilibrium vapour pressure on particle surface (Pa)*/
       real D; /*Diffusivity of benzene in nitrogen (m^2/s)*/
       real dm_dt; /*rate of increase of particle size (kg/s)*/
       real Supersat;
       real Kn; /*particle knudsen number*/
       real mf; /*mass fraction of benzene in the gas*/
       real binary_lambda; /*binary mean free path of benzene in nitrogen (m)*/
       real ca; /*mean molecular speed of benzene gas (m/s)*/
       real FL_corr; /*Flagan and Sienfeld correction for knudsen-transition
growth*/
       P_T(p) = C_T(c, t); /*isothermal assumption*/
       mf = C_YI(c, t, 0); /*extract mass fraction of benzene gas from cell*/
       Pone = 1297.126 * mf / (mf / 78.11 + (1 - mf) / 28.014); /*convert mass
fraction to partial pressure (Pa)*/
       Pd = pow(10, 12.499 - 2452.5 / P_T(p)); /*August equation for equilibrium
vapour pressure on particle surface*/
       Supersat = Pone / Pd;
       if (Supersat > 1.) /*if condensation is possible*/
       {
              D = C_DIFF_L(c, t, 0, 1); /*extract diffusivity of benzene in
nitrogen in the cell, from Fluent*/
              ca = sqrt(8 * 8.314462175*C_T(c, t) / (M_PI*0.07811)); /*calculate
molecular speed based on cell temperature*/
              binary_lambda = D / (3 * M_PI / 32 * (1 + 78.11 / 28.014)*ca);
/*calculate binary mean free path of benzene in nitrogen using the diffusivity*/
              Kn = 2 * binary_lambda / dp; /*calculate particle Knudsen number from
binary mean free path*/
              FL_corr = (1 + Kn) / (1 + (4 * D / (ca*binary_lambda))*Kn*(1 + Kn));
/*calculate Flagan and Sienfeld correction*/
              dm_dt = 1016 * (2 * M_PI*D*dp*1.27670273229366e-28*(Pone - Pd) /
(1.38064852e-23*C_T(c, t)))*FL_corr; /*find dm_dt*/
       }
       else
       {
              dm_dt = 0;
       }
       P_MASS(p) += dm_dt * P_DT(p); /* add the growth in mass to the mass, then
update the diameter via the mass*/
       P_DIAM(p) = pow(6.0 * P_MASS(p) / (P_RHO(p) * M_PI), 1. / 3.);
}
DEFINE_DPM_SOURCE(dpm_growth_source,c,t,S,strength,p)
{
       real mp_dot;
       mp_dot = (P_MASS0(p) - P_MASS(p)) * strength; /*checked model and it
balances - division by cell vol not needed*/
       S->species[0] += mp_dot;
       S->mass += mp_dot;
```

```
      S->energy += mp_dot * -568429;
}
/*DPM switching law forces the condensation law to always on*/
DEFINE_DPM_SWITCH(cond_allways_on, p, coupled)
{
             P_CURRENT_LAW(p) = DPM_LAW_USER_1;

}
```

## 8.5 Meshes in Grid Independence Study

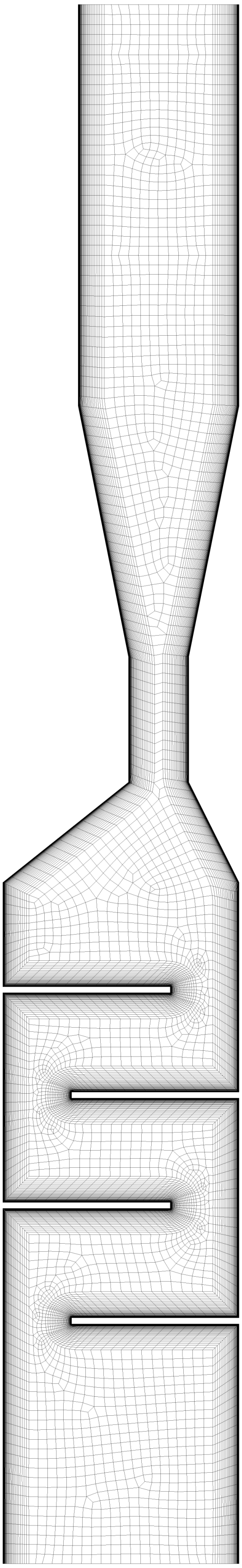
(i)

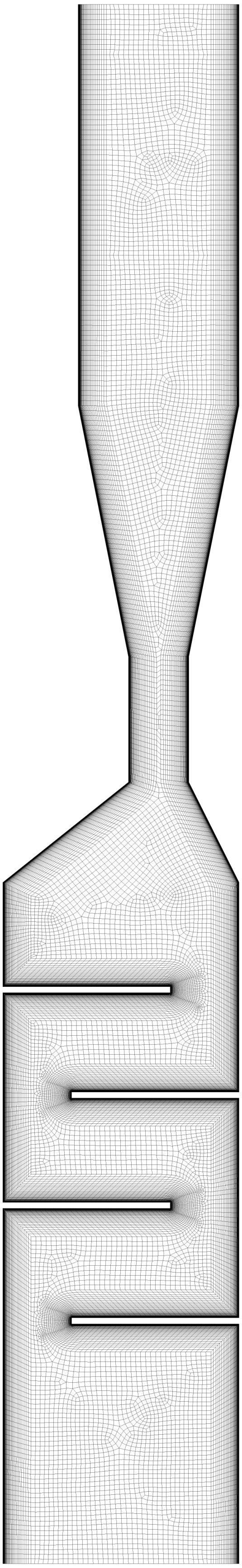
(ii)

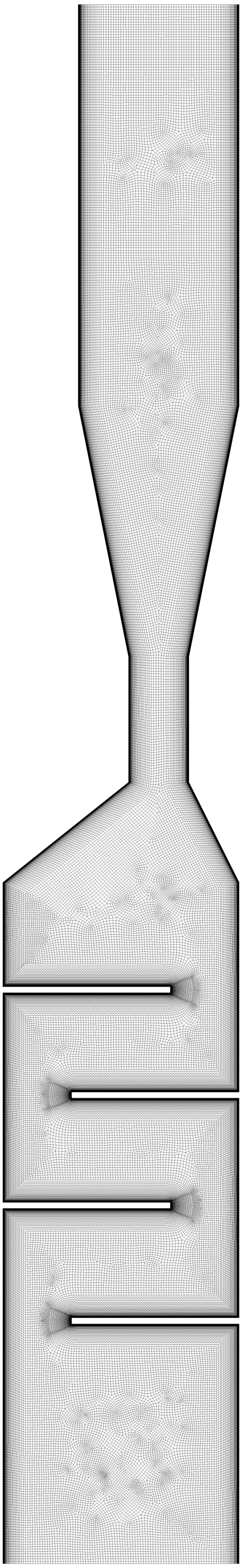
(iii)

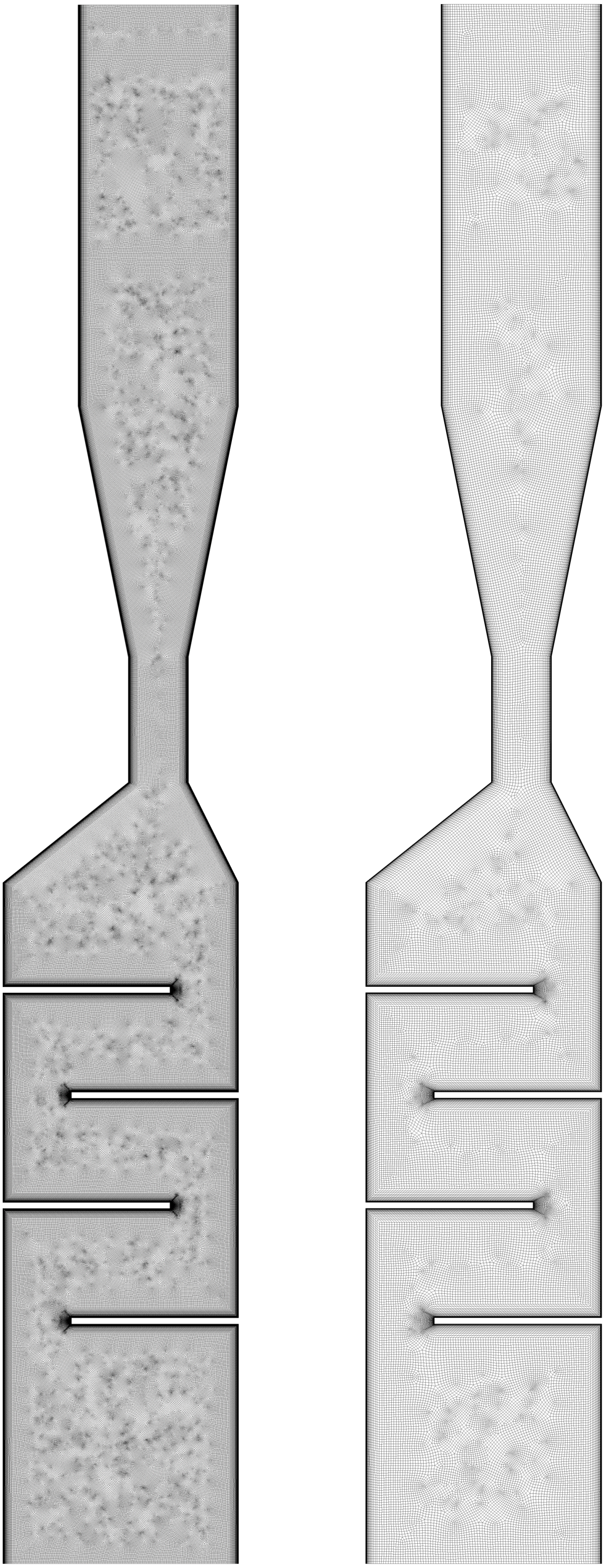

(iv) (v)

Mesh refinement for grid independence study. Left to right:

(vi) very coarse mesh
(vii) coarse mesh
(viii) medium mesh
(ix) fine mesh
(x) medium mesh with a growth rate of 1.2.